Dissertation

submitted to the

Combined Faculties of the Natural Sciences and Mathematics

of the Ruperto-Carola-University of Heidelberg, Germany

for the degree of

Doctor of Natural Sciences

Put forward by

CHRISTIAN TOBIAS LENZ

born in Frankfurt am Main, Germany

Oral examination: 28th of July, 2020

SEMI-ANALYTICAL MODELING OF PLANETESIMAL FORMATION

IMPLICATIONS FOR PLANET FORMATION AND THE SOLAR NEBULA

REFEREES:

APL. PROF. DR. HUBERT KLAHR

PROF. DR. MARIO TRIELOFF

“Der Anfang der sich bildenden Planeten ist nicht allein in der Newtonischen Anziehung zu suchen. Diese würde bei einem Partikelchen, von so ausnehmender Feinigkeit, gar zu langsam und schwach sein. Man würde vielmehr sagen, dass in diesem Raume die erste Bildung durch den Zusammenlauf einiger Elemente, die sich durch die gewöhnlichen Gesetze des Zusammenhanges vereinigen, geschehe, bis derjenige Klumpen, der daraus entstanden, nach und nach so weit angewachsen, dass die Newtonische Anziehungskraft an ihm vermögend geworden, ihn durch seine Wirkung in die Ferne immer mehr zu vergrößern.”

– Immanuel Kant (1755)

Abstract

Planetesimals are the hypothetical building blocks of planets, halfway between dust aggregation and the formation of planetary embryos. The typical diameter of newborn planetesimals was found to be around 100 km. The time-dependent production of these planetesimals and their radial distribution in disks around young stars is still unclear. This thesis proposes a semi-analytical model for the planetesimal formation rate that is regulated by the radial pebble flux. The model is implemented into a code that solves the evolution of gas as well as the growth and radial motion of grains. Within this model, planetesimals form as soon as micron-sized dust has grown to pebble-size (typically $\sim \mathrm{mm} - \mathrm{cm}$) and a critical pebble flux is reached. The resulting spatial planetesimal profile is steeper compared to the initial dust and gas distribution. E.g., for a temperature profile $T \propto r^{-0.5}$, the planetesimal profile is expected to follow $\Sigma_\mathrm{p} \propto r^{-2.25}$ in the inner disk regions. The maximum local planetesimal production is reached for a planetesimal formation efficiency that allows the planetesimal formation timescale and the pebbles drift timescale to be equal. A disk parameter study is performed which enables to set limits on possible parameters for the Solar Nebula by comparing the produced planetesimal profiles with mass constraints for initial planetesimals. This thesis shows that the Solar Nebula was not too large, enclosing most of the mass within 50 au. Outside of 50 au, particle traps needed several hundreds of orbits to form or never formed there. Compared to the mass constraints, the most appealing case that is analyzed in this thesis has a disk mass of around 0.1 solar masses, a fragmentation speed of particles of $2\,\mathrm{m\,s^{-1}}$, and moderate to weak turbulence ($\alpha_\mathrm{t} = 3 \cdot 10^{-4}$). The model introduced in this thesis does not require fine tuning in order to meet mass constraints for the Solar Nebula which stresses the applicability of the proposed parameterization to models of planet formation. By sorting pebbles by their origins, this thesis shows that a significant amount of pebble mass passed major ice lines before forming planetesimals in the inner Solar Nebula or before they were accreted by planetary embryos at the current positions of the asteroid belt and Earth. The relative contribution to planetesimals from regions of different particle origins changes for different times of planetesimal formation. This thesis concludes with the importance of pebble transport and the planetesimal formation efficiency for shaping the spatial distribution of planetesimals. The presented planetesimal formation rate model can be used to bridge the gap between the phases of dust growth and the formation of planetary embryos.

Zusammenfassung

Planetesimale sind die hypothetischen Bausteine von Planeteten auf halbem Weg zwischen Staubwachstum und der Bildung von planetaren Embryonen. Der typische Durchmesser von neugeborenen Planetesimalen beläuft sich auf ungefähr 100 km. Die zeitabhängige Entstehung dieser Planetesimale und deren radiale Verteilung in Scheiben um junge Sterne ist noch ungeklärt. In dieser Dissertation wird ein semi-analytisches Modell für die Planetesimalentstehungrate vorgeschlagen, welche vom radialen Fluss kieselsteingroßer Partikel reguliert wird. Dieses Modell ist in einen Code implementiert, der die Entwicklung von Gas und das Wachstum sowie die radiale Bewegung von Partikeln berechnet. Innerhalb dieses Modells werden Planetesimale gebildet, sobald mikrometergroßer Staub zu Kieselsteingröße (typischerweise $\sim \mathrm{mm} - \mathrm{cm}$) herangewachsen und ein kritischer Partikel-Fluss erreicht ist. Das resultierende radiale Planetesimalprofil ist steiler als die anfängliche Verteilung von Staub und Gas. Beispielsweise ist für ein Temperaturprofil von $T \propto r^{-0.5}$ ein Planetesimalprofil zu erwarten, welches dem Potenzgesetz $\Sigma_{\mathrm{p}} \propto r^{-2.25}$ folgt. Das Maximum lokaler Planetesimalentstehung wird für eine Planetesimal-Entstehungs-Effizienz erreicht, die gleiche Werte der Planetesimal-Entstehungs-Zeitskala und der Partikel-Drift-Zeitskala impliziert. Weiterhin führe ich eine Scheibenparameterstudie durch, die durch einen Vergleich zwischen der entstandenen Planetesimalprofilen (für jedes Set der getesteten Parameter) und den Massenbeschränkungen für anfängliche Planetesimale erlaubt, Grenzen für mögliche Parameter für den solaren Nebel zu finden. Diese Arbeit zeigt, dass der solare Nebel nur so groß sein konnte, dass die meiste Masse innerhalb von 50 au lag. Außerhalb von 50 au haben Partikelfallen mehrere hundert Umläufe benötigt, um zu entstehen, oder haben sich dort nie gebildet. Das zur Entstehung des Sonnensystems passendste Set von Scheibenparametern, das in dieser Dissertation untersucht wird, hat eine anfängliche Scheibenmasse von 0.1 Sonnenmassen, eine Fragmentationsgeschwindigkeit der Partikel von $2\,\mathrm{m\,s^{-1}}$, sowie moderate bis schwache Turbulenz ($\alpha_{\mathrm{t}} = 3 \cdot 10^{-4}$). Das in dieser Arbeit eingeführte Modell erfordert nicht viel Feinabstimmung, um die Massenbeschränkungen des solaren Nebels zu erfüllen, was die Anwendbarkeit der vorgeschlagenen Parameterisierung für Planetenentstehungsmodelle unterstreicht. Durch Sortierung von Partikeln nach deren Ursprungsort wird gezeigt, dass ein signifikanter Anteil der kieselsteingroßen Objekte wichtige Eislinien passiert hat, bevor diese Planetesimale im inneren solaren Nebel bilden oder bevor sie durch planetare Embryonen akkretiert werden. Dies gilt insbesondere für die aktuellen Positionen der Erde und des Asteroidengürtels. Der relative Beitrag von verschiedenen Ursprungsregionen der Partikel zu Planetesimalen variiert mit der Zeit. Diese Doktorarbeit zeigt, dass Partikeltransport und der Wert der Planetesimalentstehungseffizienz entscheidende Rollen für die räumliche Planetesimalverteilung spielen. Das vorgeschlagene Modell für die Entstehungsrate von Planetesimalen kann genutzt werden, um die Brücke zwischen der Phase von Staubwachstum und der von planetarer Embryonenentstehung zu schlagen.

For my family and the people I worked with.

Contents

1

Introduction

How did Earth form, the only planet we know of that allowed life to develop? This is the question humans asked themselves since many thousands of years. By looking at our own solar system, we find terrestrial planets, gas giants, and ice giants. In order to find answers to the question how Earth formed we also have to understand the formation of other planets. There is theoretical and observational evidence that planets form inside of disks consisting of gas and growing dust around young stars. Understanding those disks with their gas and particle dynamics is crucial for understanding planet formation.

1.1 Historical overview

Kant (1755) suggested that planets form out of local enhancements of dust and gas orbiting the sun, where he further hypothesized that small particles stick together until they reach a certain size and become gravitationally unstable. In the year 1796, Pierre Simon de Laplace put forward the theory of a flat disk inside which condensing rings form, leading to planet formation (Laplace & Young, 1821). Weizsäcker (1943) combined these ideas with the physical understanding and mathematical tools of that time. He found that mixing due to turbulent motions separates the solar nebula into a central object and an infinite disk. The former contains most of the mass while most of the angular momentum is in the disk. Weizsäcker (1948) derived equations of motion for a circumstellar disk. He also argued that turbulent viscosity should be the dominating process of dissipation and used a mixing length description where this length follows a disk radius power-law. Lüst (1952) and Lynden-Bell & Pringle (1974) used this idea to compute a solution for the time evolution of the gas disk.

Planet formation is a by-product of star formation. If a molecular cloud exceeds a critical mass, namely the Jeans mass (Jeans, 1902), it becomes gravitationally unstable and collapses. Turbulence, rotational energy, and magnetic fields, however, could stabilize the cloud. Turbulence acts as a double-edged sword, where on the one hand it leads to concentrations on large scales, on the other hand it can disrupt particle concentrations on small scales (Klessen et al., 2005). Rotational energy can cause the formation of a binary star system and the formation of circumstellar disks, while magnetic fields can drive outflows (e.g. Larson, 2003). Our theoretical understanding of dynamical evolution of accretion disks, such as a circumstellar disk, is still based on Shakura & Sunyaev (1973) and Lynden-Bell & Pringle (1974). Safronov (1969) presented equations on particle growth, the formation of asteroid-sized material (so-called planetesimals), and more that are still used today.

Today it is commonly accepted that planetesimal formation has roughly four different stages, see Fig. 1.1. The initial stage starts with a molecular cloud consisting of gas and dust that is massive and cool enough to collapse (Class 0), forming a protostar in the center. This is followed by a phase in which a disk is forming while the envelope is still accreted and outflows at the stellar poles might occur (Class 1). Once the envelope disappeared, a gas and dust disk surrounding the star is left (Class 2). This is the stage within most of the tiny dust grains grow about 4 to 5 orders of magnitude in size, the building blocks of planets are formed, and planets might be produced. Planets must form before the gas disk is gone. Without a gas disk, debris and a potential planetary system are visible (Class 3). The focus of this thesis is Class 2 disks that transition to Class 3.

The high resolution of telescopes like the Atacama Large Millimeter/submillimeter Array (ALMA) allow the analysis of substructures of circumstellar disks. One example would be the Disk Substructures at High Angular Resolution Project (DSHARP; e.g., Andrews et al., 2018) that allows analysis of ring structures (e.g. Dullemond et al., 2018) and shows indirect indications for the formation of asteroid-sized objects (Stammler et al., 2019), so-called planetesimals.

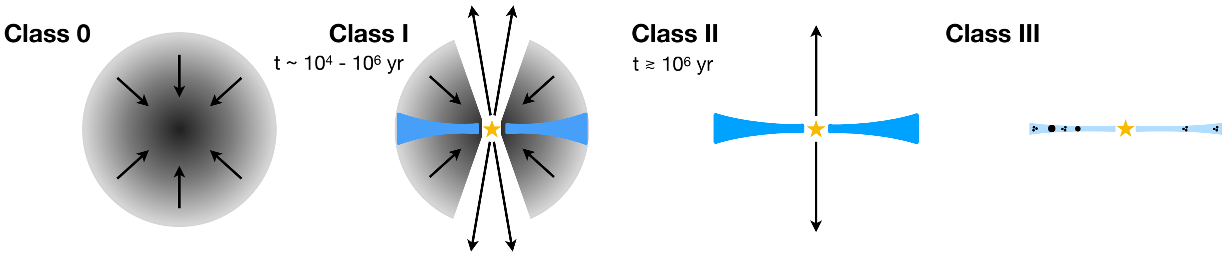

Figure 1.1: Schematic illustration of different stages of young stellar objects (not to scale). The different stages of planet formation starting from a collapsing molecular cloud are classified as follows. (0) A molecular cloud collapses due to its own gravity forming a protostar (Class 0). (1) A disk forms (blue) while the stellar envelope is accreted (Class 1). (2) Once the circumstellar disk is not embedded into a cloud anymore it is called Class 2. Once the gas disk dissipates, a debris disk remains with a potential planetary system (Class 3). This picture is taken from Pohl (2018).

1.2 Gas dynamics in a circumstellar disk

1.2.1 Gas disk pressure scale height

Once a collapsing molecular cloud reaches densities leading to the regime of fluid dynamics, the pressure gradient force supports the gas against gravity, leading to a hydrostatic equilibrium, see Fig. 1.2. Disks are thin in the sense of a small height over disk radius ratio (e.g. D'Alessio et al., 1998; Pfeil & Klahr, 2019). Cylindrical coordinates are commonly used to describe the geometry of disks with cylindrical radius r and height z. We can assume that circumstellar disks efficiently cool via radiation over their large surface areas. Higher densities in the mid-plane cause a vertical pressure gradient that stabilizes the disk on scales of a pressure scale height h_g. In a steady-state situation, the pressure gradient acceleration and vertical component of the stars gravitational attraction $g_{\star,z}$ (see Fig. 1.3) balance each other. For radial distances much larger than the vertical distance from the mid-plane, $r \gg z$, the central star can be approximated as point mass. As shown in Fig. 1.3, the vertical gravitational acceleration toward the mid-plane for

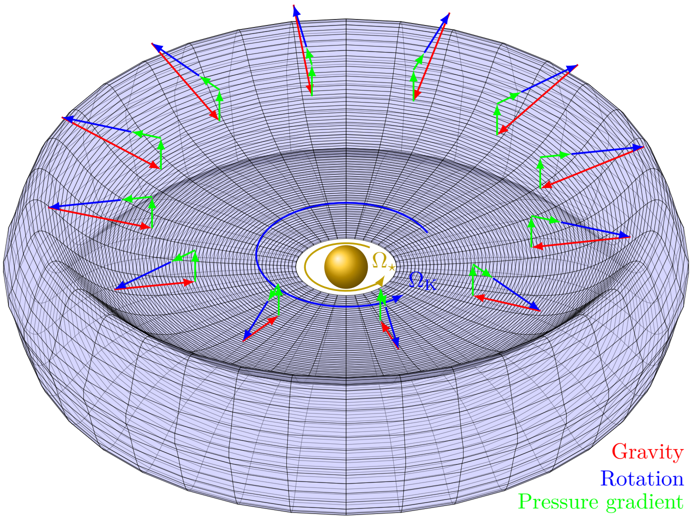

Figure 1.2: Force balance acting on gas in a circumstellar disk. Red arrows show the direction of gravitational attraction toward the star, blue arrows indicate the centrifugal force, and the pressure gradient force is depicted as green arrows. The disk is rotating with Keplerian angular frequency Ω_K while the star is spinning with $\Omega_\star$. The figure is taken from the author's master thesis (Lenz, 2016).

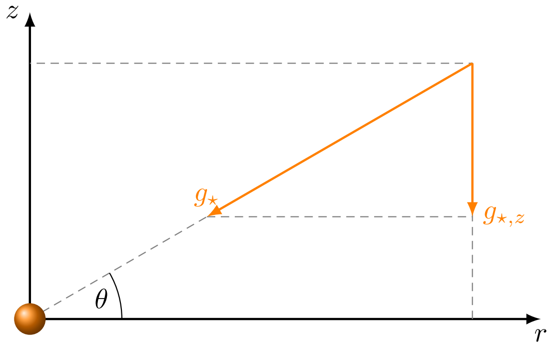

Figure 1.3: Considering the central star as point mass and neglecting self-gravity from the disk, at a given height z one can compute the vertical gravity component $g_{\star,z}$. The cylindrical radius r is equal to the distance to the star in the mid-plane. The figure is taken from the author's master thesis (Lenz, 2016).

a gas parcel at a distance r and height z is given by

$$g_{\star,z} = g_\star \sin\theta = \frac{GM_\star}{r^2+z^2}\cdot\frac{z}{(r^2+z^2)^{1/2}} \overset{r \gg z}{\simeq} \frac{GM_\star z}{r^3} = \Omega^2 z, \tag{1.1}$$

where G is Newton's gravitational constant, $M_\star$ is the mass of the star, and the Keplerian angular frequency is

$$\Omega = \sqrt{\frac{GM_\star}{r^3}}. \tag{1.2}$$

Using the ideal gas law, we can write

$$P = \rho_\mathrm{g} c_\mathrm{s}^2, \tag{1.3}$$

with *isothermal* sound speed

$$c_\mathrm{s} = \sqrt{\frac{\mathrm{k_B} T}{m_\mathrm{g}}}. \tag{1.4}$$

Here, $\mathrm{k_B}$ is the Boltzmann constant, T the temperature, and m_g the mean molecular mass of the gas. The pressure of the gas is denoted as P and the gas density as ρ_g (mass per 3-d volume). In hydrostatic equilibrium the pressure gradient force is in balance with the gravitational pull:

$$\frac{c_\mathrm{s}^2}{\rho_\mathrm{g}}\frac{\mathrm{d}\rho_\mathrm{g}}{\mathrm{d}z} \simeq -\Omega^2 z. \tag{1.5}$$

For a vertically isothermal disk, integration leads to

$$\rho_\mathrm{g}(r,z) = \rho_{\mathrm{g},0}(r)\cdot\exp\left(-\frac{z^2}{2h_\mathrm{g}^2}\right), \tag{1.6}$$

where the *vertical disk scale-height* is defined as

$$h_\mathrm{g} := \frac{c_\mathrm{s}}{\Omega}. \tag{1.7}$$

The density in the mid-plane is given by

$$\rho_{\mathrm{g},0}(r) = \frac{1}{\sqrt{2\pi}}\frac{\Sigma_\mathrm{g}(r)}{h_\mathrm{g}(r)}, \tag{1.8}$$

where the *column density* is defined as

$$\Sigma_\mathrm{g}(r,t) := \int_{-\infty}^{\infty} \rho_\mathrm{g}(r,z,t)\,\mathrm{d}z. \tag{1.9}$$

If the disk is heated by radiation from the central star only, the temperature scales as $T \propto r^{-0.5}$ (e.g. Armitage, 2010). This yields a scale height-to-disk radius ratio of $h_\mathrm{g}/r \propto r^{1/4}$, i.e. a flaring disk.

1.2.2 Turbulent viscosity

Shakura & Sunyaev (1973) introduced the so-called α-model for gas transport due to turbulent motion. In this original paper the model was used to explain the brightness of disks around black holes. The model uses a dimensionless scaling factor for the turbulent viscosity and became the canonical turbulent angular momentum transport prescription for circumstellar disks. While Shakura & Sunyaev (1973) used the α_t parameter as a scaling factor of the turbulent velocities, D. N. C. Lin (1980) and Pringle (1981) split it onto the turbulent velocity and turbulent length scale. The turbulent viscosity then reads

$$\nu = (\alpha_\mathrm{t}^s c_\mathrm{s}) \cdot (\alpha_\mathrm{t}^{1-s} h_\mathrm{g}). \tag{1.10}$$

The parameter $0 \leq s \leq 1$ controls how α_t splits up into a characteristic turbulent velocity and length scale. The value of the turbulence parameter is expected to be in the range $0 \leq \alpha_\mathrm{t} \leq 1$ since supersonic motions would lead to shocks and eddies should not be larger than the gas pressure scale height h_g. Cuzzi et al. (2001) argued for $s = 1/2$. They assume that Rossby numbers of at least unity are required to allow a Kolmogorov cascade (Kolmogorov, 1991). This Rossby number is given by the frequency of the largest eddies over the orbital frequency of the disk. Assuming that the Rossby number has a value of unity, this leads to $s = 1/2$. Typical values for the turbulence parameter are in the range $10^{-4} \lesssim \alpha_\mathrm{t} \lesssim 10^{-2}$ as shown in simulations (for a review see e.g. Turner et al., 2014) and by observations (Teague et al., 2016; Flaherty et al., 2017).

1.2.3 The disk evolution equation

Combining conservation of mass and conservation of angular momentum, yields a partial differential equation for the evolution of the gas column density (Pringle, 1981)

$$\frac{\partial \Sigma_\mathrm{g}}{\partial t} = \frac{3}{r}\frac{\partial}{\partial r}\left[r^{1/2}\frac{\partial}{\partial r}\left(\nu\Sigma_\mathrm{g} r^{1/2}\right)\right] + \dot{\Sigma}_\mathrm{w}, \tag{1.11}$$

where $\dot{\Sigma}_\mathrm{w}$ is a loss term due to photoevaporative winds.

For viscously evolving disks with no additional sink term ($\dot{\Sigma}_\mathrm{w} = 0$) and a viscosity that scales as $\nu \propto r^\gamma$, the solution to the gas column density evolution equation is self-similar and can be written as (Lynden-Bell & Pringle, 1974; Hartmann et al., 1998)

$$\Sigma_\mathrm{g}(r,t) = \Sigma_\mathrm{c}(t)\left(\frac{r}{r_\mathrm{c}(t)}\right)^{-\gamma} \exp - \left(\frac{r}{r_\mathrm{c}(t)}\right)^{2-\gamma}, \tag{1.12}$$

where the time dependent normalization is proportional to the initial disk mass, M_disk,

$$\Sigma_\mathrm{c}(t) := (2-\gamma)\frac{M_\mathrm{disk}}{2\pi {r_1}^2}\left(\frac{r_\mathrm{c}(t)}{r_1}\right)^{-5/2}, \tag{1.13}$$

the time dependent characteristic radius is

$$r_\mathrm{c}(t) = r_1 \tau_\mathrm{c}^{1/(2-\gamma)}, \tag{1.14}$$

and the dimensionless viscous time is defined as

$$\tau_\mathrm{c} := \frac{3(2-\gamma)^2 \nu_1 t}{{r_1}^2} + 1. \tag{1.15}$$

Adopting the turbulent viscosity from Shakura & Sunyaev (1973), the initial viscosity is given by $\nu_1 = \alpha_\mathrm{t} c_\mathrm{s}(r_1) h_\mathrm{g}(r_1)$.

1.2.4 Observed gas structures and disk lifetimes

Disk lifetimes were observed to be around $3 \cdot 10^6$ yr Haisch et al. (2001); Mamajek (2009). According to these observations, only a few exist for $6 \cdot 10^6$ yr or longer. However, the data of these studies is based on stars very close to the cluster center. Those disks are expected to be prone to disk erosion due to many-body effects. Hence, disk lifetimes can potentially reach around 10^7 yr (Pfalzner et al., 2014). After that time the gas disk is gone and a Class 3 system remains. If a planetary system is observed, this means that these planets must have formed within that time.

The high resolution of modern telescopes allow the resolution and analysis of structures in circumstellar disks. For instance, the DSHARP survey (Andrews et al., 2018) reveals (multiple) ring structures, gaps, spirals, and non-axisymmetric dust concentrations. In the most cases it is still unclear whether these structures are a result of sufficiently massive planets, axisymmetric gas pressure bumps, vortices, or other effects. Since (magneto-)hydrodynamical effects, planets embedded in the disk, or observational effects can influence the observed structures, the interpretation of these observations relies on theoretical modeling.

1.3 Particle dynamics in a circumstellar disk

1.3.1 Friction and Stokes number

The regime of particle friction depends on the gas mean free path and particle size. In the Epstein regime (Epstein, 1924), the gas mean free path is larger than the radius of particles and the drag force F_D scales linearly with the relative velocity v_rel of gas and particles. For spherical particles the drag force is given by

$$F_\mathrm{D} = -\frac{4\pi}{3} a^2 \rho_\mathrm{g} v_\mathrm{th} v_\mathrm{rel}. \tag{1.16}$$

The radius of particles is a, the gas density (mass per 3-d volume) is given by ρ_g, and the mean thermal velocity of gas by v_th. If the mean free path of gas is smaller than the particles, the gas can be considered as a fluid on the scales of the particle radius and the friction force becomes

$$F_\mathrm{D} = -\frac{C_\mathrm{D}}{2} \pi a^2 \rho_\mathrm{g} {v_\mathrm{rel}}^2, \tag{1.17}$$

where C_D is the dimensionless drag coefficient that can be described as a function of the Reynolds number (Cheng, 2009).

Particles adapt to the motion of the gas on the stopping timescale

$$\tau_\mathrm{s} := \frac{m v_\mathrm{rel}}{F_\mathrm{D}}. \tag{1.18}$$

The Stokes number of particles is defined as this stopping time over the dynamical timescale of the gas. For circumstellar disks this gives

$$\mathrm{St} := \Omega \tau_\mathrm{s}. \tag{1.19}$$

For the particles in the Epstein drag regime, the Stokes number in the mid-plane can be obtained via Eq. (1.8) and $m = 4\pi a^3 \rho_\mathrm{m}/3$ (ρ_m is the internal material density of particles) which yields

$$\mathrm{St}_\mathrm{Ep,0} = \frac{\pi}{2} \frac{a \rho_\mathrm{m}}{\Sigma_\mathrm{g}}. \tag{1.20}$$

Particles in the fluid drag regime stay most likely in the Stokes drag regime in which case the drag coefficient is given by (see Eq. (126) in Stokes, 1851)

$$C_{\mathrm{D}} = 24/\mathrm{Re} \tag{1.21}$$

with Reynolds number

$$\mathrm{Re} := \frac{2av_{\mathrm{rel}}}{\nu_{\mathrm{mol}}}. \tag{1.22}$$

The molecular viscosity is given by (Chapman, 1916)

$$\nu_{\mathrm{mol}} = \frac{1}{2} v_{\mathrm{th}} \lambda_{\mathrm{g}}. \tag{1.23}$$

The mean free path of gas λ_{g} depends on the velocity distribution and is derived in Appendix D, where different cases are discussed. The Stokes number in the mid-plane for particles in the Stokes drag regime is given by

$$\mathrm{St}_{\mathrm{St},0} = \frac{2\pi}{9} \frac{a^2 \rho_{\mathrm{m}}}{\Sigma_{\mathrm{g}} \lambda_{\mathrm{g}}}. \tag{1.24}$$

1.3.2 Particle motion

In order to hold a specific orbit at a given cylindrical distance from the star r, particles need to be in a force balance between an outward pointing centrifugal force and the inward pointing gravitational pull from the star, leading to Keplerian azimuthal velocities. Gas parcels feel support from the pressure gradient force against the gravitational pull. Hence, to hold the same orbit as particles, gas parcels need slower azimuthal velocities. Particles that are coupled to the gas ($\mathrm{St} < 1$) move with the gas that is moving sub-Keplerian. The result is a centrifugal deficiency causing those particles to drift inward. Particles that are decoupled from the gas ($\mathrm{St} > 1$) feel a headwind induced by the relative velocities between gas and the particles. This headwind slows down these particles, leading to drift toward higher gas pressure. These effects lead to radial drift (Whipple, 1972; Adachi et al., 1976; Weidenschilling, 1977a; Nakagawa et al., 1986)

$$v_{\mathrm{drift}} := v_{\mathrm{r}} - v_{\mathrm{K}} = \frac{\mathrm{St}}{\mathrm{St}^2 + 1} \frac{h_{\mathrm{g}}}{r} \frac{\partial \ln P}{\partial \ln r} c_{\mathrm{s}} \tag{1.25}$$

and azimuthal drift (Nakagawa et al., 1986)

$$v_{\varphi} - v_{\mathrm{K}} = \frac{v_{\mathrm{drift}}}{2} \frac{1}{\mathrm{St}}. \tag{1.26}$$

Vertical settling for particles coupled to the gas ($\mathrm{St} < 1$) can be computed via equilibrium of the vertical gravity component of the star with the drag force. This give the terminal settling velocity (Safronov, 1969, p. 26)

$$v_{\mathrm{sett}} = -z\Omega \mathrm{St}. \tag{1.27}$$

These equations are valid if the back-reaction of particles on the gas is negligible. If this effect is significant, the size distribution of particles needs to be taken into account (Tanaka et al., 2005).

1.3.3 Particle growth and fragmentation

Particle growth depends on the number densities of collision partners, the cross section, and the relative velocities. For the latter there are five sources leading to relative velocities. For a velocity distribution that follows the Maxwell-Boltzmann distribution (Maxwell, 1860; Boltzmann, 1872), the mean relative velocity due to Brownian motion is

$$\Delta v_{\mathrm{BM},i,j} = \sqrt{\frac{8 k_{\mathrm{B}} T (m_i + m_j)}{\pi m_i m_j}}. \tag{1.28}$$

Brownian motion is a random motion caused by thermal gas dynamics. The relative velocities induced by the gas are faster for smaller particles. As long as the mean free path of gas is larger than the particles, the mean free path of particles between collisions is ballistic. Only if the gas mean free path is smaller than the particle, its trajectory overlaps with itself. For those particle sizes at which Brownian motion contributes significantly to the total relative velocities between grains in circumstellar disks, the gas mean free path is always larger than the grains, thus, only the ballistic case needs to be considered.

The relative velocities of the systematic motions are given by relative radial and azimuthal drift,

$$\Delta v_{r,i,j} = \frac{c_\mathrm{s}^2}{v_\mathrm{K}} \frac{\partial \ln P}{\partial \ln r} \left| \frac{1}{\mathrm{St}_i + \mathrm{St}_i^{-1}} - \frac{1}{\mathrm{St}_j + \mathrm{St}_j^{-1}} \right|, \tag{1.29}$$

$$\Delta v_{\varphi,i,j} = \frac{1}{2} \frac{c_\mathrm{s}^2}{v_\mathrm{K}} \frac{\partial \ln P}{\partial \ln r} \left| \frac{1}{\mathrm{St}_i^2 + 1} - \frac{1}{\mathrm{St}_j^2 + 1} \right|. \tag{1.30}$$

Assuming that the Stokes number does not change over the vertical extent in which is most of the mass, the mass weighted average of the relative settling velocity, another source of systematic relative velocities, can be estimated as

$$\Delta v_{z,i,j} = \frac{\int_{-\infty}^{\infty} \left|\mathrm{St}_i - \mathrm{St}_j\right| \Omega |z| \rho_i \rho_j \,\mathrm{d}z}{\int_{-\infty}^{\infty} \rho_i \rho_j \,\mathrm{d}z} = \frac{2}{\sqrt{2\pi}} \left|\mathrm{St}_i - \mathrm{St}_j\right| \frac{h_i h_j}{\sqrt{h_i^2 + h_j^2}} \Omega. \tag{1.31}$$

The particle scale height of particle i depends on its Stokes number and is for $\mathrm{St} < 1$ given by (Dubrulle et al., 1995)

$$h_i = \left(1 + \frac{\mathrm{St}_i}{\delta_z}\right)^{-1/2} h_\mathrm{g}, \tag{1.32}$$

with δ_z being the dimensionless vertical particle diffusion which is for isotropic turbulence usually assumed to be equal to the turbulence parameter α_t. Radial drift, azimuthal drift, and vertical motion scale with size. Hence, these systematic velocities cause relative motion between particles of different sizes. Another random motion such as Brownian motion are turbulence induced ones. Different regimes apply for different Stokes and Reynolds numbers, giving ($\mathrm{St}_i \geq \mathrm{St}_j$; Ormel & Cuzzi, 2007)

$$\Delta v_{\mathrm{turb},i,j} = \begin{cases} \sqrt{\alpha_\mathrm{t}} c_\mathrm{s} \sqrt{\dfrac{\mathrm{St}_i - \mathrm{St}_j}{\mathrm{St}_i + \mathrm{St}_j}} \sqrt{\dfrac{\mathrm{St}_i^2}{\mathrm{St}_i + \mathrm{Re}^{-1/2}} - \dfrac{\mathrm{St}_j^2}{\mathrm{St}_j + \mathrm{Re}^{-1/2}}} & , \mathrm{St}_{i,j} \leq \mathrm{Re}^{-1/2} \\ \sqrt{\alpha_\mathrm{t}} c_\mathrm{s} \sqrt{2.2\mathrm{St}_i - \mathrm{St}_j + \dfrac{2\mathrm{St}_i^2}{\mathrm{St}_i + \mathrm{St}_j} \left(\dfrac{1}{2.6} + \dfrac{\mathrm{St}_j^3}{1.6\mathrm{St}_i^3 + \mathrm{St}_i^2 \mathrm{St}_j} \right)} & , \mathrm{Re}^{-1/2} \leq \mathrm{St}_i \leq 1\,. \\ \sqrt{\alpha_\mathrm{t}} c_\mathrm{s} \sqrt{\dfrac{1}{1 + \mathrm{St}_i} + \dfrac{1}{1 + \mathrm{St}_j}} & , 1 > \mathrm{St}_i \end{cases} \tag{1.33}$$

Here, $\sqrt{\alpha_\mathrm{t}} c_\mathrm{s}$ is the typical eddy velocity and the Reynolds number is defined as

$$\mathrm{Re} = \frac{\nu}{\nu_\mathrm{mol}} \overset{(1.10)}{=} \frac{\alpha_\mathrm{t} c_\mathrm{s} h_\mathrm{g}}{\nu_\mathrm{mol}} \overset{(1.7)}{=} \frac{\alpha_\mathrm{t} c_\mathrm{s}^2}{\nu_\mathrm{mol}} \tag{1.34}$$

with molecular viscosity ν_mol.

Fig. 1.4 shows the five sources of relative velocities and the square root of the quadratic sum. Early growth of micron-sized particles is dominated by Brownian motion. Typically around ten micron relative turbulent motions are the dominant source of relative particle velocities. For larger grains, all sources can contribute significantly except Brownian motion. Since collisions of the most massive particles with each other leads to the strongest mass gain per time, particles will follow the path close to the diagonal of equal-sized collision partners until hitting one of the growth barriers. This enables us to simplify the process of particle growth significantly by approximating growth of the most

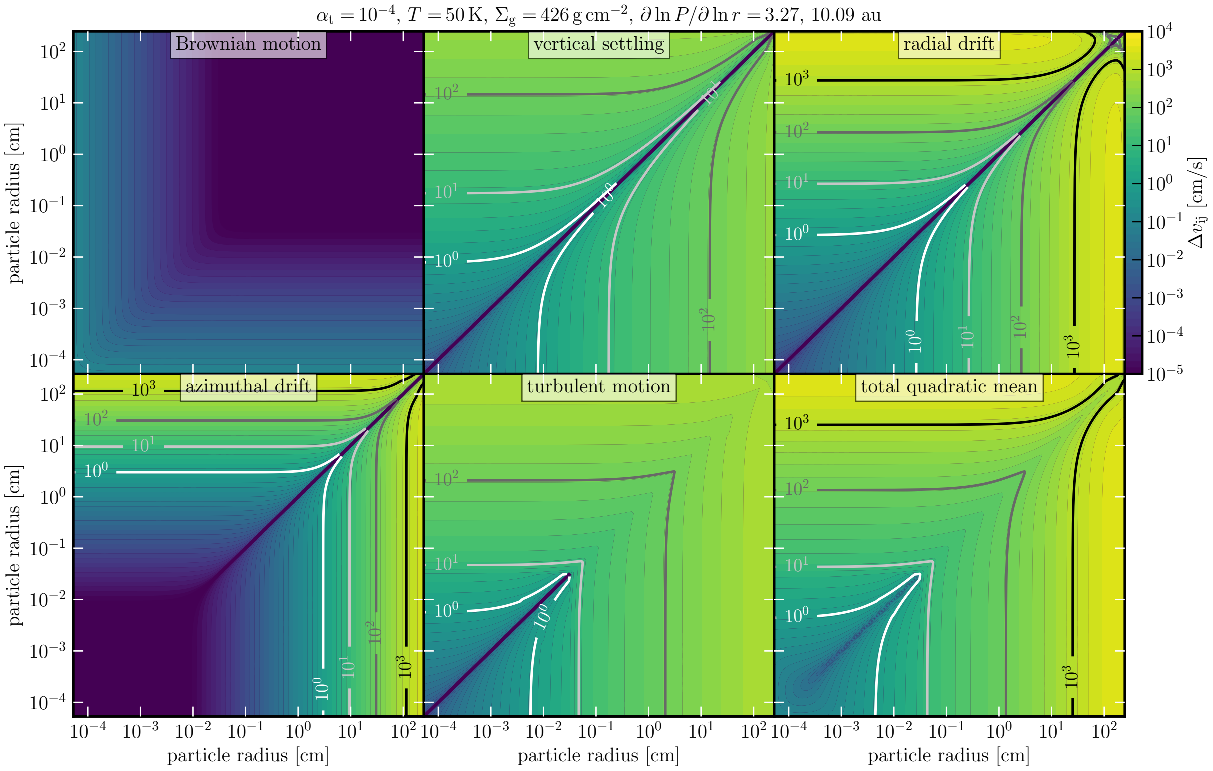

Figure 1.4: Relative velocities of particles due to Brownian motion vertical settling, radial drift, azimuthal drift, and turbulent motion. In the lower right panel, the square root of the quadratic sum of these sources of relative velocity is shown. Along the diagonals, i.e. for collision partners with equal Stokes numbers, the relative velocity is zero for vertical settling, radial and azimuthal drift, as well as for the first turbulence regime. For this plot, a turbulence parameter of $\alpha_t = 10^{-4}$, a mid-plane temperature of $T = 50\,\mathrm{K}$, a gas column density $\Sigma_g = 425\,\mathrm{g\,cm^{-2}}$, and a logarithmic pressure gradient of 3.27 were used which can be typical values at 10 au.

massive grains via a monodisperse growth model, see Appendix E.

For sufficiently low collision energies, this means low enough relative velocities, particles can grow via sticking. However, once a critical relative velocity v_f is reached, particle collisions lead to disruption. The distribution of fragments is canonically described by a power-law,

$$n_m(m)\,\mathrm{d}m \propto m^{-\xi}\,\mathrm{d}m. \tag{1.35}$$

Here, $n_m\,\mathrm{d}m$ is the number density (mass per 3-d volume) of fragments in an infinitesimally small mass interval $\mathrm{d}m$. Both experiments (see e.g. Davis & Ryan, 1990; Blum & Münch, 1993; Musiolik et al., 2016) and theoretical studies (Ormel et al., 2009) find values for ξ between 1 for lower velocity impacts and 2 for high-velocity impacts. Steady state solutions between coagulation and fragmentation (Dohnanyi, 1969) lead to a value of $\xi = 1.83$. Tanaka et al. (1996) argued that this value is an implication of self-similarity of the particle size distribution. The mass given in intervals of $[m, m + \mathrm{d}m]$ is given by

$$n_m(m)m\,\mathrm{d}m \propto m^{1-\xi}\,\mathrm{d}m \tag{1.36}$$

which implies that fragments are equal in mass for $\xi = 2$, most of the mass is in largest fragments for $\xi < 2$, and most of the mass is in the smallest fragments for $\xi > 2$. However, the number of fragments is always dominated by the smallest fragments.

Collisional outcomes depend on the relative velocities as well as the grain size and internal structure of collision partners. An example situation is depicted in Fig. 1.5. The possible outcomes can be categorized into five types. For sufficiently low collision velocities, particles grow via sticking (green regions in Fig. 1.5). Compact colliding

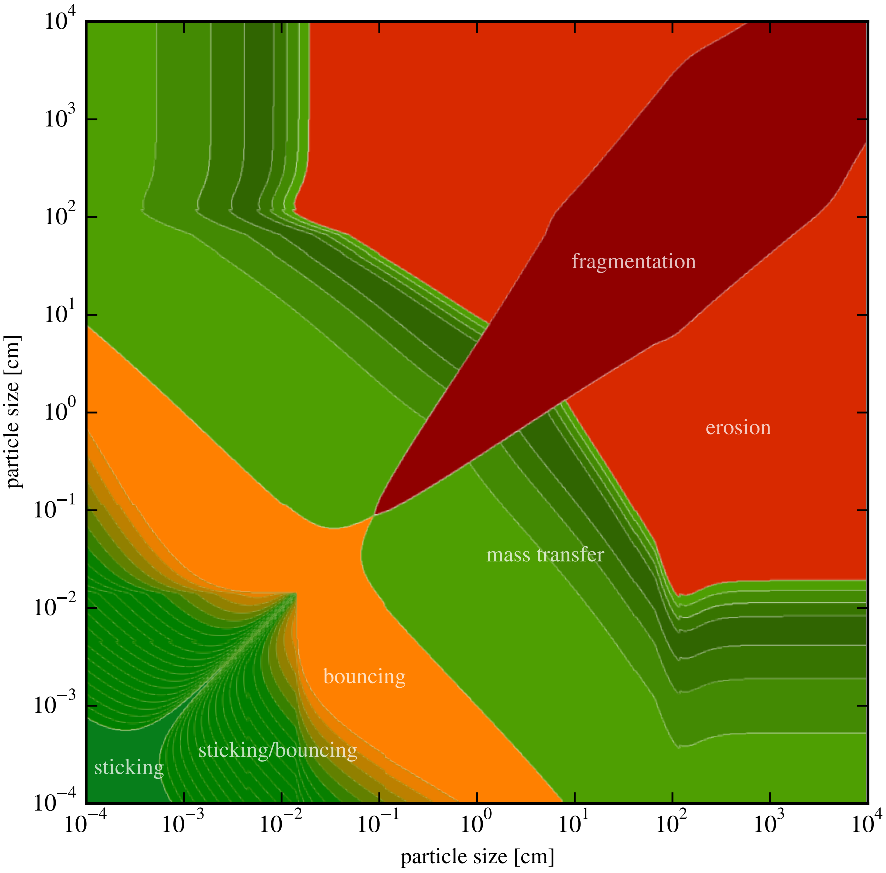

Figure 1.5: Collisional outcomes of silicates with contributions to relative velocities by Brownian motion, radial and azimuthal drift, vertical settling, and turbulence. Green regions indicate net-growth of the larger colliding grain, orange denotes bouncing which does not lead to growth or disruption, and red regions indicate mass loss. These collisional outcomes were computed according to Windmark et al. (2012a) for conditions expected from a minimum mass Solar Nebula (Weidenschilling, 1977b) at 1 au. The picture was taken from Birnstiel et al. (2016).

grains with sizes around mm or cm lead to bouncing, i.e. the collision partners conserve their mass with possible compactification. If one of the collision partners is significantly larger than the other, the smaller projectile fragments after colliding with the larger target, depositing some fraction of its mass on the target (e.g. Teiser & Wurm, 2009; Kothe et al., 2010). For higher impact velocities, smaller projectiles remove mass from the larger collision partner and/or lead to cratering while the projectile fragments. Larger grains of similar size with high impact velocities lead to disruption where the size distribution of fragments typically follows a power-law.

1.3.4 Growth barriers

Extremely fluffy grains can grow continuously in the inner disk ($\lesssim 10\,\mathrm{au}$). In this scenario even planetesimals can be formed (Okuzumi et al., 2012; Kataoka et al., 2013). However, if grains are not very porous, particle growth stops due to different reasons. One of them is due to timescales. The size doubling timescale does not depend on particle size for the largest particles as long as they are still in the Epstein drag regime. However, for $\mathrm{St} < 1$ particles, the drift timescale becomes shorter for larger grains. The consequence is that at a given size, particles drift faster than they can potentially grow. For a particle with radius a, the growth timescale is defined as

$$\tau_{\mathrm{growth}} := \frac{a}{\dot{a}}. \tag{1.37}$$

The growth rate $\dot{a}$ can be calculated via two different approaches assuming monodisperse growth, see Appendix E. Taking the growth rate in the mid-plane from Eq. (E.97) that is based on the Smoluchowski equation for particle growth (von Smoluchowski, 1916), one obtains

$$\tau_{\mathrm{growth}} := \frac{2\sqrt{2\pi} a h_{\mathrm{d}} \rho_{\mathrm{m}}}{\Delta v \Sigma_{\mathrm{d}}}.$$

The relative speed between two colliding particles Δv can be modeled to be the dominant source of relative velocities. If α_{t} is sufficiently high, relative turbulent velocities are dominating. Monodisperse growth models, i.e. particle growth due to collisions of particles equal in size, describe the growth of the largest particles very well. The reason is that collision velocities of similar-sized particles are not much slower than the combination of a very large and very small collision partner, see Fig. 1.4. However, the mass gained by collisions of the largest grains with similar-sized particles is the highest. The collision rate depends on the number densities of both particle species colliding, their relative speed, and on the collision cross section. The collision cross section $\sigma = \pi(a_i + a_j)^2$ is only a factor of 4 smaller for collisions between the largest and smallest grains compared to the largest grains colliding with themselves. Thus, the number of collisions per time should be dominated by the former kind of collisions (large and small grains colliding). However, smaller grains are significantly less massive which leads to smaller mass growth rates. Hence, in the most cases the particle growth timescale of the largest grains can be modeled via collisions with similar-sized particles. Setting the timescales of particle growth and radial drift equal to each other leads to the drift limit (see Eq. (E.101) and Klahr & Bodenheimer, 2006; Birnstiel et al., 2012)

$$a_{\mathrm{drift}} \approx 0.543 \frac{2}{\pi} \left(\frac{v_{\mathrm{K}}}{c_{\mathrm{s}}}\right)^2 \frac{\Sigma_{\mathrm{d}}}{\rho_{\mathrm{m}}} \left|\frac{\partial \ln P}{\partial \ln r}\right|^{-1}.$$

In the Stokes number space, the drift limit is different in the Epstein and Stokes drag regime because of the explicit size dependence of the growth timescale. Since the particle size is linked differently to the Stokes number in both regimes, the expressions differ as well. But note that the drift limit is the same in both regimes in the particle size space.

For $\mathrm{St} < 1$ particles, collision speeds are increasing with particle size. Once a critical speed is reached, collisions no longer lead to growth but fragmentation. The size at which this critical speed v_{f} is reached is called fragmentation limit. For a threshold velocity v_{f} independent of particle size and collision speeds depending on Stokes number, the fragmentation limit is the same for all drag regimes in the Stokes number space but different in the particle size space. The analytical estimate for that growth limit depends on the dominating source of relative velocities. For particles with $\mathrm{St} < 1$ in the mid-plane and collision speeds dominated by turbulent motion of equal-sized particles, i.e. (Ormel & Cuzzi, 2007)

$$\Delta v \simeq c_{\mathrm{s}} \sqrt{3\alpha_{\mathrm{t}} \mathrm{St}}, \tag{1.38}$$

the size at which $\Delta v = v_{\mathrm{f}}$ is given by

$$a_{\mathrm{frag}} = \begin{cases} \dfrac{2}{3\pi} \dfrac{\Sigma_{\mathrm{g}}}{\rho_{\mathrm{m}} \alpha_{\mathrm{t}}} \left(\dfrac{v_{\mathrm{f}}}{c_{\mathrm{s}}}\right)^2 & \text{Epstein drag} \\ \sqrt{\dfrac{3}{2\pi}} \sqrt{\dfrac{\Sigma_{\mathrm{g}} \lambda_{\mathrm{g}}}{\rho_{\mathrm{m}} \alpha_{\mathrm{t}}}} \dfrac{v_{\mathrm{f}}}{c_{\mathrm{s}}} & \text{Stokes drag} \end{cases}. \tag{1.39}$$

It was found that around a size of mm particles start bouncing off each other (Zsom et al., 2010), leading to further compactification rather than growth. However, (Steinpilz et al., 2019) observed that charging effects can lead to growth to one order of magnitude larger compared to this barrier.

1.3.5 Particle trapping

Radial drift of particles (see Eq. (1.25)) can be very fast compared to typical lifetimes of circumstellar disks. A particle originally located at 10 au ends up in the star after a few ten thousand up to a few hundred thousand years. This is much shorter than the lifetimes of disks which are about a few million up to about ten million years. One way to stop radial

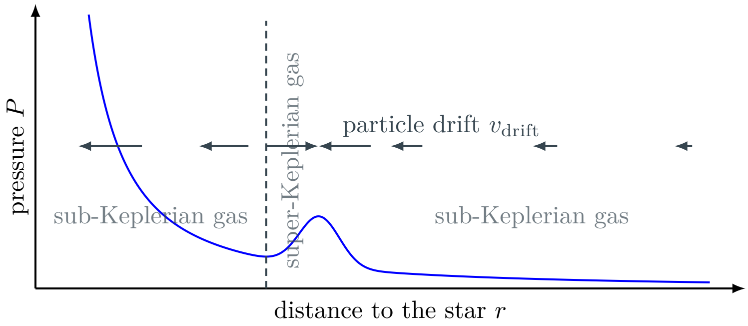

Figure 1.6: Schematic plot showing the concept of particle trapping in gas pressure bumps. Longer arrows correspond to faster particle drift. This figure is adopted from the author's master thesis (Lenz, 2016).

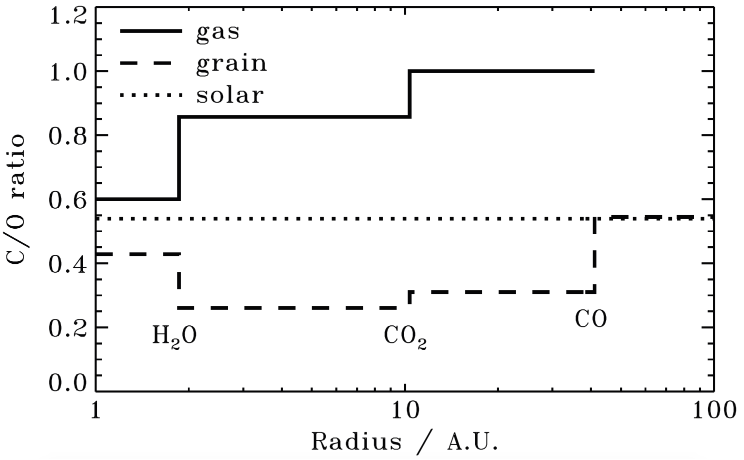

Figure 1.7: Carbon-to-oxygen mass ratio in gas (solid line) and solids (dashed line). The solar value is given by the dotted line. The water, CO_2, and CO ice lines change this ratio which leads to kinks. The picture is taken from Öberg et al. (2011).

drift is by trapping pebbles in gas pressure bumps (Whipple, 1972). As can be seen in Eq. (1.25), radial drift scales with the gas pressure gradient. The stronger the pressure gradient force pointing away from the star, the more sub-Keplerian is the azimuthal gas velocity. For weaker gas pressure gradients, gas is moving azimuthally closer to Keplerian speed. This reduces the centrifugal deficiency experienced by grains. Fig. 1.6 is a schematic illustration of particle trapping in a gas pressure bump. Axisymmetric gas pressure bumps can cause particle ring structures. These axisymmetric regions of high pressure can be produced by, for example, zonal flows. While radial drift forces particles to move closer to the pressure maximum, radial turbulent mixing works against this effect. Dullemond et al. (2018) showed that indeed equilibrium between radial drift and radial mixing can describe the observed ring structures in some disks. Dullemond et al. (2018) have also shown that the optical depths in their observed rings are always around a value of 0.5. Stammler et al. (2019) performed numerical simulations on one of these rings. They have added planetesimal formation to their simulations such that particle-to-gas mass ratios trigger planetesimal formation. With help of this effect, they were able to explain an optical depth as natural outcome inside of particle rings. The conditions that allow retention of particles in the outer disk regions were investigated by Pinilla et al. (2012). Bumps in the gas profile need to be sufficiently pronounced to allow particle trapping that is holding back drifting particles long enough to be present after a few million years. Particle enhancements can also be triggered by major ice lines, where desublimation outside of these ice lines leads to mass accumulation, an effect that is discussed in the next Section.

1.3.6 Ice lines

Ice lines are locations at which the transition from the solid phase to the gas phase of a volatile species occurs. This means that material that was in solid ice in colder regions evaporates once a critical temperature at a given pressure is reached (e.g. Cuzzi & Zahnle, 2004). Hence, the composition of gas and solids is complementary. Sublimating ice enhances the gas mass while desublimating vapor increases the mass in solids. This effect influences the chemical evolution of solid and gaseous material (e.g. Stammler et al., 2017). An example within a simple model is depicted in Fig. 1.7. Thus, depending on the formation location, the (chemical) composition of planetesimals and planets is directly affected by ice lines. Water ice vapor within the ice line can be transported outward and freeze out on the surface of grains, enhancing the mass significantly within a narrow region just outside the ice line (Drążkowska & Alibert, 2017; Schoonenberg et al., 2018). This effect could be an indication that the region just outside the water ice line favors planetesimal formation and, thus, embryo formation.

Gas giants must form within ~million years to contain a high amount of hydrogen and helium. If these gas giants formed by a solid core accreting gas rather than direct disk fragmentation due to self-gravity, it requires a core as massive as roughly $10\,M_\oplus$. The timescales to form such cores is rather long compared to the lifetime of disks. However, pebble accretion can shorten the formation time of core masses needed to allow significant gas accretion (e.g. Lambrechts & Johansen, 2012). Consequently, the loss in mass stored in pebbles at various ice lines as well as the change in composition is likely also important for the formation of giants.

1.4 Planetesimal formation

1.4.1 Definition of planetesimals

Defining the term "planetesimals" is not straight forward. The term itself is a combination of the words "planet" and "infinitesimal", i.e. it means the smallest building blocks of planets. Usually one thinks of asteroid-sized ($\gtrsim 1\,\mathrm{km}$) bodies. Since pebbles (typically mm–cm in size) seem to significantly contribute to growth of planetary embryos, these km-sized objects are not believed to be the smallest building blocks anymore. To quantify the definition, one has to define the features required by planetesimals. Three examples would be the following:

- The escape velocity of the body is at least equal to the headwind velocity of a pebble with given Stokes number.
- The gravitational focusing factor (Safronov, 1969; Lissauer, 1993)

  $$\sigma_{\mathrm{grav}} = \pi a^2 \left(1 + \frac{v_{\mathrm{esc}}}{\Delta v}\right) \tag{1.40}$$

  is larger than the geometrical cross section $= \pi a^2$. Here, the escape velocity is given by

  $$v_{\mathrm{esc}} = \sqrt{\frac{2G(m_i + m_j)}{a_i + a_j}} \tag{1.41}$$

  and Δv is the relative velocity between two bodies i and j with radii $a_{i/j}$ and masses $m_{i/j}$.
- The object is bound by its own gravity rather than molecular forces (such as Van der Waals).

The typical planetesimal size of $\sim 1 - 100\,\mathrm{km}$ remains even though these definitions depend on aerodynamic behavior of pebbles, the mean relative velocity of potentially colliding bodies, or binding forces.

Before becoming a planet, planetesimals have to grow to embryo size or mass if these embryos are not created by collapsing massive pebble clouds. The term "embryo" is not well-defined either. After a self-similar growth phase, a runaway phase is reached. A reasonable definition of embryos would be the mass at the onset of this runaway growth phase. Unfortunately, this onset depends on dynamical stirring of planetesimals and model-dependent relative velocities in general. In the literature, embryos are sometimes objects more massive than the moon or of sizes larger than 1000 km, leaving the definition of "embryos" open.

1.4.2 How are planetesimals formed and what is their typical size?

In our solar system, most asteroids are present in ring structures, i.e. the asteroid main belt at distances between roughly 2 and 3.4 au, and the Kuiper belt at $30 - 50\,\mathrm{au}$ (so-called Kuiper Belt Objects or trans-Neptunian Objects). The number density is larger and the orbital timescale is shorter in the asteroid main belt compared to the Kuiper belt. Hence, collisional evolution in the Kuiper belt is much slower and a significant amount of mass likely remained pristine. Both the asteroid main belt (Bottke Jr et al., 2005a) and the Kuiper belt (Fuentes & Holman, 2008; Fraser & Kavelaars, 2008) share a characteristic feature in their cumulative size distribution, see Fig. 1.8. Around $60 - 100\,\mathrm{km}$

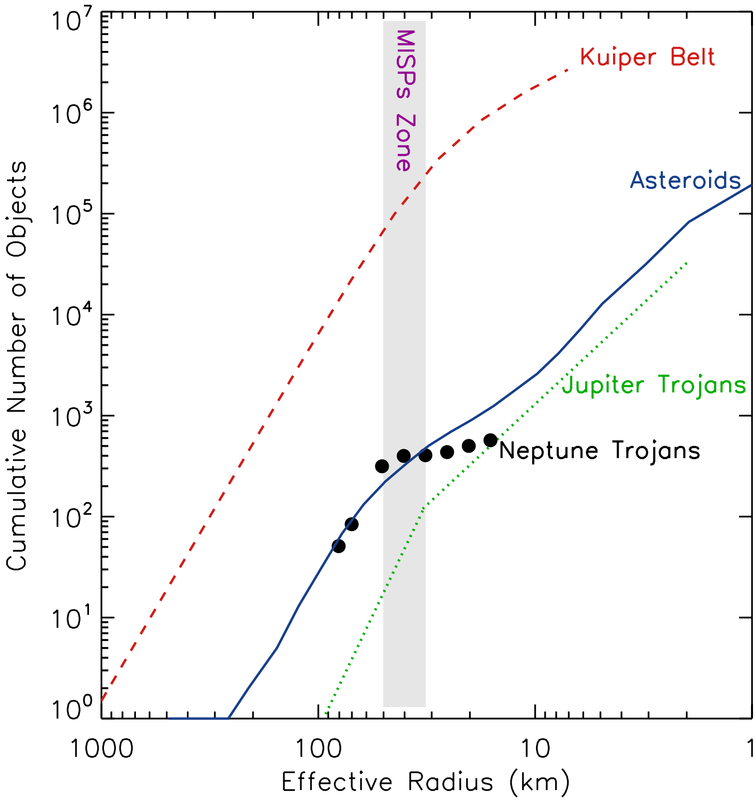

Figure 1.8: Cumulative size distribution of objects in the main asteroid belt (blue solid line; Bottke Jr et al., 2005a), the Kuiper belt (red dashed line; Fuentes & Holman, 2008; Fraser & Kavelaars, 2008), Jupiter (green dotted line; Jewitt et al., 2000) and Neptune (black circles Sheppard & Trujillo, 2010) Trojans. The gray shaded area shows the Zone of Missing Intermediate-Sized Planetesimals (MISPs). This figure was taken from Sheppard & Trujillo (2010).

in diameter, a plateau in the size distribution can be identified, i.e. a flat slope. This means that not many objects in that size range are found compared to all other sizes. The plateau in the size distribution is sometimes interpreted as an imprint of the size distribution of initial planetesimals and was shown to only be reproduceable if initial planetesimals had at least 80 km in diameter (Morbidelli et al., 2009). The plateau in the cumulative size distribution is also present for Jupiter (Jewitt et al., 2000) and Neptune Trojans (Sheppard & Trujillo, 2010). These Trojans are trapped asteroids in the Lagrange points that are dynamically stable locations. The cumulative size distributions for the asteroid belt, Kuiper belt, and Trojans are shown in Fig. 1.8.

Overcoming the growth barriers is necessary to allow planet formation. One possible path is by trapping pebbles in gas pressure bumps where turbulence leads to further particle concentrations. Star formation and planetesimal formation follow similar rules, although the details of their formation conditions are different. The basic condition for star formation is described by the *Jeans criterion* (Jeans, 1902). It requires the self-gravity of a molecular cloud to be stronger than the pressure from the internal temperature, see left part of Fig. 1.9. If gravity is stronger, a star can form. Otherwise the cloud must cool to allow further shrinking or no star is formed, leading to a dispersed cloud. A similar but somewhat different situation applies for planetesimal formation. A pebble cloud that collapses due to its own gravity must collapse faster than turbulent motions that lead to particle diffusion are disrupting the particle cloud. Hence, it is no longer a question of force imbalance that favors gravitational collapse. It becomes a timescale issue, i.e., the particle cloud must contract faster than diffusion can disperse it (see right part of Fig. 1.9). Additionally, the cloud must be stabilized against tidal shear which is assumed to be the case once Hill density ρ_{Hill} (Hill, 1878) is reached,

$$\rho_{\mathrm{Hill}} = \frac{9}{4\pi}\frac{M_\star}{r^3}. \tag{1.42}$$

The described planetesimal formation process shall be called “diffusion limited planetesimal formation”.

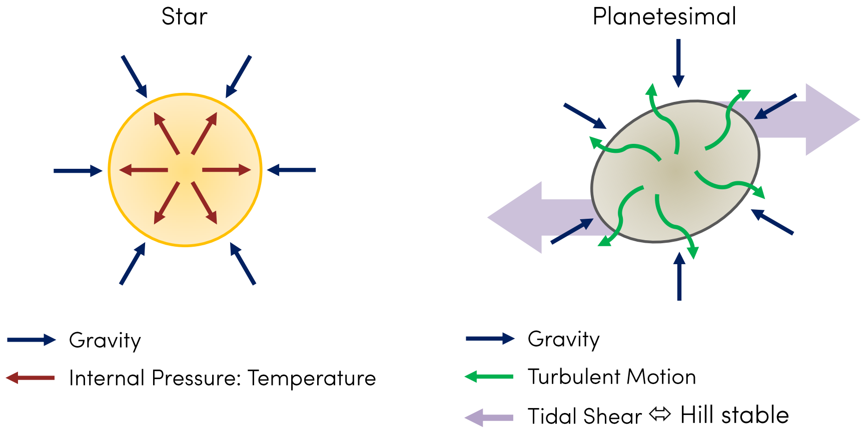

Figure 1.9: Comparison of the conditions of star formation (left) and planetesimal formation (right). In order to allow star formation, gravity has to overcome internal pressure. For planetesimal formation, particle diffusion and tidal shear are working against particle cloud collapse. Shear stability is assumed to be reached at Hill density. Since particle diffusion is disrupting the particle cloud over time, it seems natural to derive a collapse criterion based on timescales. Picture adapted from Schreiber (2018).

The interplay of particle diffusion within a collapsing particle cloud and the particles collapse timescale leads to a typical planetesimal diameter of about 100 km (Klahr & Schreiber, 2015; Schreiber, 2018; Gerbig et al., 2020). Setting the particle diffusion timescale and the collapse timescale equal to each other defines the *Klahr-Schreiber criterion* for planetesimal formation and leads to a planetesimal diameter of (Klahr & Schreiber, 2015; Schreiber, 2018)

$$d_{\mathrm{ptes}} = \left(\frac{q}{1}\right)^{1/3} \left(\frac{1}{f}\right)^{1/6} \sqrt{\frac{\delta}{2.6 \cdot 10^{-6}} \frac{h_{\mathrm{g}}/r}{0.04}} \sqrt{\frac{0.1}{\mathrm{St}}} \sqrt{\frac{\rho_\odot}{\rho_{\mathrm{m}}}} 98\,\mathrm{km}. \tag{1.43}$$

In each factor the given parameters are compared to typical values. Here, $0 < q \leq 1$ indicates how much mass of the initial particle cloud is ending up in the formed planetesimal. The scaling parameter $f \approx 1$ gives the amount of Hill densities—the density at which a particle cloud is stable against tidal forces—that are needed to allow collapse. But it has been shown that the value of f does not exceed unity by much (Schreiber, 2018) and the predicted size does only weakly depend on this parameter. The internal mean density of the formed object might be a function of particle Stokes number since particles that are stronger coupled to the gas are expected to collapse slower. But for now we assume that the factor with the mean solar density $\rho_\odot$ and mean internal planetesimal density ρ_{m}, $\sqrt{\rho_\odot/\rho_{\mathrm{m}}}$, is roughly 1 as it would not change the result by more than roughly 50% at most for typical mean solid densities of individual asteroids. In this formula, the particle diffusion δ is given in units of $c_{\mathrm{s}} h_{\mathrm{g}}$ and might depend on the particles Stokes number (Schreiber, 2018). However, even though the true dependency on the particles Stokes number is hidden in δ, one can see that stronger particle diffusion, i.e. higher values of δ, lead to bigger and thus more massive planetesimals. This is due to the fact that shorter collapse timescales are needed if stronger particle diffusion is disrupting particle clouds too fast. For weaker turbulence, smaller objects can form. Delbo et al. (2017) indeed observed an initial Gaussian size distribution for the asteroid belt with a peak around 100 km in diameter.

There exist also other models for planetesimal formation such as the fluffy growth model and the lucky particle model. The former model suggests a pathway to surpass growth barriers via highly porous grains. In this model, particles become very massive while they are strongly coupled to the gas. As a result, particle drift and relative velocities are low, allowing to overcome the drift and fragmentation barriers (Okuzumi et al., 2012; Kataoka et al., 2013). In the lucky particle model, particle growth benefits from the low velocities present in a velocity distribution of the particles and the associated low-velocity impacts (Windmark et al., 2012b). Both of these models, however, are not able to explain the kink feature in the size distributions shown in Fig. 1.8. More details are discussed in Sec. 2.5.2.

1.4.3 On planetesimal density profiles

The planetesimal density profile, i.e. the disk radius dependence of the planetesimal column density, determines how the mass that is in planetesimals is radially distributed. For a planetesimal profile of $\Sigma_\mathrm{p} \propto r^{-2}$, the mass is distributed equally on a logarithmic grid, i.e. each circumference has the same mass in planetesimals. For a steeper slope, more mass is in the inner regions, whereas a shallower slope leads to more mass in the outer disk. The mass budget in a certain disk region can be important for further formation of planetary embryos and planets.

But the question remains, how a typical spatial distribution planetesimals looks like. Weidenschilling (1977b) and Hayashi (1981) used the current positions of the planets of our Solar System, spreading the mass of each planet out to its nearest neighbors.

Around 2.7 au a jump is expected due to the water ice line within which water ice sublimates, i.e. water from the solid phase enters the gaseous phase due to low pressure and sufficiently high temperatures. The location of 2.7 au is assumed to be the ice line in the Solar Nebula since the water-rich meteorite class of carbonaceous chondrites is found only outside of that radius. The result is a column density profile for solids that follows (Hayashi, 1981)

$$\Sigma_\mathrm{solids} = \left(\frac{r}{\mathrm{au}}\right)^{-3/2} \begin{cases} 7.1\,\mathrm{g\,cm^{-2}} & , 0.35 \le r/\mathrm{au} \le 2.7 \\ 30\,\mathrm{g\,cm^{-2}} & , 2.7 < r/\mathrm{au} < 36 \end{cases} \tag{1.44a}$$

and for the gas it was found

$$\Sigma_\mathrm{g}(r) = 1700\,\mathrm{g\,cm^{-2}} \left(\frac{r}{\mathrm{au}}\right)^{-3/2} \quad , 0.35 < r/\mathrm{au} < 36. \tag{1.44b}$$

However, this approach neglects any dynamical interaction in the stages of gravitational interactions between embryos and of the formed planets. This profile is called minimum mass Solar Nebula (MMSN) and has a total mass in solids (rocky and icy) of $\approx 65\,\mathrm{M}_\oplus$ and the gas of $\approx 1.3 \cdot 10^{-3}\,M_\odot$, where $M_\oplus$ and $M_\odot$ are the mass of Earth and the sun, respectively. The profile for solids—or up to a few times this profile—is often used as initial profile for planetesimals. However, the steep slope of this profile is inconsistent with the density profiles of gas and dust expected from viscous disk evolution which is expected to be proportional to r^{-1}. Both observations (e.g. Andrews et al., 2010) and theoretical models (e.g. Lynden-Bell & Pringle, 1974; Birnstiel et al., 2010) are indicating much shallower density profiles than the MMSN model. Hence, the question remains how the density profile of planetesimals evolves with time, starting with tiny dust grains. This is one of the problems explored in this thesis (see Chapter 2).

1.5 The general picture: from dust to planets

This Section summarizes one possible path to form planets starting with tiny dust grains. First, micron-sized dust grains grow to pebble size but stop at the growth barriers that do not allow to grow beyond $\sim$ 10cm. In this stage, coupling to the gas plays a crucial role, controlling the motion and relative velocities of grains. Particle trapping allows accumulation of pebbles in narrow regions in the disk. These traps can be, for instance, zonal flows or vortices. In these narrow regions, turbulence (e.g. the streaming instability, see Youdin & Goodman (2005)) leads to particle clouds that can collapse to planetesimals (Johansen et al., 2006) if enough mass is provided to collapse on similar timescales as the particles are diffused apart by random turbulent motion (Klahr & Schreiber, 2015; Schreiber, 2018). This means there is a jump from pebble-size (typically mm–cm) to $\sim$ 100 km planetesimals. Water vapor that is transported outside the water ice line can desublimate on grains, enhancing the mass budget in pebbles which leads to potentially more planetesimals (Drążkowska & Alibert, 2017; Schoonenberg et al., 2018). A discussion about other planetesimal formation models can be found in Sec. 2.5.2.

Once a planetesimal population has formed, further evolution is dominated by gravitational interactions. Planetesimals can then grow further to embryo sizes and beyond by collisions with other planetesimals (e.g. Kobayashi et al., 2016). Once the relative velocities between planetesimals exceed the escape velocities, runaway growth occurs, i.e. the largest objects grow much faster than smaller ones. Accretion of pebbles onto planetesimals (Ormel & Klahr, 2010) can potentially boost the formation timescales of embryos and planets. However, Visser & Ormel (2016) found that the growth timescale due to pebble accretion peaks for planetesimals with diameters of around 100 km. For larger planetesimals, this timescale becomes much shorter. The peak in the pebble accretion growth timescale occurs when the headwind velocity of the grains equals the surface escape velocity of planetesimals. This implies that 100 km-sized planetesimals first have to collide with other planetesimals to build bigger objects of several 100 km in size before pebble accretion can significantly contribute. This scenario would explain the lack of objects with diameters $\sim 100\,\mathrm{km}$ which is depicted in Fig. 1.8. Objects larger than this size range would have formed by planetesimal-planetesimal collisions that lead to growth while smaller objects are a result of a fragmentation cascade.

Once a mass of around $M_\oplus$ has formed, coupling to the gas via gravity becomes important. This coupling leads to damping of eccentricities and angular momentum exchange with the gas, an effect that leads to migration of planets. At a critical mass of about $10\,M_\oplus$ (Pollack et al., 1996), gas accretion becomes very efficient which allows the formation of gas giants. Between the described processes and observations lie many millions to billions of years which present a playground for theoretical modeling.

1.6 Outline of this thesis

This thesis is a direct continuation of the author's master thesis (Lenz, 2016). The goal of this work is to find answers to the following questions:

- When and where do planetesimals form in a circumstellar disk? How is the resulting planetesimal density profile affected by different disk parameters?
- What are the disk parameters that allow the formation of our Solar System? For instance, what are the constraints for the initial disk mass, disk size, turbulence strength, or the planetesimal formation efficiency?
- Where does the material that forms planetesimals originate from? How much mass is contributed by different regions of origin to planetesimals formed in different disk locations? Was this material crossing major ice lines before forming planetesimals?

I approach these problems from three directions that are linked to each other: numerical simulations, analytical modeling, and comparison to Solar System data. This work focuses on the early stages of planet formation where micron-sized dust grains grow to pebble size (typically mm–cm) out of which planetesimals are formed. The further evolution of planetesimals is not considered. Planetesimal formation in circumstellar disks is in particular interesting because it reduces the dust and pebble content. Dust and pebbles, as the main source of opacity, are linked to particle transport and planetesimal formation. Consequently, planetesimal formation might also be important for the interpretation of observations. The thesis is structured as follows.

Chapter 2 introduces a new model for the planetesimal formation rate. This model is based on the idea that pebbles are transformed to planetesimals on a length scale that shall be called *conversion length*. The flux of pebbles regulates the supply of planetesimal forming material. One example would be pressure bumps that appear and disappear on a given timescale with an average radial distance to each other. This Chapter explores the impact of the planetesimal formation model parameters on the dynamical planetesimal production. Additionally, an analytical estimate for the slope of the resulting planetesimal density profile is presented and shown to reproduce the numerical results.

Chapter 3 presents a numerical study, based on the model presented in the previous Chapter, exploring a much wider parameter space which includes disk parameters that are not exclusively given by the planetesimal formation rate model. Based on literature, mass constraints for initial planetesimals in different regions of the Solar Nebula are suggested. The numerical simulations use variations of nine different disk parameters. The results are compared to the discussed mass constraints in order to in turn set limits for the possible range for each of the analyzed disk parameters to allow the formation of the Solar System. Analytical estimates based on timescale arguments are used to find a criterion for which the slope of the initial planetesimal density profile deviates from the initial condition of dust and gas.

Chapter 4 introduces an analytical model for the computation of the origins of planetesimal forming material. This model is based on the gained understanding how planetesimal formation develops within the framework of the model presented in Chapter 2. The analytical model uses data from numerical simulations which are discussed in detail in Chapter 3. Material is sorted by their origins located outside of major ice lines such as the water, CO_2, and CO ice lines. Within those ice lines the respective molecules are expected to transition from the solid to the gaseous phase. Mass contributions to planetesimals with origins from regions outside these ice lines change with the planetesimal formation efficiency. I explore which trend can be expected by varying this efficiency parameter. Furthermore, mass averaged values for the final population at a given location in the current regions of Earth and the asteroid belt are computed.

This provides information on how much mass passed one or several major ice lines before forming planetesimals at the given locations, allowing to judge whether radial pebble transport was important or not for the composition of asteroids.

Chapter 5 summarizes the results and presents an outlook on potential future projects that would help understanding the complex processes of the formation of planets and minor bodies. Furthermore, both the summary and the outlook are discussed in the context of the Solar System and extrasolar systems.

2

Planetesimal Population Synthesis: Pebble Flux-regulated Planetesimal Formation

This Chapter follows Lenz et al. (2019) where I propose an expression for a local planetesimal formation rate proportional to the instantaneous radial pebble flux. The result—a radial planetesimal distribution—can be used as initial condition to study the formation of planetary embryos. I follow the idea that one needs particle traps to locally enhance the dust-to-gas ratio sufficiently such that particle gas interactions can no longer prevent planetesimal formation on small scales. The location of these traps can emerge everywhere in the disk. Their occurrence and lifetime is subject of ongoing research, thus here they are implemented via free parameters. This enables us to study the influence of the disk properties on the formation of planetesimals, predicting their time dependent formation rates and location of primary pebble accretion. I show that large α-values of 0.01 (strong turbulence) prevent the formation of planetesimals in the inner part of the disk, arguing for lower values of around 0.001 (moderate turbulence), at which planetesimals form quickly at all places where they are needed for proto-planets. Planetesimals form as soon as dust has grown to pebbles ($\sim$ mm to dm) and the pebble flux reaches a critical value, which is after a few thousand years at $2-3\,$au and after a few hundred thousand years at $20-30\,$au. Planetesimal formation lasts until the pebble supply has decreased below a critical value. The final spatial planetesimal distribution is steeper compared to the initial dust and gas distribution which helps to explain the discrepancy between the minimum mass solar nebula and viscous accretion disks.

2.1 Introduction

The original ideas about planet formation—valid for terrestrial planets as well as gas- and ice-giants—assume that pebble-sized material, which has grown from tiny dust and ice grains via successive collisions and sedimented towards the midplane of the disk, directly collapses into $\sim 10-100\,$km sized planetesimals (Safronov, 1969; Goldreich & Ward, 1973). By definition planetesimals are bodies massive enough to be bound by, and able to accrete further solid material via, gravitational attraction. A critical size or mass for boulders to be called planetesimal can be estimated by requiring that pebbles settle toward the planetesimal with a higher velocity compared with the typical headwind the planetesimal experiences in the gaseous environment (Ormel & Klahr, 2010). The precise mass depends on the location in the disk and the size of the pebbles. The fact that their binding force is gravity makes it plausible gravity could also be involved in their formation in the first place. Nevertheless, Weidenschilling (1995) showed that Safronov (1969) and Goldreich & Ward (1973) neglected the effect of friction between particles and gas, and the associated momentum transfer from the solids to the gas. Sedimentation to the midplane leads to dust-to-gas ratios of the order of unity before the critical density for self-gravity among the pebbles is reached. But starting from dust-to-gas ratios of unity the drag from the particles accelerates the gas disk, which is usually pressure supported and sub-Keplerian, to the Keplerian speed.

The feedback from the dust onto the gas modifies the average azimuthal velocity of the gas which leads to resonant drag instabilities (Squire & Hopkins, 2018a,b), for example the streaming instability (Youdin & Goodman, 2005). The resulting turbulence will then prevent further vertical sedimentation and, ultimately, gravitational collapse of pebble clouds to planetesimals, because the necessary critical density in the pebble cloud cannot be reached. Originally this effect was identified as a Kelvin-Helmholtz instability (Sekiya, 1998; Johansen et al., 2006), yet in modern 3D simulations (Johansen et al., 2009b) one finds streaming instability to dominate the dynamical evolution.

After this important discovery, research was focused on the growth from grains to planetesimals via sticking collisions. Yet this model was also facing several problems like the drift and fragmentation barriers, because either the drift time becomes shorter than the growth time (drift limit) (Klahr & Bodenheimer, 2006; Birnstiel et al., 2012) or the turbulence in the nebula induces collision speeds among the solids that lead to bouncing (Güttler et al., 2010; Zsom et al., 2010) and fragmentation (Blum & Münch, 1993; Blum & Wurm, 2008; Gundlach & Blum, 2014). Aggregates charging can also act as a growth barrier (Okuzumi, 2009). Neither bouncing, nor charging is considered in this work. In the early stages of circumstellar disks, micrometer-sized dust grows to pebble-size (typically $\sim$ mm – dm) via collisions. Particle growth models have been developed and improved in the past (Zvyagina et al., 1974; Weidenschilling, 1980; Dullemond & Dominik, 2005; Brauer et al., 2008a; Birnstiel et al., 2010; Windmark et al., 2012b; Krijt et al., 2016a,b; Stammler et al., 2017). Birnstiel et al. (2012) have shown that the radial dynamics are mostly determined by particles with sizes close to the growth barriers.

Following the path of fluffy particle growth (Okuzumi et al., 2012; Kataoka et al., 2013), it becomes feasible to form planetesimals, at least within 10 au in the disks. Yet, Blum et al. (2017) have shown that the resulting planetesimals would have too large a tensile strength to explain the properties of comets, which are believed to be remnants from the planetesimal formation episode in the solar nebula.

The idea of Safronov (1969) and Goldreich & Ward (1973) was extended by Youdin & Shu (2002), showing that this gravitational instability can develop despite Kelvin-Helmholtz instability for sufficiently high dust-to-gas column density ratios at least in a laminar gas disk.

The work by Johansen et al. (2006) started a revival of gravity assisted planetesimal formation, because it was the first work that incorporated turbulence generated via the magneto rotational instability [MRI] (Balbus & Hawley, 1991). They found that turbulence not only leads to diffusion and prevents sedimentation, but also causes solid particles to get trapped and concentrated in non-laminar flow features reaching locally a critical Hill density to undergo collapse. These were created as by-products of the magneto rotational instability. They were able to show that the over-densities are in fact sufficient to trigger gravitational collapse.

This idea is different from the gravitational collapse envisioned by Cuzzi et al. (2008), in which grains get stochasticaly concentrated locally between vortices for a short time. The vortices there are part of a Kolmogoroff cascade and only live for a short time.

In the paper by Johansen et al. (2007) they found that a zonal flow feature arose in a box simulation of the MRI simulation, in which sufficiently many particles got trapped to trigger a gravitational collapse, without being diffused by the streaming instability. In test simulations in the same paper without MRI and thus no zonal flows, the streaming instability prevented the formation of planetesimals. These simulations of planetesimal formation in zonal flows were expanded to higher resolutions in order to study the size of forming planetesimals in Johansen et al. (2012), and the properties of zonal flows were further studied in Dittrich et al. (2013) and Bai & Stone (2014). Zonal flows appear to be transient features in any accretion disk subject to magnetic instabilities (Johansen et al., 2009a). In the simulations of Dittrich et al. (2013) they found a typical separation between the zonal flows of 5 pressure scale heights and a lifetime of about 100 local orbits. Whereas the above mentioned simulations were ideal magneto-hydrodynamic (MHD) runs, non ideal MHD simulations, especially those including the Hall-term, also showed the phenomenon of creating zonal flows (Bai & Stone, 2014; Béthune et al., 2016).

In situations where magnetic effects are weak because of the typically low ionization of disks around young stars, dust absorbs free electrons and the field-lines decouple from the gas. In this situation potentially hydrodynamical instabilities could drive turbulence and structure formation. For instance a radial temperature gradient leads to vertical shear in the disk, which is unstable for short thermal relaxation times (Urpin & Brandenburg, 1998; Arlt & Urpin, 2004; Nelson et al., 2013; Stoll & Kley, 2014; Barker & Latter, 2015; Stoll & Kley, 2016; Latter & Papaloizou, 2017; Manger & Klahr, 2018; Lyra & Umurhan, 2018; Klahr et al., 2018). This was demonstrated to trigger zonal flows, long lived vortices (Raettig et al., 2013; Raettig et al., 2015; Manger & Klahr, 2018), and instability based on radial buoyancy. The same can happen in disks which are radially buoyant, but for longer thermal relaxation times. Then, convective overstability (Klahr & Hubbard, 2014; Lyra, 2014) and its non-linear version, Subcritical Baroclinic Instabilities (Klahr & Bodenheimer, 2003; Petersen et al., 2007a,b; Lesur & Papaloizou, 2010; Lyra & Klahr, 2011), can produce and sustain vortices.

Johansen & Youdin (2007) performed 2D simulations on the Kelvin-Helmholtz instability of sedimenting particles and found that while on average particles were still diffused out of the midplane, the turbulence also led to strong fluctuations.

In order to form planetesimals grains have to circumvent the growth barriers. One possibility is a jump from a clump of condensed pebbles directly to planetesimals as first shown in the above mentioned shearing-box simulations by Johansen et al. (2007) in the gravo-turbulent scenario.

Also in the complete absence of turbulence in the disk, which seems unlikely given the observation of accretion in these systems, sedimentation of pebbles in disks with high enough dust to gas ratios, that is 2 – 3 times solar metalicity, can lead to gravitational instability and planetesimal formation, regulated by the streaming instability as originally explored by Youdin & Shu (2002) and since then demonstrated in a series of numerical simulations (Johansen et al., 2009b; Simon et al., 2016).

Independent from the source of turbulence (S.I. or external) there may exist a typical planetesimal diameter regulated by particle diffusion (Klahr & Schreiber, 2015; Schreiber, 2018). Grain evolution models, including radial transport, leading to planetesimal formation, have been performed by various authors. Brauer et al. (2008b) have shown that particles with a radius of $\sim 10^2$ m can be produced at the edges of regions from low turbulence (called the "dead zone") to higher turbulence levels. A particle velocity distribution can lead to "lucky particles" which are able to circumvent the growth barriers via low relative speed collisions (Windmark et al., 2012b; Drążkowska et al., 2014b). But this effect may be suppressed by lower breakup speeds (Blum & Münch, 1993; Blum & Wurm, 2008) within the (water) ice line, and in the outer disk by rapid removal due to radial drift as indicated by Estrada et al. (2016). We will discuss this in more detail in section 2.5.2. Drążkowska et al. (2013) have shown that planetesimal formation can occur in a pressure bump at the inner edge of the dead zone via sweep-up growth. Another possibility would be that particles become fluffy, and grow continuously to planetesimal size. This model will be further discussed in section 2.5.2. But particles can also pile up due to back-reaction of particles onto gas and evaporation and re-condensation at the water ice line (Drążkowska et al., 2016; Drążkowska & Alibert, 2017) which we discuss in section 2.5.2.

We will follow a different path where a plethora of various instabilities can create turbulent structures in almost the entire disk either by hydrodynamical (Pfeil & Klahr, 2019) or magnetic instabilities in the non ideal regime (Béthune et al., 2016). For a review see Klahr et al. (2018). Indeed observations find a lot of structure in protoplanetary disks, see e. g. the Disk Substructures at High Angular Resolution Project (DSHARP; e. g., Andrews et al., 2018; Huang et al., 2018; Dullemond et al., 2018). Hence, one can assume that trap structures will appear everywhere in the disk. These can then trap the incoming particles, which are concentrated to particle clouds collapsing to planetesimals.

This Chapter is structured as follows. In section 2.2 I present a new model for the planetesimal formation rate. Section 2.3 summarizes the numerical disk model and explains how I implemented the parameterized planetesimal formation within it. In section 2.4 I show the first results. I discuss limitations of the model and compare with other planetesimal formation models in section 2.5. Particular attention should be paid to section 2.5.2, where I explain that streaming instability is not mandatory to form planetesimals. I conclude in section 2.6.

2.2 Rational of pebble flux-limited planetesimal formation: trapping mode.

In order to mimic planetesimal formation in our simulations, we use findings from fluid dynamical simulations which include particles. To keep it simple and feasible we use a probabilistic toy model based on parameterization. The important disk model parameters for this model are the lifetime of pebble traps τ_l (e. g. vortices or zonal flows) and their radial separation d. Strictly speaking, one doesn't necessarily need a pressure *bump* with a local maximum. If the pressure profile is flattened a bit without a local maximum, this would slow down the particles since smaller pressure gradients lead to slower drift speeds (Whipple, 1972) and conservation of mass flux leads to denser particle accumulations. Instead, the density is increased which may lead to critical Σ_d/Σ_g values to trigger streaming instability. In this scenario, the d parameter has to be interpreted as the distance between such flat pressure structures. Or in general, d is the distance between structures leading to streaming instability conditions with sufficient density increase to reach Hill density. In our case we just assume that the flux concentrators are vortices or zonal flows with typical numerically measured radial distance $5h_g$ (Dittrich et al., 2013).

The Stokes number St describes the aerodynamic behavior of particles surrounded by gas. It is the ratio of the friction time (timescale of coupling to the gas) and the dynamical timescale of the gas (here the inverse of the Keplerian frequency $1/\Omega$). Particles with $\mathrm{St} \ll 1$ are well coupled to the gas whereas $\mathrm{St} \gg 1$ are decoupled from the gas. From the particle side, the parameters of our model are the Stokes number of the smallest ($\mathrm{St}_{\mathrm{min}}$) and largest ($\mathrm{St}_{\mathrm{max}}$) particles that are able to participate in the streaming instability to facilitate gravitational collapse of the particle heaps. And finally an efficiency parameter ε that defines how much of the actual radial mass flux in pebbles can be trapped *and* transformed into planetesimals. Then one can convert the column density of drifting pebbles into column density of planetesimals with the following recipe:

$$\dot{\Sigma}_{\mathrm{p}}(r) = \frac{\varepsilon}{d(r)} \frac{\dot{M}_{\mathrm{peb}}}{2\pi r}, \tag{2.1}$$

where we defined the mass flux of pebbles for a full circumference as

$$\dot{M}_{\mathrm{peb}} := 2\pi r \sum_{\mathrm{St}_{\mathrm{min}} \leq \mathrm{St} \leq \mathrm{St}_{\mathrm{max}}} \left| v_{\mathrm{drift}}(r, \mathrm{St}) \right| \Sigma_{\mathrm{d}}(r, \mathrm{St}). \tag{2.2}$$

Here, v_{drift} is the radial velocity with which particles drift and $\Sigma_{\mathrm{d}}(r, \mathrm{St})$ is the column density in particles with Stokes number St within a given bin in particle size. The units of this column density are still $\mathrm{g/cm^2}$. The cylindrical radius, i. e., distance to the star in the midplane, is given by r. Eq. (2.2) is written in discretized form, as we treat it in our simulations.

The *conversion length* over which pebbles are transformed into planetesimals is given by

$$\ell := d/\varepsilon. \tag{2.3}$$

If, for example, there is only one pebble species with drift speed v_{drift} and column density Σ_{peb}, we distribute the new planetesimal column density over the trap distance d. ℓ/v_{drift} gives the timescale of conversion, thus $v_{\mathrm{drift}}/\ell \cdot \Sigma_{\mathrm{peb}}$ is the rate at which the transformation from Σ_{peb} to Σ_{p} occurs. If this is added up for all particle species, one obtains the column density formation rate of planetesimals as shown in Eq. (2.1). We barely resolve the expected radial trap structures with a few radial bins at maximum.

To give another explanation, $1/d$ is the radial trap density, meaning that the closer the traps are packed radially, the more planetesimals can be produced. For the flux, only v_{drift} without the gas velocity is considered to take the relative radial velocity between particles and gas. Hereby we assume that the spatial pressure structures (e. g., real pressure-bump traps like vortices) move radially with the gas of the smooth profile.

We assume theoretically infinitesimal structures as traps even though they are practically extended. Since we assume a non-zero α_{t} value everywhere anyway, we also assume that turbulent structures can be found everywhere. For our numerical radial grid, the grid cells are smaller than the trap distance parameter d. This ensures that we can distribute the mass of newborn planetesimals accordingly (probabilistic ansatz). If the resolution is too low, i. e., $\Delta x \gg d$, a "distribution" of this mass is not physical or one cell traps too much mass. Also, the condition of accumulated particles may not be treated correctly anymore because a bigger cell can also host more mass. At the same time, we are far from resolving the length scale on which planetesimal formation occurs. This length scale is typically on the order of $0.01 h_{\mathrm{g}}$ (Schreiber, 2018, see his Eq. (3.40)), depending on particle diffusion on these small scales and on particle Stokes number. Even though we may be able to resolve trap structures of the order of a gas pressure scale height with only a few radial bins, it is not enough to reach a proper resolution of the substructure. The properties of the traps in terms of particle trapping and planetesimal formation is embedded in our efficiency parameter ε.

The material density is assumed to be $\rho_{\mathrm{m}} = 1.2\,\mathrm{g/cm^3}$ for all solid particles, according to asteroid data (e. g., Carry, 2012). For simplicity we again assume particles to be spherical objects with constant material density ρ_{m}, such that the representative planetesimal mass with a diameter of 100 km (Klahr & Schreiber, 2015; Schreiber, 2018) is given by

$$m_{\mathrm{p}} = \frac{4\pi}{3} (50\,\mathrm{km})^3 \rho_{\mathrm{m}} \approx 6.28 \cdot 10^{20}\,\mathrm{g} \approx 1.05 \cdot 10^{-7} M_{\oplus} \tag{2.4}$$

where $M_{\oplus}$ is the mass of the earth. The idea of planetesimals of diameter around 100 km is also supported by data from our solar system (Morbidelli et al., 2009; Delbo et al., 2017).

Planetesimal formation will only occur if, within one (average) lifetime of a trap τ_{l}, enough mass can be accumulated to form at least one planetesimal, i. e. if the following condition holds

$$\varepsilon \tau_{\mathrm{l}} \dot{M}_{\mathrm{peb}} > m_{\mathrm{p}}. \tag{2.5}$$

Hence, there is a critical flux

$$\dot{M}_{\mathrm{cr}} := \frac{m_{\mathrm{p}}}{\varepsilon \tau_{\mathrm{l}}} \tag{2.6}$$

that must be reached to allow planetesimal formation. If condition (2.5) is fulfilled, we call the flux *critical*, otherwise we call it *sub-critical*. We give more detailed information on that criterion in Appendix A.7.

We further assume that the relative speed between the gravoturbulence triggering structures and the particles is the drift speed v_{drift}. But in reality, e.g., zonal flows can have radial velocities which would change this relative velocity.

As long as the radial speed of the pressure bump structure is much smaller than the drift speed, the error is small. In this work, again for simplicity, we assume that the relative speed is always given by v_{drift}. Additionally, since we don't know how ε would change with St and r, we assume that it is a constant. As long as condition (2.5) is fulfilled, only the value of the conversion length ℓ matters. That is, one can change the value of ε and d by the same factor, leading to the same result for planetesimals.

2.3 Numerical model

2.3.1 The disk and dust model

In the following, we will summarize the disk and dust model of the dust and gas evolution code from Birnstiel et al. (2010) in which we have implemented our planetesimal formation model.

We assume that turbulence is described by an effective kinematic viscosity of (Shakura & Sunyaev, 1973)

$$\nu = \alpha_{\mathrm{t}} c_{\mathrm{s}} h_{\mathrm{g}}. \tag{2.7}$$

The dimensionless parameter α_{t} describes the strength of turbulence, since it determines the turbulent velocities. Most likely, the turbulent velocities of the largest eddies is roughly given by $\sqrt{\alpha_{\mathrm{t}}} c_{\mathrm{s}}$ as argued by Cuzzi et al. (2001).

We assume further that the gas is vertically in hydrostatic balance (Weizsäcker, 1948) and that consequently the particle and gas density follow the Gaussian profile (Safronov, 1969; Pringle, 1981)

$$\rho_i(r,z) = \rho_{i,0}(r) \cdot \exp\left[-\frac{1}{2}\left(\frac{z}{h_i}\right)^2\right], \tag{2.8}$$

where i is either dust/particles (d) or gas (g). To eliminate the z-dependence, we use column densities[1]

$$\Sigma_i(r,t) := \int\limits_{-\infty}^{\infty} \rho_i(r,z,t)\,\mathrm{d}z. \tag{2.9}$$

The mass density of the gas at the mid-plane ($z = 0$) can then be expressed as

$$\rho_{i,0}(r) = \frac{1}{\sqrt{2\pi}} \frac{\Sigma_i(r)}{h_i}. \tag{2.10}$$

The gas pressure scale height is given by

$$h_{\mathrm{g}} = c_{\mathrm{s}}/\Omega \tag{2.11}$$

and the dust/particle scale height for St < 1 by (Dubrulle et al., 1995)

$$h_{\mathrm{d}} = \left(1 + \frac{\mathrm{St}}{\alpha_{\mathrm{t}}}\right)^{-1/2} h_{\mathrm{g}}. \tag{2.12}$$

Here we assumed that turbulence is isotropic such that the dimensionless vertical diffusion coefficient is just given by α_{t}. In the code, another expression for h_{d} is used which is essentially equivalent to the one in this equation (see Eq. (51) of Birnstiel et al. (2010) for details). Since we use a one-dimensional model with z-integrated values, and the coagulation equation scales with the density squared, the Stokes number is calculated at mid-plane values where densities are the highest. Furthermore, we assume we always stay in the Epstein drag regime (Epstein, 1924) which leads to (Birnstiel et al., 2010; Birnstiel et al., 2012)

$$\mathrm{St} = \frac{\rho_{\mathrm{m}}}{\rho_{\mathrm{g}}} \frac{a}{v_{\mathrm{th}}} \Omega \overset{z=0}{\approx} \frac{\pi}{2} \frac{a \rho_{\mathrm{m}}}{\Sigma_{\mathrm{g}}}. \tag{2.13}$$

Since we use $\mathrm{St}_{\max} = 10$ throughout in this work, one might think that in this case one would be in the Stokes drag

---

[1] In Eq. (2.9) i can also be planetesimals (p).

Table 2.1: Parameters which are kept constant in this Chapter. Values of the disk mass and of r_c can be compared with the statistics in Fig. 3 of Andrews et al. (2010). Per size decade we use 27 grid points.

Symbol	Value	Meaning
$M_\star(t_0)$	$1\,M_\odot$	Initial mass of the central star
$M_{\rm disk}$	$0.05\,M_\odot$	Total initial disk mass (gas+particles)
$r_{\rm c}$	35 au	Transition radius from power-law to exponential drop off for $\Sigma_{\rm g}$, Eq. (2.20)
d	$5\,h_{\rm g}$	Pebble trap distance, Eq. (2.1)
$\tau_{\rm l}$	$100\,t_{\rm orb}$	Lifetime of pebble traps
$f_{\rm ice}$	$1/3$ for $T > 170\,$K	Dust ice parameter, Eq. (2.26)
$Z(t_0)$	10^{-2}	Initial dust-to-gas column density ratio, $\Sigma_{\rm d}/\Sigma_{\rm g}$
γ	1	Power-law index in gas density profile, Eq. (2.20)
q	0.4	Power-law index of temperature profile, Eq. (2.25)
ξ	1.83	Power-law index for fragment distribution, Eq. (A.6)
$v_{\rm f}$	$1-10\,$m/s	Fragmentation threshold speed, Eq. (2.18)
a_0	$0.1\,\mu$m	Smallest grain radius for all times
a_1	$1\,\mu$m	Largest grain radius for initial condition
n	$\propto a^{-3.5}$	Initial number density distribution, Eq. (2.24)
$\rho_{\rm m}$	$1.2\,{\rm g/cm^3}$	Internal density of all solids (dust, pebbles, planetesimals)
$m_{\rm p}$	$1.05\cdot 10^{-7}\,M_\oplus$	Planetesimal mass of 100 km diameter planetesimals, Eq. (2.4)
${\rm St}_{\rm min}$	10^{-2}	Minimum Stokes number participating in trapping & planetesimal formation
${\rm St}_{\rm max}$	10	Maximum Stokes number participating in trapping & planetesimal formation

regime (see Eq. (126) of Stokes, 1851). The transition between Epstein and Stokes drag occurs if the gas mean free path is around 4/9 the radius of the particle (Weidenschilling, 1977a). Since Stokes numbers of 10 are only reached in the very outer part of the disk, where the gas density is sufficiently low, the gas mean free path is many orders of magnitude larger than the size of any particle. Dependent on the gas density, dust grains don't have to grow by much, if at all, to reach these large Stokes numbers. The Stokes drag regime is only reached within a few au. But, again, we will ignore this regime here to avoid overlapping effects with our model.

For growth and fragmentation we solve the Smoluchowski equation (von Smoluchowski, 1916). It considers all binary combinations of particle size bins. It uses a probability for fragmentation and coagulation, depending on the collision speed. This method is identical to the one of Birnstiel et al. (2010), but more details on the Smoluchowski equation can be found in Appendix A.1.

The relative speed of collisions, Δv, can have different contributions. There are systematic velocities from radial drift (Weidenschilling, 1977a; Nakagawa et al., 1986), azimuthal drift (Nakagawa et al., 1986), and vertical settling (Safronov, 1969, p. 26). These scale with the particles Stokes number and vanish for equally sized grains. On the other hand, random speeds such as turbulence (Ormel & Cuzzi, 2007) and Brownian motion lead to non-vanishing relative velocities between equally sized particles. The relative turbulent velocities are proportional to $\sqrt{\alpha_{\rm t}}$, thus $\alpha_{\rm t}$ can be interpreted as a measure not only of turbulence strength in terms of typical turbulent gas velocities, but also of particle collision speed.

The radial gas velocity is given by (Lynden-Bell & Pringle, 1974)

$$u_{\rm r} = -\frac{3}{\Sigma_{\rm g}\sqrt{r}}\frac{\partial}{\partial r}(\Sigma_{\rm g}\nu\sqrt{r}). \tag{2.14}$$

Since the gas motion is determined by a balance of forces among stellar gravity, the gas pressure gradient force, and the centrifugal force, it orbits the star with a different speed than solids, which don't feel a pressure gradient force. Due to a lack in centrifugal force (St < 1), single particles drift radially with a velocity of (Adachi et al., 1976; Weidenschilling, 1977a)

$$v_{\rm drift} = \frac{\rm St}{{\rm St}^2+1}\frac{h_{\rm g}}{r}\frac{\partial \ln P}{\partial \ln r}c_{\rm s}, \tag{2.15}$$

with $P = c_{\rm s}^2\rho_{\rm g}$, i. e., assuming an isothermal case with adiabatic index 1. Since radial gas motion drags dust along, the total radial dust velocity is given by (Takeuchi & Lin, 2002)

$$v_\mathrm{r} = \frac{u_\mathrm{r}}{1+\mathrm{St}^2} + v_\mathrm{drift}. \tag{2.16}$$

We model the fragmentation probability as a smooth transition from 1, for collision speeds above the breakup speed v_f, to 0 for collision speeds below,

$$p_\mathrm{f} := \begin{cases} 0.5 \cdot \exp\left[2(\Delta v - v_\mathrm{f})/(\mathrm{cm/s})\right] & \Delta v \leq v_\mathrm{f} \\ 1 - 0.5 \cdot \exp\left[-2(\Delta v - v_\mathrm{f})/(\mathrm{cm/s})\right] & \Delta v > v_\mathrm{f} \end{cases}, \tag{2.17}$$

where the radius dependent fragmentation velocity is modeled by the smooth function

$$\frac{v_\mathrm{f}(r)}{\mathrm{m/s}} = \begin{cases} 10^{0.5 \cdot \exp\left[4(r - r_\mathrm{ice})/\mathrm{au}\right]} & r \leq r_\mathrm{ice} \\ 10^{1 - 0.5 \cdot \exp\left[-4(r - r_\mathrm{ice})/\mathrm{au}\right]} & r > r_\mathrm{ice} \end{cases}. \tag{2.18}$$

The coagulation probability is given via $P_\mathrm{c} + p_\mathrm{f} = 1$. Experiments with silicate dust grains measured velocities of 1 m/s for the onset of fragmentation (Blum & Münch, 1993; Blum & Wurm, 2008), and theoretical studies (Leinhardt & Stewart, 2009) found similar values. It was found numerically (Wada et al., 2009) that the fragmentation velocity for 10 µm sized icy dust aggregates can reach 50 m/s. Laboratory studies found threshold speeds about 10 m/s for icy grains (Gundlach & Blum, 2014). But this speed depends on the monomer size. Experiments show that v_f decreases with grain size for silicate dust grains (Beitz et al., 2011), which could be partly attributed to the increasing influence of inhomogeneities with growing grain size. For ice, measured erosion threshold velocities are around 15 m/s (Gundlach & Blum, 2014). However, we choose $v_\mathrm{f} = 10\,\mathrm{m/s}$ outside the water ice line. As already mentioned by Birnstiel et al. (2010), the decrease of the threshold collision speed within the ice line leads to a traffic jam effect since inward drifting particles are forced to fragment to smaller sizes, which in turn drift slower.

We follow Youdin & Lithwick (2007) and model the radial particle diffusivity as

$$D_\mathrm{d} = \frac{D_\mathrm{g}}{1+\mathrm{St}^2} \tag{2.19}$$

and we assume that the radial gas diffusivity D_g equals the turbulent viscosity of Eq. (2.7).

Our initial but also fixed gas column density profile follows the self-similar profile as found by Lynden-Bell & Pringle (1974),

$$\Sigma_\mathrm{g}(r) = \Sigma_\mathrm{c} \left(\frac{r}{r_\mathrm{c}}\right)^{-\gamma} \exp\left[-\left(\frac{r}{r_\mathrm{c}}\right)^{2-\gamma}\right]. \tag{2.20}$$

The normalization constant is given by

$$\Sigma_\mathrm{c} = (2-\gamma) M_\mathrm{disk} / [2\pi {r_\mathrm{c}}^2 \cdot (1 + Z(t_0))]. \tag{2.21}$$

At the so-called characteristic radius r_c, the transition between the power-law and the exponential law occurs. The initial profile of the total dust amount is assumed to follow

$$\Sigma_\mathrm{d}(t_0) = Z(t_0)\Sigma_\mathrm{g}(t_0). \tag{2.22}$$

The initial dust-to-gas ratio is set to $Z(t_0) = 0.01$ for all simulations, as found for the interstellar medium (e. g., Savage & Jenkins, 1972). We also fix $\gamma = 1$ and $r_\mathrm{c} = 35\,\mathrm{AU}$ in this Chapter. Furthermore, we keep the static gas column density profile and do not let the disk (viscously) evolve. This has the advantage that we can see the effects of our model parameters for planetesimal formation more clearly without overlapping effects from gas mass transport. Even though we don't let Σ_g evolve, we allow a radial gas velocity according to Eq. (2.14). This leads to outward transport of small grains in the outer disk. For our model parameters, this occurs roughly from 20 au to 200 au and below a particle Stokes number of ($\mathrm{St} \ll 1$)

$$\begin{aligned}\mathrm{St} &\leq \frac{6\left|2-q-\gamma-(2-\gamma)\left(\frac{r}{r_\mathrm{c}}\right)^{2-\gamma}\right|}{2\gamma+3+q+2(2-\gamma)\left(\frac{r}{r_\mathrm{c}}\right)^{2-\gamma}}\alpha_\mathrm{t} \\ &\underset{q=0.4}{\overset{\gamma=1}{=}} \frac{6\left|0.6-r/r_\mathrm{c}\right|}{5.4+2r/r_\mathrm{c}}\alpha_\mathrm{t}\end{aligned} \tag{2.23}$$

as derived in Appendix A.2. For the initial size distribution we assume the dust to follow the distribution in the interstellar medium found by Mathis et al. (1977). I. e., the number density n is described by the power-law

$$n(a) \propto a^{-3.5} \tag{2.24}$$

with dust radii ranging from $a = 0.1\,\mu\mathrm{m}$ to $1\,\mu\mathrm{m}$. For a review on dust evolution in circumstellar disks see, e. g., Birnstiel et al. (2016).

We fix the temperature to a profile similar to that of a radiative equilibrium disk (Chiang & Goldreich, 1997, they derived $T \propto r^{-3/7}$)

$$T(r) = 158.9\,\mathrm{K} \cdot \left(\frac{r}{\mathrm{au}}\right)^{-2/5}. \tag{2.25}$$

The ice line is defined as the position where $T = 170\,\mathrm{K}$ in this Chapter. Within the ice line we reduce the mass of particles to 1/3 of their value for planetesimal formation, i. e. we assume an ice mass fraction of 2/3. For this, we define the rocky-to-(ice and rocky) mass parameter

$$f_\mathrm{ice} = 1/3 \cdot \theta(T - 170\,\mathrm{K}) + \theta(170\,\mathrm{K} - T). \tag{2.26}$$

Lodders (2003) summarizes her findings in Table 11 where the total rock/(total rock+H_2O ice) ratio gives 0.46. In section 3.3 of Min et al. (2011) they find values around 0.54. Hayashi (1981) uses a value of 0.24 for this ratio. We choose a value in between by assuming 1/3 but in the results it is only important to notice the kink in the final planetesimal distribution at the water ice line. For the particle dynamics and growth processes this reduction in mass is not considered. Within the water ice line our simulation thus has too much mass in particles, but the maximum particle size is only weakly affected by this since, in the fragmentation limit, particles grow to the limit again faster than they drift inward. To be able to analyze the impact of our planetesimal model parameters, we do not include accretion heating (Pringle, 1981), opacity effects, or radiative evolution.

2.3.2 Parameterized planetesimal formation

Do we need to restrict the particle species contributing to planetesimal formation? This is the question we are facing in this section. Since particle dynamics depend on the Stokes number, one could think that there exists an interval $[\mathrm{St}_\mathrm{min}, \mathrm{St}_\mathrm{max}]$ between which particles have the right properties for trapping and building clumps of Hill density. The pebble flux regulates the rate at which material is delivered, so this does not need to be restricted by a Stokes number interval. The question is whether there exist particles which cannot participate in trapping *and* planetesimal formation. We know that both trapping, either in zonal flows (Dittrich et al., 2013) or vortices (Fu et al., 2014; Raettig et al., 2015), and collapse to planetesimals (Schreiber, 2018) work for particles with $\mathrm{St} = 10^{-2}$. From Carrera et al. (2015) we learned that $\mathrm{St}_\mathrm{max} \approx 10$. Yang et al. (2017) have shown that streaming instability is possible for $\mathrm{St} = 10^{-3}$ particles if $Z \geq 4 \cdot 10^{-2}$. We know that particles with $\mathrm{St} = 10^{-2}$ still contribute to trapping and gravitational collapse to planetesimals. But so far, we cannot entirely exclude that smaller particles can take part in this process as well—especially for mixtures of different particle species with some mass distribution depending on their Stokes number. However, we use $\mathrm{St}_\mathrm{min} = 10^{-2}$ and $\mathrm{St}_\mathrm{max} = 10$ in this work.

The velocity field of a vortex or zonal flow is modified around pressure bumps, and thus gas motion here differs from the gas motion in a smooth pressure structure. We assume that this motion can be neglected in comparison to the drift velocity.

We further assume that these structures have an average lifetime τ_l proportional to the orbit time. It has been shown

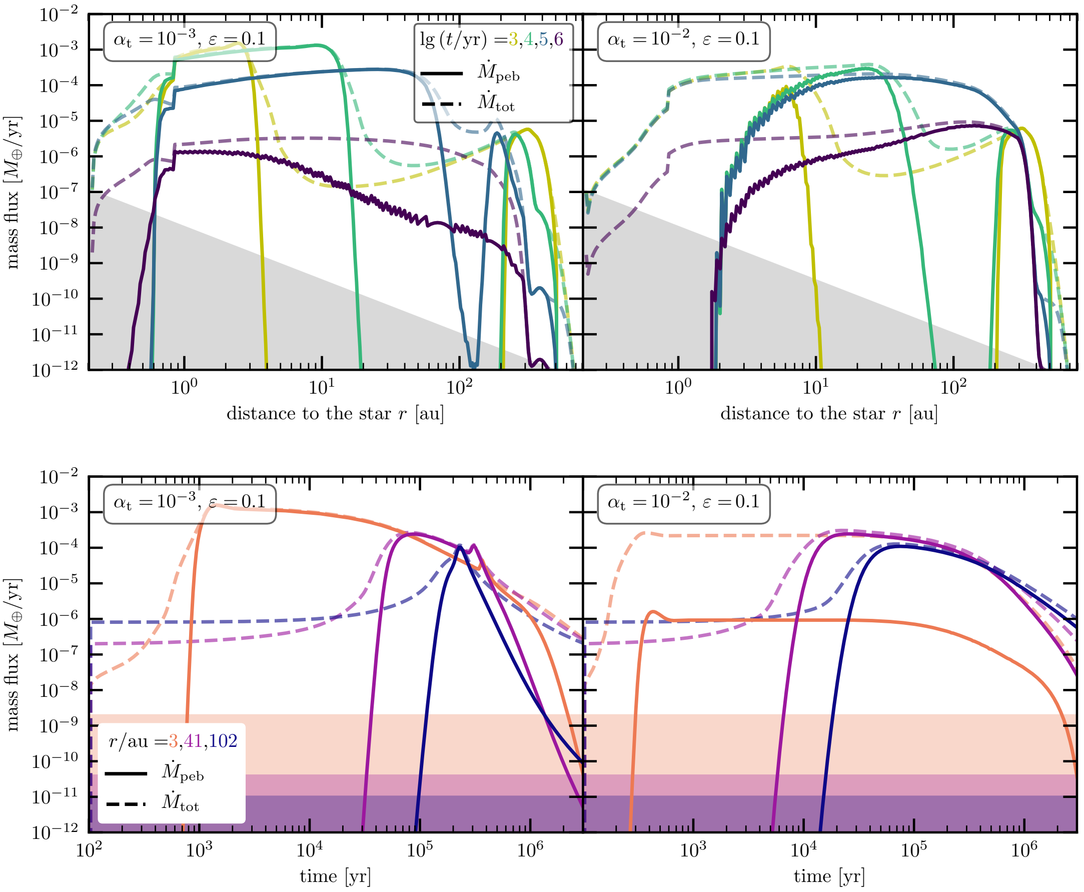

Figure 2.1: Local pebble flux $\dot{M}_{\mathrm{peb}}$ of particles in the range $10^{-2} < \mathrm{St} < 10$ in Earth masses per year (solid lines) for two different assumptions of the disk turbulence: $\alpha_t = 10^{-3}$ (left panels) and $\alpha_t = 10^{-2}$ (right panels), both at a trap efficiency $\varepsilon = 0.1$. The upper panels present a time series of the pebble flux as a function of disk radius for times from 10^3 (yellow) to 10^6 years (purple) in steps of decadic factors. The lower panels show the evolution at different radii as a function of time at 3 (orange), 41, and 102 au (dark blue). In addition we overplot the total mass flux $\dot{M}_{\mathrm{tot}}$, i.e. pebbles plus smaller grains (dashed lines). In the lower panels, within the shaded areas and below, the mass flux is smaller than the critical particle flux $\dot{M}_{\mathrm{cr}}$ below which planetesimal formation does not occur in this model. This is marked by the gray zone in the upper panels.

that both zonal flows (Dittrich et al., 2013) and vortices (Manger & Klahr, 2018) can endure up to hundreds of orbits. Hence, we assume $\tau_1 = 100\,t_{\mathrm{orb}}$ in this Chapter. Based on work by Dittrich et al. (2013) we assume an average radial separation of $d = 5h_g$.

Our analytical description of planetesimal formation arises in the code as a sink term in the advection-diffusion equation for the column density of a single particle species of mass m_i, given by

$$\begin{aligned}
&\frac{\partial \Sigma_d^i}{\partial t} + \frac{1}{r}\frac{\partial}{\partial r}\left\{ r\left[\Sigma_d^i v_r^i - D_d^i \frac{\partial}{\partial r}\left(\frac{\Sigma_d^i}{\Sigma_g}\right)\Sigma_g\right]\right\} \\
&= -\frac{\varepsilon}{d}\left|v_{\mathrm{drift}}^i\right| \Sigma_d^i \cdot \theta(\dot{M}_{\mathrm{peb}} - \dot{M}_{\mathrm{cr}}) \\
&\quad \theta(\mathrm{St}_i - \mathrm{St}_{\min}) \cdot \theta(\mathrm{St}_{\max} - \mathrm{St}_i).
\end{aligned} \tag{2.27}$$

The Heaviside functions $\theta(\cdot)$ represent our conditions that the pebble flux must be critical and that only particles with $\mathrm{St}_{\min} \le \mathrm{St} \le \mathrm{St}_{\max}$ are allowed to build planetesimals. We use the flux conserving implicit donor-cell scheme from

Appendix A.1 of Birnstiel et al. (2010), where we set

$$L_i = -\frac{\varepsilon}{d}\left|v^i_{\mathrm{drift}}\right| \cdot \theta(\dot{M}_{\mathrm{peb}} - \dot{M}_{\mathrm{cr}}) \\ \theta(\mathrm{St}_i - \mathrm{St}_{\mathrm{min}})\theta(\mathrm{St}_{\mathrm{max}} - \mathrm{St}_i) \tag{2.28}$$

in their Eq. (A.1) in order to have an implicit loss term due to planetesimal formation. The number of new planetesimals created within the time step $\mathrm{d}t$ is then given, in terms of column density, by

$$\mathrm{d}\Sigma_{\mathrm{p}} = \dot{\Sigma}_{\mathrm{p}}\,\mathrm{d}t = -\sum_{\mathrm{St}_{\mathrm{min}} \leq \mathrm{St}_i \leq \mathrm{St}_{\mathrm{max}}} L^i\,\mathrm{d}t. \tag{2.29}$$

The pebble flux $\dot{M}_{\mathrm{peb}}$ is estimated from the last time step, but the resulting error from this is very small.

2.4 Results

We start our analysis with the pebble flux because it is directly linked to our planetesimal formation. Particle dynamics is mostly determined by the growth barriers (Birnstiel et al., 2012), i. e. the fragmentation barrier

$$\mathrm{St}_{\mathrm{frag}} = \frac{1}{3\alpha_{\mathrm{t}}}\left(\frac{v_{\mathrm{f}}}{c_{\mathrm{s}}}\right)^2 \tag{2.30}$$

and the drift limit (here in the Epstein regime only)

$$\mathrm{St}_{\mathrm{drift}} = \frac{\Sigma_{\mathrm{d}}}{\Sigma_{\mathrm{g}}}\left(\frac{v_{\mathrm{K}}}{c_{\mathrm{s}}}\right)^2 \left|\frac{\partial \ln P}{\partial \ln r}\right|^{-1}. \tag{2.31}$$

As can be seen in Fig. 2.1, for stronger turbulence levels (here $\alpha_{\mathrm{t}} = 10^{-2}$) the particle flux stays high for longer times because particles are smaller and thus drift slower, see Fig. 2.2. Here we defined the dust column density distribution per logarithmic bin of grain radius a as

$$\sigma_{\mathrm{d}} := \int_{-\infty}^{\infty} n_a(a,r,z) m_{\mathrm{d}}(a) a\,\mathrm{d}z \tag{2.32}$$

with n_a being the number density per grain size bin. The total dust column density can then be written as

$$\Sigma_{\mathrm{d}}(r) = \int_{-\infty}^{\infty} \sigma_{\mathrm{d}}(r,a)\,\mathrm{d}\ln a. \tag{2.33}$$

In the early stages, the flux is smaller for lower α_{t} for the same reason. The pebble growth front, which is the radius at which $\mathrm{St}_{\mathrm{min}}$ particles form the first time, moves from the inside to the outside, while particles drift inward from the outer disk because their Stokes number is high. When these two fronts clash, the density suddenly rises and a particle wave propagates inward which is why one can see a small local peak in the curves of the lower left panel. In the lower right this is not visible since fragmentation is damping this effect.

At late times ($\sim 10^6$ yr) the pebble to total mass flux ratio drops significantly in the $\alpha_{\mathrm{t}} = 10^{-3}$ case. This is due to the drift barrier, which drops to smaller sized particles since Σ_{d} is decreasing, see Fig. 2.3. The gray zone in the upper panels mark the sub-critical flux values, i. e., the fluxes that are too low to allow formation of planetesimals within a trap lifetime. One could change τ_{l} or m_{p} by a factor of 10 without changing the results significantly because the flux is orders of magnitude larger then the critical value.

Since the mass reservoir is in the outer disk where gas densities are very low, the pebble flux in the outer region around $\sim 200-400$ au already reaches critical values, and leads to planetesimal formation, in the early phase ($\lesssim 10^4$ yr).

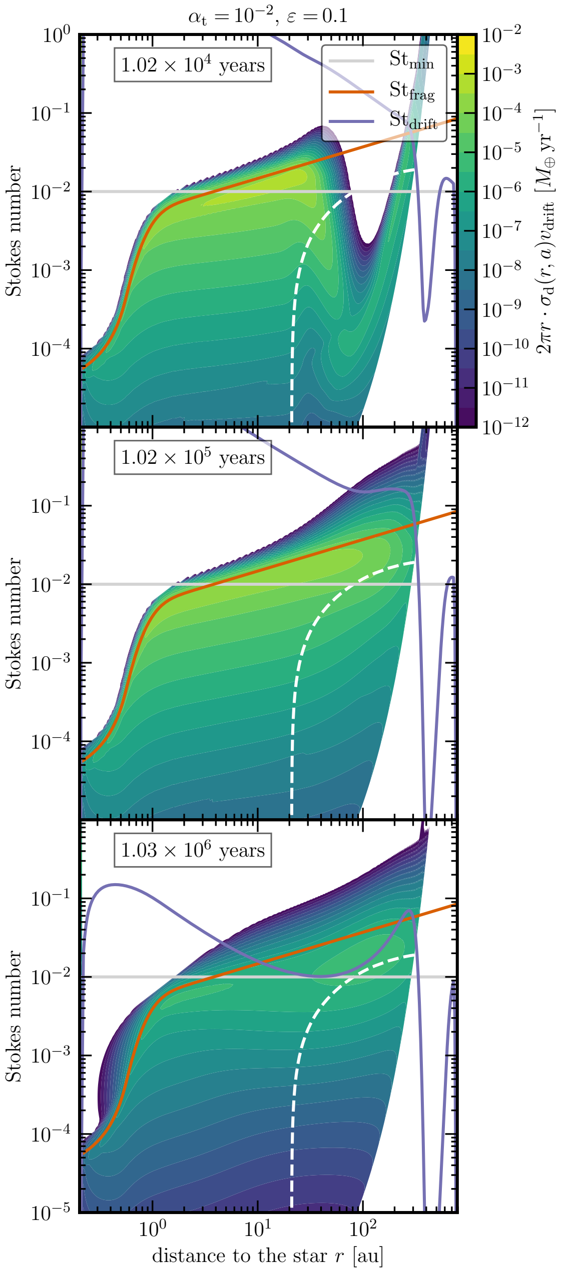

Figure 2.2: Local particle flux due to the radial drift velocity per size bin (color) as a function of Stokes number and disk radius. The turbulence level is $\alpha_t = 0.01$ with an efficiency parameter for planetesimal formation of $\varepsilon = 0.1$. Particles below the white dashed line move outward. Even though we only show the flux resulting from v_{drift}, for the white dashed line we also considered the gas velocity according to Eq. (2.16). For this line, motion due to diffusion is not considered but it is included in the simulation. The horizontal gray line shows the lower limit for which we allowed the particles to participate in the gravoturbulent planetesimal formation process. The purple and red lines show the drift (Eq. (2.31)) and fragmentation barrier (Eq. (2.30)), respectively. In Appendix A.6 we explain where the particles greater than the growth barriers stem from.

When the slope of Σ_p is steeper than r^{-2} (see Fig. 2.4), the mass contribution to the total planetesimal population in the disk will not rise with r. I. e., the contribution becomes less the further out in the disk the considered regions are.

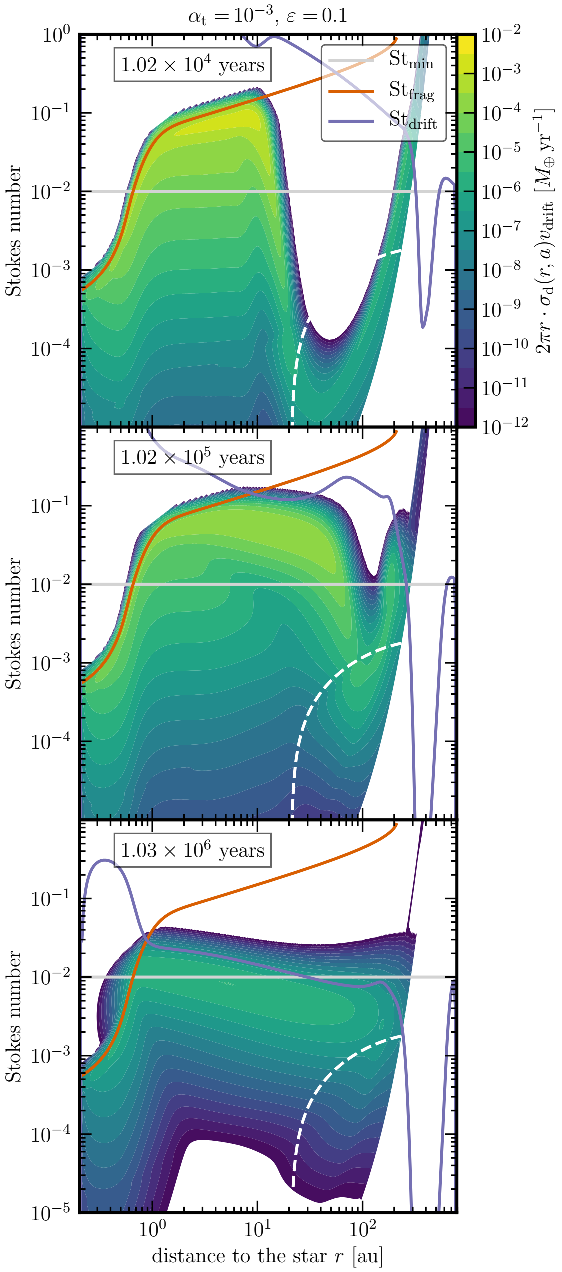

Figure 2.3: Same as Fig. 2.2 but with $\alpha_t = 10^{-3}$ and $\varepsilon = 0.1$. Since the fragmentation barrier is inversely proportional to α_t, the maximum size and thus also the maximum Stokes number is much larger. Most of the time the disk is primarily limited by drift which causes a top-heavy size distribution. Growth is slower compared to the $\alpha_t = 0.01$ simulation because of smaller relative turbulent velocities leading to lower collision rates.

For a fixed logarithmic binning, this can be seen by writing the planetesimal mass between disk radius r_1 and r_2 as

$$M_p(r_1, r_2) = 2\pi \int_{\ln r_1}^{\ln r_2} \Sigma_p r^2 \,\mathrm{d}\ln r. \tag{2.34}$$

Hence, the probably unphysical outer bump in Σ_p doesn't contribute significantly if the slope is steeper than r^{-2}.

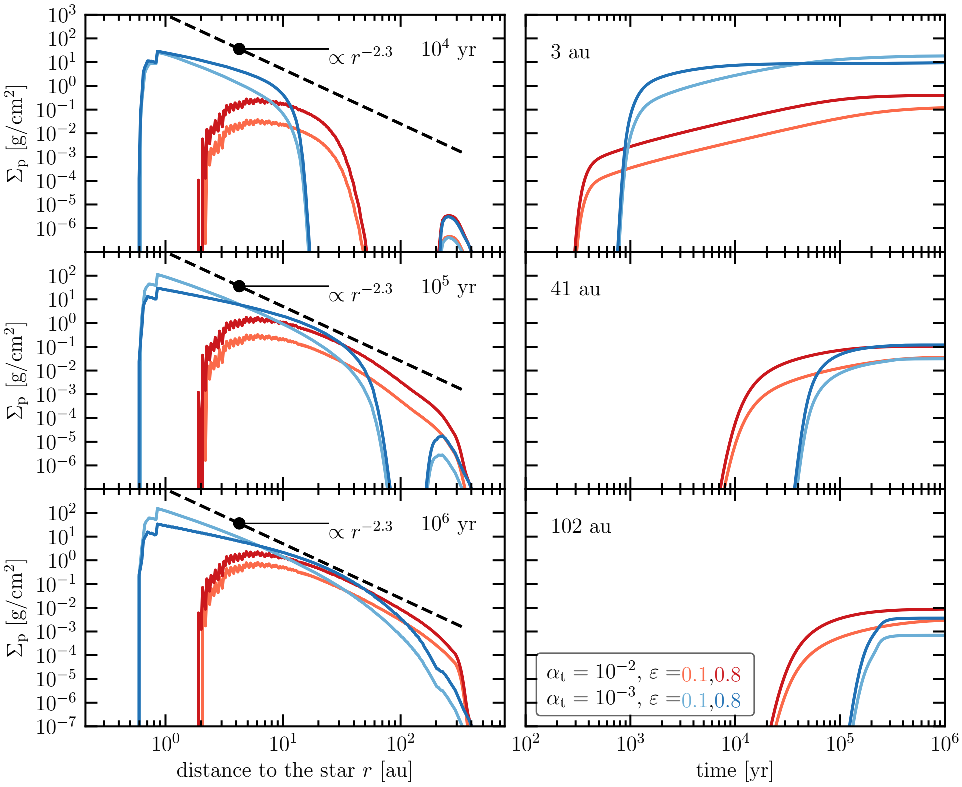

Figure 2.4: Planetesimal column density for different snapshots (left panels) vs. disk radius and for different radial disk positions as a function of time (right panels). The fact that the final Σ_p at 40 au (see middle right panel) of the $\alpha_t = 10^{-2}$ and 10^{-3} simulations is roughly the same for the same ε is pure coincidence. The initial characteristic radius was $r_c = 35$ au and the initial total disk mass $M_{\text{disk}} = 0.05\,M_\odot$. The black dashed line shows the predicted slope for a r-independent pebble flux after Eq. (2.37). The zigzag structure which can be seen within 10 au for $\alpha_t = 0.01$ stems from a lack of mass resolution. This is also visible in Fig. 2.2 above the St_{min} line. The sharp kink at large radii for $\alpha_t = 10^{-2}$ is caused by $\text{St}(0.1\,\mu\text{m}) = \text{St}_{\text{max}}$, i. e., by a rapidly decreasing pebble flux. A viscously evolving disk with dispersal would smear out this kink.

We think this outer formation region would not exist in the *early* evolution of the disk, since the formation time of structures such as vortices means they need a few orbits to form, which would take much longer in the outer than in the inner disk.

If turbulence is strong (here $\alpha_t = 10^{-2}$), fragmentation will be the growth limiting process. In that case not only is the maximum grain size smaller, but there are also more small grains in general. Hence, in comparison to simulations with weaker turbulence (here $\alpha_t = 10^{-3}$), particles in the outer disk stay there for longer and can form planetesimals. Fig. 2.4 and 2.5 show the resulting planetesimal column density Σ_p and formation rate $\dot{\Sigma}_p$, respectively, both for different snapshots showing the entire disk and for local evolutions. For the latter, we chose 3 au (~ position of the main Asteroid Belt), 40 au (~ position of the Kuiper Belt), and 100 au to show the behavior in the outer disk. Planetesimal formation basically starts shortly after the first pebbles have formed. We summarize the effects as follows:

- $\alpha_t = 10^{-2}$: higher ε generally lead to higher planetesimal formation rates but these also decline faster. In the end this nevertheless ends in a more abundant planetesimal population for higher ε in the entire disk.
- $\alpha_t = 10^{-3}$: in the outer disk $\dot{\Sigma}_p$ is also higher for larger ε, such as in the higher α_t case. Radial drift removes the largest particles of the top-heavy size distribution. The fewer particles were converted into planetesimals in the outer disk, the more material is available at later times in the inner regions (conservation of mass). This can lead to more planetesimals in the inner disk for smaller ε. This effect cannot be seen in the results of the $\alpha_t = 10^{-2}$ simulations since fragmentation events slow down the radial motion and the feeding zones of planetesimals are much narrower.

If the mass flux of pebbles is roughly r-independent, one can estimate the slope of the outcoming planetesimal

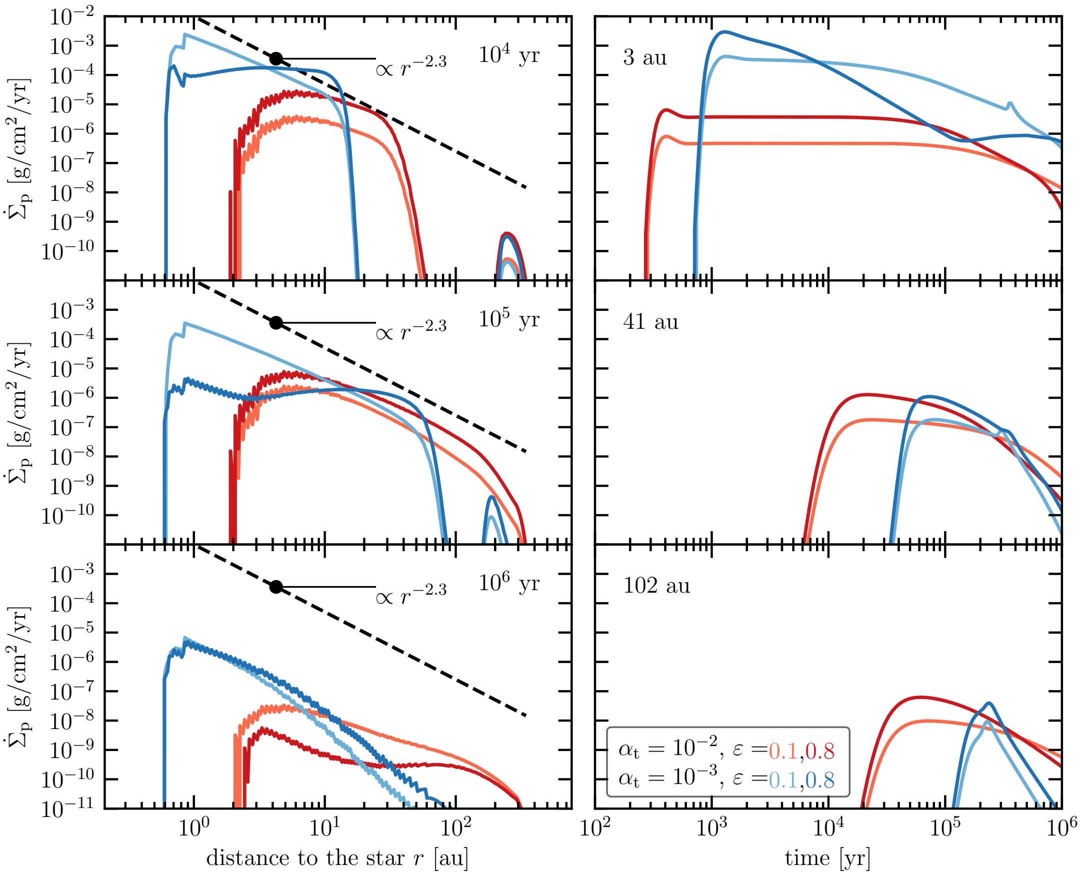

Figure 2.5: Same as Fig. 2.4 but showing the planetesimal column density formation rate $\dot{\Sigma}_p$.

profile as we show in section 2.4.2.

In Fig. 2.6 we show the column densities of gas, dust and planetesimals for different snapshots and locations in the disk. This way one can not only see that for $\alpha_t = 10^{-3}$ plantesimals form at $2-3$ au after a few thousand years, but also after a few ten to hundred thousand years at $20-30$ au. Fig. 2.6 also shows the ratios of dust to gas, planetesimals to dust and planetesimals to initial dust. For $\alpha_t = 10^{-2}$, the zone where planetesimals are formed moves faster outward due to faster growth from dust to pebbles. We summarize the different ratios as follows:

dust-to-gas ratio Σ_d/Σ_g

This ratio is constantly decreasing since we kept the gas density constant. In the early stages of evolution ($\lesssim 10^6$ yr) Σ_d/Σ_g decreases faster for smaller α_t because particles drift faster.

planetesimals-to-dust ratio Σ_p/Σ_d

- $\alpha_t = 10^{-3}$: from 10^4 yr on, values above unity are reached within 2 au. At 10^6 yr this ratio is > 1 almost everywhere in the disk.
- $\alpha_t = 10^{-2}$: only at late times ($\gtrsim 10^6$ yr) values above unity are reached.

planetesimals-to-initial dust ratio $\Sigma_p/\Sigma_d(t_0)$

- $\alpha_t = 10^{-3}$: at $10^5 - 10^6$ yr within 10 au values above unity are reached, indicating a larger feeding zone of planetesimals, i. e. material significantly contributing to planetesimals can come from far outside.

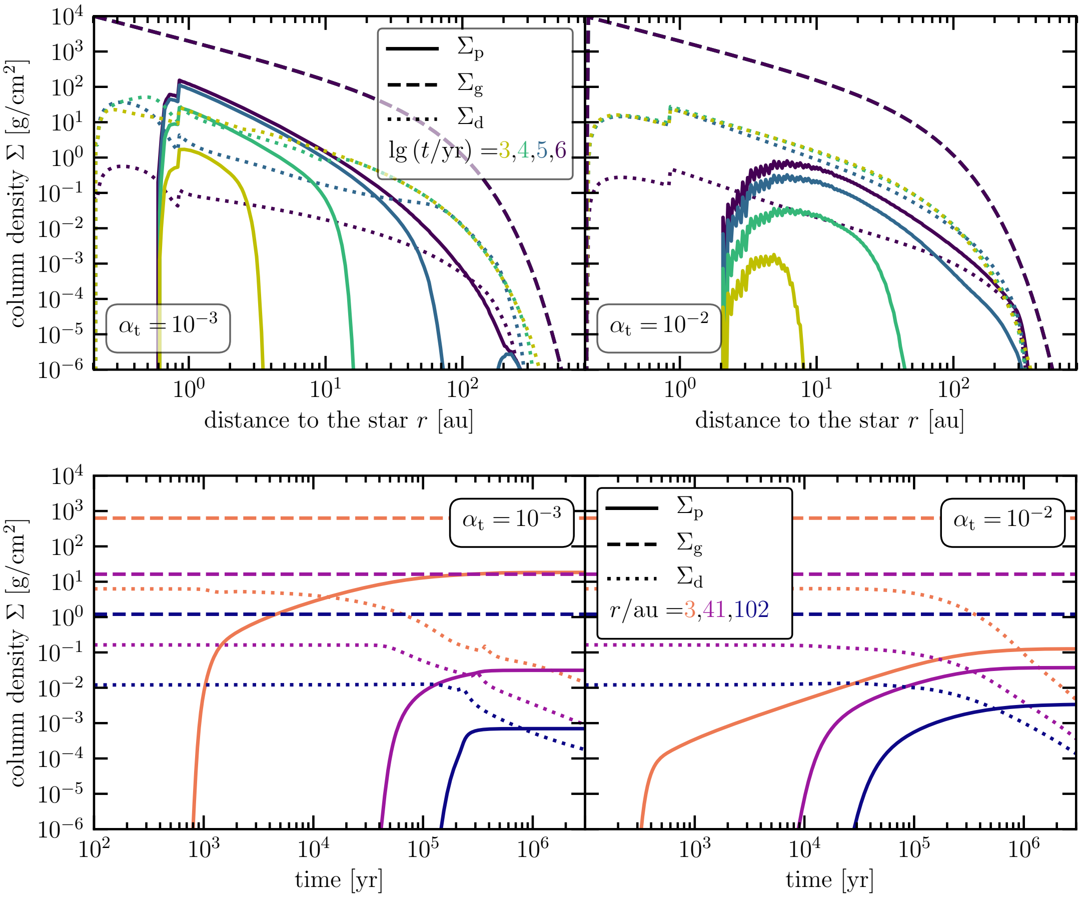

Figure 2.6: Evolution of the gas (dashed lines), dust (dotted lines), and planetesimal (solid lines) column densities for simulations with $\alpha_t = 10^{-3}$ (left panels) and $\alpha_t = 10^{-2}$ (right panels) where $\varepsilon = 0.1$. The upper panels show a time series of the column densities as a function of radius and the lower ones the densities at local positions as a function of time. The characteristic kink around 0.8 AU is caused by the ice line, which does not move because the temperature $T(r)$ is not allowed to change.

- $\alpha_t = 10^{-2}$: the ratio never becomes greater than 1 which indicates that fragmentation allows more time to form planetesimals out of the available material, i. e. the drift timescale of single particles *including* destruction events is slower than the timescale of planetesimal formation.

2.4.1 Necessity for lower turbulence (α_t) to form Earth

If our assumptions are correct, no planetesimals are formed within 2 au. The reasons for that are on the one hand the value of $\mathrm{St}_{\mathrm{min}}$ and on the other hand the temperature profile. The latter dictates the radial shape of the fragmentation barrier. For a more realistic temperature model, accretion heating would lead to higher temperatures in the inner disk and a steeper slope. As a result of that the water ice line would be shifted further out. Hotter temperatures lead to a larger gas scale height and thus also to larger d. At the same time particles would be smaller due to the lower fragmentation barrier. Both effects would cause a planetesimal free zone, or at least a much smaller planetesimal population in the inner disk ($\lesssim 3$ au). I. e., these problems we see here would be even worse, which makes it very likely that our conclusion still holds if more physics is taken into account. As we show in Appendix A.5, the total mass of planetesimals in the entire disk is also problematic if α_t is high.

Yang et al. (2018) measured in shearing box simulations with non-ideal MHD and a dead zone values of the order of $\alpha_t \sim 10^{-4}$ to 10^{-3}. In layered accretion theory values of $\alpha_t \sim 10^{-6}$ to 10^{-4} seem to be preferred (Johansen et al., 2015). Hence, our finding is congruent with their findings.

2.4.2 Planetesimal column density steeper than that of initial gas and dust

Fig. 2.6 shows that for lower turbulence (here $\alpha_{\mathrm{t}} = 10^{-3}$) the slope of the planetesimal column density can be steeper than that of initial gas and dust. This result stems mostly from the r-dependency of $d \propto h_{\mathrm{g}}$. On top of this, transport phenomena can change it as well. For $\varepsilon = 0.1$, this can even be shown analytically since the pebble flux does not depend on r over a larger region of the inner disk (Fig. 2.1). We find that the final slope of the planetesimal column density is steeper than that of the gas if the effective efficiency ε/d is sufficiently small (here $0.02/h_{\mathrm{g}}$, $\varepsilon = 0.1$). If this effective efficiency is large (e. g., $0.16/h_{\mathrm{g}}$, $\varepsilon = 0.8$), the feeding zone of planetesimals is much smaller, i. e., planetesimal material stems from a local region, leading to a slope much closer to the initial dust density, which is the same as for the gas in our simulations.

If the pebble flux is constant for all r, i. e., for size distributions dominated by particles with Stokes numbers $\mathrm{St}_{\mathrm{min}} \leq \mathrm{St} \leq \mathrm{St}_{\mathrm{max}}$ and sufficiently small ε/d, then we can conclude that

$$\Sigma_{\mathrm{p}} \propto \dot{\Sigma}_{\mathrm{p}} \propto \frac{v_1 \Sigma_{\mathrm{peb}}}{h_{\mathrm{g}}} \tag{2.35}$$

where v_1 is the pebble drift speed. For a constant pebble flux, $\dot{M}_{\mathrm{peb}}$, the pebble column density is given by

$$\Sigma_{\mathrm{peb}} = \frac{\dot{M}_{\mathrm{peb}}}{2\pi} \frac{1}{r v_1} \tag{2.36}$$

leading to

$$\Sigma_{\mathrm{p}} \propto \dot{\Sigma}_{\mathrm{p}} \propto 1/(r h_{\mathrm{g}}) \propto r^{(q-5)/2}. \tag{2.37}$$

For the temperature power-law index we used throughout this Chapter, $q = 0.4$, this gives a planetesimal column density profile of $\Sigma_{\mathrm{p}} \propto r^{-2.3}$, independent of the gas column density profile. In this case, the *slope* of the planetesimal column density Σ_{p} does not depend on ε, but the total value of Σ_{p} scales with it linearly. For regions limited by fragmentation, the condition that the flux must be dominated by pebbles ($\mathrm{St}_{\mathrm{min}} \leq \mathrm{St} \leq \mathrm{St}_{\mathrm{max}}$) is almost always violated since fragmentation grinds particles to sizes with Stokes numbers smaller than $\mathrm{St}_{\mathrm{min}}$. Due to fragmentation events small particles are constantly replenished. But the result on the right side of proportionality (2.37) does not, in principal, depend on whether growth is limited by drift or fragmentation—as long as the conditions for a radius-independent pebble flux are fulfilled. Furthermore, as can be seen in Fig. 2.1, the pebble flux may only vary with r within roughly one order of magnitude, which is still good enough to estimate the slope of Σ_{p}.

2.5 Discussion

2.5.1 Limitations of the current model

In this Chapter, the gas density is kept constant, i. e., we neither allow the disk to evolve viscously (Lüst, 1952; Pringle, 1981) nor do we include sink terms such as photoevaporation (e. g. Owen et al., 2012). We also don't include a disk build up phase as tested by Birnstiel et al. (2010) or Drążkowska & Dullemond (2018). In order to isolate the influence of the new parameters of the model for analysis, we assume a constant temperature profile according to Eq. (2.25) and ignore viscous heating (Pringle, 1981). We keep v_{drift} as for a smooth gas profile, but regions with shallow pressure profiles or even pressure bumps would slow down the drift speed. This effect was not considered here since we have a lack of information about how exactly v_{drift} would be affected by zonal flows, vortices, or other structures leading to a significant slow-down of particles and subsequent gravoturbulent planetesimal formation. Also, planetesimals stay in the annulus where they are born. Their mass and radius are not allowed to change, i. e., we ignore collisions between them and also growth due to pebble accretion (Ormel & Klahr, 2010), as well as radial motion. Furthermore, we can only give a first impression of how planetesimal formation is described and behaves in this model, since we have not explored the full parameter space (M_{disk}, r_{c}, $Z(t_0)$,...).

The turbulence parameter α_{t} mostly controls the relative velocities between grains (Brauer et al., 2008a). Though this parameter from Eq. (2.7) can be given by disk winds which cause the transport of angular momentum (see e. g. Papaloizou & Lin, 1995; Béthune et al., 2017), it can also be entangled in, e. g., vortex formation. Hence, a trap formation time, together with a $\alpha_{\mathrm{t}}(r,t)$ model, would make the results more realistic—especially in the outer disk region where it may take a long time to form vortices. Due to conservation of momentum, there is not only the influence of gas on dust but also a back-reaction of particles on gas (Tanaka et al., 2005; Nakagawa et al., 1986). This back-reaction becomes important only for $Z \gtrsim 0.1$, which is not reached in the simulations presented in this Chapter. But without planetesimal formation, this value can be reached in the vicinity of the ice line where particles are forced to fragment and, thus, to slow down. The sink term of pebbles due to planetesimal formation confines this effect. Furthermore, we do not consider the bouncing or charging barrier and we do not trace volatiles.

As pointed out by Drążkowska et al. (2014a), Smoluchowski solvers need a high resolution in mass to mimic the upper end of the size distribution well enough. Especially in the high $\alpha_\mathrm{t} = 0.01$ case this upper end can be important for planetesimals formation.

2.5.2 Comparison to other models

In this section we will compare with the most prominent models for planetesimal formation.

Continuous fluffy growth

Okuzumi et al. (2012) and Kataoka et al. (2013) describe continuous growth to planetesimals. They assume that the threshold velocity for fragmentation is never reached, thus avoiding disruptive events. Without replenishment of small particles these shouldn't be seen in observations. This "fluffy path" of planetesimal formation is highly sensitive to the disk parameters (e. g. α_t) and works roughly up to 10 au for the conditions presented in these papers. Another problem would be that the size distribution of initial planetesimals cannot explain the kink feature we see in the size distribution of the Asteroid belt (Bottke Jr et al., 2005a), the Kuiper belt (Fuentes & Holman, 2008; Fraser & Kavelaars, 2008), Jupiter trojans (Jewitt et al., 2000), and of Neptune trojans (Sheppard & Trujillo, 2010, see their Fig. 4 for an overview) today. Even though runaway growth may start at the size of the kink feature (Kobayashi et al., 2016) which depends on the turbulence level α_t and the mass which is initially available (see their Fig. 6). But this feature is covered by the theory of planetesimal formation via gravitational instability (Morbidelli et al., 2009; Klahr & Schreiber, 2015; Schreiber, 2018), almost independent of disk radius and very robust against changes in α_t. However, one cannot dismiss the idea of fluffy growth entirely, especially in the early stages of particle growth. Even some planetesimal could be formed this way without a conflict with today's data.

However, as shown by Krijt et al. (2015), erosion, where particles lose mass due to collisions with smaller projectiles, may prevent growth through the radial drift barrier. They also show that only for high erosion velocity values of 60 m/s porous particles can overcome this barrier within 10 au for a minimum mass solar nebula (Weidenschilling, 1977b; Hayashi, 1981).

Lucky particle growth

By including a Maxwell-Boltzmann like velocity distribution, lucky particle effects can occur as described by Windmark et al. (2012b) and tested by Drążkowska et al. (2014b) and Estrada et al. (2016). I. e., growth barriers are smoothed out or can be overcome by low velocity collisions leading to growth where the mean collisional speed would lead to bouncing or fragmentation. Although these low velocity collisions have a low probability, by experiencing multiple lucky collisions in a row, the growth barriers can be overcome. In the case of the bouncing barrier, this effect is even stronger because higher collision velocities lead only to bouncing, i. e. no disruption but possible further compactification, but low velocity collisions let the grains grow. Therefore, the bouncing barrier may not be a strict solid barrier as long as the growth timescale (considering bouncing) is sufficiently small. By overcoming the bouncing and fragmentation barrier, these particles present the seeds for a sweep-up scenario which can cause a growth process toward planetesimal size.

But this path is quite inefficient in forming planetesimals and it did not take drift into account. The key here is to have most collision partners leading to mass transfer or sticking. But a lower fragmentation threshold speed within the ice line would basically make it impossible to grow beyond the barriers (or very unlikely). And in the outer disk, drift is removing the lucky particles faster than they can grow beyond the bouncing barrier (Drążkowska et al., 2014b; Estrada et al., 2016).

Planetesimal formation directly regulated via streaming instability

Drążkowska et al. (2014a) and Drążkowska et al. (2016) proposed a parameterized formation model of planetesimals by asking when and where the pebble density (St > 0.01) in the disk midplane reaches a critical value of $\rho_\mathrm{d}/\rho_\mathrm{g} = 1$,

Table 2.2: Overview of different approaches leading to streaming instability (SI) or planetesimals (ptes). With $\alpha_t = 0$ we mean that there is no turbulence active, or only turbulence stemming from streaming instability itself. The second quantity is the sub-Keplerianness, defined as $\eta := 1/2 \cdot (h_g/r)^2 \cdot \mathrm{d}\ln\rho_g / \mathrm{d}\ln r$. In the third column with "feedback" we mean particle-gas coupling such that momentum is also transferred to the gas if particles loose momentum due to the interaction with the gas. The velocity dispersion of particles is δv, Ω is the Kepler frequency, and G the gravitational constant. For larger particles δv decreases, allowing gravitational instability for large particles (Weidenschilling, 1995). The question mark in the third row indicates that one cannot be entirely sure that streaming instability is active.

input				result		
α_t	η	feedback	$Z = \Sigma_d/\Sigma_g$	SI	ptes	references
$= 0$	$= 0$	no	$> \Omega\delta v/(\pi G \Sigma_g)$	no	yes	Safronov (1969); Goldreich & Ward (1973); Youdin & Shu (2002)
> 0	> 0	no	0.01	no	yes	Johansen et al. (2006)
> 0	> 0	yes	0.01	?	yes	Johansen et al. (2007)
$= 0$	> 0	yes	0.01	yes	no	Johansen et al. (2007)
$= 0$	> 0	yes	$\gtrsim 0.03$	yes	yes	Johansen et al. (2009b); Simon et al. (2016); Abod et al. (2018, $Z = 0.1$, η varies)

assuming a balance of sedimentation and vertical diffusion of pebbles. At this critical dust-to-gas ratio it can be argued that the streaming instability will be triggered (Youdin & Goodman, 2005). But as was shown by Johansen et al. (2009b), Carrera et al. (2015), and Yang et al. (2017) triggering the streaming instability at $\rho_d(\mathrm{St} > 10^{-2})/\rho_g = 1$ is not sufficient to create strong enough over-densities to lead to gravitational collapse. The additional criterion to have the total local column density dust-to-gas ratio (Σ_d/Σ_g) increased by a factor of 2–4 seems to be implicitly tested by having sufficient sedimentation even at $\alpha_t = 10^{-4}$ as vertical diffusion. But, as argued by Drążkowska et al. (2016), and also shown by Carrera et al. (2017, see their Fig. 2), reaching the critical midplane dust-to-gas ratio is typically the stronger condition. Similar to our ansatz, Drążkowska et al. (2016) convert pebbles into planetesimals with a certain efficiency per orbit, where the column density formation rate $\dot{\Sigma}_p \propto \Sigma_d(\mathrm{St} > 10^{-2})$ in their model. I. e., they use a local approach whereas we focus on the pebble delivery via the local pebble flux.

In the work of the follow-up paper by Drążkowska & Alibert (2017), they follow a trap that will actually show up in 1D radial disk models, e.g. pebble pile beyond the (water) ice line due to traffic jam and recondensation of water vapor. This means planetesimal formation will mainly happen outside of and close to the ice line in their model. As a result, planetesimals will be confined to a relatively narrow region between 2 and 5 au. Besides that they likely will be too water rich to explain the composition of terrestrial planets. Not only are planetesimals only formed where the water ice line is moving (relatively small annulus compared to the disk size), but the time for planetesimal formation is also very limited ($\sim 2-3 \cdot 10^5$ yr).

Since in our model planetesimals are also formed in the outer disk, less material will reach the inner part. Hence, we may not reach their condition $\rho_d(\mathrm{St} > 10^{-2})/\rho_g \geq 1$, which we illustrate in Fig. 2.7. Even though the back-reaction of particles on gas and the effect of collective drift may not be important here, tracing water vapor could make a difference. Nevertheless, we don't reach the condition used by Drążkowska et al. (2016) since the midplane dust-to-gas ratio is more than one order of magnitude below the critical value of unity over almost the entire disk. In principle, a combined formation model of both pebble flux regulated formation in pressure bumps and the local conversion could coexist. Maybe photoevaporation can reduce the gas content at late times ($\gtrsim 10^6$ yr) so much that the condition can be reached in some parts of the disk.

We would like to emphasize that streaming instability per se is *not* mandatory for gravitational assisted planetesimal formation, and in fact it prevents planetesimal formation for low enough overall dust-to-gas ratios in the disk (Johansen et al., 2007). As in star formation (Klessen et al., 2005), turbulence plays a dual role. On global scales it promotes planetesimal formation by leading to clumps and enhancing the local dust-to-gas ratio, while at the same time it can prevent collapse on smaller scales by diffusing material away. I. e., turbulence stabilizes dust against collapse on small scales (Schreiber, 2018). Also the resulting planetesimal size is a question of particle diffusion, which does not necessarily have to stem from streaming instability. We summarize the work that has been done on fundamental research concerning planetesimal formation with and without turbulence in Table 2.2. If disk models assume some non-zero value for α_t as in Drążkowska et al. (2016), it means that large scale turbulence is active. Whether there is a critical Z, ρ_d/ρ_g or streaming instability criterion for these turbulent cases (magneto-rotational instability (MRI) etc.) in order to form planetesimals has not been studied so far. The simulations by Johansen et al. (2007) and

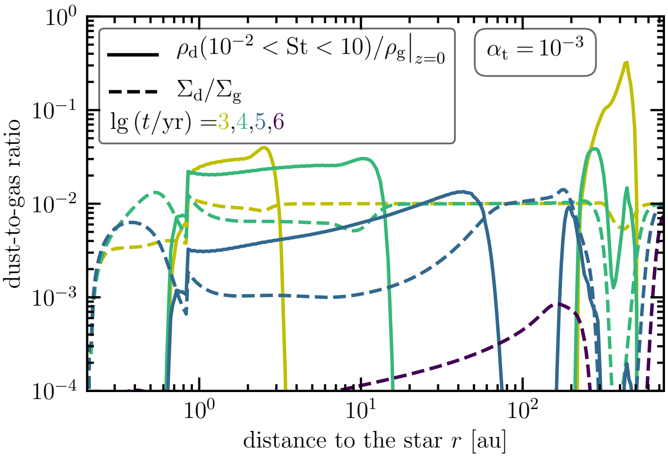

Figure 2.7: Snapshots from 10^3 yr (yellow) to 10^6 yr (purple) of the dust-to-gas ratio in the disk midplane of $10^{-2} < \mathrm{St} < 10$ particles (solid) and the column density ratio $Z = \Sigma_d/\Sigma_g$ of all particles (dashed). The turbulence level is $\alpha_t = 10^{-3}$. Though the dust scale height from Dubrulle et al. (1995), see Eq. (2.12), is only valid for $\mathrm{St} < 1$ particles, to follow and compare to Drążkowska et al. (2016) we adopted this expression also for particles with larger Stokes numbers (in the outer disk). Particles close to the outer edge of the disk can reach large Stokes numbers > 1 due to the low gas density. At 10^6 yr the midplane dust-to-gas ratio is smaller than Z since most of the mass is not in $10^{-2} < \mathrm{St} < 10$ particles anymore.

Johansen et al. (2011) were in fact for MRI turbulent cases, and found planetesimal formation in zonal flows with streaming instability playing a minor role in enhancing perturbations on smaller scales. Planetesimals formed with and without particle feedback, i. e., streaming instability. These simulations unfortunately had to use quite large particles ($\mathrm{St} = 0.25$), which is due to the problem of covering the large scales of MRI turbulence on scales of $\sim h_g$, whereas the streaming instability unstable wavelength for smaller Stokes number particles of $\mathrm{St} = 0.1 - 0.01$ is more like $0.01 h_g$. This makes 3D simulations of MRI and streaming instability leading to planetesimal formation for small Stokes numbers too challenging at the moment.

Higher Z damps streaming instability (Schreiber, 2018), which means lower diffusion. And when there is less diffusion, planetesimals form (i. e., for weaker streaming instability), as seen in Bai & Stone (2010, see their table 2 and their section 7.2.4.). In our Table 2.2 we collect evidence that streaming instability is not needed for planetesimal formation, but it is a controlling effect—it can even prevent the formation. Hence, we suggest following Johansen et al. (2006) and calling the process "gravoturbulent planetesimal formation". Remember, in a disk without a local radial pressure gradient, there is no streaming instability and the Goldreich & Ward (1973) mechanism will work perfectly as recently demonstrated by Abod et al. (2018).

Auffinger & Laibe (2017) find streaming instability to be active in local pressure maxima, despite the pressure gradient vanishing locally. Whether this triggering of streaming instability has an impact on the formation of planetesimals has not been studied in detail. Yet, Johansen et al. (2007) and Johansen et al. (2011) find indeed the formation of planetesimals in these bumps, leaving the role of streaming instability undetermined so far. Furthermore, there can also be streaming instability in the r-φ (radial-azimuthal) plane (Schreiber & Klahr, 2018).

2.6 Conclusion and Outlook

I presented a new model for the planetesimal formation rate that is directly linked to the local pebble flux—and not local dust-to-gas ratio or local density—relying on parameters such as lifetime of pressure-bump structures, contributing particle Stokes numbers ($\mathrm{St}_{\mathrm{min}}$ & $\mathrm{St}_{\mathrm{max}}$), the radial particle trap density ($1/d$), and an efficiency parameter ε describing the conversion from pebbles to planetesimals. I have implemented the presented model into a sophisticated dust and gas evolution code, where I switched off gas evolution. This model was investigated for two different values of the turbulence parameter, $\alpha_t = 10^{-3}$ (moderate turbulence) and 10^{-2} (strong turbulence), as well as two different efficiency values, $\varepsilon = 0.1$ and 0.8. The results can be summarized as follows:

- This model is the first one creating planetesimals *everywhere* in the disk from a few au to a few hundred au.

- The resulting planetesimal distribution and the total mass of initial planetesimals highly depends on the level of turbulence (α_t value), i. e. whether particle growth is limited by fragmentation or drift.
- If the disk is fragmentation limited, higher ε/d leads to higher planetesimal formation rates, but these also decline faster. Nevertheless, higher efficiencies yield more planetesimals.
- If the disk is mostly limited by drift, material drifts faster and particles which were not converted into planetesimals in the outer disk can build planetesimals in the inner part. That is, if the level of turbulence is not too high (here moderate turbulence for $\alpha_\mathrm{t} = 10^{-3}$), the slope of the final planetesimal profile can be steeper than that of initial dust and gas. The overall planetesimal profile Σ_p looks also more like a power-law in the inner disk part, with an exponential roll off in the outer part for lower turbulence.
- A few planetesimals should have formed in the terrestrial region. Thus, strong turbulence ($\alpha_\mathrm{t} = 10^{-2}$) seems to be unlikely for the Solar Nebula in order to form the Solar System, especially Earth— at least as long as the minimum Stokes number contributing to planetesimal formation is as high as $\mathrm{St}_\mathrm{min} = 10^{-2}$ and the efficiency parameter ε is not very high ($\gtrsim 0.8$ for $d = 5h_\mathrm{g}$).
- The late stage planetesimal-to-dust ratios indicate a larger feeding zone of planetesimals, i. e. material forming planetesimals can originate from far away if ε/d is small. Here, it is difficult to tell how small exactly, since the feeding zone will stretch with smaller values of that ratio. In this work, $0.1/(5h_\mathrm{g})$ is small compared to $0.8/(5h_\mathrm{g})$. But one has to investigate in the future how exactly this feeding zone scales with ε/d.

Future work will analyze the influence of disk evolution and other disk parameters such as the initial disk mass and disk size. Implementing of a proper temperature model with accretion heating, photoevaporation, planetesimal collisions, and pebble accretion will be the focus of future work. For an upcoming study, one could compare the outcome of our simulations for the initial planetesimal population with constraints in special regions of the solar nebula to exclude certain pairings of disk parameters, or even extreme cases for specific parameters such as $\alpha_\mathrm{t} \geq 10^{-2}$. The efficiency parameter ε of the combination of trapping and planetesimal formation can depend on both the particle Stokes number and the disk radius. Fluid dynamics codes have to show how this efficiency depends on particle and disk properties. In this Chapter, we assumed that particle traps are present from the beginning of the simulation. In reality these traps will take some time to form. Thus, one could introduce another parameter which describes the trap formation time. During this time, particles can drift inward, reducing the mass reservoir and the pebble flux available for transformation into planetesimals once particle traps are considered to be active.

3

Toward Constraining the Parameter Space for the Solar Nebula

When we want to understand planetesimal formation, the only data set we have is our own Solar System. It is in particular interesting as it is so far the only planetary system we know of that developed life. Understanding the conditions under which the Solar Nebula evolved is crucial in order to understand different processes and subsequent dynamical interaction between (proto-)planets once the gas disk is gone. Protoplanetary disks provide a plethora of different parameters to explore. The question is whether this parameter space can be constrained allowing simulations to reproduce the Solar System. Models and observations of planet formation provide constraints on the initial planetesimal mass in certain regions of the Solar Nebula. By making use of pebble flux-regulated planetesimal formation (Lenz et al., 2019), I perform a parameter study with nine different disk parameters like the initial disk mass, initial disk size, initial dust-to-gas ratio, turbulence level, and more. I find that the distribution of mass in planetesimals in the disk depends on the planetesimal formation timescale and the pebble's drift timescale. Multiple disk parameters can influence pebble properties and thus planetesimal formation. However, it is still possible to draw some conclusions on possible parameter ranges. Pebble flux-regulated planetesimal formation seems to be very robust, allowing a wide range of parameters in order to meet the initial planetesimal constraints for the Solar Nebula. I.e., it does not require a lot of fine tuning.

3.1 Introduction

In order to form planets, tiny micron sized dust grains have to grow to hundreds or thousands of kilometers. First, grains grow by collisions with other grains. But at some point they cannot continue to grow because (1) either the relative velocities become so high such that a collision leads to fragmentation (Blum & Münch, 1993; Blum & Wurm, 2008; Gundlach & Blum, 2014) or (2) they start to drift faster toward the star then they could potentially grow (Klahr & Bodenheimer, 2006; Birnstiel et al., 2012). There exists also the bouncing barrier (Zsom et al., 2010) but charging effects might lead to growth to one more order of magnitude in size compared to this barrier (Steinpilz et al., 2019). Laboratory experiments point to the direction of low fragmentations speed for icy particles (Musiolik & Wurm, 2019) of around $1\,\mathrm{m\,s^{-1}}$. This could cause particles to hit the fragmentation barrier first which is why we are not considering bouncing in this work.

It is believed that planets are formed by so-called planetesimals with a few to hundreds of kilometers in size. These planetesimals are the building blocks of planets. Once they have formed, accretion of pebbles (Ormel & Klahr, 2010) may become important too (for a review see, e.g., Ormel, 2017). But since grains stop growing at some point, there would be a missing link between roughly mm–dm to planetesimal diameters ($\sim 100\,\mathrm{km}$) via continuous growth.

If there is a pressure bump in the disk, e. g., caused by a vortex or zonal flow, particles can get trapped around the center of the bump (Whipple, 1972; Barge & Sommeria, 1995). After accumulation of enough pebbles, the streaming instability (Youdin & Goodman, 2005) can potentially be the dominant turbulent process to trigger fragmentation in the laminar case ($\alpha_\mathrm{t} = 0$) or in the turbulent case ($\alpha_\mathrm{t} > 0$) gravoturbulent planetesimal formation can occure (Johansen et al., 2006; Johansen et al., 2007).

To summarize, we follow the idea that pebbles form planetesimals in a gravoturbulent process leading to a Gaussian-like size distribution of planetesimals that peaks around 100 km in diameter (Klahr & Schreiber, 2015; Schreiber, 2018). These planetesimals can then build planetary embryos which can grow via further accretion of both planetesimals and pebbles to form (proto-)planets.

The initial distribution of planetesimals is one of the biggest unknowns in planet formation models. The radial distribution in the disk is important for embryo formation and subsequent accretion of planetesimals onto embryos. While we can observe protoplanetary disks and debris disks around other stars, we cannot observe planetesimal populations. There is only one system where we have relatively good knowledge of the present day small body population which is the Solar System. This is also the system which has been modeled the most, so the strongest constraints we have on the initial planetesimal population comes from our Solar System. Even though, as we will discuss, there are a lot of uncertainties. The so-called minimum mass Solar Nebula (MMSN) (Weidenschilling, 1977b; Hayashi, 1981) is the most commonly used assumption, but it is not based on a modern understanding of planet formation.

Lenz et al. (2019) presented a pebble flux-regulated model for the planetesimal formation rate. In this model, a spatial planetesimal distribution evolves with time and leads to a physically motivated planetesimal density disk profile. So it is sensible to ask, can this model fit the constraints of our Solar System? And how finely tuned does this model have to be?

This Chapter is structured as follows. In Sec. 3.2 we discuss possible constraints for initial planetesimals in different regions of the Solar Nebula. Sec. 3.3 describes the model we are using. Sec. 3.4 presents the results and we summarize and conclude in Sec. 3.5 and 3.6.

3.2 Mass constraints for the initial planetesimal population

In this section we will review literature studies to infer constraints on the initial planetesimal mass in variious regions of the Solar Nebula. A summary of this literature research is depicted in Fig. 3.1.

3.2.1 Mercury Region: Interior to 0.7 au

There is no observed stable population of asteroids within the orbit of Mercury (Steffl et al., 2013), even though e.g. Campins et al. (1996) found a dynamically stable region in the Solar System's inner region. On top of that, no models for terrestrial planet formation require any planetesimals inside of Mercuryâs orbit (~ 0.4 au). Additionally, terrestrial planet models fit observations better if the planetesimal disk is truncated around 0.7 AU (Hansen, 2009; Walsh et al., 2011; Levison et al., 2015; Morbidelli et al., 2016). Even though, there are some models suggesting how to clear out this region (e.g. Ida & Lin, 2008; Batygin & Laughlin, 2015; Volk & Gladman, 2015), none of these are demonstrated in a comprehensive way. However, this implies that we canât define an upper limit on the mass of initial planetesimals in this region. Low mass short-period planets around other stars may indicate that in other planetary systems there were planetesimals in short period orbits that formed planets via in situ planetesimal accretion (e.g. Chiang & Laughlin, 2013; Hansen & Murray, 2012) or pebble accretion (e.g. Chatterjee & Tan, 2013), but the presence of migration implies that there is no evidence that a population of initial planetesimals was present within Mercury's orbit in our own Solar System.

Bottom line: 0 to an unknown upper limit

3.2.2 Earth/Venus Region $0.7 - 1$ au

As it was shown by Hansen (2009), placing $\sim 2\,M_\oplus$ of oligarchs within $0.7 - 1$ au can lead to good matches to the sizes and spacing of the terrestrial planets of the Solar System. The results from the parameter study of Kokubo et al. (2006) in terms of number of Earth-like planets within 0.5 to 1.5 au seem to be very robust with respect to mass and radial profile of oligarchs. They have shown that one can still obtain reasonable results with a total initial mass of $2.77\,M_\oplus$ in that region. For $\sim 23\,M_\oplus$ Super-Earth's form.

Pebble flux can allow significant amount of mass to be transported into this region. If there are enough pebbles and appropriate disk structure, it is possible to produce reasonable Solar System analogs beginning with $< 10^{-2}\,M_\oplus$ planetesimal masses (Levison et al., 2015). If Jupiter migrated inwards and then out of the Asteroid Belt (known as the grand tack; Walsh et al., 2011), to leave about the needed mass in the current Asteroid Belt, it would have implanted $\sim 1\,M_\oplus$ of material into the Earth/Venus forming region. This suggests that either primordially or after early pebble accretion there was initially $1\,M_\oplus$ of planetesimals/embryos in this region (Walsh et al., 2011). Since the grand tack removes most objects in the Asteroid Belt in simulations, the inital planetesimal population needs to be massive enough early on. This probably implies that pebble accretion only grew the mass of the Asteroid Belt by a factor of a few at most, and thus the terrestrial planet region probably only grew by a factor of a few as well. As a rough estimate we can assume the inital planetesimal mass to be around $0.1\,M_\oplus$.

Bottom Line: 0.1 (if there are enough pebbles that can be accreted) to $2.77\,M_\oplus$ (if there isnât)

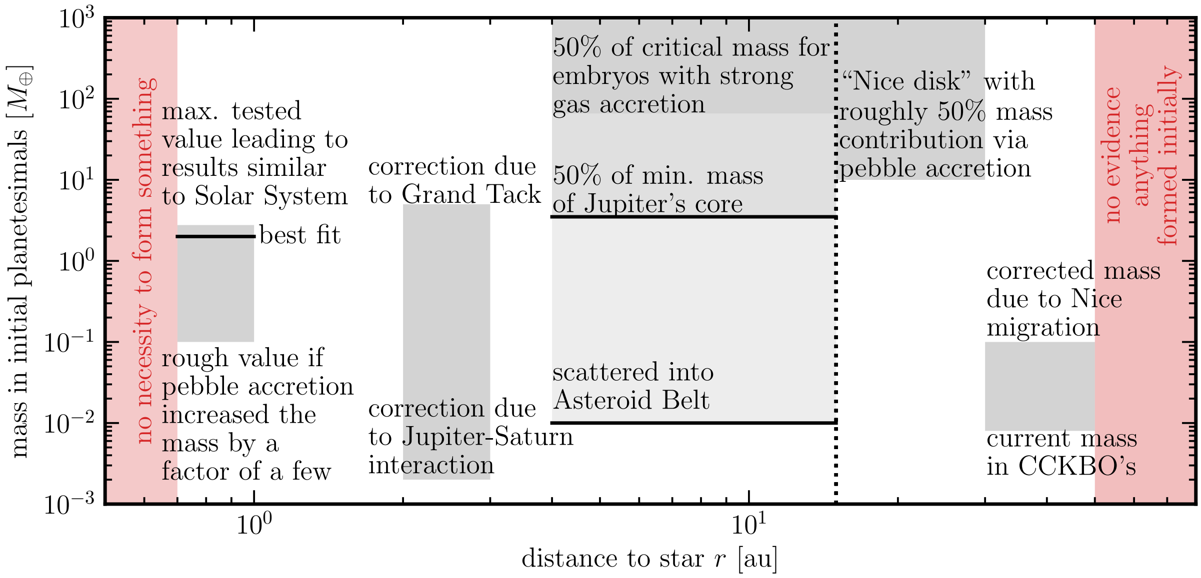

Figure 3.1: Graphical representation summarizing Sec. 3.2 on mass constraints of initial planetesimal masses in different regions of the Solar Nebula. Masses given by the values on the ordinate apply for the entire region shown by the marked regions. Boxes that extend to the border of the plot indicate unknown upper limits. The dotted vertical line separates the two touching regions.

3.2.3 Asteroid Belt: 2 – 3 au

The Asteroid Belt currently has a mass of about $5 \cdot 10^{-4}\,M_\oplus$ (e.g. Kresak, 1977), where roughly 50% of the mass is in the 4 largest objects, with 1/3 that is in Ceres. Over the history of the Solar System, it has potentially been depleted by the following effects. (1) Over the last 4 Gyr dynamical chaos in the current structure of the Solar System has removed about $\sim 50\%$ of the mass of the Asteroid Belt (Minton & Malhotra, 2010). Vesta's crust indicates that the Asteroid Belt population was only modestly larger than it is today at the time the mean collision velocities were pumped up to 5 km/s (i.e. the current mean impact velocity in the main belt region; Bottke Jr et al. (1994)). If the Asteroid Belt had substantially more 30 km-sized planetesimals in it over the last 4 Gyr than it has today, Vesta would be expected to have more than 1 large basin (Bottke Jr et al., 2005b,c; O'Brien & Greenberg, 2005). If planetesimals were "born big" (Morbidelli et al., 2009), i.e. $\gtrsim 80\,\text{km}$, this suggests that collisional evolution should not be particularly important in removing material; at least not more than a factor of a few. The late Jupiter-Saturn interaction in terms of reshuffling of the Giant planets likely depleted the Asteroid Belt by a factor of ~ 2 to ~ 10 (Minton & Malhotra, 2010). If the Grand Tack happened (Walsh et al., 2011), then only few times 10^{-3} to a few times 10^{-4} of the population would have survived (ignoring newly implanted plantesimals from other regions; see e.g. Fig. 7 in Morbidelli et al., 2015). One should also note that in this model the C-complex asteroids, which comprises about 75% of the asteroids (Gradie et al., 1989) and includes Ceres, are implanted from the outer Solar System. But these modifications are swamped by the uncertainty in the clearing rate on the migration efficiency. If pebble accretion plays a crucial role for the growth of large asteroids (> 200 km in diameter), then this also would reduce the âinitial massâ of planetesimals that is needed. This effect probably would be a factor of ~ 2 (Johansen et al., 2015).

Bottom line: $\sim 2 \cdot 10^{-3}\,M_\oplus$ (4 times current mass) to $\sim 5 M_\oplus$

3.2.4 Giant Planet Forming Region (possibly) 4 – 15 au

This region could also have an inner (outer) edge that is further in (out). But this would not change the constraints dramatically.

The lower mass limit of Saturn's core is around $8-9 M_\oplus$ (Saumon & Guillot, 2004; Helled & Schubert, 2008), Jupiter's core has at least $7 M_\oplus$ (Wahl et al., 2017). So far, we do not know how much of this mass was originally in planetesimals from the given region. Hence, for the lower limit, we will ignore Saturn and take 50% (assuming that

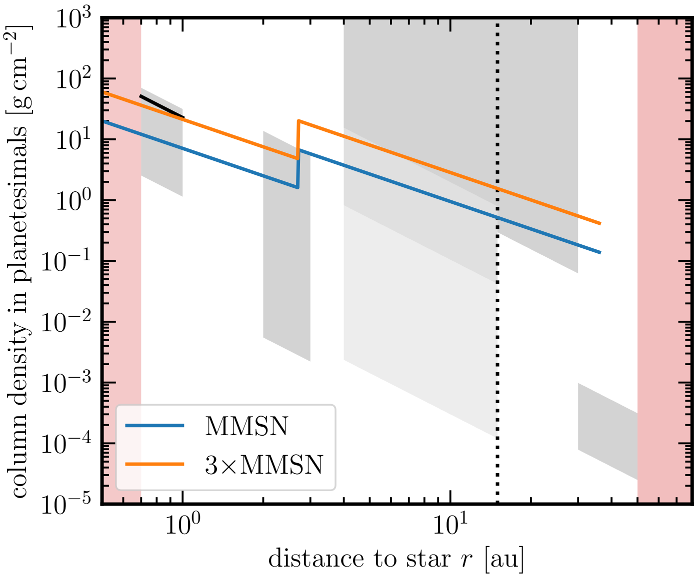

Figure 3.2: As Fig. 3.1 but converted into column densities, assuming a power-law shape $\propto r^{-2.25}$ (see Eq. (37) of Lenz et al. (2019) for a motivation). The blue (orange) line shows (three times) the minimum mass Solar Nebula profile for solids (Weidenschilling, 1977b; Hayashi, 1981).

the other half stems from pebbles, Bordukat, 2019) of the lower mass estimate from Wahl et al. (2017) which gives $3.5 M_{\oplus}$.

In order to reach critical masses for strong gas accretion, around 5 times the mass of the MMSN seems to be needed (Thommes & Duncan, 2006, these simulations used planetesimals of 20 km in diameter). This leads to $132\,M_{\oplus}$ within 4 to 15 au. Assuming that 50% of the mass was contributed by pebbles (Bordukat, 2019), the lower limit would be around $66\,M_{\oplus}$. This lower limit is still high. But desublimation effects just outside the ice line can lead to a pile-up in planetesimals by a factor of ~ 5 (Drążkowska & Alibert, 2017; Schoonenberg et al., 2018). This effect is not included in this work.

Raymond & Izidoro (2017) found that $\sim 10\%$ of the asteroids around the giant planets were scattered into the asteroid belt. So in order to explain the mass of C-type asteroids in the Asteroid Belt, there probably had to have been around few times $10^{-2}\,M_{\oplus}$ of asteroids in the giant planet forming region. This value would be the absolute minimum for this region.

Bottom line: $\sim 66\,M_{\oplus}$ to unknown high mass

3.2.5 The Nice Disk $\sim 15 - 30\,\mathrm{au}$

In order to match the observed structure of the Kuiper Belt, where many objects are in resonance with Neptune, outward migration of the giant planets is the preferred explanation. For this type of outward migration, planetesimal driven migration is the leading explanation (Fernandez & Ip, 1984; Malhotra, 1995; Thommes et al., 1999). A comprehensive model explaining how this outward planetesimal driven migration could have occurred is the Nice Model (Tsiganis et al., 2005; Morbidelli et al., 2005; Gomes et al., 2005). In this model the giant planets initially formed closer to the sun than their current locations and migrated outwards due to interactions with a planetesimal disk which is known as “the Nice disk”. Even though the details of the model have been changed (e.g. Morbidelli et al., 2007; Levison et al., 2011), a number of features in the small body reservoirs of our Solar System can be explained if this population did initially exist and the planets migrated through it. We give a few examples:

- *Jupiter’s Trojans*: Calculations showed that a mass of around $\sim 35\,M_{\oplus}$ can agree with the current population of the Jupiterâs Trojans (Morbidelli et al., 2005). With a newer variation, known as the Jumping Jupiter Model, good matches are found with planetesimal disk masses $\sim 14 - 28\,M_{\oplus}$ (Nesvornỳ et al., 2013).
- *Kuiper Belt*: Models with grainy migration of Neptune with a disk mass of $\sim 20\,M_{\oplus}$ (1000 Pluto sized objects)

match the detailed characteristics of the objects in the 3:2 resonance (Nesvornỳ & Vokrouhlickỳ, 2016).

- *Comets*: Gas drag prevents km-sized planetesimals from being scattered into the Oort Cloud while the gas disk is still around (Brasser et al., 2007). This suggests that the long period comets were scattered into the Oort cloud after the gas disk went away, a natural outcome of something like the Nice Model. An initial population of around $30\,M_\oplus$ is needed to populate the Oort Cloud (Dones et al., 2004), however the existence of more massive planets in the inner Oort Cloud (e.g. a planet 9, Batygin & Brown, 2016) could decrease the required reservoir size. However, since comets could have potentially been shared between stars in the birth cluster under favorable conditions, it is possible comets are not a reliable constraint (Levison et al., 2010).
- *Ice giant ejection*: In the models in which an ice giant is ejected from the Solar System, the best overall structure of the Solar System, for example surviving terrestrial planets, need $\sim 20\,M_\oplus$ that are in planetesimals (Nesvornỳ & Morbidelli, 2012).

Additionally, it has been found that the column density profile of planetesimals has a minimal effect on the outcomes for a relatively broad range of power-laws. This was tested by Batygin & Brown (2010) for $\Sigma_\mathrm{p} \propto r^{-k}$, where $k = 1\ldots2$, with inner edge $r_\mathrm{in} \sim 12\,\mathrm{au}$ and outer radius $r_\mathrm{out} = 30\,\mathrm{au}$. The Nice scattering occurred after the disk went away so that pebble accretion could have increased the total mass of the Nice disk. However, because the disk was very likely flaring in the outer regions, it is unlikely that pebble accretion was efficient and increased the total mass in this regions more than a factor of ~ 2 (Lambrechts & Johansen, 2012).

Bottom line: $\sim 10\,M_\oplus$ seems to be needed

3.2.6 The Cold Classical Kuiper Belt $\sim 30\,\mathrm{au} - 50\,\mathrm{au}$

There is a population of objects in the Kuiper belt with low eccentricities and inclinations which look as they are not transplanted, though likely to be primordial. Observations indicate that the mass of the current classical population is $8 \cdot 10^{-3}\,M_\oplus$ (Fuentes & Holman, 2008).

If the larger KBOs were formed by coagulation from small planetesimals, there must have been significantly more mass in this region in the early stages. For instance, Pan & Sari (2005) suggested that the high end size distribution could be matched by collisional evolution. However, if one combines more modern description laws with the need to preserve wide binaries, one cannot match the observed population in this type of collisional environment. Therefore, this suggests that planetesimals formed as large bodies and that the total mass of the cold classcial Kuiper Belt objects (CKBO), dominated by bodies larger than diameters of $\sim 100\,\mathrm{km}$ has not evolved significantly (Nesvornỳ et al., 2011).

The Nice migration may have dynamically depleted the Kuiper Belt by up to an order of magnitude (Morbidelli et al., 2008). Singer et al. (2019) found a lack in small craters on Pluto and Charon, indicating that planetesimals in the Kuiper Belt are not a collisionally evolved population, or that collisions destroyed small planetesimals.

Bottom line: 0.008 to $\sim 0.1\,M_\oplus$

3.2.7 Beyond $50\,\mathrm{au}$

A radial distance of roughly 50 au appears to be a real edge to the cold classical Kuiper belt (Jewitt et al., 1998; Trujillo & Brown, 2001; Fuentes & Holman, 2008). If there would be a population with similar size and albedoâs to the observed KBO at 60 au, it's mass cannot be more than 8% of the observed KBOs as otherwise it would have been detected (Fuentes & Holman, 2008). There are small bodies with semi-major axes greater than 50 au in the Solar System but most of them are dynamically coupled to the giant planets, suggesting that they have been scattered into their large orbits. Hence, they do not represent primordial orbits. A possible exception to the objects coupled to giant planets are the Sedna type objects (Brown et al., 2004) but these objects are on highly eccentric orbits, suggesting that they were scattered to their current locations and only decoupled from the rest of the Solar System after being scattered outward, e.g. by the tidal influence of the Sunâs birth cluster (Brasser et al., 2006, 2007; Kaib & Quinn, 2008; Brasser et al., 2012).

Bottom line: No evidence that anything formed at these distances initially

3.3 The Model

We use a new python based code version of Birnstiel et al. (2010) called `DustPy` (Stammler & Birnstiel, in prep.). This code allows to compute radial motion and growth of particles as well as gas evolution. `DustPy` is a 1-d (radial) code with analytical vertical integration, solving the Smoluchowski equation (von Smoluchowski, 1916) for particle growth. For more details see Birnstiel et al. (2010). In the following we are describing basics of the dust model, a simple accretion heating model. The sink term we have chosen for the gas due to photoevaporative winds is shown in Appendix B.1.

3.3.1 Basics

For simplicity we assume spherical compact particles with mass $m = (4/3)\pi\rho_\mathrm{m}a^3$, where ρ_m is the material density and a the particle radius. Epstein (1924) derived a friction force under the condition that $a \ll \lambda_\mathrm{g}$ and $v_\mathrm{rel} \ll v_\mathrm{th}$ for spherical particles

$$\boldsymbol{F}_\mathrm{D} = -\frac{4\pi}{3}a^2\rho_\mathrm{g}v_\mathrm{th}\boldsymbol{v}_\mathrm{rel}. \tag{3.1}$$

The drag force particles feel while moving through a fluid ($a \gg \lambda_\mathrm{g}$) is

$$\boldsymbol{F}_\mathrm{D} = -\frac{C_\mathrm{D}}{2}\pi a^2\rho_\mathrm{g}v_\mathrm{rel}\boldsymbol{v}_\mathrm{rel}, \tag{3.2}$$

ρ_g being the gas mass density and v_rel the relative velocity to the gas. C_D is called the *drag coefficient*. This drag law was already found for the impact of air on the falling motion of hollow glass spheres by Newton (1729) in section 2 and 7 of his second book, having the same form of equation but with a constant drag coefficient, where inertia is dominant over viscous forces. The first formulation of this drag formula in the form $F_\mathrm{D} = a^2\rho_\mathrm{g}{v_\mathrm{rel}}^2 \cdot f(\mathrm{Re})$ — here C_D is given by some function depending on the Reynolds number

$$\mathrm{Re} = 2av_\mathrm{rel}/\nu_\mathrm{mol}, \tag{3.3}$$

with molecular viscosity ν_mol — was given by Rayleigh (1892). The drag coefficient is for $\mathrm{Re} \leq 2\cdot 10^5$ given by (Cheng, 2009)

$$\begin{aligned} C_\mathrm{D} =& \frac{24}{\mathrm{Re}}(1+0.27\cdot\mathrm{Re})^{0.43} \\ &+0.47\left[1-\exp\left(-0.04\cdot\mathrm{Re}^{0.38}\right)\right]. \end{aligned} \tag{3.4}$$

The molecular viscosity for hard spheres, neither attracting nor repulsing, is roughly given by

$$\nu_\mathrm{mol} = \frac{1}{2}v_\mathrm{th}\lambda_\mathrm{g} \tag{3.5}$$

(Chapman, 1916, see his Eq. (249)), where the gas mean free path is

$$\lambda_\mathrm{g} = \frac{1}{\sqrt{2}}\frac{1}{n_\mathrm{g}\sigma_\mathrm{g}} \tag{3.6}$$

and we further assume that the geometrical cross section σ_g is given by that of molecular hydrogen

$$\sigma_\mathrm{H2} = 2\cdot 10^{-15}\,\mathrm{cm}^2.$$

Massey & Mohr (1933) pointed out that this classical approximation is good enough for helium and hydrogen over a large range of temperatures (see their table III on p. 450), i. e., quantum mechanics is not required. For cold temperatures (~ 10 K) quantum mechanics is important, but these temperatures are typical for the outer disk where the gas density is so low that particles are in the Epstein drag regime anyway.

We define the *stopping time* as

$$\tau_\mathrm{s} = mv_\mathrm{rel}/F_\mathrm{D}, \tag{3.7}$$

following Whipple (1972). According to Newton's second law it is

$$\dot{v}_{\mathrm{rel}} = -v_{\mathrm{rel}}/\tau_{\mathrm{s}}, \tag{3.8}$$

i. e., τ_{s} is the time for the velocity of the particle relative to the gas to be reduced from v_{rel} to v_{rel}/e. How well particles are coupled to the gas is described by their Stokes number which we define by

$$\mathrm{St} := \Omega\tau_{\mathrm{s}}, \tag{3.9}$$

where

$$\Omega = \sqrt{\frac{GM_{\star}}{r^3}} \tag{3.10}$$

is the Keplerian frequency. Since the Stokes number is the ratio of the stopping time, at which particles couple to the gas, and the dynamical gas timescale, small values ($\mathrm{St} \ll 1$) mean that particles are coupled to the gas. Large values ($\mathrm{St} \gg 1$) indicate that particles are decoupled from the gas. I.e., particles are coupled to the gas motion in less than an orbit for $\mathrm{St} \ll 1$ and large Stokes numbers ($\mathrm{St} \gg 1$) would need many orbits to synchronize to the gas motion. If the mean free path of gas molecules λ_{g} is large enough, particles are in the Epstein drag regime. If λ_{g} is small compared to the particle radius a, they are in the fluid regime. The transition between the two regimes occurs around[2] $\lambda_{\mathrm{g}} = 4a/9$. The Stokes number is thus

$$\frac{\mathrm{St}}{\Omega} = \begin{cases} \rho_{\mathrm{m}} a/(\rho_{\mathrm{g}} v_{\mathrm{th}}) & \text{, Epstein } (\lambda_{\mathrm{g}} \geq 4a/9) \\ 8/(3C_{\mathrm{D}}) \dfrac{\rho_{\mathrm{m}}}{\rho_{\mathrm{g}}} \dfrac{a}{v_{\mathrm{rel}}} & \text{, Fluid, } \mathrm{Re} \leq 2\cdot 10^5 \end{cases} . \tag{3.11}$$

If the fluid regime is reached, we follow Birnstiel et al. (2010) and assume to be in the Stokes drag law regime, i. e.,

$$C_{\mathrm{D}} = 24/\mathrm{Re} \tag{3.12}$$

for $\mathrm{Re} \leq 1$ (Stokes, 1851, his Eq. (126)). If $\lambda_{\mathrm{g}} < 4a/9$, this leads to

$$\mathrm{St} = \frac{2}{9}\frac{\rho_{\mathrm{m}}}{\rho_{\mathrm{g}}}\frac{a^2\Omega}{v_{\mathrm{mol}}}. \tag{3.13}$$

This way the velocity of particles, their relative velocity to the gas, and the Stokes number don't have to be solved iteratively together.

3.3.2 Column Densities

We make use of the definition of the column density as the mass per 3-dim volume, density ρ, vertically integrated over height z of the disk,

$$\Sigma_i := \int_{-\infty}^{\infty} \rho_i \,\mathrm{d}z = 2\int_{0}^{\infty} \rho_i \,\mathrm{d}z \tag{3.14}$$

where $i = \{\mathrm{d}, \mathrm{g}, \mathrm{p}\}$ can be dust (d), gas (g), and planetesimals (p). We use Σ_{d} as the column density including all solid particles without planetesimals. If it has St as argument, it is the column density of particles with this Stokes number. Following Birnstiel et al. (2010), we define the dust column density distribution per logarithmic bin of grain radius a as

$$\sigma_{\mathrm{d}}(r,a) := \int_{-\infty}^{\infty} n_a(a,r,z) m(a) a \,\mathrm{d}z, \tag{3.15}$$

---

[2] Following Weidenschilling (1977a), this condition can be obtained by setting either the stopping time in the Stokes drag law and the Epstein drag regime or the two drag forces equal and making use of Eq. (3.5).

where n_a is the number density per grain size bin. This way knowledge of the used size grid is not needed and the total dust column density is given by

$$\Sigma_\mathrm{d}(r) = \int_{-\infty}^{\infty} \sigma_\mathrm{d}(r,a)\, \mathrm{d}\ln a. \tag{3.16}$$

As initial condition for the gas we use the self-similar profile (Lynden-Bell & Pringle, 1974)

$$\Sigma_\mathrm{g}(r) = \frac{(2-\gamma)M_\mathrm{disk}}{2\pi {r_\mathrm{c}}^2(1+Z_0)} \left(\frac{r}{r_\mathrm{c}}\right)^{-\gamma} \exp\left[-\left(\frac{r}{r_\mathrm{c}}\right)^{2-\gamma}\right], \tag{3.17}$$

where $Z_0 = \Sigma_\mathrm{d}/\Sigma_\mathrm{g}$ is the initial solid-to-gas ratio in terms of column densities. The initial dust column density is then given by $Z_0\Sigma_\mathrm{g}(t_0)$.

3.3.3 Drift velocities

Particles, such as tiny dust grains up to boulders, are embedded in the gas disk. In force balance of gravity from the central star and centrifugal force, particles move on Keplerian Orbits. The action of the gas pressure gradient on the particles can be neglected because the internal density of the particles is so much larger than the gas density. The gas does feel gravity, centrifugal force, and the pressure gradient force. If these forces balance each other, the gas moves on slightly sub-Keplerian orbits. Particles with $\mathrm{St} \lesssim 1$ are coupled to the gas, thus they feel a centrifugal deficiency due to sub-Keplerian gas motion and drift radially inward. As long as $\mathrm{St} < 1$ this leads to a stronger radial drift for increasing St. If the particle Stokes number is larger than unity, they decouple from the gas and feel a headwind from the surrounding gas. The mass-to-surface ratio increases with size and this effect becomes weaker for increasing St (i. e. increasing stopping time τ_s). The steady-state solution for radial drift reads (Nakagawa et al., 1986)

$$v_\mathrm{drift} = \frac{\mathrm{St}}{\mathrm{St}^2 + (1+\rho_\mathrm{d}/\rho_\mathrm{g})^2} \frac{h_\mathrm{g}}{r} \frac{\partial \ln P}{\partial \ln r} c_\mathrm{s} \tag{3.18}$$

which reduces to

$$v_\mathrm{drift} = \frac{\mathrm{St}}{\mathrm{St}^2 + 1} \frac{h_\mathrm{g}}{r} \frac{\partial \ln P}{\partial \ln r} c_\mathrm{s} \tag{3.19}$$

for low dust-to-gas ratios (Weidenschilling, 1977a). We use the latter expression for this work to save computation time.

3.3.4 Planetesimal Formation Rate

For the planetesimal formation rate we follow Lenz et al. (2019). The model is based on the idea that pebble traps appear and disappear on a given timescale. In those pebble traps pebble clouds can then collapse to planetesimals. In this model, the pebble flux (in mass per time)

$$\dot{M}_\mathrm{peb} := 2\pi r \sum_{\mathrm{St}_\mathrm{min} \leq \mathrm{St} \leq \mathrm{St}_\mathrm{max}} \left| v_\mathrm{drift}(r,\mathrm{St}) \right| \Sigma_\mathrm{d}(r,\mathrm{St}). \tag{3.20}$$

is transformed into planetesimals over a *conversion length* ℓ:

$$\dot{\Sigma}_\mathrm{p}(r) = \frac{\dot{M}_\mathrm{peb}}{2\pi r \ell} = \varepsilon \frac{\dot{M}_\mathrm{peb}}{2\pi r d}. \tag{3.21}$$

We assume that this conversion length is proportional to the gas pressure scale height h_g. Mass conversion from pebbles to planetesimals according to this recipe is only allowed if the condition

$$\varepsilon \tau_1 \dot{M}_\mathrm{peb} > m_\mathrm{p}. \tag{3.22}$$

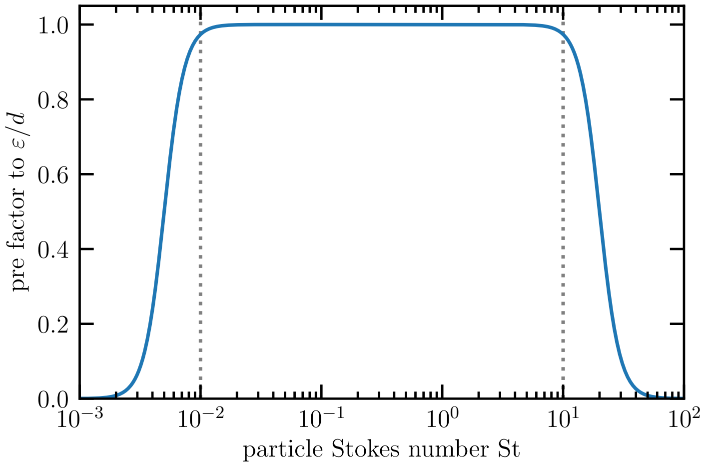

Figure 3.3: Illustration of Eq. (3.30) for $\mathrm{St}_{\mathrm{min}} = 0.01$ and $\mathrm{St}_{\mathrm{max}} = 10$.

is fulfilled, where m_p is the mass of a single 100 km planetesimal and τ_l is the lifetime of traps. In this Chapter, we assume that $\tau_\mathrm{l} = 100\,t_\mathrm{orb}$ for all simulations. ε is the efficiency with which pebbles are transformed into planetesimals. For more details we refer to Lenz et al. (2019). With help of the mean radial trap separation d, one can relate this parameter to the conversion length, $\ell = d/\varepsilon$. The jump from pebble-size to objects 100 km in diameter is a direct result of the particle diffusion timescale within the particle cloud and the collapse timescale (Klahr & Schreiber, 2015; Schreiber, 2018; Gerbig et al., 2020).

3.3.5 Comparison to other Planetesimal Formation Rate Models

The model for the planetesimal formation rate from Lenz et al. (2019) differs from other models. In Lenz et al. (2019) planetesimal formation is regulated by a conversion length scale. Particles that are drifting are converted into planetesimals. The conversion length scale depends on the radial density of pebble traps and the efficiency of concentrating particles and converting pebble clouds into bound objects. Drążkowska et al. (2016) and Schoonenberg et al. (2018) suggest models for which planetesimal formation occurs with a certain efficiency per orbit from the local particle density. These models do assume that particles are not trapped while drifting. Potentially, an equivalent situation could be reached for explicit traps that build up and vanish on a given timescale everywhere in the disk with some average radial distance to each other. Lenz et al. (2019) parameterized this via the conversion length ℓ, see Eq. (3) in their paper.

Adding a gas gap to the simulation, Stammler et al. (2019) used the model of Schoonenberg et al. (2018) to produce planetesimals just outside this gap and were able to reproduce the observed optical depth of HD 163296.

Eriksson et al. (2020) used the criterion from Yang et al. (2017) and assumed that all the available local mass is transformed into planetesimals once the condition is met for which particles in the midplane can concentrate to particle-to-gas mass ratios of more than 10.

For further discussion of other planetesimal formation models see e.g. section 5.2 of Lenz et al. (2019).

3.3.6 Advection-Diffusion Equation

The particle diffusion coefficient D_d for species i can be estimated with help of the gas diffusion coefficient

$$D_\mathrm{g} = \alpha_\mathrm{t} c_\mathrm{s} h_\mathrm{g} \tag{3.23}$$

as (Youdin & Lithwick, 2007)

$$D_\mathrm{d}^i = \frac{D_\mathrm{g}}{1 + \mathrm{St}_i^2}. \tag{3.24}$$

This means small particles are diffused with the gas and larger particles are less influenced by gas diffusion. As first described by Fick (1855, p. 66), reviewed in more modern notation of equations by Tyrrell (1964, his Eq. (1)) and derived from fundamental principles by Reeks (1983, his Eq. (25))[3] the diffusive flux is given by

$$\boldsymbol{J}^i_{\mathrm{diff}} = -D^i_{\mathrm{d}}\nabla\rho_{\mathrm{d}}{}^i \tag{3.25}$$

(see also Cuzzi et al. (1993)) which gives the z-integrated version in radial direction

$$j^i_{\mathrm{diff,r}} = -\int\limits_{-\infty}^{\infty} D^i_{\mathrm{d}}\frac{\partial\rho_{\mathrm{d}}{}^i}{\partial r}\,\mathrm{d}z \approx -D^i_{\mathrm{d}}\frac{\partial\Sigma^i_{\mathrm{d}}}{\partial r}. \tag{3.26}$$

In the last step we used that due to the Gaussian shape of $\rho_{\mathrm{d}}{}^i$ in z-direction, the highest contribution of the integral comes from the region within $[-h^i_{\mathrm{d}}, h^i_{\mathrm{d}}]$ within which the gas density does not change by much (especially because $h^i_{\mathrm{d}} < h_{\mathrm{g}}$). If the gas density is roughly constant, also the particles Stokes number stays roughly constant. If at $z = h^i_{\mathrm{d}}$ the temperature is similar to the one of the midplane, D^i_{d} can be considered as z-independent. As long as these conditions are met, the right hand side of Eq. (3.26) gives a good approximation. Since particles exhibit diffusive mixing due to turbulent gas motion, they are not able to move faster than the turbulent gas motion driving it. This maximum diffusion speed can be estimated to be (Cuzzi et al., 2001)

$$v_{\mathrm{max}} \simeq \sqrt{\alpha_{\mathrm{t}}}c_{\mathrm{s}}. \tag{3.27}$$

We would like to point out that in the expressions in e. g. Desch et al. (2017), which are based on Morfill & Völk (1984), the diffusive flux is *not* given by

$$j^i_{\mathrm{diff,r}} \neq -D^i_{\mathrm{d}}\Sigma_{\mathrm{g}}\frac{\partial}{\partial r}\left(\frac{\Sigma^i_{\mathrm{d}}}{\Sigma_{\mathrm{g}}}\right)$$

This expression is strictly spoken only valid for small particles, which couple to the gas motion on timescales shorter than the correlation time of the fastest turbulent eddy $\tau_{\mathrm{Kolmogorov}}$, i.e. the smallest eddy at the dissipation scale of turbulence (Kolmogorov scale) $\tau_{\mathrm{s}} < \tau_{\mathrm{Kolmogorov}}$ or for constant gas densities. Otherwise, Eq. (3.26) should be used. Unfortunately, we do not know the value of $\tau_{\mathrm{Kolmogorov}}$. For further details on the different turbulence regimes see e.g. Ormel & Cuzzi (2007). The difference between the two diffusion terms can be significant if the gas density drops quickly as it is the case for gap opening due to photoevaporation. Despite Dubrulle et al. (1995) used this diffusive flux for the vertical direction (z derivative instead of r derivative), their result for the particle scale height is still valid since the gas density does not change much in vertical direction within one particle scale height. By making use of Eq. (3.26), the advection-diffusion equation reads

$$\begin{aligned}\frac{\partial\Sigma^i_{\mathrm{d}}}{\partial t} + \frac{1}{r}\frac{\partial}{\partial r}\left\{r\left[\Sigma^i_{\mathrm{d}}v^i_{\mathrm{r}} - D^i_{\mathrm{d,eff}}\frac{\partial\Sigma^i_{\mathrm{d}}}{\partial r}\right]\right\}\\ = -\frac{f_{\mathrm{St}}\varepsilon}{d}\left|v^i_{\mathrm{drift}}\right|\Sigma^i_{\mathrm{d}}\cdot\theta(\dot{M}_{\mathrm{peb}} - \dot{M}_{\mathrm{cr}}).\end{aligned} \tag{3.28}$$

Here, $\theta(\cdot)$ is the Heaviside function and

$$\dot{M}_{\mathrm{cr}} := \frac{m_{\mathrm{p}}}{\varepsilon\tau_{\mathrm{l}}} \tag{3.29}$$

is the critical pebble flux to allow planetesimal formation (Lenz et al., 2019). We introduce a smoothing function for

---

[3] Note that in some works the diffusive flux is written in a form where it is proportional to the gradient of "concentration" which is meant in the sense of mass per volume—not mass over mass fraction. In our notation this is given by the density ρ.

the Stokes number dependency of the efficiency parameter ε

$$f_{\mathrm{St}} = \left\{ \left[\exp\left(-12 \cdot (\lg(\mathrm{St}) - \lg(\mathrm{St_{min}}/2))\right) + 1 \right] \times \left[\exp\left(12 \cdot (\lg(\mathrm{St}) - \lg(2\mathrm{St_{max}}))\right) + 1 \right] \right\}^{-1}. \tag{3.30}$$

This pre factor is displayed in Fig. 3.3. The idea is to smooth out the strong dependence on the fragmentation speed—which is similar as the idea presented in Windmark et al. (2012b), where particles have a velocity distribution.

The evolution of the gas follows is given by (Pringle, 1981)

$$\frac{\partial \Sigma_\mathrm{g}}{\partial t} = \frac{3}{r}\frac{\partial}{\partial r}\left[r^{1/2} \frac{\partial}{\partial r}\left(\nu \Sigma_\mathrm{g} r^{1/2}\right)\right] + \dot{\Sigma}_\mathrm{w}, \tag{3.31}$$

where $\dot{\Sigma}_\mathrm{w}$ is a loss term due to photoevaporative winds. The photoevaporation model is based on Picogna et al. (2019) and described in Appendix B.1. For the viscosity ν we choose the turbulent viscosity according to Shakura & Sunyaev (1973) which is the same expression as Eq. (3.23).

3.3.7 Temperature Model

In order to calculate the midplane gas temperature, one needs the contribution from radiation (internal and external) as well as from accretion heating. From pure radiation heating (e.g., Armitage, 2010, his section 2.4.2) one obtains

$$T_\mathrm{rad} = \left(\frac{L_\star}{4\pi\sigma_\mathrm{SB} r^2}\theta + T_\mathrm{bg}^4 \right)^{1/4}, \tag{3.32}$$

where $\theta \approx \tan\theta \approx h_\mathrm{g}/r \approx 0.04$ (e.g. Chiang & Goldreich, 1997; Pfeil & Klahr, 2019). We set the background temperature due to external sources to $T_\mathrm{bg} = 10\,\mathrm{K}$.

Gough (1981) gives a luminosity evolution of the sun according to

$$L_\star(t) = \frac{L_\odot}{1 + 2/5 \cdot (1 - t/t_\odot)}. \tag{3.33}$$

As the age of the sun is roughly $t_\odot \approx 4.6 \cdot 10^9\,\mathrm{yr}$ and our simulations run for a few $10^6\,\mathrm{yr}$, we can make the approximation

$$L_\star \approx 5L_\odot/7 \approx 2.73 \cdot 10^{33}\,\mathrm{erg\,s^{-1}}.$$

For pure accretion heating (i.e. ignoring radiation heating for the moment), the midplane temperature that would be produced locally, without taking optical depth effects into account and assuming that $T_\mathrm{acc} \propto c_\mathrm{s}^2$, can be calculated as (Nakamoto & Nakagawa, 1994; Pringle, 1981)

$$T_\mathrm{acc} = \left(\alpha_\mathrm{t} \Sigma_\mathrm{g} \Omega \frac{9 \mathrm{k_B}}{8 m_\mathrm{g} \sigma_\mathrm{SB}} \right)^{1/3}. \tag{3.34}$$

Following Ostriker (1963) and Armitage (2010, his Eq. (3.37)), we approximate the midplane temperature due to accretion and radiation heating as

$$T = \left[\left(\frac{3}{4}\tau_\mathrm{R} + 1 \right) T_\mathrm{acc}^4 + T_\mathrm{rad}^4 \right]^{1/4}. \tag{3.35}$$

The Rosseland optical depth τ is approximated by

$$\tau_\mathrm{R} \approx \kappa_\mathrm{R} \frac{1}{2} \Sigma_\mathrm{d}, \tag{3.36}$$

where κ_R is the size and wavelength averaged Rosseland opacity (Birnstiel et al., 2018) that is calculated in every time step based on the local size distribution and Σ_d is the column density of all particles except planetesimals. We use this

Table 3.1: Parameters that are checked in this study. Standard values are marked in gray. Those for the second fiducial set are shown in bold. Disk mass M_{disk}, characteristic radius r_c, viscosity power-law index γ which is also the power-law index of the column density of our initial condition for $r \ll r_c$, breakup speed of grains v_f, initial dust-to-gas ratio Z_0, trap formation time τ_f, turbulent viscosity parameter α_t, planetesimal formation efficiency ε, and X-ray luminosity L_X. For comparison, the disk mass of the MMSN is roughly $0.013 M_\odot$. In a separate row, we highlight our most appealing case which includes a simple model for accretion heating that is not used in all other simulations.

M_{disk} [$M_\odot$]	r_c [au]	γ	v_f [cm s^{-1}]	Z_0	τ_f [t_{orb}]	α_t	ε	L_X [erg s^{-1}]
0.02	10	0.5	**100**	0.001	0	10^{-5}	0.01	0
0.05	**20**	0.8	300	0.003	300	$\mathbf{10^{-4}}$	**0.03**	$3 \cdot 10^{28}$
0.10	35	**1**	1000	**0.0134**	600	10^{-3}	0.1	10^{29}
	50	1.2		0.02	**1000**	10^{-2}	0.3	$3 \cdot 10^{29}$
	100	1.5		0.03			1	$\mathbf{10^{30}}$
								10^{31}
0.10	20	1	200	0.0134	1600	$3 \cdot 10^{-4}$	0.05	$3 \cdot 10^{29}$

accretion heating model only for some further test cases. For the majority of presented simulations in the main text, we stick to radiation heating only, see Eq. (3.32).

3.3.8 Analyzed Parameters

For the total disk masses we used values between the MMSN ($0.013\,M_\odot$) and roughly the critical value at which disk fragmentation can occur, $\sim 0.1\,M_\odot$ (Toomre, 1964; Goldreich & Lynden-Bell, 1965). However, for collapse due to the disks own gravity also the cooling time is important as an additional criterion (Baehr et al., 2017).

The disk size, which is roughy given by the characteristic radius r_c of our initial condition, spans from 10 au to 100 au, based on observations (Andrews et al., 2010).

For the viscosity power law index γ we also allowed extreme cases, i.e. $0.5 \leq \gamma \leq 1.5$, and made the turbulence parameter disk radius dependent for the cases $\gamma \neq 1$:

$$\alpha_t = \alpha_0 \left(\frac{r}{r_c} \right)^g, \tag{3.37}$$

where $g = \gamma + q - 3/2$ and $T \propto r^{-q}$.

For the fragmentation speed, recent work by Musiolik & Wurm (2019) indicated that the value should be around $1\,\text{m}\,\text{s}^{-1}$. We still analyze values up to former default values of $10\,\text{m}\,\text{s}^{-1}$.

Values for the solar metallicity span from $Z = 1.34\%$ (Asplund et al., 2009) to $Z = 2\%$ (for a review see Vagnozzi, 2019). We will use $Z = 0.0134$ as our fiducial initial dust-to-gas ratio.

For the trap formation time τ_f we took typical values of disk instabilities to evolve significantly such as the convective overstability, vertical convective instability, subcritical baroclinic instability, or vertical shear instability (Pfeil & Klahr, 2019), as well as Hall MHD (Bai & Stone, 2014; Béthune et al., 2016). The values can span from a few hundred to thousands of orbits, depending on how fast the instability evolves and how fast it can then also create pressure bumps. Therefore, we should also consider the viscous timescale

$$\tau_{\text{visc}} \sim \frac{1}{\alpha_t \Omega} = \frac{t_{\text{orb}}}{2\pi\alpha_t} \tag{3.38}$$

(e.g. Armitage, 2010) on which structures could form. For example, for $\alpha_t \sim 10^{-4}$ this would give $\sim 1600 t_{\text{orb}}$.

We look at turbulence levels that represent an almost laminar case ($\alpha_t = 10^{-5}$) up to a very turbulent state ($\alpha_t = 10^{-2}$).

For the planetesimal formation efficiency, here defined as $\varepsilon = 5h_g/\ell$, we rely on numerical experiments in order to judge whether values are high or low. We found that $\varepsilon = 0.3$ is already high in the sense of having almost all the mass that was originially in dust in planetesimals in the end of the simulations, see Fig. 3.4. If this ratio is around 0.1, we consider the efficiency to be rather low, which is the case for $\varepsilon \approx 0.01$.

X-ray luminosities are found in the range (Güdel et al., 1997; Vidotto et al., 2014)

$$10^{28} \lesssim L_X/(\mathrm{erg/s}) \lesssim 10^{31}. \tag{3.39}$$

Table 3.1 summarizes all the different parameters that we checked for this Chapter.

3.4 Results

3.4.1 Effect of Planetesimal Formation Efficiency

Before analyzing the results of all nine different disk parameters, we would like to concentrate on the planetesimal formation efficiency first. Since many processes that we do not fully understand yet are hidden in this parameter, we first have to clarify which values are rather low or high. In the left panel of Fig. 3.4 we show for the first fiducial parameter set the final mass in planetesimal within a given disk region over the total initial dust mass as a function of planetesimal formation efficiency. All simulations were stopped at 10 Myr or when essentially all the gas was drained. One can identify a linear regime for small ε which makes sense since the formation rate scales linearly with this parameter (Eq. (3.21)). For very high efficiency values, the mass in all the shown regions should reach a plateau as then the planetesimal profile should be very close to the initial condition of the dust. For an extreme case, the conversion length is infinitaly small and pebbles are all instantly transformed into planetesimals. Once a critical large value of ε/d is reached, basically the initial structure is reproduced which leads to a plateau in this plot. Now that we understood the extreme cases, a consequence would be a sweet spot, i.e. for a given efficiency the final planetesimal mass reaches a local maximum. This behavior can be described by looking at timescales. How fast planetesimals can be build locally from pebbles is determined by the planetesimal formation timescale

$$\tau_{\mathrm{ptes}} = \frac{\Sigma_{\mathrm{peb}}}{\dot{\Sigma}_{\mathrm{p}}} = \frac{\ell}{v_{\mathrm{drift}}}. \tag{3.40}$$

At the same time pebbles are removed from their location by radial drift which is happening on the drift timescale

$$\tau_{\mathrm{drift}} = \frac{r}{v_{\mathrm{drift}}}. \tag{3.41}$$

If $\tau_{\mathrm{ptes}} < \tau_{\mathrm{drift}}$, pebbles are transformed faster into planetesimals than particles are removed from their location by radial drift, i.e. the planetesimal profile becomes closer to the initial dust profile. Setting those timescales equal and

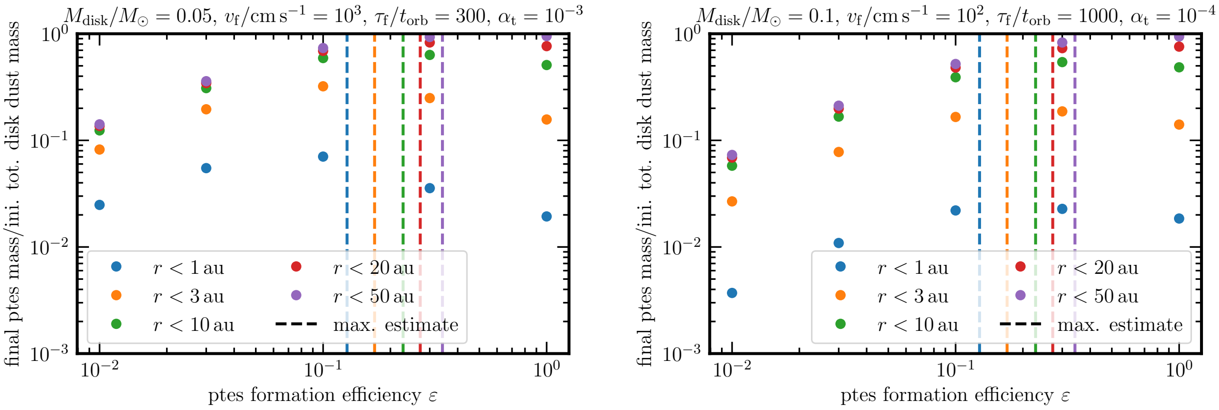

Figure 3.4: Final mass that is in planetesimals within a given disk radius shown in the legend normalized to the initial total disk dust mass as a function of planetesimal formation efficiency. Defining $\varepsilon = 5h_g/\ell$, where ℓ is the conversion length over which pebbles are transformed into planetesimals. The vertical dashed lines show the predicted maximum at the outer edge of the considered zone, respectively. I.e., the blue dashed line shows the predicted maximum at 1 au and the purple line at 50 au. This plot shows ε variations from the first fiducial run (gray values in Tab. 3.1) in the left panel and from the second fiducial run in the right panel (bold values in Tab. 3.1).

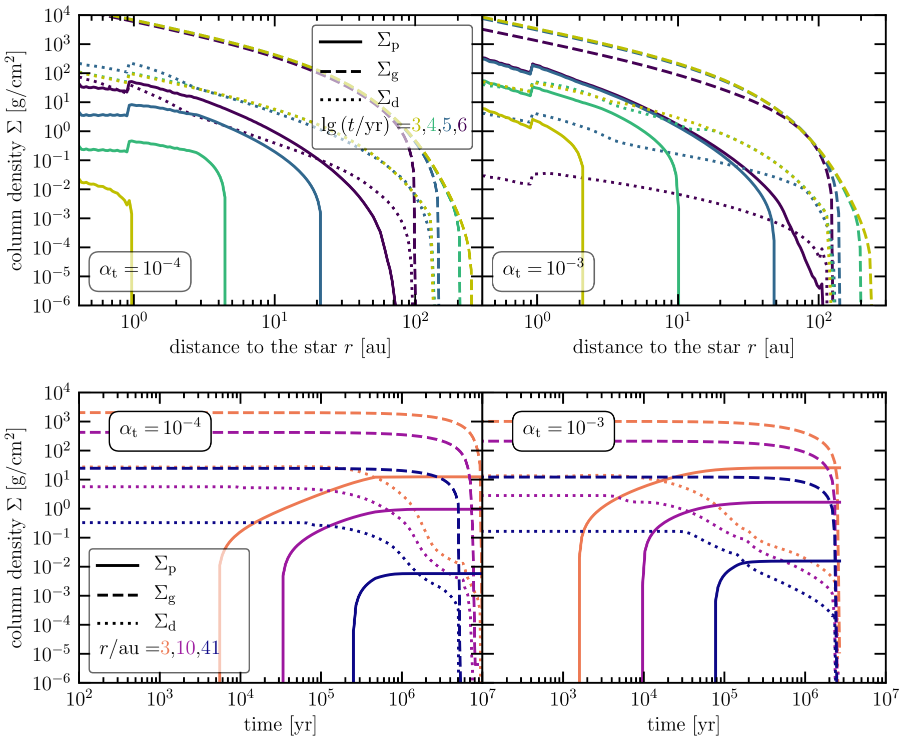

Figure 3.5: *Top panels*: planetesimal (solid), gas (dashed), and total dust (dotted) vertically integrated density profiles at different times. *Bottom panels*: The same quantities are shown but as a function of time for three different disk locations. Both fiducial simulations are compared, where the first (gray values in Tab. 3.1) is shown in the right and the second (bold values in Tab. 3.1) in the left panels.

making use of $\ell = \varepsilon/d$, one obtains

$$\varepsilon = \frac{d}{r} \tag{3.42}$$

which means that, for a fixed location in the disk, only the gas temperature matters since $d \propto h_\mathrm{g} \propto \sqrt{T}$. Starting from very low ε, the mass increases linearly until the sweet spot where planetesimal formation and drift occur on similar timescales. If ε is increased even more, pebbles are transformed into planetesimals before they can significantly drift, leading to a profile that is the closer to the initial dust profile the higher ε.

However, considering the simplicity of the estimate for the maximum, the prediction works surprisingly well for both parameter sets (compare the left and right panels of Figure 3.4). The difference in the shape of the curves may be related to whether the disk is mostly limited by drift or fragmentation as well as the mass budget in pebbles. For the fragmentation limited case, material stays longer within a certain region in the disk as fragmentation events force to start growing again from tiny very slowly drifting dust grains or small dust being swept up by larger grains. As can be seen in Figure 3.6, the high fragmentation speed in the first parameter set allows the disk to be mostly fragmentation limited in the inner disk and drift limited in the outer disk over the typical time span of planetesimal formation. However, for the second parameter set the fragmentation speed is so low that during the time of planetesimal formation basically the entire disk is fragmentation limited. Also compare to the findings of Birnstiel et al. (2012) that did not include planetesimal formation.

The vertical purple lines in Figure 3.4 mark the point beyond which all the initial dust mass has ended up in planetesimals since there is not much planetesimal mass outside of 50 au and since this is a prediction for the maximum in mass at 50 au. For the radial positions further in the required planetesimal formation efficiency to reach a maximum in mass is even smaller.

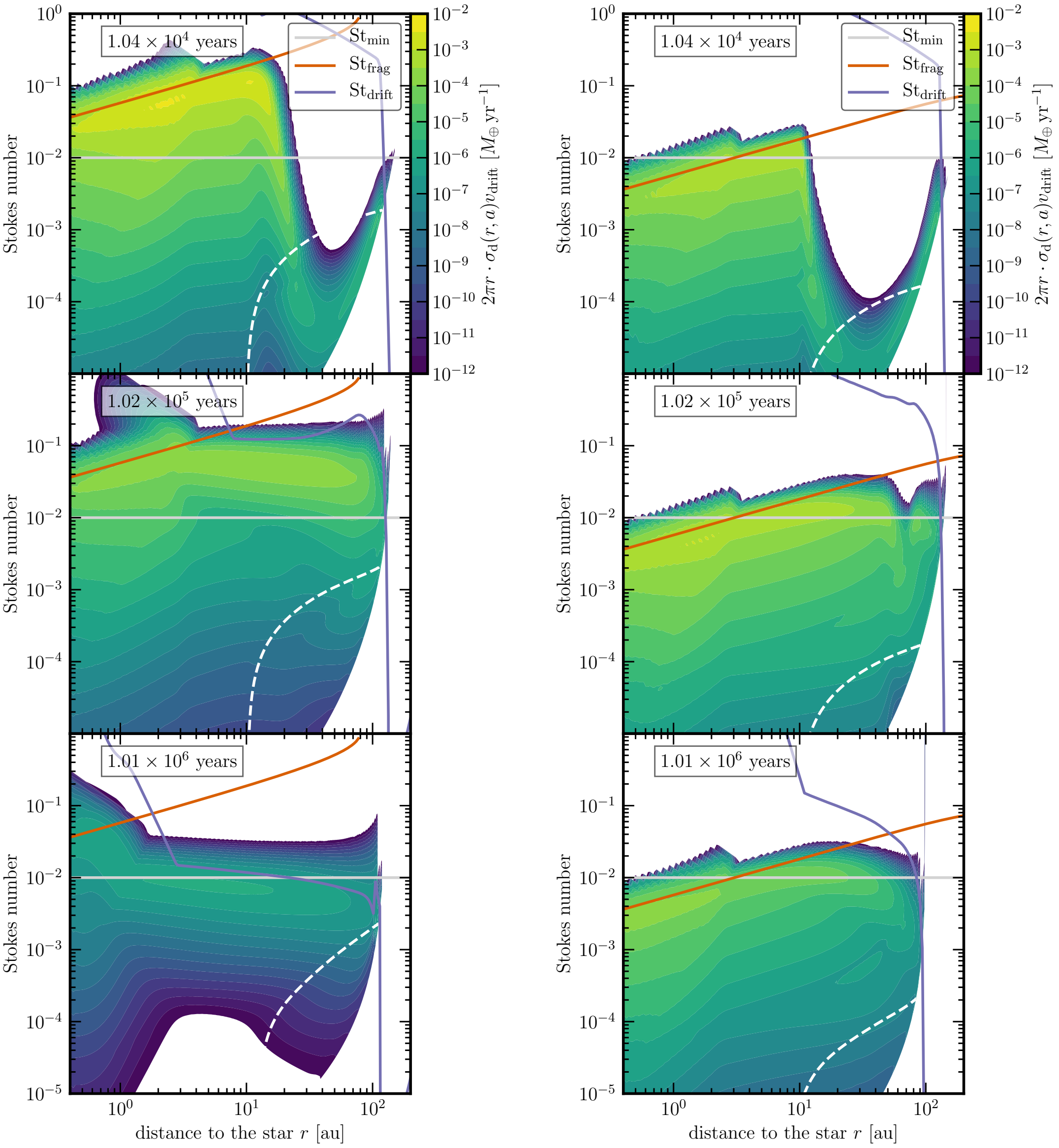

Figure 3.6: Local particle flux in Earth masses per year resulting from pure radial drift per size bin (color) as a function of Stokes number and disk radius. Here, we show the first fiducial run in the left panels (gray values in Tab. 3.1) and the second fiducial run (bold values in Tab. 3.1) in the right panels, both at three different snapshots. The orange (purple) line shows the fragmentation (drift) limit and the gray line the threshold Stokes number required to participate in planetesimal formation (but see the smoothing function Eq. (3.30)). Particles in the region below the dashed white line have positive *total* radial velocities, i.e. are moving outward. For the simulation shown in the left panels, outside of ~ 10 au the disk is limited by drift over the majority of the time of planetesimal formation. For the simulation shown in the right panels, the disk is mostly limited by fragmentation.

3.4.2 Deeper analysis of special cases

In this section we will focus on the two fiducial runs and the most appealing simulation, where only the latter contains a simple model for accretion heating that we described in section 3.3.7. Fig. 3.5 shows the time evolution of the gas, dust, and planetesimal profiles (top panels) as well as the local values of these at three different disk radii (bottom panels). The kink in the planetesimal profiles (solid lines) and dust profiles (dotted lines) inidcate the possition of the water ice line in the given simulation. Interior to the water ice line it is assumed to lose water ice due to sublimation. Fig. 3.5 compares both fiducial runs (see gray and bold values in Tab. 3.1). Those two simulations have two major

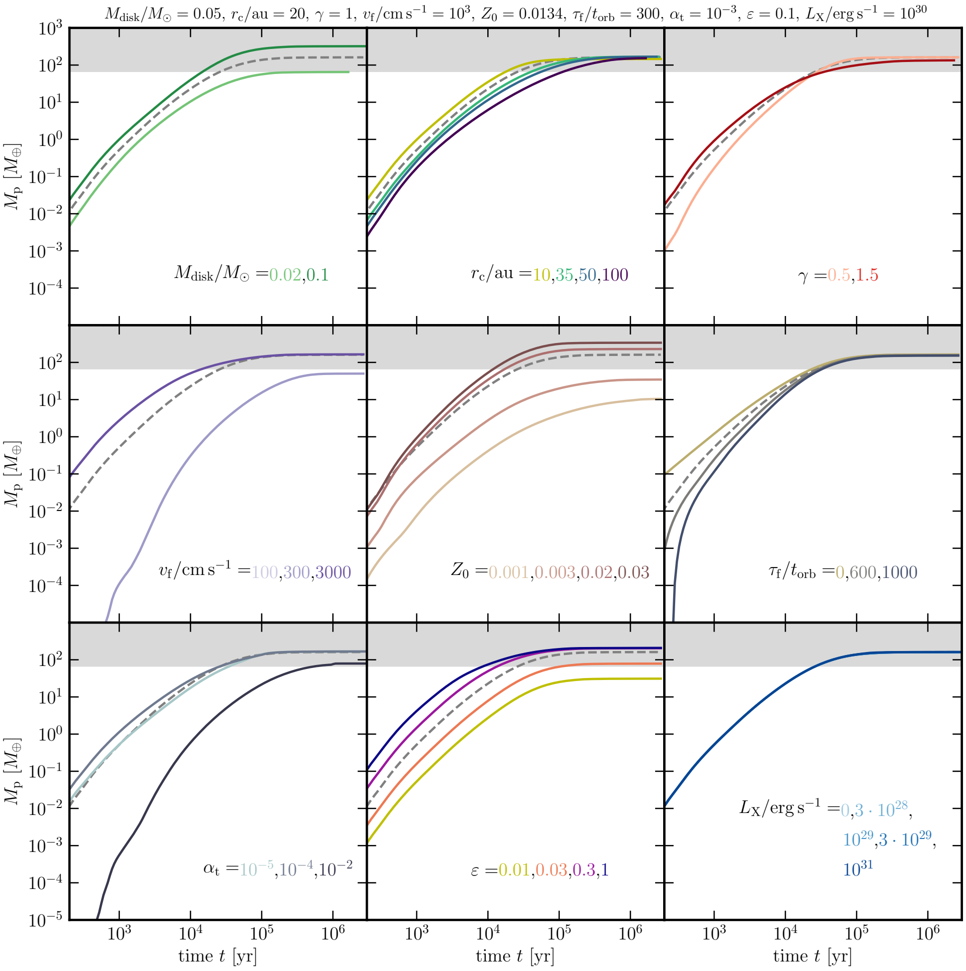

Figure 3.7: Total planetesimal mass as a function of time for the first sample (gray values in Table 3.1). The fiducial values for this set of simulations is shown as header of the plot. In each panel the simulation with all those parameters is shown as dashed gray line. The solid lines with colors show simulation results where only one parameter of the set was changed. The gray area shows values more massive than the solids of the MMSN (Weidenschilling, 1977b; Hayashi, 1981).

differences. For the first fiducial run we used a turbulence strength parameter of $\alpha_{\rm t} = 10^{-3}$ and a fragmentation speed of $v_{\rm f} = 10\,{\rm m\,s^{-1}}$, whereas the second fiducial run we have set $\alpha_{\rm t} = 10^{-4}$ and $v_{\rm f} = 1\,{\rm m\,s^{-1}}$. Despite the fact that for the latter case both values are one order or magnitude smaller compared to the former, the smaller $v_{\rm f}$ in the second fiducial run leads to much smaller maximum particle sizes since the fragmentation barrier scales quadratically with $v_{\rm f}$ but only inversely linear with $\alpha_{\rm t}$ (Birnstiel et al., 2012). As a result, in the second parameter set almost the entire disk is limited by fragmentation over the major time of planetesimal formation while the first becomes drift limited much faster (see Figure 3.6). In Fig. 3.5 one can also see that higher $\alpha_{\rm t}$ let the disk spread faster where material is removed in the very outer regions due to the constant external FUV sink term that we used.

Figure 3.6 shows the particle flux for particles of different sizes in the Stokes number space as a function of disk radius at three different snapshots. The fragmentation (red lines) and drift limit (purple lines) set the maximum size of the flux dominating particle species. The horizontal gray line marks the Stokes number beyond which particles are assumed to contribute to particle trapping and planetesimal formation, see also Fig. 3.3. Within ∼ 3 au, some particles have higher Stokes numbers forming a kink feature because they enter the Stokes drag regime (see Figure 3.6 and B.7). However, it looks much less extreme in the grain size space.

More details on the special case including accretion heating can be found in Appendix B.2, where we show the time evolution of the pebble flux and of the planetesimal, dust, and gas profiles.

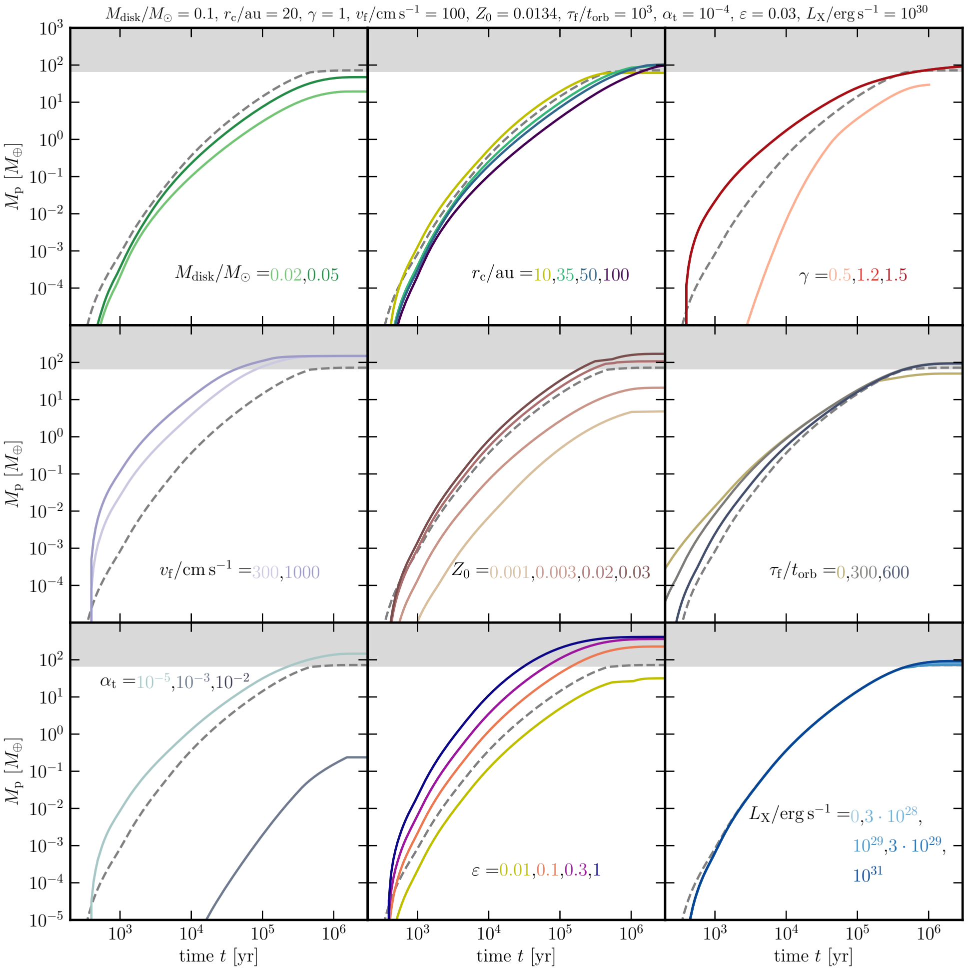

Figure 3.8: As Fig. 3.7 but for the second sample (variations to the bold values in Table 3.1). The fiducial run just produces enough planetesimal mass in the disk to reach the MMSN mass in solids even though the disk mass is at the high end already. From this point of view, one needs either a higher initial dust-to-gas ratio, a higher planetesimal formation efficiency, or a larger fragmentation speed. For the bottom left panel, no line is visible for $\alpha_{\rm t} = 0.01$ as no planetesimals are formed in that case.

3.4.3 Mass Evolution

It might be a valuable information if and when the total mass in planetesimals saturates. This saturated mass can be compared with the MMSN solid mass. If this mass is not reached, we consider the parameter set of that simulation to be unable to reproduce the Solar System as usually several times the MMSN are needed in order to get results that are comparable to the Solar System. Figures 3.7 and 3.8 show the time evolution in mass of the first and second sample, respectively. In each panel only one parameter was changed compared to the ficucial parameter set shown in the title of both figures. The final value of the time evolution of the total disk mass that is in planetesimals can be compared to the minimum mass for the solar nebula based on Weidenschilling (1977b) and Hayashi (1981). The required mass for initial planetesimals is marked as gray regions. If the final mass is below the gray region for a given parameter set, this set can be excluded for the solar nebula. In both figures one can see that initial dust-to-gas ratios of 0.003 and lower are not able to lead to the MMSN mass in planetesimals. A fragmentation speed of $v_{\rm f} = 10^2\,{\rm cm\,s^{-1}}$ seem to be a critical value under which the MMSN mass cannot be reached unless the initial dust-to-gas ratio $Z_0 > 0.0134$, the turbulence strength $\alpha_{\rm t} \leq 10^{-4}$ (here this parameter ist also used for vertical and radial particle diffusion as well as relative turbulent velocities), or $\varepsilon > 0.03$. For a disk starting with $M_{\rm disk} < 0.1\,M_\odot$, ε or Z_0 might need even higher values to reach a final planetesimal disk mass more massive than the MMSN.

The yellow line in the middle lower panel of Fig. 3.8 shows a case of low planetesimal formation efficiencies

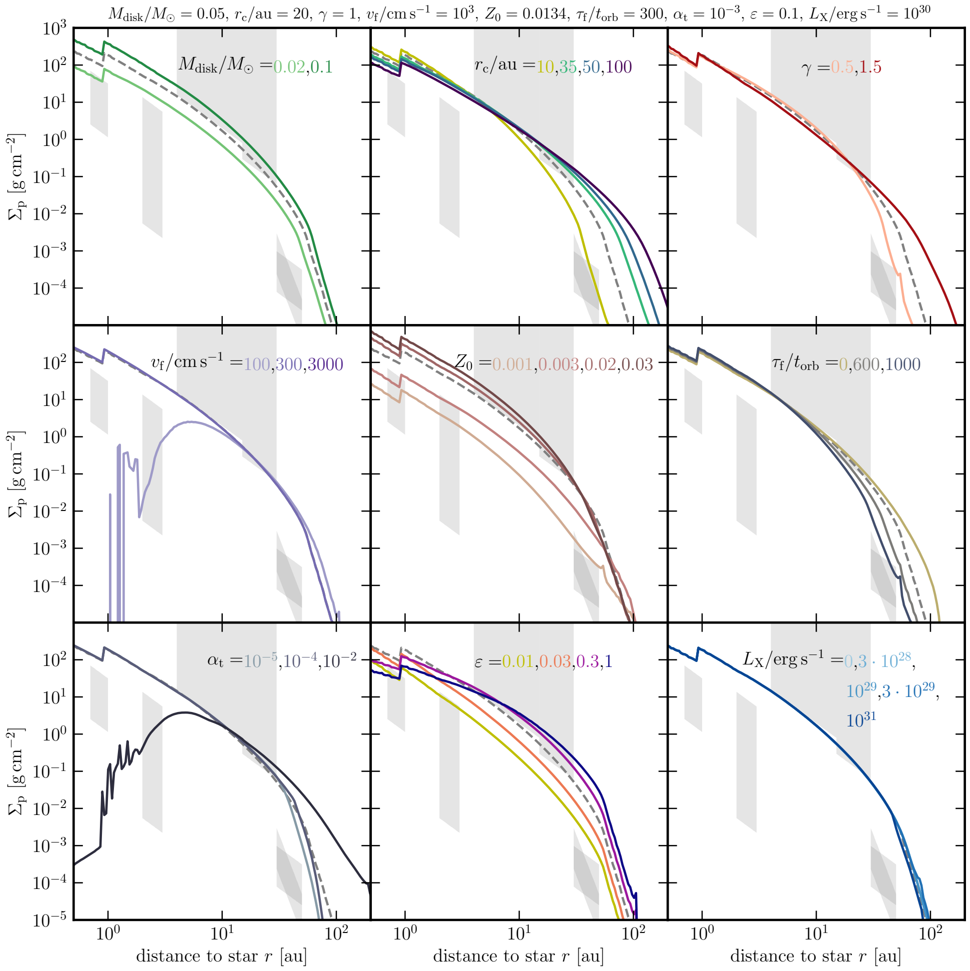

Figure 3.9: Final (at 10 Myr) planetesimal column density as a function of disk radius for the first sample (gray values in Table 3.1). The fiducial values for this set of simulations is shown as header of the plot. In each panel the simulation with all those parameters is shown as dashed gray line. The solid lines with colors show simulation results where only one parameter of the set was changed. The gray areas represent the constraints that we described in sec. 3.2, where the mass in the given region was translated into a column density, assuming a planetesimal profile $\propto r^{-2.25}$ (see Eq. (37) of Lenz et al. (2019)). For the outermost region, we also overplotted a box $\propto r^{-8}$.

in a mostly fragmentation limited disk. In this case after about 10^5 yr photoevaporation allows another phase of planetesimal formation after the planetesimal mass in the disk reached a plateau already. The same effect shows up for high initial dust-to-gas ratios, see the case of $Z = 0.03$ in the centered panel of Fig. 3.8. In both cases the reason for the second planetesimal formation phase is the higher mass budget. For low ε, particles survive longer in a fragmentation limited disk since their average radial drift velocity is much slower due to disruptive collisions that replenish slowly drifting dust grains and less mass is transformed into planetesimals. For $Z \gtrsim 0.03$, the initial particle mass budget is already so high that there remains enough mass for planetesimal formation at later times when photoevaoration has removed a significant amount of gas mass. However, this effect of a second planetesmial formation phase only occurs if the disk is mostly fragmentation limited, which applies for the results shown in Fig. 3.8 but not for those shown in Fig. 3.7 in which case the disks are mostly drift limited. Additionally, the second planetesimal formation phase induced by photoevaporation is not sufficient to reach the mass of the MMSN for low planetesimal formation efficiencies, i.e. for $\varepsilon \lesssim 0.01$.

The first sample, shown in Fig. 3.7, leads to higher masses of the planetesimal population compared to the second sample, shown in Fig. 3.8. The reason for this is that in the first sample grains can grow to larger sizes due to the higher fragmentation speed. However, both samples used the parameterized planetesimal formation model of Lenz

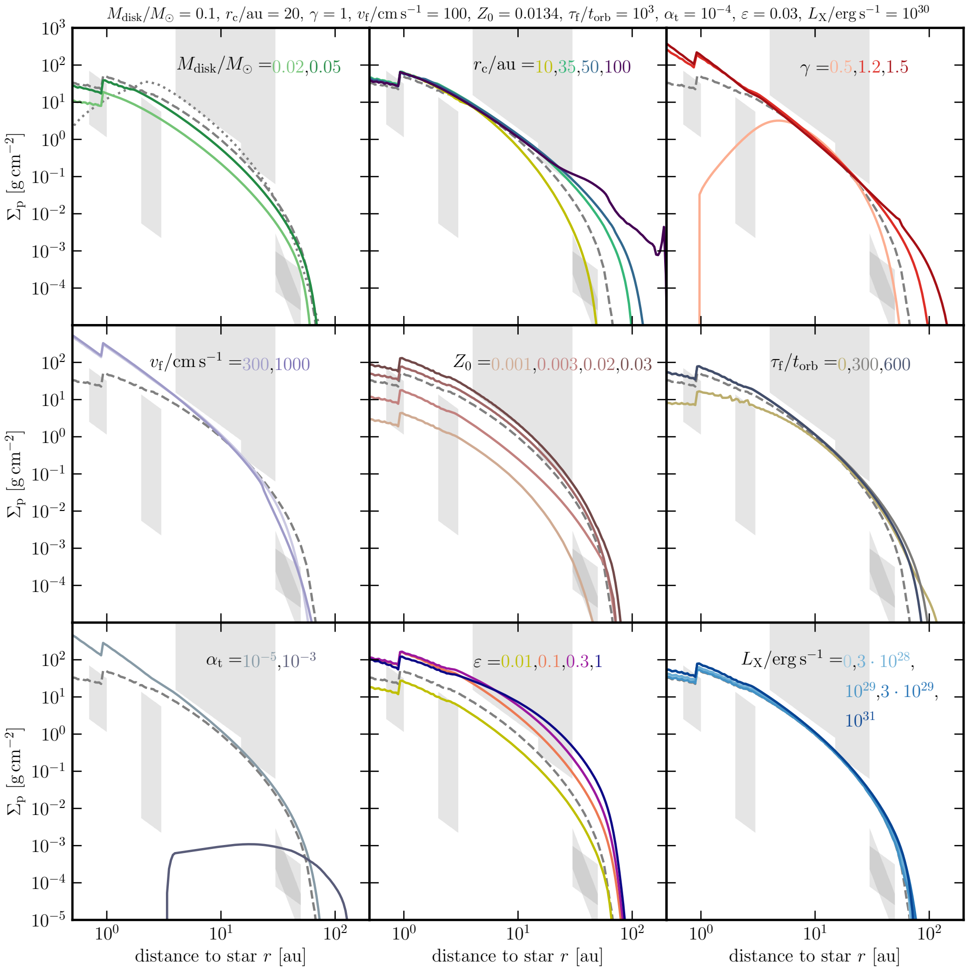

Figure 3.10: As Fig. 3.9 but for the second sample (variations to the bold values in Table 3.1). If ε is high enough, photoevaporation does not change the result significantly. But it seems to have an effect for low ε, see yellow line in the bottom middle panel of Fig. 3.8. In the top left panel we also plot the most appealing case as dotted line (last row in Tab. 3.1).

et al. (2019), see Section 3.3.4. Again, in this model particle traps are only considered via parameters but the gas profile is smooth, without pressure bumps or gaps, unless caused by photoevaporation. Pressure bumps in the gas profile would lead to a reduction in radial drift speed, allowing particles to remain longer in certain disk regions (e.g. Pinilla et al., 2012), even if these traps would appear and disappear on a given timescale. This could lead to longer planetesimal formation and more impact of photoevapotation. However, this might not change the results significantly, leaving the presented conclusions untouched.

3.4.4 Deep Parameter Analysis

By looking at the final planetesimal profiles for all nine parameters, we find a huge variety of possible parameters for the Solar Nebula. It is reassuring that the model works not only for a very finely tuned subset of parameter choices. Though the different parameters can influence each other, it is still possible to draw some conclusions. Table 3.2 shows which parameters fail to fulfill the outer Solar System constraints or the MMSN mass. In Table 3.3 we present disk parameter ranges that could potentially reproduce the Solar System. Those conclusions are based on Table 3.2. How much mass the initial disk should contain depends on the fragmentation speed since the latter determines how much mass is in particles with $\mathrm{St} \gtrsim 0.01$.

Our parameter analysis is based on Figs. 3.7, 3.8, 3.9, and 3.10. The last two of these figures show the column

Table 3.2: Parameters that can be excluded to reproduce the Solar Nebula based on Figures 3.9, 3.10, 3.7, and 3.8. We cannot exclude values for L_X within the range we have checked. For all the simulations presented in this table we used $L_\mathrm{X} = 10^{30}\,\mathrm{erg\,s^{-1}}$. Here we concentrate on three constraints only: (1) the Cold Classical Kuiper Belt (CCKB) mass constraints, (2) the necessary mass to fulfill the Nice disk condition, (3) and the minimum mass solar nebula (MMSN) mass. In each row we highlight in bold those parameters that deviate from the default values.

M_disk [$M_\odot$]	r_c [au]	γ	v_f [$\mathrm{cm\,s^{-1}}$]	Z_0	τ_f [t_orb]	α_t	ε	reason
0.05	**≥ 35**	1	1000	0.0134	300	10^{-3}	0.1	fails CCKB condition
0.05	20	**1.5**	1000	0.0134	300	10^{-3}	0.1	fails CCKB condition
0.05	20	1	1000	**≤ 0.03**	300	10^{-3}	0.1	<MMSN; fails Nice disk condition
0.05	20	1	1000	0.0134	**< 300**	10^{-3}	0.1	fails CCKB condition
0.05	20	1	1000	0.0134	300	**10^{-2}**	0.1	fails CCKB condition
0.05	20	1	1000	0.0134	300	10^{-3}	**≤ 0.03**	<MMSN (for $\varepsilon \lesssim 0.01$); fails Nice disk cond.
0.05	20	1	1000	0.0134	300	10^{-3}	**$\gtrsim 0.3$**	fails CCKB condition
0.02	20	1	100	0.0134	1000	10^{-4}	0.03	<MMSN; fails Nice disk condition
0.05	20	1	100	0.0134	1000	10^{-4}	0.03	<MMSN; fails Nice disk condition
0.1	**≤ 10**	1	100	0.0134	1000	10^{-4}	0.03	fails Nice disk condition
0.1	**≥ 35**	1	100	0.0134	1000	10^{-4}	0.03	fails CCKB condition
0.1	20	**0.5**	100	0.0134	1000	10^{-4}	0.03	<MMSN
0.1	20	**≥ 1.2**	100	0.0134	1000	10^{-4}	0.03	fails CCKB condition
0.1	20	1	**< 100**	0.0134	1000	10^{-4}	0.03	<MMSN
0.1	20	1	100	**≤ 0.003**	1000	10^{-4}	0.03	<MMSN; fails Nice disk condition
0.1	20	1	100	0.0134	**0**	10^{-4}	0.03	fails CCKB condition
0.1	20	1	100	0.0134	1000	**$\geq 10^{-3}$**	0.03	<MMSN; fails almost every cond.
0.1	20	1	100	0.0134	1000	10^{-4}	**≤ 0.01**	<MMSN; fails Nice disk condition
0.1	20	1	100	0.0134	1000	10^{-4}	**$\gtrsim 0.3$**	fails CCKB condition

density profiles of the final planetesimal population. In each panel only one parameter is varied compared to the fiducial parameter set (dashed lines). In the background the gray boxes represent the mass constraints discussed in Sec. 3.2.

The initial characteristic radius r_c has two major effects. One is the radial position beyond which the dust and gas density drops exponentially. The second is that for smaller (larger) r_c there is more mass in the inner (outer) disk region. If the disk is too large, there is simply too much mass available around 40 au and beyond to form planetesimals. Too much mass in the outer disk then leads to violation of the upper CCKBO constraint. Whether this constraint is indeed violated depends also on the initial disk mass, the planetesimal formation efficiency, the initial dust-to-gas ratio, and the viscosity power-law index γ. However, for a narrow set of these four parameter, finding constraints for r_c is possible.

The fragmentation speed v_f changes the outcome by a lot since the fragmentation limit depends quadratically on this parameter. For $v_\mathrm{f} \gtrsim 10\,\mathrm{m\,s^{-1}}$ $\gamma \sim 0.5$ is actually beneficial due to the stronger density drop in the outer disk, see orange line in the top right panel of Fig. 3.9. However, for $v_\mathrm{f} \gtrsim 1\,\mathrm{m\,s^{-1}}$ one would need more than $M_\mathrm{disk} \gtrsim 0.1 M_\odot$ to create enough mass to build all planets, specifically in the inner disk part ($\lesssim 15$ au), see orange line in the top right panel of Fig. 3.10.

If $v_\mathrm{f} < 1\,\mathrm{m\,s^{-1}}$, too few or no particles with $\mathrm{St} \gtrsim 0.01$ would be formed which is the necessary Stokes number to make trapping and collapse to planetesimals from pebble clouds work. Already with $v_\mathrm{f} = 1\,\mathrm{m\,s^{-1}}$ it is difficult to meet all the constraints, especially a total mass in planetesimals larger than the minimum mass Solar Nebula (Weidenschilling,

Table 3.3: Parameter ranges that could work for reproducing the Solar System.

Symbol	Meaning	Comments
$M_{\rm disk}$	total disk mass	$M_{\rm disk} \gtrsim 0.1 M_\odot$ for $v_{\rm f} \sim 1\,{\rm m\,s^{-1}}$ and $M_{\rm disk} \gtrsim 0.02 M_\odot$ for $v_{\rm f} \gtrsim 10\,{\rm m\,s^{-1}}$
$r_{\rm c}$	char. radius	$\lesssim 50\,{\rm au}$
γ	initial inner column dust and gas density power-law index	For $v_{\rm f} \gtrsim 10\,{\rm m\,s^{-1}}$ $\gamma \sim 0.5 - 1$. For $v_{\rm f} \gtrsim 1\,{\rm m\,s^{-1}}$ and $M_{\rm disk} \gtrsim 0.1 M_\odot$, $\gamma \sim 0.5$ could work but $\gamma \sim 1$ seems more likely
$v_{\rm f}$	frag. speed	$\gtrsim 1\,{\rm m\,s^{-1}}$ to allow pebbles with ${\rm St} \gtrsim 10^{-2}$ to form
Z_0	initial dust-to-gas ratio	$0.01 \lesssim Z_0 \lesssim 0.03$ works more or less equally well, whereas $Z_0 \lesssim 0.003$ fails
$\tau_{\rm f}$	trap formation time	Traps needed at least $300\,t_{\rm orb}$ to form outside of 50 au or never formed there
$\alpha_{\rm t}$	turbulence parameter	$\alpha_{\rm t} \sim 10^{-5} - 10^{-3}$ (or only up to a few 10^{-4} if $v_{\rm f} \sim 1\,{\rm m\,s^{-1}}$)
ε	planetesimal formation efficiency	$0.002 < \varepsilon h_{\rm g}/d \lesssim 0.06$ (if ε and $d/h_{\rm g}$ are constant)
$L_{\rm X}$	X-ray luminosity	For $r_{\rm c} \lesssim 20\,{\rm au}$, photoevaporation does not affect the final planetesimal profile significantly

1977b; Hayashi, 1981), see the lowest line in the middle left panel of Fig. 3.7 and the dashed lines in Fig. 3.8.

The initial dust-to-gas ratio Z_0 determines how much mass is initially in particles but also the dust dynamics as a low dust-to-gas ratio leads to a drift limited disk that looses particles quickly due to drift. Large Z_0 of up to roughly 0.03 seem to allow fulfilling the mass constraints on initial planetesimals. However, values of $\lesssim 0.003$ lead to too little mass in the final planetesimal population as can be seen in Figs. 3.7, 3.8, 3.9, and 3.10.

The more time particles have to drift from the region outside of $\sim 50\,{\rm au}$ to the inner parts before planetesimal formation, the better the CCKB constraints can be met. Alternatively, traps might not occur outside of 50 au at all (Pfeil & Klahr, 2019). From the simulations we conclude that the trap formation time must be $\tau_{\rm f} > 300\,t_{\rm orb}$ or even $\gtrsim 1000\,t_{\rm orb}$. Other values lead to masses between $\sim 30\,{\rm au}$ and 50 au that are orders of magnitudes higher than the upper limit.

Constraining values for the turbulence parameter $\alpha_{\rm t}$ is also linked to the fragmentation speed because the fragmentation limit scales inversely linear with $\alpha_{\rm t}$ but quadratically with $v_{\rm f}$. For this limit, only the relative velocity matters. However, we assumed that vertical and radial diffusion as well as the viscosity parameter for the gas have the same value $\alpha_{\rm t}$ that we used for the turbulent velocities. For smaller $\alpha_{\rm t}$, particles can settle closer to the midplane. If this value is low enough, growth is not limited by relative turbulent velocties but by relative settling speeds or relative radial drift. In case $\alpha_{\rm t}$ is high ($\sim 10^{-2}$), relative turbulent velocities are too high to allow ${\rm St} > 0.01$ particles. At the same time, the radial viscous gas motion drags dust along to the outer regions of the disk, leading to too much mass in planetesimals outside of 30 au. Hence, for $v_{\rm f} \sim 10\,{\rm m\,s^{-1}}$ we suggest $\alpha_{\rm t} \sim 10^{-5} - 10^{-3}$, while the upper end should be up to a few 10^{-4} if $v_{\rm f} \sim 1\,{\rm m\,s^{-1}}$.

Values of $\varepsilon/d \leq 0.002/h_{\rm g}$ can be excluded for the solar nebula (if ε and $d/h_{\rm g}$ are constant) as both the total final planetesimal mass in the disk is below the MMSN and the mass required for the Nice disk can not be reached. Unless the solar nebula was not very small ($r_{\rm c} \lesssim 10\,{\rm au}$), planetesimal formation should not have been too efficient, i.e., $\varepsilon/d \lesssim 0.06/h_{\rm g}$. Otherwise too many planetesimals are formed outside of 30 au. Thus, the range of possible values is $0.002 < \varepsilon h_{\rm g}/d \lesssim 0.06$.

Photoevaporation did not influence the final planetesimal profile significantly for small enough disks ($r_{\rm c} \lesssim 20\,{\rm au}$). However, for large disks ($r_{\rm c} \sim 100\,{\rm au}$) it can make a difference. But this case is not interesting for finding similar conditions to the solar nebula as in this case too much mass ends up in planetesimals in the outer disk regions anyway.

In the left panel of Fig. 3.4 compared to its right panel, the plateau is reached for smaller values of ε/d which is linked to the smaller pebble mass that is available for planetesimal formation since the smaller fragmentation velocity lead to smaller maximum Stokes numbers.

3.4.5 With Accretion Heating

Accretion heating leads to a hotter inner disk which is good since not a single planetesimal got detected inside the orbit of Mercury. I.e., the planetesimal profile has to drop drastically in the inner region before reaching Mercury's current radial position. This can be satisfied due to the higher gas temperatures as these are forcing the fragmentation limit to be at lower Stokes numbers and a larger conversion length ($\ell \propto h_g \propto \sqrt{T}$). In this simulation the ice line is moving radially over time which is why there is no distinct kink feature in the profile. The constraints in the outer disk, that is the Nice disk and the CCKB, are the strongest ones we have. The other constraints may be a bit more flexible. These constraints are roughly met by this simulation.

Since the temperature model presented in this Chapter was not tested in a comprehensive way, e.g. by comparing with Hubeny (1990) or Nakamoto & Nakagawa (1994), we only use it to show one special case. In addition, planetesimal-planetesimal collisions would replenish the small dust population (Gerbig et al., 2019). This effect is not taken into account in this work but could change the gas midplane temperature via the mean dust opacity.

We are highlighting one special case with parameters $M_{\mathrm{disk}}/M_{\odot} = 0.1$, $r_{\mathrm{c}}/\mathrm{au} = 20$, $\gamma = 1$, $v_{\mathrm{f}}/\mathrm{cm\,s^{-1}} = 2 \cdot 10^2$, $Z_0 = 0.0134$, $\tau_{\mathrm{f}}/t_{\mathrm{orb}} = 1600$, $\alpha_{\mathrm{t}} = 3 \cdot 10^{-4}$, $\varepsilon = 0.05$, and $L_{\mathrm{X}}/\mathrm{erg\,s^{-1}} = 3 \cdot 10^{29}$. We will refer to this as the most appealing simulation in this Chapter. The final planetesimal profile is shown in the top left panel of Fig. 3.10 as dotted line.

3.5 Summary

We used an extended version of the Lenz et al. (2019) model, including Stokes drag for particles and allowing the gas to evolve viscously while photoevaporation is removing gas over time. The analyzed parameter space was largely increased. While this Chapter provides a parameter study for pebble flux-regulated planetesimals formation, we focussed on meeting Solar System constraints for initial planetesimals. Therefore, we used two different default parameter sets and varied one out of nine parameters per simulation. Overall, while some parameters can be excluded, the model seems to be very robust, thus it does not require parameter fine tuning in order to fulfill the constraints.

The computation times of the presented simulations were between roughly a week and six months while running on ten cores each. Using more than ten cores for a simulation would not decrease the computation time significantly since the code cannot make use of further parallelization. Especially the runs of the second sample were running for months. To shorten the computation time, a simple model must be used such as the two population model presented by Birnstiel et al. (2012). However, this simplified model was only tested for a narrow set of parameters and causes deviations from `DustPy` simulations for certain parameters. Additionally, the two population model was not yet tested in detail including the planetesimal formation model that was used in this study. A simple model reproducing the results shown in this study is likely possible, however, we preferred to use `DustPy` in order to rely on fundamental physics principles and a sophisticated growth and fragmentation model rather than simplified and untested models.

In sec. 3.2 we suggested mass constraints for initial planetesimals in different regions of the disk:

- $0.7-1\,\mathrm{au}$: $0.1-2.77\,M_{\oplus}$
- $2-3\,\mathrm{au}$: $0.002-5\,M_{\oplus}$
- $4-15\,\mathrm{au}$: $66-\mathrm{unknown}\,M_{\oplus}$
- $15-30\,\mathrm{au}$: $10-\mathrm{unknown}\,M_{\oplus}$
- $30-50\,\mathrm{au}$: $0.008-0.1\,M_{\oplus}$

Within 0.7 au and outside of 50 au there might have been nothing or a very low mass in planetesimals. These suggested constraints are illustrated in Figures 3.1 and 3.2.

The fragmentation speed v_{f} that leads to breakup in particle collisions and the turbulence parameter of relative velocities α_{t} determine how large particles can grow. If the combination of both leads to a fragmentation limit that is close to Stokes numbers of 0.01, the available mass for planetesimal formation becomes affected by these parameters. This is why a constraint in total initial disk mass has to be linked to (mostly) v_{f}. To fulfill the constraints we suggested, we need $M_{\mathrm{disk}} \gtrsim 0.1 M_{\odot}$ for $v_{\mathrm{f}} \sim 1\,\mathrm{m\,s^{-1}}$ and $M_{\mathrm{disk}} \gtrsim 0.02 M_{\odot}$ for $v_{\mathrm{f}} \gtrsim 10\,\mathrm{m\,s^{-1}}$. In addition, the solar nebular was not larger than $r_{\mathrm{c}} \lesssim 50\,\mathrm{au}$ (r_{c} is the initial transition radius between a power-law and a dropping exponential profile). The power-law index of that inner region was likely around $\gamma \sim 1$ but for large fragmentation speeds $\gamma \sim 0.5$ can be beneficial for the outer region due to the density drop (if traps can be formed outside of 50 au). To allow pebbles with $\mathrm{St} \gtrsim 10^{-2}$ to form, which is roughly the needed Stokes number for trapping and subsequent planetesimal formation, one needs $v_\mathrm{f} \gtrsim 1\,\mathrm{m\,s^{-1}}$. For the initial dust-to-gas ratio, many values $0.01 \lesssim Z_0 \lesssim 0.03$ could work, but $Z_0 \lesssim 0.003$ leads to too low mass in planetesimals. Outside of 50 au traps needed at least $300\,t_\mathrm{orb}$ or never formed there. For the turbulence parameter we find a wide range of possible values $\alpha_\mathrm{t} \sim 10^{-5} - 10^{-3}$ (or only up to a few 10^{-4} if $v_\mathrm{f} \sim 1\,\mathrm{m\,s^{-1}}$). Since disk parameters can affect each other, we also find a wide range for the radial pebble to planetesimal conversion length: $0.002 < h_\mathrm{g}/\ell \lesssim 0.06$. If the disk is sufficiently small ($r_\mathrm{c} \lesssim 20\,\mathrm{au}$), photoevaporation does not change the final planetesimal profile by much.

The parameters of our most appealing case that includes a simple accretion heating model are the following: $M_\mathrm{disk}/M_\odot = 0.1$, $r_\mathrm{c}/\mathrm{au} = 20$, $\gamma = 1$, $v_\mathrm{f}/\mathrm{cm\,s^{-1}} = 2 \cdot 10^2$, $Z_0 = 0.0134$, $\tau_\mathrm{f}/t_\mathrm{orb} = 1600$, $\alpha_\mathrm{t} = 3 \cdot 10^{-4}$, and $\varepsilon = 0.05$, and $L_\mathrm{X}/\mathrm{erg\,s^{-1}} = 3 \cdot 10^{29}$ (see dotted line in the top left panel of Fig. 3.10).

We estimated the maximum mass in planetesimals by equating the planetesimal formation and drift timescale. This approach leads to $\ell = r$, see Eq. (3.42), which seems to fit our simulation results well (see Figure 3.4). If the planetesimal formation timescale is much shorter than the drift timescale, the planetesimal profile reproduces the initial dust profile. Planetesimal formation efficiencies smaller than the value corresponding to this sweep-spot lead to planetesimal profiles steeper than the initial dust profile or even steeper than the minimum mass Solar Nebula profile. This effect was already observed in Lenz et al. (2019) and this study provides an estimate for the transition to more local planetesimal formation that is linked to slopes closer to the initial dust profile.

Within the model, further limitations would be that no pebble accretion was included which could affect especially the planetesimal profile in the inner disk as pebbles get accreted before reaching that zone. In addition, our simulations did not consider planetesimal-planetesimal collisions which would lead to multiple generations in planetesimals, pebbles, and dust.

3.6 Conclusions

The MMSN is not consistent with viscous disk evolution models and does not provide enough mass in the giant planet forming region to allow strong gas accretion (see Fig. 3.2). While typically the MMSN distribution is assumed to be present from the beginning, the timing of substantial planetesimal formation could also matter for further embryo formation and evolution. We have shown that pebble flux-regulated planetesimal formation produces beneficial planetesimal distributions for a wide range of parameters, both with respect to planetesimal formation and initial conditions of the disk. Even though the impact of disk parameters on the evolution of initial planetesimals influence each other, some constraints on these parameters were found in this study. A narrow set of parameters allowing to reproduce the Solar System would have indicated model fine tuning. This stresses the applicability of our parameterization to models of planet formation, e.g. population synthesis models.

4

On Planetesimal Formation Feeding Zones and Tracing Their Material

Planetesimals together with pebbles are the building blocks of planets. The building bricks of planetesimals itself can originate from different regions in a protoplanetary disk since particles undergo significant radial drift once they have grown to a certain size. While particles are drifting inward, they can be trapped by large scale pressure bumps and form planetesimals via gravoturbulent collapse.

In this Chapter I discuss a few example cases to determine where a certain percentage of mass contribution to a planetesimal (e.g., 90%), at a given position in the disk and a given time, originates from. Linking this information to the local planetesimal mass production over time, one obtains the contribution to a final local planetesimal population with different origins of their building blocks. Since a significant amount of mass can be evaporated at different ice lines, changing e.g. the carbon abundance, this raises the question how much mass passed one or several (major) ice lines on their way to the inner disk regions before forming planetesimals.

By dividing the disk into regions where planetesimal formation is (in)active, a survival probability of single particles can be calculated. Radial velocities and densities of particles that are taken from simulations are used to trace the front of a pebble swarm that can form planetesimals on its way to the innermost disk regions.

The results, mass contributions to planetesimals linked to their original disk position, dependent on the disk radius and time, are very sensitive to the planetesimal formation efficiency as well as the duration and extent of the fragmentation limited disk regions.

Mass originating from far distant regions contribute significantly to planetesimal compositions. On their way to disk regions further inside, a significant amount of material crosses the CO, CO_2, or water ice line(s) before forming a planetesimal at the current locations of Earth or the asteroid belt.

4.1 Introduction

The composition of extrasolar terrestrial planets is very diverse (e.g. Bond et al., 2010). The composition of planets is set by the composition of gas and solids in protoplanetary disks out of which planets form. The solids that are the building blocks of planets are planetesimals and pebbles. Planetesimals are objects that are both big enough to enlarge the collisional cross section and bound due to their gravitational attraction. Pebbles are solids (typically mm–cm in size) that can be accreted onto planetary embryos (Ormel & Klahr, 2010), for a review see e.g. Ormel (2017).

Due to centrifugal deficiency (for particle Stokes numbers smaller than unity), particles that are marginally coupled to the gas drift to regions of higher gas pressure (Whipple, 1972; Adachi et al., 1976; Weidenschilling, 1977a; Nakagawa et al., 1986). For a smooth disk without any pressure bumps this means drifting toward the star. Starting with micron-sized dust grains, particles grow until relative velocities lead to fragmentation (Blum & Münch, 1993; Blum & Wurm, 2008; Gundlach & Blum, 2014) or the radial drift timescale becomes shorter than the growth timescale (Klahr & Bodenheimer, 2006; Birnstiel et al., 2012). In the former case, these regions are called fragmentation limited and in the latter case drift limited.

Bodies in the terrestrial planets region contain very small mass fractions of carbon, but it is observed a high carbon fraction that is bound in solid carbonaceous material for bodies formed in the outer regions of the solar nebula (e.g. Wooden, 2000, 2008; Ehrenfreund et al., 2004). The carbon abundance of Earth is significantly lower compared to the solar abundance or interstellar medium (e.g. Pontoppidan et al., 2014). During disk evolution, a high fraction of the carbon originally contained in solid phases is converted into gaseous material and lost. Hence, only a small amount can be incorporated into planetesimals, especially those forming in the inner disk (Gail & Trieloff, 2017). Lifting particles to higher and thus hotter vertical regions in the disk due to turbulence, can lead to significant loss in carbon (Lee et al., 2010; Anderson et al., 2017). However, radial particle transport prevents the depletion of carbon as shown by Klarmann et al. (2018).

The local mass in particles at a given location in the disk can originate from different disk regions. While particles are drifting inward, they can loose mass at various ice lines, especially at the water ice line (e.g. Cuzzi & Zahnle, 2004). An additional sink term for the pebble swarm is planetesimal formation. The distribution of origins of the planet(esimal) forming material includes information on how much mass from different disk regions spanning out to the cold outskirts contributed to a planet(esimal). The more material is able to drift through the outer disk regions without forming planetesimals or being accreted by planetary embryos, the more mass is available in the inner disk to form planetesimals or enlarge embryos. Hence, the feeding zones of planetesimal forming material cause the steepness of the planetesimal density profile. A large feeding zone also includes that particles have crossed one or multiple major ice lines which affects the chemistry of an inward drifting pebble swarm and thus planet(esimal) compositions.

This study is based on the planetesimal formation model of Lenz et al. (2019) which uses a conversion length for the transformation from pebbles to planetesimals in a 1-dimensional simulation for particle growth and transport. Meanwhile the model is used in population synthesis (Völkel et al., 2020). Hence, it is interesting what planetesimals are made of.

In Section 4.2 we present the planetesimal formation model that was used in the simulations on which our study is based on. The second part of that section shows the planetesimal formation feeding zone model which computes the distribution of material origins within a given pebble swarm. Section 4.3 shows the results for both a disk that is mostly limited by drift and in the other case by fragmentation. We discuss limitations, (dis)advantages, and other implications of our model in Section 4.4. This work is summarized in Section 4.5 and we give final conclusions in Section 4.6.

4.2 The model

This section describes the planetesimal formation model used in the simulations on which our results are based on and the model for calculating the mass contributions with different origins to planetesimals. The simulations were performed with the `DustPy` code that is a python based version of Birnstiel et al. (2010) (Stammler & Birnstiel, in prep.).

4.2.1 Planetesimal formation

The planetesimal formation model follows the one presented in Lenz et al. (2019). This model is based on the idea that radial gas structures can trap particles and thus convert pebbles to planetesimals over a radial conversion length ℓ. This conversion length can be interpreted as the mean radial separation of particles traps d over an efficiency parameter for planetesimal formation ε. For $d = 5h_\mathrm{g}$ this would translate into $\varepsilon := 5h_\mathrm{g}/\ell$. In Appendix C.3 we show analytical estimates for the probability of a single pebble to survive planetesimal formation while drifting through a planetesimal forming region. If d is roughly constant, this would lead to a situation where mass is lost exponentially with the radial distance Δr traveled away from the starting position, i.e.

$$\text{mass lost after drifting in by } \Delta r \approx 1 - \exp{-\varepsilon\frac{\Delta r}{d}}.$$

For instance, after drifting in over a distance $\Delta r = d$ and for $\varepsilon = 1$, roughly 63% of the mass is lost due to planetesimal formation.

The transformation to planetesimals is regulated by the pebble flux (Lenz et al., 2019)

$$\dot{M}_\mathrm{peb} := 2\pi r \int_{\mathrm{St}_\mathrm{min}}^{\mathrm{St}_\mathrm{max}} \left|v_\mathrm{drift}(r,\mathrm{St})\right| \frac{\mathrm{d}\Sigma_\mathrm{d}(r,\mathrm{St})}{\mathrm{dSt}}\,\mathrm{dSt}. \tag{4.1}$$

The cylindrical disk radius is given by r, v_drift is the radial drift velocity, and Σ_d the vertically integrated density in

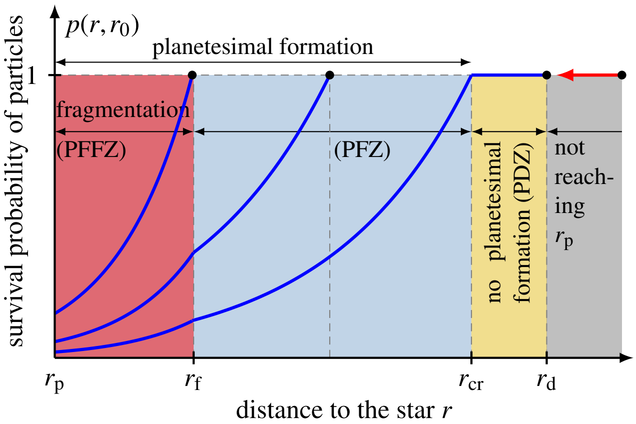

Figure 4.1: Schematic illustration of the survival probability p of individual particles. Particles are born at different positions r_0, denoted by the black dots. In the blue region the conditions for planetesimal formation are fulfilled and thus p decreases while particles are drifting inward as mass is transformed into planetesimals. In the beige region the conditions for planetesimal formation are not reached and thus p stays constant. Particles born in the gray region are not reaching r_p — but they may reach the blue or red region — and therefore do not participate in the formation of planetesimals at that radius. In the red region not only the condition of planetesimal formation is satisfied, but also fragmentation becomes efficient and thus p is also reduced due to disruptive collisions which leads to a steeper slope in the red zone. r_cr and r_d will increase for larger times t and $r_\mathrm{d} - r_\mathrm{cr}$ may vary with time. Usually, $r_\mathrm{d} - r_\mathrm{cr}$ is small compared to r_cr. The case that the PDZ (beige) is embedded into the fragmentation zone (red) is not considered here, as this would only be interesting for very early planetesimals.

solids that are not planetesimals. The rate of planetesimal formation is given by

$$\dot{\Sigma}_\mathrm{p}(r) = \frac{\dot{M}_\mathrm{peb}}{2\pi r \ell} = \frac{\varepsilon}{d(r)} \frac{\dot{M}_\mathrm{peb}}{2\pi r}, \tag{4.2}$$

where planetesimal formation only occurs if the following condition is satisfied:

$$\varepsilon \tau_\mathrm{t}(r) \dot{M}_\mathrm{peb} \geq m_\mathrm{p}. \tag{4.3}$$

This condition is satisfied when the pebble rate (mass per time) — here, pebbles are considered as particles with Stokes numbers between $\mathrm{St}_\mathrm{min} = 0.01$ and $\mathrm{St}_\mathrm{max} = 10$ — is sufficiently large such that enough pebbles can be trapped within the trap life time, τ_t, with a pebble capture efficiency of ε to form at least one planetesimal with mass $m_\mathrm{p} \approx 10^{-7}\, M_\oplus$, corresponding to a diameter of 100 km (Klahr & Schreiber, 2015; Schreiber, 2018; Gerbig et al., 2020). The trap lifetime is assumed to be $\tau_\mathrm{t} = 100\, t_\mathrm{orb}$ (e.g. Dittrich et al., 2013; Manger & Klahr, 2018), where t_orb is the time of a local orbit.

In the literature, $2\pi r$ times velocity and surface density is sometimes called "flux", even though it is actually a mass rate. To avoid confusion with the term "accretion rate", we will adopt the term "flux" in this Chapter.

Both the planetesimal formation rate model as well as the planetesimal formation condition are simple enough to allow tracing back the material that has formed planetesimals in the post-processing using a simple toy model. From the simulations, one needs the column density and radial velocity of all particle species (different masses) at enough snapshots to resolve the particle's dynamics. For simplicity, we assume that once a planetesimal has formed, it stays there and does not collide with other planetesimals or grow, i.e. both planetesimal-planetesimal collisions and pebble accretion are not included.

4.2.2 Planetesimal formation feeding zones

We would like to find the answer to the following question: Considering a radial segment in the disk enclosing a region where the condition for planetesimal formation is fulfilled, where does the material for the planetesimals at a certain position come from? In other words, can we trace back the origin of asteroid material, the place in the disk it has formed, before drifting and getting transformed to planetesimals?

We introduce the *survival probability* of individual particles, $p(r, r_0)$, at the position r and with birth place r_0. When drifting material is born at r_0, it is $p(r_0, r_0) := 1$. In this work, we assume that the lost mass of a radially moving pebble swarm due to fragmentation is always compensated by material that was deposited at the respective locations before. For an overview of this model see Fig. 4.1. The beige zone is called "pure drift zone" (PDZ), the blue region "planetesimal formation zone" (PFZ), and the red region "planetesimal formation and fragmentation zone" (PFFZ), where fragmentation here means that the planetesimal building blocks (pebbles) undergo disruptive collisions — not the planetesimals. The probability p is determined by the probability further outside and a sink term, which is proportional to the inverse conversion length $1/\ell = \varepsilon/d$ as we are considering the interval $[r, r+\Delta r]$, the lost fraction of the probability is proportional to $\Delta r/\ell$. Additionally, fragmentation and re-coagulation could affect p as well. We denote the net probability as p_f, which is another loss term but is assumed to be zero and is only shown for completeness. In the discrete picture this means

$$\begin{aligned} p(r) = p(r+\Delta r) - \varepsilon p(r)\frac{\Delta r}{d}\theta(r_\mathrm{cr}-r) \\ -\Delta r\frac{\partial p_\mathrm{f}(r)}{\partial r}\theta(r_\mathrm{f}-r)\ . \end{aligned} \tag{4.4}$$

The radius within which planetesimal formation is possible is be called *critical radius* r_cr and the radius within which growth is limited by fragmentation is be called *fragmentation radius* r_f. In the limit $\Delta r \to 0$ we obtain the differential equation ($r \leq r_0$)

$$\frac{\partial p}{\partial r} = \frac{\varepsilon}{d} p \cdot \theta(r_\mathrm{cr}-r) + \frac{\partial p_\mathrm{f}(r)}{\partial r} \cdot \theta(r_\mathrm{f}-r) \tag{4.5}$$

with

$$p(r_0) := p(r_0, r_0) = 1,$$

i.e. the survival probability with spawn radius r_0 at r_0 is 1. The first argument of p is the current position and the second the spawn radius. With this model it is also possible to predict the chemical composition of planetesimals if the initial distribution of the most important chemical components is known. Then, $p(r_0, r_0)$ would be reduced by the mass ratio of a specific chemical component to the total mass of newly born particles. Therefore, we will explicitly use $p(r_0, r_0)$ throughout this Chapter, even though we are not considering chemistry here and the value is always unity. But if this model is used in order to predict chemical composition, one needs to take the relevant ice-lines into account. Even for the total traced mass ice lines can change the mass budget and thus should reduce the survival probability for the swarm—an effect that is ignored in this work for the sake of simplicity. If this effect is included, the models would have more different zones than Fig. 4.1 as the ice lines of different chemical species can be located within any of these zones in this figure. In addition, calculation of the dynamically changing chemistry is very complex and requires a code which calculates chemical evolution (e.g. Semenov et al., 2010; Semenov & Wiebe, 2011; Facchini et al., 2017; Booth & Ilee, 2019), see also Bergin (2009).

If the velocity v_d of the particles is known as a function of time, starting at the time of birth t_birth, when particles begin to move inward significantly, we can write:

$$r_0 - r_\mathrm{p} = -\int_{t_\mathrm{birth}}^{t} \bar{v}_\mathrm{r}(t')\,\mathrm{d}t' \tag{4.6}$$

with flux averaged radial particle velocity $\bar{v}_\mathrm{r}$ (see Eq. 4.9). That is, the place of birth for which particles are just reaching r_p within the time $t - t_\mathrm{birth}$ and contributing to planetesimal formation at r_p at the time t, is given by $r_0 = r_\mathrm{d}$. The birth time t_birth represents that due to fragmentation events, particles can stay at a local position for longer. Once those tiny dust grains have grown to pebble size at later times they drift inward. Alternatively, dust grains can get swept up by larger particles and join a pebble swarm that way. I.e., the time at which small grains transition to pebbles is given by t_birth. In this work we will use $t_\mathrm{birth} = 0$ by default.

The zone of planetesimal formation (see blue region in Fig. 4.1) lies within r_cr and is solely determined by the planetesimal formation condition. According to this condition, the edges of the planetesimal formation zone depend for a fixed radius exclusively on the pebble flux, which may vary with time. Since pebbles are reaching r_cr at the time t within the time span $t - t_\mathrm{birth}$, r_cr may depend also on t_birth or the birth place r_0. What counts is when a pebble swarm front is entering the zone inside of r_cr. Summing up these thoughts, we have $r_\mathrm{cr}(r_0, t)$

Particle growth is limited in the outer disk by drift (Birnstiel et al., 2012), where the drift limit is given by

$$\mathrm{St}_{\mathrm{drift}} \simeq \frac{1}{4}\sqrt{\frac{3\pi}{2}} \cdot Z \frac{v_{\mathrm{K}}^2}{c_{\mathrm{s}}^2} \left| \frac{\partial \ln P}{\partial \ln r} \right|^{-1} . \tag{4.7}$$

Here, P is the gas pressure in the mid-plane, c_{s} the isothermal sound speed, v_{K} the Keplerian velocity, and Z the particle-to-gas ratio $\Sigma_{\mathrm{d}}/\Sigma_{\mathrm{g}}$. The border between the PFFZ and PFZ, i.e. r_{f}, is where the dominant species in the fragmentation limit and the drift limit are equal to each other, i. e., at the position for which $\mathrm{St}_{\mathrm{drift}} = \mathrm{St}_{\mathrm{frag}}$ (see Eq. (C.43b) for a definition of the fragmentaiton limit $\mathrm{St}_{\mathrm{frag}}$).

We have to take into account that the mass of local material is reduced due to radial drift. The loss rate is proportional to the material that is still there over the timescale of removing this material. This timescale is assumed to be the drift timescale

$$\tau_{\mathrm{drift}}(r,t) = \frac{r}{\left|\bar{v}_{\mathrm{r}}(r,t)\right|}, \tag{4.8}$$

where we use the size distribution averaged radial velocity

$$\bar{v}_{\mathrm{r}}(r,t) = \frac{\int_{-\infty}^{\infty} v_{\mathrm{r}}(r,t)\sigma_{\mathrm{d}}(r,t)\,\mathrm{d}\ln a}{\int_{-\infty}^{\infty} \sigma_{\mathrm{d}}(r,t)\,\mathrm{d}\ln a} = \frac{\int_{-\infty}^{\infty} v_{\mathrm{r}}(r,t)\sigma_{\mathrm{d}}(r,t)\,\mathrm{d}\ln a}{\Sigma_{\mathrm{d}}(r,t)}. \tag{4.9}$$

Note that this expression also considers the growth phase since the size distribution of the simulation output is used. Following the idea of treating the system of different populations in terms of simple differential equations (see e.g. Gerbig et al., 2019), we estimate the loss of initial local material as

$$\frac{\mathrm{d}\Sigma_{\mathrm{peb}}}{\mathrm{d}t} = \frac{\Sigma_{\mathrm{peb}}}{\tau_{\mathrm{drift}}}, \tag{4.10}$$

leading to the solution

$$\Sigma_{\mathrm{peb}}(r,t) = \Sigma_{\mathrm{peb}}(r,t_0) \cdot \exp - \int\limits_0^t \frac{\mathrm{d}t'}{\tau_{\mathrm{drift}}(r,t)}. \tag{4.11}$$

However, this is just an approximation for a drift limited region. Once material enters a fragmentation limited region, radial transport of deposited mass is slowed down significantly. This is due to the fact that per definition growth is faster than drift in a fragmentation limited region. Modeling a mean growth timescale, however, is very challenging as there are many ways for a tiny dust grain to grow up to pebble size again. E.g. via continuous monodisperse growth, sweep-up by the largest particles, or any combination of particle sizes available (see e.g. Birnstiel et al., 2011). Hence, it is very difficult to calculate the mass contribution to a drifting pebble swarm without actually tracing the particles with different origins in the numerical simulation. E.g., Misener et al. (2019) illustrate the interplay between local coagulation, fragmentation, and drift for both individual particles and swarms of particles.

In a drift limited region, material that was drifting away cannot be caught up. If particles are inside of a fragmentation limited region, material originating from further out that was deposited there via fragmentation events can join a pebble swarm passing that region later. Since we use the flux averaged radial velocity that considers the evolution of the size distribution (Eq. (4.9)), the slower effective radial motion of the pebble swarm front is taken care of, even though it might not be a complete model. Birnstiel et al. (2012) found that for a simplified model with only a slowly drifting and a significantly drifting particle population, assuming a ratio between those populations of 0.75 in fragmentation limited regions reproduces roughly the results from simulations that use multiple particle masses. Hence, it is possible to assume that in a situation in which particles are locally well-mixed with respect to their origins that 75% of the deposited mass can join pebble swarms passing by. However, drift and radial diffusion can change the situation significantly. For simplicity, we assume that the entire deposited mass can join the pebble swarm. Since the transport of material in the fragmentation limited regions is both challenging and would make the model very complicated, we will instead assume that the mass that can contribute to a pebble swarm is proportional to Eq. (4.11). In Appendix C.1, we show that the sweep-up timescale of tiny fragments is longer than the timescale of planetesimal formation. In this study, a decrease of the survival probability due to fragmentation effects is not considered but we suggest an approach how to mimic this effect in Appendix C.2.

To solve the problem of tracing material for planetesimal formation within our simple model, we follow the following recipe:

1. As a first step one needs to choose a birth time t_{birth} after which particles are allowed to join pebble swarms. By default, this time is set to zero. With help of the flux averaged radial velocities from the simulation output, one can calculate for a given r_{p} the maximum distance of origin r_{d}, see Eq. (4.6). Now the intersection radius and time of this pebble swarm with origin r_{d} with r_{cr} (and potentially r_{f}) can be determined.

2. Secondly, we determine the integrals in (C.51b) or (C.51d) to obtain the survival probabilities $p(r_{\mathrm{p}}, r_0)$ for any given radius of planetesimal formation r_{p} at time t starting from any birth place r_0.

3. The mass that can contribute at the time a pebble swarm reaches the position r_0 is modeled by a line density (mass per radial extent)

   $$2\pi r_0 \Sigma_{\mathrm{peb}}(r_0) := 2\pi r_0 \Sigma_{\mathrm{peb}}(r_0, t_{\mathrm{pass}}), \tag{4.12}$$

   where Eq. (4.11) is used and $t_{\mathrm{pass}}(r_0, r_{\mathrm{d}})$ is the time at which a pebble swarm starting from r_{d} is reaching r_0.

4. We are now able to calculate the *normalization constant* C according to

   $$1 \overset{!}{=} C \int_{r_{\mathrm{p}}}^{r_{\mathrm{d}}} 2\pi r_0 \Sigma_{\mathrm{peb}}(r_0) p(r_{\mathrm{p}}, r_0)\, \mathrm{d}r_0. \tag{4.13}$$

5. With knowledge of C, we finally obtain the *cumulative probability function* ($r_{\mathrm{p}} \le r \le r_{\mathrm{d}}$)

   $$F(r_{\mathrm{p}}, r) \ := 1 - C \int_{r}^{r_{\mathrm{d}}} 2\pi r_0 \Sigma_{\mathrm{peb}}(r_0) p(r_{\mathrm{p}}, r_0)\, \mathrm{d}r_0. \tag{4.14}$$

Eq. (4.14) gives the mass fraction that contributes to a planetesimal formed at radial position r_{p} at time t with origins in the range $r_{\mathrm{p}} \le r \le r_{\mathrm{d}}$, i.e. between the position of interest (r_{p}) and the maximum distance that pebbles were able to drift inward within the given time $t - t_{\mathrm{birth}}$ (from r_{d} to r_{p}). This cumulative function can be calculated for both different times and planetesimal formation radii.

4.3 Results

In this section we analyze two different simulations. Simulation S1.1 is a case where the drift limited region in the outer disk growths inward until the entire disk is drift limited. Another focus of our analysis is the case of a mostly fragmentation limited disk (simulation S2.1). Since the results depend on the time of evolution, we highlight the case of $t = 3.6 \cdot 10^5$ yr around which the the majority of planetesimals is formed (Lenz et al., 2019). In the Appendix we analyze also the cases of different times and higher planetesimal formation efficiencies. The simulations are taken from Chapter 3 and the disk parameters are summarized in Tab. 4.1. These simulations include gas mass loss due to photoevaporation, viscous disk spreading, particle evolution (growth, fragmentation, and radial transport), and planetesimal formation. Note that the initial setup of these simulations was chosen such that the density of particles with Stokes numbers larger than $\mathrm{St} = 10^{-4}$ are set to zero to avoid an inward moving particle wave. This implies that the maximum radius of origin is not the last radial bin but the one at which the particle-to-gas ratio is set to zero.

4.3.1 Feeding zones at a given time

Disk with developing drift limited region: Simulation S1.1

Fig. 4.2 shows different trajectories of pebble swarm fronts calculated via data on radial velocities and densities provided by the simulation output (see also e.g. Krijt et al., 2016b), i.e. Eq. (4.9). Also shown are the disk radius r_{cr} within which planetesimals can be formed, i.e. a critical pebble flux is reached and $t > \tau_{\mathrm{f}}$, and the outer edge of the

Table 4.1: Parameters of the presented simulations. We present the values for the conversion length ℓ via the efficiency parameter $\varepsilon := 5h_\mathrm{g}/\ell$. For all simulations presented in this work we use $r_\mathrm{c} = 20\,\mathrm{au}$, $\gamma = 1$, $Z_0 = 0.0134$, and $L_\mathrm{X} = 10^{30}\,\mathrm{erg\,s^{-1}}$. For all simulations α_t is used for the turbulent viscosity, vertical and radial diffusion, as well as for collision speeds of particles. The simulations only use radiation heating, i.e. accretion heating is not included but should only affect the regions within $\sim 3\,\mathrm{au}$.

name	M_disk $[M_\odot]$	v_f $[\mathrm{m\,s^{-1}}]$	τ_f $[t_\mathrm{orb}]$	α_t	ε
S1.1	0.05	10	300	10^{-3}	0.1
S1.2	0.05	10	300	10^{-3}	1.0
S2.1	0.10	1	1000	10^{-4}	0.03
S2.2	0.10	1	1000	10^{-4}	1.00

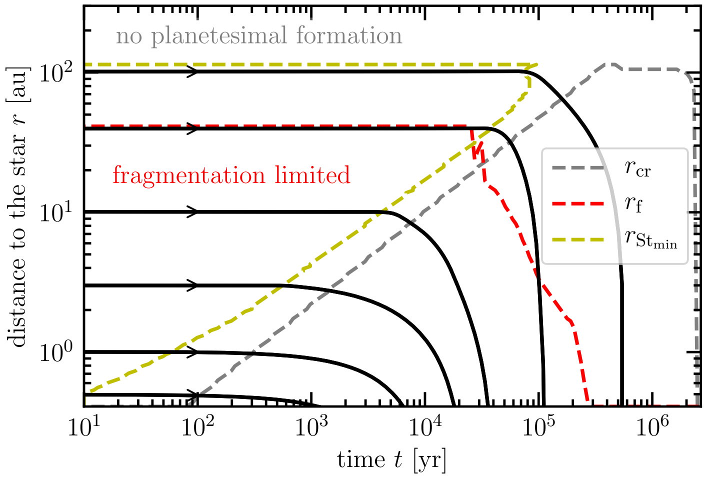

Figure 4.2: Solid lines show the pebble swarm front trajectories for different locations of origin. For the radial velocity the size distribution averaged value was used. Hence, the initial growth phase is included and can be identified by the time over which solid lines are horizontal. For this plot, data from simulation S1.1 was used.

fragmentation limited region r_f. For origins further away from the star, pebble swarms spend only a small amount of time in the inner disk regions compared to the total time of moving radially inward before ending up in the star, getting evaporated, or forming planetesimals. The yellow dashed line shows the time-radius relation $r_{\mathrm{St}_\mathrm{min}}(t)$ at which the peak of the size distribution first reaches a Stokes number of $\mathrm{St}_\mathrm{min} = 0.01$. The time difference between $r_{\mathrm{St}_\mathrm{min}}(t)$ and $r_\mathrm{cr}(t)$ is either the time the pebble flux needs to build up or or represents the additional time needed for traps to form (parameterized via the trap formation time τ_f) after pebbles (defined as $\mathrm{St}_\mathrm{min} \leq \mathrm{St} \leq \mathrm{St}_\mathrm{max}$ particles) have formed.

Fig. 4.3 illustrates the line density $2\pi r \Sigma_\mathrm{peb}(r_0)$ that is used as the potential mass that can join an inward moving pebble swarm. For this, the fraction of masses at different radii matters, not the total value, because we are interested in the relative mass contribution only. The blue line shows the initial line density before particles were allowed to grow and/or move. This curve would overestimate the masses in the inner regions as a fraction of this mass is drifting inward while a pebble swarm from the outer regions moves inward as well. At the time the pebble swarm front reaches radii further in, a significant amount of mass of *local origin* will not be present anymore. We model this effect via Eq. (4.12) and show two examples as blue dashed and blue dotted lines in Fig. 4.3. For the dashed and dotted blue lines only the radial range that a pebble swarm contributing to planetesimal formation at r_p was moving through is shown. Note that each point of these curves are taken at the time the pebble swarm is passing by. I.e. for radii further in there was more time for particles to drift away. For later times, these lines shift toward larger radii and show lower potential density contributions at all locations compared to previous times. Already from these two examples at $r_\mathrm{p} = 3\,\mathrm{au}$ and $40\,\mathrm{au}$, without taking the survival probabilities into account, we conclude that the majority of mass in the inner disk

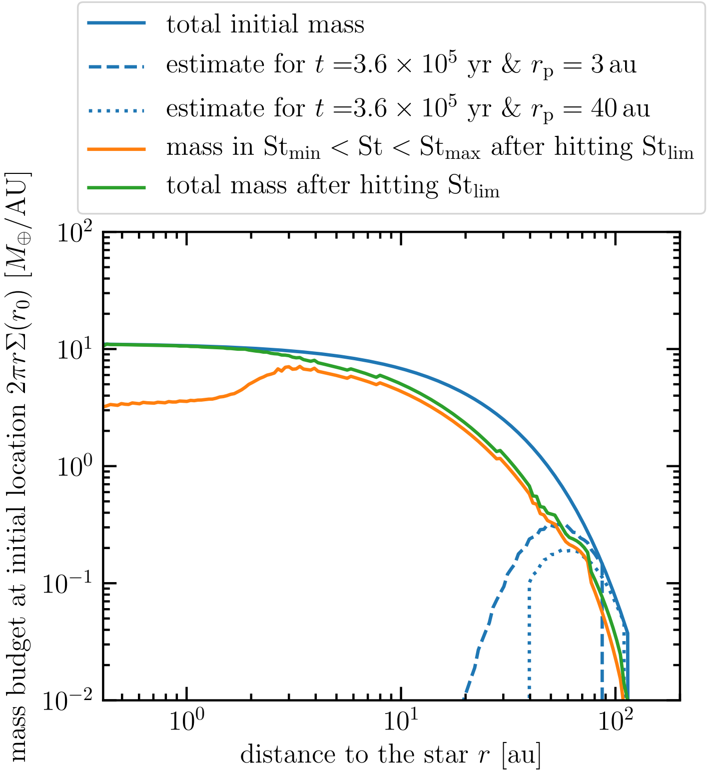

Figure 4.3: Different line densities (mass per radial extent) are shown. The blue solid line shows the initial line density of all particles. The dashed blue and dotted blue lines represent the potential mass contribution to a pebble swarm that formed planetesimals at the time $t = 3.6 \cdot 10^5$ yr at positions $r_\mathrm{p} = 3$ au and 40 au, respectively. These two lines were computed via Eq. (4.12) and are used to estimate the remaining local material at the time a pebble swarm reaches a certain location. Locations that do not contribute to planetesimal formation at r_p at the given time are set to zero. The orange and green lines show the line densities after particles have grown to their size limit and reached size distribution equilibrium. The orange lines takes only particles in the range $0.01 = \mathrm{St_{min}} \leq \mathrm{St} \leq \mathrm{St_{max}} = 10$ into account whereas the green line considers all particles. For this plot, data from simulation S1.1 was used, see Tab. 4.1 for parameters. $\alpha_\mathrm{t} = 10^{-3}$, $\varepsilon = 0.1$.

regions consists of material that originated from the outer disk.

We assume that the growth timescale of the largest particles is given by (Birnstiel et al., 2012)

$$\tau_\mathrm{grow} \approx \frac{1}{Z\Omega}. \tag{4.15}$$

The green and orange lines in Fig. 4.3 display the line density at three growth timescales later after the mass bin with highest density hits the growth limit $\mathrm{St_{lim}} = \min\left\{\mathrm{St_{frag}}, \mathrm{St_{drift}}\right\}$ to ensure that equilibrium for the size distribution is reached. I.e. the shown line densities at different radii correspond to different times where these times are shorter for the inner and larger for the outer radii due to growth timescales increasing with radius. The orange line only takes particles in the range $10^{-2} = \mathrm{St_{min}} \leq \mathrm{St} \leq \mathrm{St_{max}} = 10$ into account whereas the green line includes all particles. The orange line is linked to the potential mass that could form planetesimals in situ if the pebble flux is critical at the times particles hit the growth barriers and particle trapping can happen (but it is not, see e.g. the time difference between the yellow dashed and gray dashed line in Fig. 4.2).

Following the recipe listed at the end of Sec. 4.2, the feeding zones for different planetesimal formation radii can be computed. The term "feeding zone" is not strictly defined and depends on a subjective value. Hence, we will show different percentages of mass contribution. Therefore, we define the feeding zone as the radius within which a certain percentage $0 \leq y \leq 100$ of contributed mass is originating from:

$$x_{y\%} := \text{radius for which } F(r_\mathrm{p}, x_{y\%}) = y\%. \tag{4.16}$$

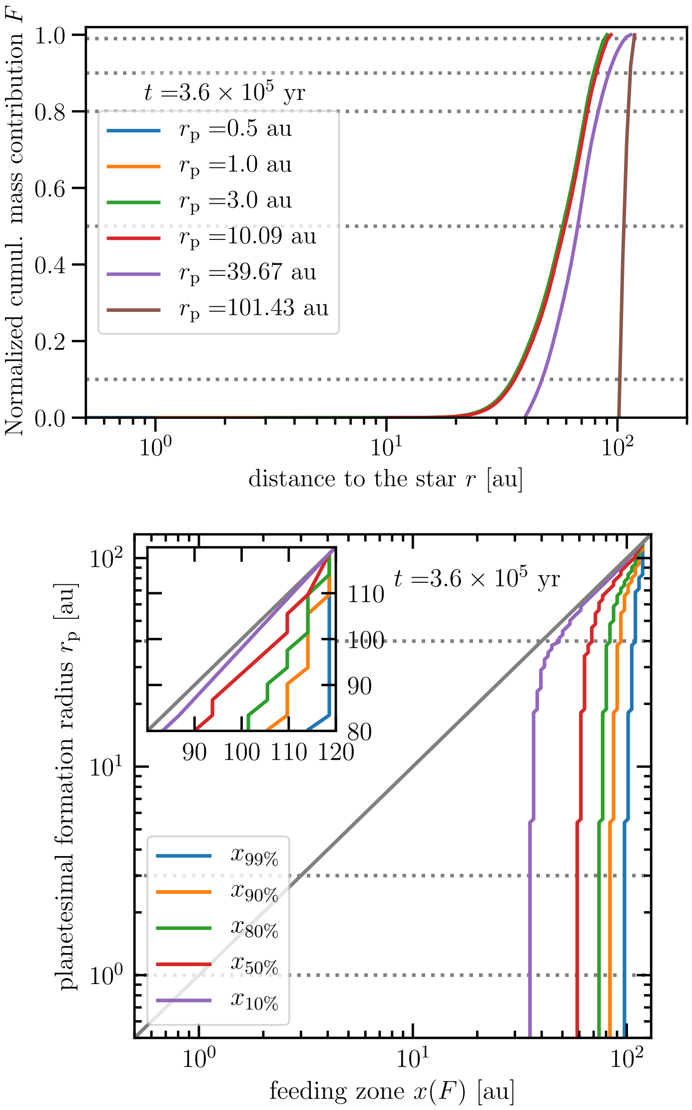

Figure 4.4: *Top panel*: Normalized cumulative mass contribution to planetesimals formed at different radii r_p at $3.6 \cdot 10^5$ years. All lines are cut off once they reached a value of one since this shows the position of maximum origin for the given time. *Bottom panel*: For each disk radius r_p at which planetesimals are forming (ordinate) at time $t = 3.6 \cdot 10^5$ years different feeding zones are shown. E.g., the purple line shows the radius within which 10% of planetesimal forming material at r_p originates from and the blue line shows within which 99% comes from, see Eq. (4.16). The diagonal gray line would correspond to in situ formation of planetesimals. This plot used data from simulation S1.1, see Tab. 4.1.

Note that the feeding zone alone does not provide information on the formation rate or total amount of planetesimals formed with a specific feeding zone.

Fig. 4.4 shows in the top panel the cumulative mass contribution to planetesimals formed at the time $t = 3.6 \cdot 10^5$ yr at different radii r_p. The bottom panel displays for all radii at which planetesimals are formed where a given percentage of mass originates from.

In Fig. 4.4 one can see that, regardless of which percentage is chosen, the feeding zones are almost identical within a given radius of $r_p \approx 30$ au. Feeding zones in the outermost parts have to become more local due to the fact that only little mass is there originally and we were cutting off the particle densities initially where particles reached $\mathrm{St} > 10^{-4}$. But even without such a cut off a similar result is expected, potentially with a little bit more extended feeding zones in these outermost disk regions.

In this simulation, growth is limited by drift except in the very inner regions ($\lesssim 1$ au). Very fast drift that is not

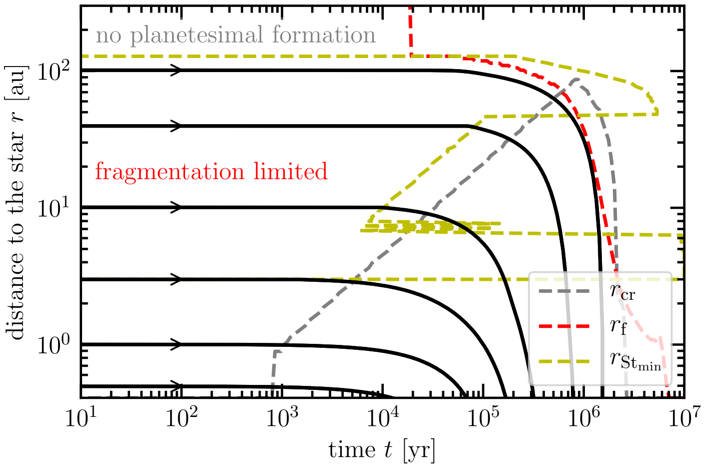

Figure 4.5: Solid lines show the pebble swarm front trajectories for different locaitons of origin. For the radial velocity the size distribution averaged value was used, see Eq. (4.9). Hence, the initial growth phase is included and can be identified by the time over which solid lines are horizontal. We have chosen $t = 3.6 \cdot 10^5$ yr as the time of planetesimal formation since it is typically very active at this time and also occurs over a wide region. The yellow line shows jumps within ≈ 7 au that are caused by size distributions at the given distances that barely reach St = 0.01 (see Fig. 3.6). For this plot, data from simulation was used S2.1

slowed down via fragmentation events leads to small retention times. This effect combined with rather high survival probabilities (low ε) leads to (1) large feeding zones for planetesimals forming at $r_{\mathrm{p}} \lesssim 40$ au and (2) the same feeding zones within that region. These results can be expected by looking at Fig. 4.2. If for a chosen time of planetesimal formation, here $t = 3.6 \cdot 10^5$ yr, the trajectories are very steep (i.e. almost vertical), particles do not spend much time at a given location before they are removed by radial drift. The result is a particle population that was transported inward from the outer regions but contains only a small amount of mass that originates from the vicinity.

Mostly fragmentation limited disk: Simulation S2.1

In this section, we show the same kind of figures that were presented in the previous section but now for a simulation where the disk is mostly limited by fragmentation, see disk parameters of simulation S2.1 in Tab. 4.1.

Fig. 4.5 is the same as Fig. 4.2 but for simulation S2.1. A crucial difference between the two is the much larger fragmentation limited region for simulation S2.1. The fragmentation limit scales quadratically with the fragmentation speed v_{f} but inversely linear with the turbulence strength parameter α_{t}, see Eq. (C.43a). This implies that a pebble swarm front needs much more time before the innermost radial bin is reached. The yellow dashed line ($r_{\mathrm{St_{min}}}(t)$) has jumps for $r \lesssim 10$ au because the peak in the size distribution either barely or never reaches $\mathrm{St_{min}}$.

Fig. 4.6 shows the different line densities that were already discussed in the previous section but for simulation S2.1. Two big qualitative differences for the blue dashed and dotted lines compared to Fig. 4.3 can be identified: First, the green line is much closer to the blue line (initial condition) which is a result of much slower size distribution averaged radial drift. Secondly, the blue dashed and dotted lines reveal already that larger feeding zones compared to simulation S1.1 can be expected. The line densities at the initial snapshot look similar (blue solid lines in both Figures) and differences stem from different initial disk masses only, the green and orange curves look very different due to different drift speeds and maximum Stokes numbers. While a swarm of pebbles is drifting inward the swarm will change composition with respect to material origins. This can be illustrated via the pebble swarm fraction, i.e. the normalized contribution to a pebble swarm, that can be computed via ($r_{\mathrm{p}} \leq r \leq r_{\mathrm{d}}$)

$$f_{\mathrm{peb}}(r_0, r) := \frac{\int_{r_0}^{r_{\mathrm{d}}} 2\pi r_0' \Sigma_{\mathrm{peb}}(r_0') p(r, r_0') \, \mathrm{d}r_0'}{\int_{r}^{r_{\mathrm{d}}} 2\pi r_0' \Sigma_{\mathrm{peb}}(r_0') p(r, r_0') \, \mathrm{d}r_0'}, \tag{4.17}$$

where the starting position of the pebble swarm r_{d} depends on the position (r_{p}) and time of planetesimal formation. Since this is a normalized expression, a value of f_{peb} close to unity means that a region of origin dominates the mass

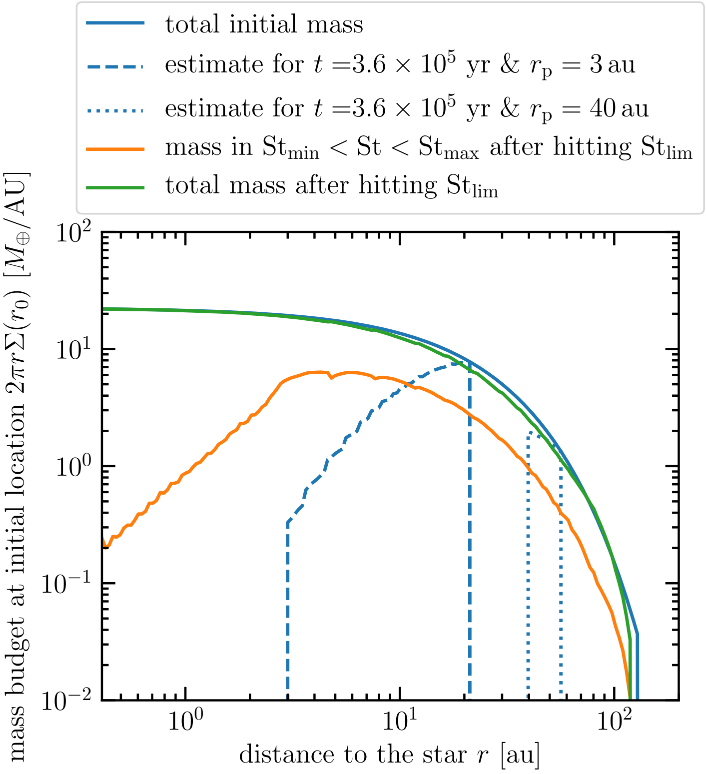

Figure 4.6: The same as Fig. 4.3 but for simulation S2.1.

in a pebble swarm whereas a value close to zero implies that those regions do not significantly contribute. Fig. 4.7 illustrates an example case for a swarm that forms planetesimals at $r_\mathrm{p} = 3$ au after $t = 3.6 \cdot 10^5$ yr for simulations S2.1 and S2.2. The latter simulation used a much higher planetesimal formation efficiency leading to smaller feeding zones. In both panels one can see that while the swarm is drifting inward, new material that originates further in is mixed in. If drift was fast enough to remove most of the original mass in the inner disk regions, the swarm will quickly consist of mostly material that came from the outer regions. This effect can be seen in the upper panel of Fig. 4.7 as the mass that stems from the yellow and black regions (i.e., originally coming from outside of ∼ 15au) provides 50% of the mass when $r_\mathrm{p} = 3$ au is reached whereas mass from further in contributes less and less.

However, for higher planetesimal formation efficiencies much more mass is dropping out due to planetesimal formation on its way to r_p. As a result, mass originating from regions much closer to r_p contribute more (see bottom panel of Fig. 4.7). In general, for later times the pebble swarm fraction will be dominated more by mass with origins further away from r_p and also the width of the feeding zone will spread out.

Fig. 4.8 illustrates different feeding zones for planetesimals formed at time $3.6 \cdot 10^5$ yr in the simulation. The top panel displays the normalized cumulative mass contribution to planetesimals formed at different positions r_p. The steeper these curves are the more mass is coming from the respective regions. Very steep curves such as the purple line imply that all the material forming planetesimals at 40 au originate from a very narrow region in the disk.

The lower panel in Fig. 4.8 shows the origin of the innermost 10%…99% mass contributions for each planetesimal formation radius r_p. Slower effective radial velocities in the much larger fragmentation limited disk region compared to simulation S1.1 allow local material to survive long enough to contribute significantly to planetesimal compositions. Hence, the presented feeding zones are significantly smaller compared to simulation S1.1, see lower panel of Fig. 4.4.

In those cases where most of the mass comes from regions outside the water ice line (∼ 3 au), planetesimals formed within the water ice line do not imply that the formed planetesimals are very water rich. When particles drift inside the water ice line they lose water (e.g. Cuzzi & Zahnle, 2004; Drążkowska & Alibert, 2017; Schoonenberg et al., 2018), especially if growth is fragmentation limited because protecting water ice in the particles interior from getting evaporated becomes much less likely. However, again we would like to emphasize that proper ice lines (including evaporation and desublimation effects) are not included in either the simulations or the analytical model presented in

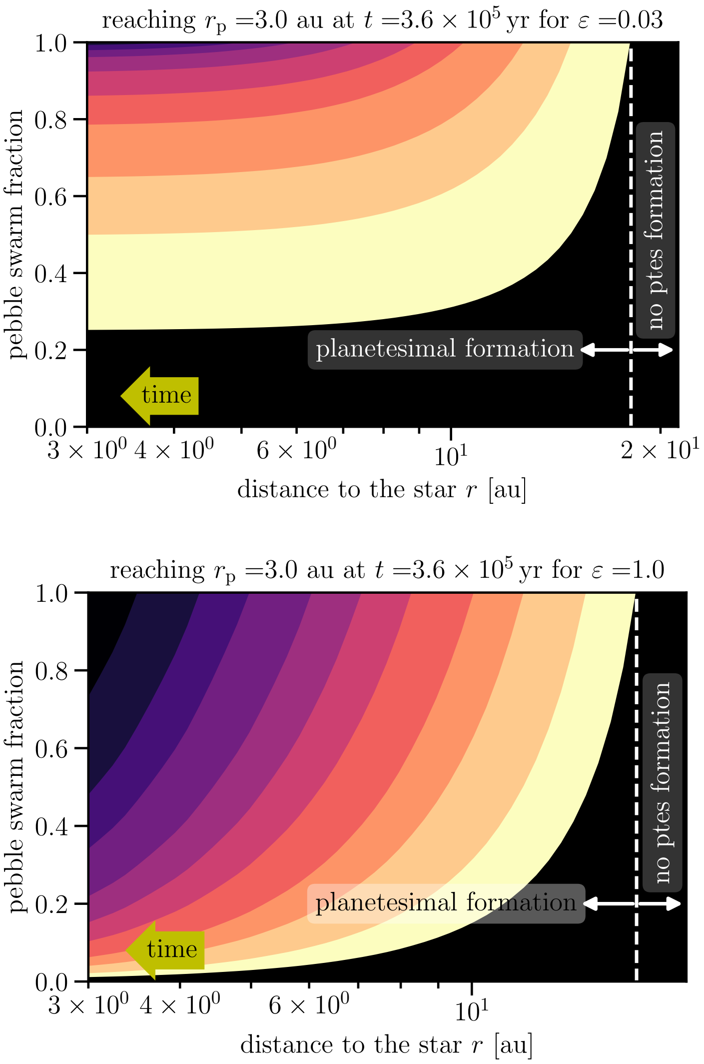

Figure 4.7: Pebble swarm fraction of a swarm moving inward. Positions further to the left correspond to later times. The mass contribution at each radial position of the swarm is normalized to the total mass of the swarm. A pebble swarm is traced that forms planetesimals at $r_p = 3\,\text{au}$ after $t = 3.6 \cdot 10^5\,\text{yr}$ of evolution. The upper panel shows the result of simulation S2.1 ($\varepsilon = 0.03$) and the lower panel of simulation S2.2 ($\varepsilon = 1$). Logarithmical equidistant interval contributions are shown, distinguishable by colors: particles born within the planetesimal formation zone (PFZ) are located to the left of the vertical dashed line. Particles born in the pure drift zone (PDZ) to the right of the vertical dashed line are shown in black. While the swarm drifts inward it accumulates pebbles born further inside. This plot is discussed in the text after Eq. (4.17).

this work.

How the feeding zones are changing for different times of disk evolution and smaller pebble-to-planetesimal conversion lengths ℓ is discussed in Appendix C.4.

4.3.2 Linking feeding zones and planetesimal population masses

So far, we were only looking at the origin of mass forming planetesimals at different positions r_p at a given time. However, this information has to be linked to the local planetesimal production. I.e., instead of looking at one snapshot in time (so far $3.6 \cdot 10^5$ yr), we will adding planetesimals that formed at different times at the same location. After the pebble flux becomes sub-critical, planetesimal formation stops and the planetesimals produced during that time will have different feeding zones. The question remains how much of the local planetesimal population mass originated

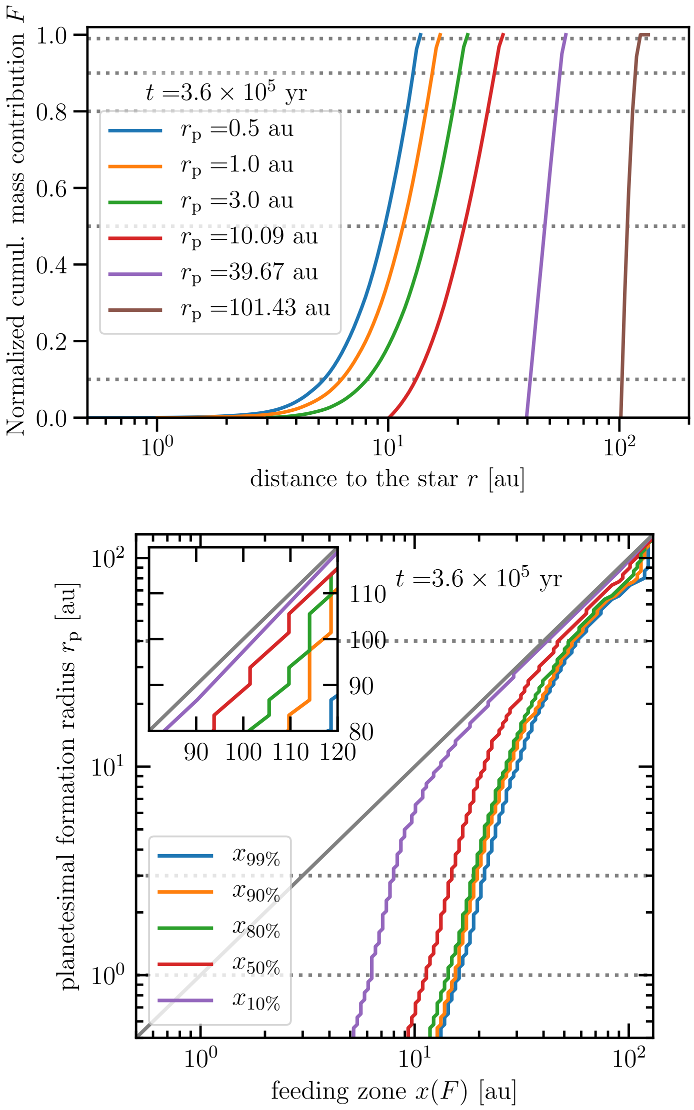

Figure 4.8: The same plot as Fig. 4.4 but for simulation S2.1. A much larger fragmentation limited region compared to simulation 2.1 that prolongs for a long time leads to smaller feeding zones compared to simulation in which the disk is mostly drift limited (e.g. S1.1).

from the vicinity and how much came from far away.

We sort the pebbles by their origin. We call, e.g., CO pebbles those, which originated in a region that contained CO in frozen form etc.. We can not model the effects of the ice lines onto the pebbles, yet we can show that this is vital for any future study, because a significant percentage of the material incorporated into the asteroid belt started with coagulation beyond 9 au or even beyond 20 au. The study we present investigates the origin of asteroid material and Earth forming material.

For later comparison, Fig. 4.9 shows the initial cumulative particle mass in different regions. As we are not interested in radii smaller than 1 au, only particle mass beyond that is considered. The purple region will be called silicate region, the blue H_2O region, the green CO_2 region, and the yellow CO region. The locations of the water ice line (≈ 3 au), CO_2 ice line (≈ 9 au), and CO ice line (≈ 20 au) are taken from Öberg et al. (2011). Fig. 4.9 shows that initially around 40% of the solid mass is in pebbles with CO in frozen form (yellow). Roughly 25% is initially both in CO_2 (green) and H_2O (blue) pebbles and around only 10% in pure silicates (purple).

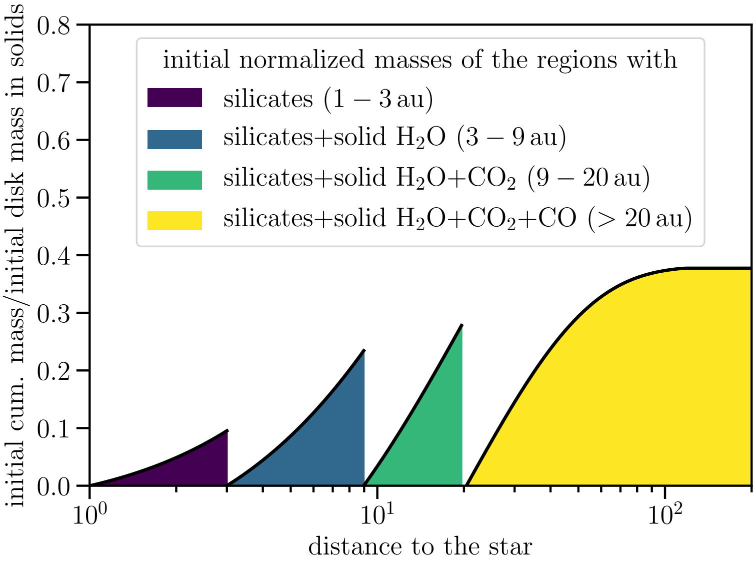

Figure 4.9: Cumulative initial masses in regions from 1 – 3 au (silicates), 3 – 9 au (silicates and water ice), 9 – 20 au (silicates, water ice, and CO_2 ice), and ≥ 20 au (silicates, water ice, CO_2 ice, and CO ice). All values are normalized to the total initial mass in the region beyond 1 au.

Disk with developing drift limited region: Simulation S1.1

Fig. 4.10 shows the mass fraction with origins inside the water ice line (purple), between the water and CO_2 ice line (blue), between the CO_2 and CO ice line (green), and beyond the CO ice line (yellow) as a function of formed local planetesimal mass normalized to their final values for four different locations of planetesimal formation r_p. Any vertical line in this plot corresponds to a different time and shows the normalized distribution of material origins in the local pebble swam from which planetesimals are formed. The time needed to reach sub-critical pebble fluxes is a few million years. However, 90% of the local planetesimal population is formed already after $\approx 10^5$ yr. Since the disk is mostly limited by drift, particles drift inward very fast and the planetesimal feeding zones grow rapidly, leading to significant mass contributions from the outer disk regions. For $r_\mathrm{p} = 2$ au the mass averaged contribution from the pure silicate (purple) and water ice regions (blue) changes significantly compared to $r_\mathrm{p} = 1$ au, where less mass originates from the former and more from the latter, mostly due to the initial mass that is available in those regions initially (e.g. around 50% less mass from the purple region of Fig. 4.9 between 2 – 3 au compared to 1 – 3 au). For r_p further out, here 3 au and 10 au planetesimal forming material originates from even further out, both as a function of time and for the mass average of the local planetesimal population (bar on the right of each panel in Fig. 4.10). The timescales for planetesimal formation are roughly the same for all four presented r_p because, again, the major parts of the disk are limited by drift.

At $r_\mathrm{p} = 1$ au (top left panel in Fig. 4.10) the first 20% of planetesimals are exclusively made of material with origins inside the water ice line but on average the final population consists of 35.75% with those origins. Almost 18% of the mass was passing three different ice lines on its way to $r_\mathrm{p} = 1$ au. However, for the last 10% of planetesimals formed at the four presented r_p, almost the entire pebble swarm crossed the ice lines of CO, CO_2, and water.

Now that we understand the results for different positions of planetesimal formation, one could ask what the influence of the planetesimal formation efficiency is. Larger planetesimal formation efficiencies ε lead to both smaller feeding zones and shorter timescales for planetesimal formation, leading to higher average contributions to planetesimals from regions nearby r_p. Fig. 4.11 shows the mass averaged final contributions to planetesimals as a function of planetesimal formation efficiency at the same four locations as in Fig. 4.10. Here, five different efficiency values ($\varepsilon = \{0.01, 0.03, 0.1, 0.3, 1\}$) are used. These simulations were already presented in Chapter 3.

The mass weighted contributions for the different regions of origin for all four presented distances are very similar for low planetesimal formation efficiencies ($\varepsilon = 0.01$ and 0.03) but change dramatically for high $\varepsilon \sim 1$. For the case of $\varepsilon \sim 1$, around $\gtrsim 90\%$ of the mass was not crossing a single ice line before reaching r_p, at least between $r_\mathrm{p} = 1$ au and 10 au. On the other hand, for $\varepsilon \lesssim 0.1$ more than roughly 50% of the mass was crossing at least one ice line before

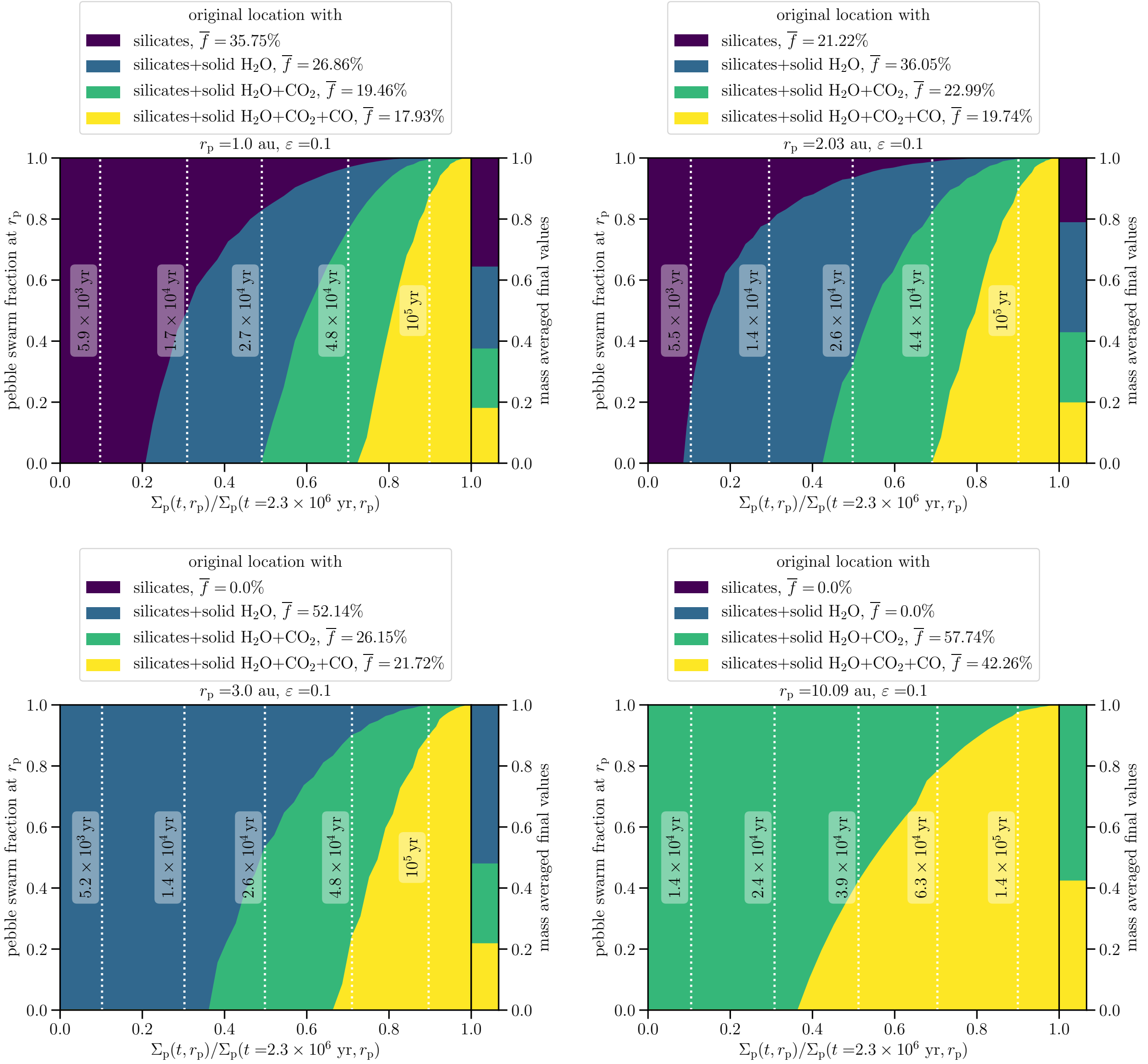

Figure 4.10: Distribution of material origins from the four different regions shown in Fig. 4.9 as a function of time dependent local planetesimal mass normalized by the final mass in planetesimals, where the time at which the final value is reached is given as argument in the normalization factor. The label of the ordinates "pebble swarm fraction" means that the different colors show the contribution of their respective origins to a pebble swarm at r_p at a given time. Shown are four different locations of planetesimal formation r_p: 1 au (top left panel), 2 au (top right panel), 3 au (lower left panel), and 10 au (lower right panel). In the legends, $\overline{f}$ is the respective contribution to the mass averaged final values shown as bars attached to the right of each panel. This plot displays the results for simulation S1.1, see Tab. 4.1. Vertical dotted lines show different times.

forming planetesimals at the respective r_p. For r_p = 1 au and 2 au $\gtrsim 20\%$ of this mass was even moving through all three ice lines of CO, CO_2, and H_2O.

Mostly fragmentation limited disk: Simulation S2.1

For a mostly fragmentation limited disk the interpretations are not as straight forward as it is for the mostly drift limited disks. Slower average drift allows longer timescales for planetesimal formation (e.g. compare the times at which 90% of the local planetesimal mass is formed in Figs. 4.10 and 4.12). This allows for more distant origins. On the other

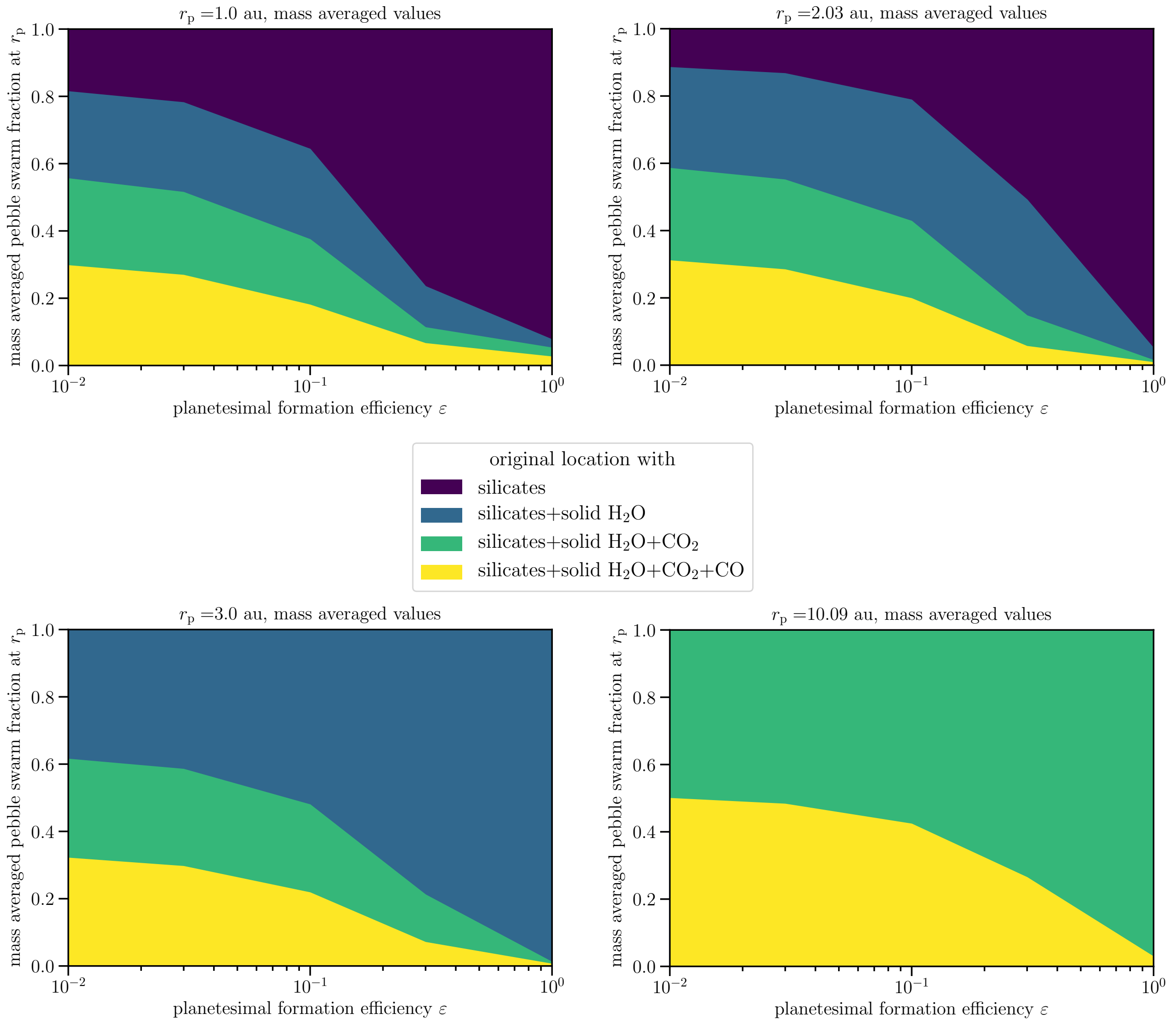

Figure 4.11: Mass averaged contributions to planetesimals formed at different r_p with the different origins presented in Fig.4.9 as a function of planetesimal formation efficiency ε. This efficiency parameter is defined via the conversion length ℓ such that $\varepsilon := 5h_g/\ell$. Since the model assumes that pebble traps build up and vanish on a timescale proportional to the local orbit time, a value of $\varepsilon = 1$ does *not* mean that all the local pebble mass is immediately transformed into planetesimals. The presented results are based on simulations with setups identical to simulation S1.1 and S1.2 (see Tab. 4.1) but for $\varepsilon = \{0.01, 0.03, 0.1, 0.3, 1\}$.

hand, more local material "survives" drift for longer due to fragmentation events that lead to continuous replenishment of small slowly drifting particles which favors smaller feeding zones.

Fig. 4.12 shows the mass contribution to a pebble swarm at different r_p with origins outside of three different ice lines (water, CO_2, and CO) as a function of the percentage of initial planetesimals formed. For $r_p = 1$ au the feeding zone is stretching out too slowly to allow significant contributions from regions outside the CO ice line (yellow). Although the first ~ 15% of initial planetesimals were made of material that did not pass one of the presented ice lines, after local planetesimal formation stopped particles originating within the water ice line contribute ~ 30% to the final local planetesimal population. At $r_p = 2$ au and 3 au the contribution from regions outside the CO ice line is significant ($\approx 7\%$) even though these particles are incorporated in planetesimals that formed later (after $\sim 4 \cdot 10^5$ yr). In general, the most planetesimals contain material that passed at least one or even up to three of the presented different ice lines for all four presented locations. Hence, the radial motion of pebbles cannot be neglected for the interpretation of asteroid compositions (see also Fig. 4.10 in the previous section where the contribution from more distant regions

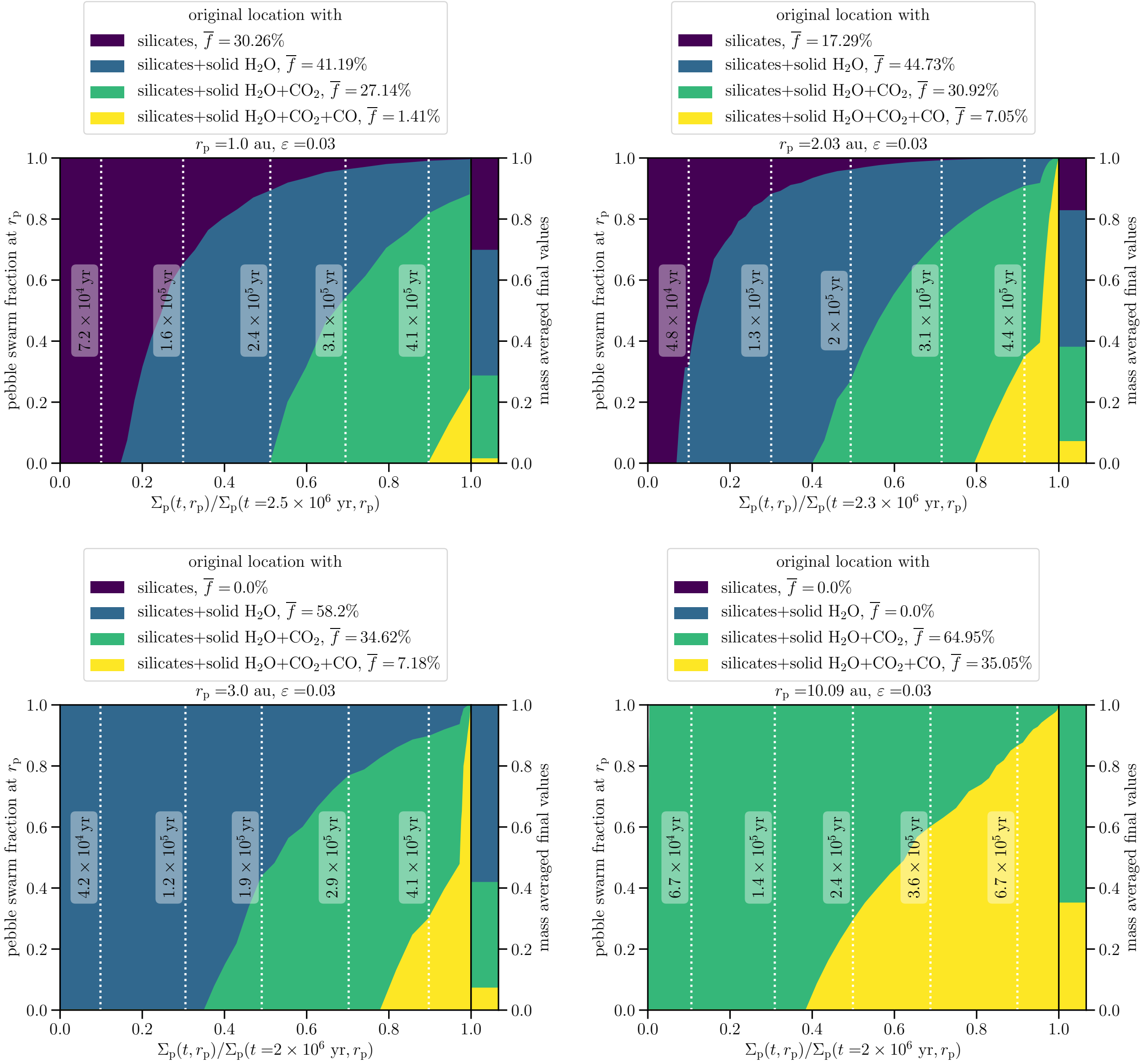

Figure 4.12: The same as Fig. 4.10 but for simulation S2.1, see Tab. 4.1.

is even more pronounced).

So far we have analyzed the time evolution and mass average of the contribution to planetesimals of our preferred regions of origin. How the mass averaged contribution of these different regions of origin changes with larger or smaller conversion lengths ℓ, i.e. smaller or larger ε, is shown in Fig. 4.13.

Interestingly, the mass averaged contribution from particles originating outside the CO ice line (shown in yellow) is not declining monotonically with ε. Instead, a peak can be identified around $\varepsilon \approx 0.1$ for $r_p \sim 1 \ldots 3$ au. This peak does not show up for the mostly drift limited simulations, see Fig. 4.11. The reason for this peak is a longer timescale over which most of the local planetesimal mass is formed, allowing for wider feeding zones. The peak feature shows up around the value of ε where the timescale of drift and planetesimal formation are about the same value (see Fig. 3.4). This peak does not show up for the mostly drift limited simulations as the time particles stay at a given disk radius is much shorter. To the right of the peak the contributions become more local as expected. However, very high planetesimal formation efficiencies ε seem to be unlikely for the Solar Nebula as these lead to too much mass in the region of the cold classical Kuiper belt (Chapter 3). Roughly speaking, a significant amount of the final planetesimal population mass moved through up to three of the major ice lines for $\varepsilon \gtrsim 0.3$ before forming planetesimals at $r_p \lesssim 10$ au.

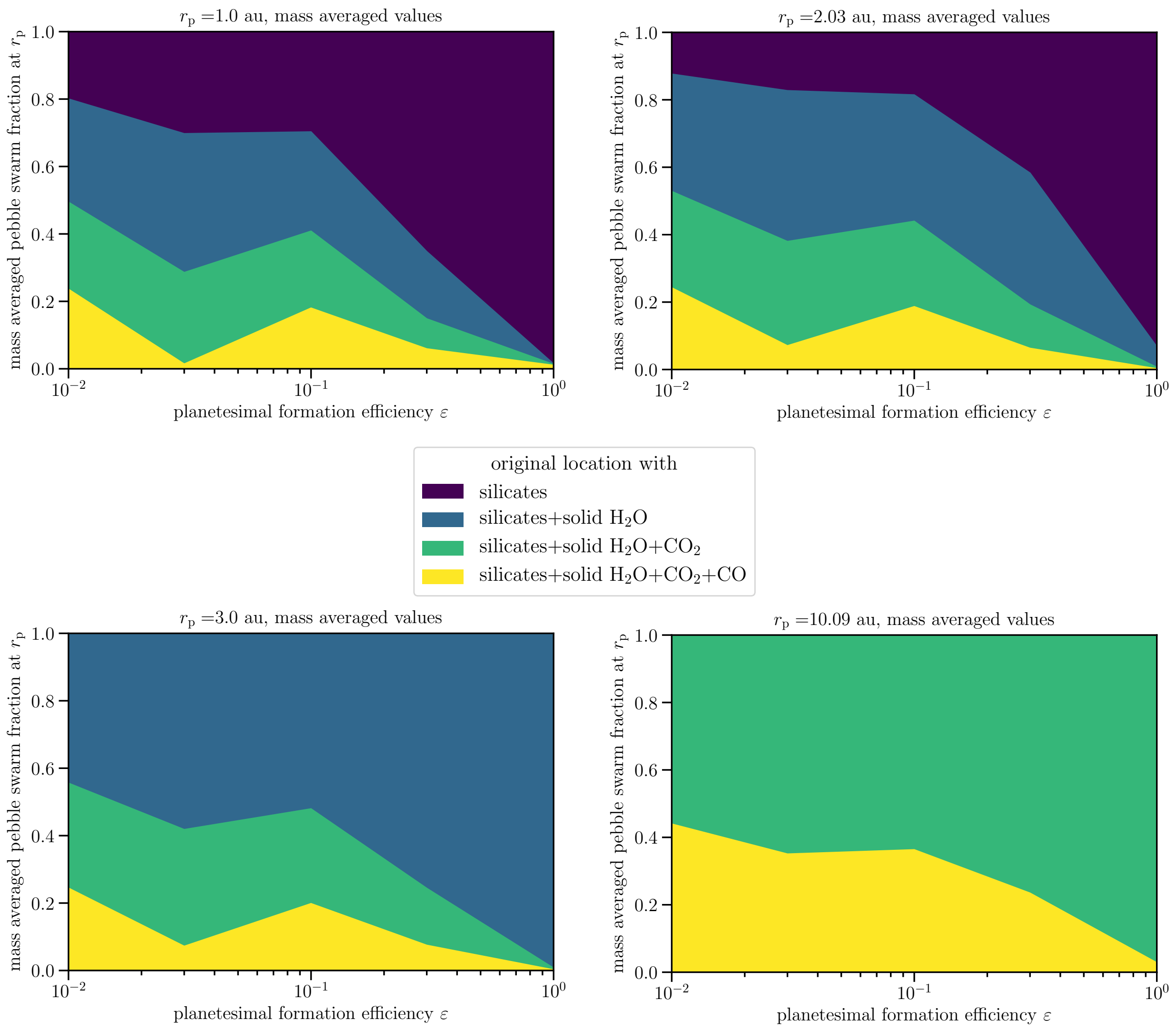

Figure 4.13: The same as Fig. 4.11 but for simulations of type S2.1, see Tab. 4.1 and Chapter 3. S2.1.

4.4 Discussion

In this section we discuss advantages, disadvantages, and limitations of the presented model. Furthermore, we discuss the case of a pebble accretion dominated situation even though the simulations do not include pebble accretion.

4.4.1 Limitations

The biggest advantage of the analytical approach is that it can be used in the post-processing. This means that only radial particle velocities, the initial particle density profile, and the time evolution of planetesimal densities are needed. Moreover, since it is an analytical approach, more insights on physical processes can be achieved. I.e., we can analyze the reasons for a specific result as a swarm of pebbles drifts inward and the disk evolves.

However, there are also obvious disadvantages of the model. One is that assumptions are needed, especially on the mass budget with which particles can join an incoming pebble swarm at different locations (i.e. the line density). Particle mixing in the fragmentation limited regions could be underestimated. One would need a simulation that traces the distribution of origins as the disk evolves to ensure more realistic particle mixing.

Another limitation of our approach is that radial diffusion is not taken into account and particle dynamics in the disk got simplified. We can estimate the timescale on which particles would radially mix due to particle diffusion with

$$t_{\rm diff} \approx \frac{r^2}{D} = \frac{r^2}{\alpha_{\rm t} c_{\rm s} h_{\rm g}} = \frac{\sqrt{rGM_\star} m_{\rm g}}{{\rm k_B} T}. \tag{4.18}$$

Here, D is the diffusion constant, $\alpha_{\rm t}$ the turbulence parameter, $c_{\rm s}$ the isothermal sound speed, *hscale* the gas pressure scale height, G Newton's gravitaitonal constant, $m_{\rm g}$ the mean molecular gas mass, and $\rm k_B$ Boltzmann's constant. If the mid-plane gas temperature is a result of radiation heating from the central star, this temperature scales as $T \propto r^{-1/2}$ which leads to $t_{\rm diff} \propto r$. For $\alpha_{\rm t} = 10^{-4}$, this yields a diffusion timescale at 10 au of a few ten million years. Hence, the majority of planetesimals formed before diffusion can mix material over a larger region significantly. For high $\alpha_{\rm t} \gtrsim 10^{-3}$ and radii $r \lesssim 1$ au, the diffusion timescale can become short enough to lead to significant large scale radial mixing that influences the distribution or origins of pebble swarms. This goes hand in hand with mixing of particles of different origins, especially in the fragmentation limited regions. However, the diffusion timescale at 10 au over a radial extent of 1 au is 100 times shorter. In general, the smaller the radial region over which material is considered to mix due to diffusion, the shorter the timescale. The radial diffusive flux also depends on the particles radial density gradient, which is not considered for this estimate.

Planetesimal-planetesimal collisions are neglected but could enrich all particle populations from tiny dust grains to pebble sizes (Gerbig et al., 2019). These fragments might have different sticking properties and different chemistry compared to the original material. This would influence the inner disk regions the most due to higher initial planetesimal densities.

Another limitation of both the analytical model presented in this work and the simulations is that ice line effects are not included. Drift of icy pebbles across (major) ice lines should result in elevated gas-phase abundances interior to these lines (e.g. Cuzzi & Zahnle, 2004; Stammler et al., 2017; Krijt et al., 2018) and affect planetesimal formation (e.g. Drążkowska & Alibert, 2017; Schoonenberg et al., 2018). Observational evidence seems to suggest these elevated gas-phase abundances are not occurring around the CO_2 ice line (Bosman et al., 2018a), but is possible for CO (Zhang et al., 2019, 2020). But significant drift (i.e., high radial mass flux) across ice lines could still occur and be consistent with such observations if chemical processing (which we do not include here) is fast compared to transport (Bosman et al., 2018b; Booth & Ilee, 2019).

The simulations used smooth disks but zonal flows and other pebble traps would create structure in both gas and particles. These traps are only considered in the form of parameters for planetesimal formation via the conversion length ℓ but not in the gas profile and thus also not in the drift velocities of particles. If there would be actual pressure bumps in the gas, radial transport is slowed down, see e.g. Pinilla et al. (2012). This is an effect that would also lead to a delay for planetesimal formation. As trapped particles cannot drift through traps, this would shift the shown feeding zones to longer times. But since radial particle transport would be slowed down as well, the impact on the distribution of origins is probably not too big.

If a significant amount of planetesimal mass is formed over a long time (up to $\sim 10^6$ yr), the formation time of giant planets (especially Jupiter) is crucial. A gap in gas formed due to the giant planet would block the incoming pebble flux, changing the types of meteorites forming (Desch et al., 2018). However, if after this gap formation the pebbles that are interior to it already originated from the outer disk, planetesimal forming material at these late times moved already through several ice lines.

Implications for pebble accretion

Since Figs. 4.10 and 4.12 show the distribution of origins at a given time (see vertical time stamps) for a local pebble swarm at different radii of planetesimal formation $r_{\rm p}$, those material origins would also apply for pebble accretion on embryos. However, planetesimal formation affects the material mixture with respect to their origins. A possible extreme case is a simulation with long pebble-to-planetesimal conversion lengths where planetesimal formation is so inefficient that the pebble flux is allowed to stay radius independent. For pebble accretion the timing of embryo formation is crucial since for different times the mixture of the pebble's origins changes. The definition of a planetary embryo is not straight forward but can be considered to be an object in the runaway growth phase (e.g. Wetherill & Stewart, 1993; Kokubo & Ida, 1996; Rafikov, 2003; Levison et al., 2012; Kobayashi et al., 2016). In the terrestrial-planet region embryos would form on timescales of roughly a few 10^4 yr to a few 10^5 yr. For planetesimals with around 100 km in diameter, pebble accretion is the least efficient (Visser & Ormel, 2016). This is the size at which the headwind velocity of pebbles is equal to the planetesimal surface escape velocity. Bigger planetesimals accrete pebbles more efficiently due to gravitational focusing.

4.4.2 The need of extreme cases

In principle, one would need a numerical model that tracks growth and transport of solid material including another dimension for the position of origin. The computation time of such a simulation time would scale with the number of radial grid points. Such a code, however, is currently not available and would require a simplification of particle growth such as presented in e.g. Booth & Ilee (2019) based on Birnstiel et al. (2012).

Since the simulations used in this work do not trace the material with respect to their origin, we need to model the local mass contribution to a pebble swarm in a simple way. I.e., we need to model the situation of a pebble swarm drifting in from an outer disk region r_{out} to a region further in, say r_{in}. What is the mass contribution of solid material (dust or pebbles) that was originally at r_{in} at the same radius when the pebble swarm with maximum origin radius r_{out} passes by. Since we are not able to calculate that for the given simulations, we can choose from two extreme cases:

1. We assume that the relative mass contribution follows the one given by the mass available after hitting the growth barriers. In this case, the mass inside of r_{d} is overestimated.

2. The other extreme would be given by a mass weighting function that follows the initial condition but scales exponentially with the loss due to radial drift. For the drift limited regions in the outer disk the size distribution is very top-heavy, leading to fast mean radial drift velocities. Fragmentation events are redistributing mass down to monomer sizes (e.g. Birnstiel et al., 2011). Such fragmentation events lead to a lower effective drift velocity of a hypothetically tracked mass of given origin, causing slower mean radial velocities.

We picked the latter approach for this work since it reflects the radial transport over time. However, the proper material mixing due to fragmentation events is something only a numerical code tracing the particles origins can do.

4.5 Summary

In this Chapter, we analyzed where planetesimal material originates from. We based our analysis on numerical simulations performed by in Chapter 3 following the planetesimal formation model of Lenz et al. (2019). This model assumes pebble traps to appear and disappear on a timescale of ~ 100 orbits. The planetesimal formation efficiency and radial density of these traps are parameterized as a conversion length ℓ. This model is simple enough to allow modeling the loss due to planetesimal formation for a traced pebble swarm while drifting inward. The disk can be divided into three different zones: (1) a region from which particles can not contribute to planetesimal formation at r_{p} at a given time, (2) a zone within which pebble swarms do not lose mass due to planetesimal formation, and (3) a planetesimal formation zone where the survival probability for single particles becomes lower due transformation from pebbles to planetesimals while drifting inward.

We introduced a survival probability for single particles which depends on the efficiency of planetesimal formation, the birth place, and the current position (see Fig. 4.1, Eq. (4.5), and Appendix C.3). We used two types of simulation data where in one case the particles growth in the disk is mostly limited by drift and in the other case by fragmentation (see Tab. 4.1 for a parameter overview). The size distribution averaged radial velocity of particles was used to calculate the mean radial trajectories of pebble swarms. For a given time of disk evolution and a chosen planetesimal formation radius r_{p}, we calculated the origins within which a certain percentage of mass contributed to planetesimals formed at r_{p}.

The feeding zones for planetesimal formation depend on time, location in the disk, and the conversion length $\ell = \varepsilon/d$ (see Appendix C.4). Later times of disk evolution lead to wider feeding zones as most of the material from the inner disk drifted away or is in planetesimals already. The relative feeding zone, i.e. the radius of origin enclosing a certain percentage of material forming planetesimals at r_{p}, is larger for the inner disk. The more efficient planetesimal formation is, i.e. shorter conversion lengths, the more in situ the feeding zones become since most of the pebble mass is converted into planetesimals while a pebble swarm is drifting inward.

The results depend a lot on the radial extent of the fragmentation limited disk region. If a disk is limited by fragmentation (i.e. low v_{f} or high α_{t}), the mean radial velocity of a pebble swarm is much slower compared to a drift limited disk, allowing local material to stay for longer before drifting away. Hence, fragmentation limited disks have smaller feeding zones compared to drift limited disks at the same time of evolution. However, this information has to be linked to the planetesimal production rate to obtain knowledge on the time dependence and mean mass contributions of different regions of origin. In Section 4.3.2 we show the time evolution of the distribution of origins, see Figs. 4.10 and 4.12. For the presented cases, over 90% of the final local planetesimal mass formed within $\sim 4 \cdot 10^4$ yr inside of 3 au. While material with origins inside the water ice line dominates during the early phase ($\sim 1.5 \cdot 10^4 - 1.5 \cdot 10^5$ yr) of planetesimal formation at 1 au, later planetesimals have only little contributions from that region. The mass averaged contributions from different regions of origin show that radial particle transport leads to significant contributions from material that passed several ice lines, especially for drift limited disks.

Nevertheless, numerical simulations are indispensable in order to verify or falsify the results of the analytical model.

4.6 Conclusions

Sorting planet forming material by their origin within or outside of major ice lines (water, CO_2, CO), we find that most asteroid material at 1 au originates from far beyond the water ice line and that original nebula condensates from within the water ice line are only a minor contribution. This general statement is true for both types of simulations where most of the disk is either limited by drift or fragmentation. This finding holds for direct pebble accretion like it does for intermediate storage in planetesimals. Thus almost all material incorporated into Earth, independent from planetesimal or pebble accretion was heavily processed across several ice lines.

5

Summary and Outlook

5.1 Thesis summary

The formation of planetesimals is believed to be necessary in order to explain the formation of planets. Planetesimal formation means that µm-sized dust grains have to be transformed into roughly 100 km planetesimals. This is a journey along about 36 orders of magnitude in mass. The solids in circumstellar disks are embedded in gas which is controlling the dynamics of particles. The relative velocities upon grains and radial particle velocities, both induced by the gas, lead to growth barriers that prevent growth beyond a size of roughly a few $\sim 10\,\mathrm{cm}$. These growth barriers need to be overcome to allow planet formation. The most promising formation process is gravoturbulent planetesimal formation (Johansen et al., 2006). In this scenario, pebbles are concentrated, preferably inside of gas pressure bumps, and turbulence is regulating the formation of Hill-stable pebble clouds that can collapse to planetesimals if particle diffusion is slower than the collapse time (Klahr & Schreiber, 2015; Schreiber, 2018). This is a fast and elegant way of overcoming the growth barriers by jumping several orders of magnitude in size and mass from typically mm – cm-sized pebbles to $\sim 100\,\mathrm{km}$ planetesimals. The typical planetesimal diameters of about 100 km that is a result of diffusion limited planetesimal formation is supported by numerical simulations on the reproduction of the size distribution in the asteroid belt (Morbidelli et al., 2009) and by observations (Delbo et al., 2017). The density of formed planetesimals determines how strongly they interact with each other. In order to enable the formation of different planet types (e.g. Earth-like or gas giant), the mass in planetesimals in preferred regions of formation for the different planets have to meet constraints. Here, the slope of the radial planetesimal density distribution is important. For steeper profiles, more mass is in the inner regions whereas shallower profiles have more mass in the outer disk.

A planetesimal formation rate model capable of reproducing the Solar System

In Chapter 2 I proposed a new model for the planetesimal formation rate $\dot{\Sigma}_\mathrm{p}$, see Eq. (2.1). This model is based on the idea of pebbles being converted into planetesimals on a given conversion length ℓ. This conversion length is a free parameter but is assumed to scale with the gas pressure scale height. The planetesimal formation rate is proportional to the flux of pebbles which is providing the mass for planetesimal formation and inversely proportional to the conversion length. That means more planetesimals can be produced locally for a higher pebble flux and smaller ℓ. The conversion length is an unknown parameter that reflects the density of pebble traps and the efficiency of trapping and converting pebbles to planetesimals. An example for such a situation is appearing and disappearing pressure bumps in the disk. If those pressure bumps live long enough to build planetesimals from the inflowing pebble flux, the planetesimal formation rate shown in Eq. (2.1) applies. However, if those traps do not live long enough or the efficiency of trapping and converting pebbles into planetesimals is too low, no planetesimals are formed. This defines the planetesimal formation condition shown in Eq. (2.5). The planetesimal formation model was implemented into a dust and gas evolution code (Birnstiel et al., 2010) which follows the radial motion of particles and gas, and solves for particle growth and fragmentation based on the Smoluchowski equation (von Smoluchowski, 1916). The code assumes a Gaussian shape of gas and particles in the vertical direction. The simulations presented in Chapter 2 show that once the critical flux needed for planetesimal formation is reached it is exceeded over the majority of time within which planetesimals are produced, see Fig. 2.1. This model produces planetesimals everywhere between around $\sim 1 - 100\,\mathrm{au}$. In contrast to that, the models by, e.g., Drążkowska et al. (2016) and Schoonenberg & Ormel (2017) produce planetesimals in a rather narrow region of the disk. The planetesimal formation rate model presented in this thesis produces planetesimals shortly after the first pebbles have formed locally. Since particle growth timescales are shorter in the inner disk, pebbles are produced first in the inner regions. Radii further out lag behind that growth front. In the presented model, this implies planetesimal formation to start in the inner regions as well while planetesimals at larger radii are formed later. Furthermore, I found that for disks that are mostly fragmentation limited, larger conversion lengths ℓ (smaller planetesimal formation efficiencies) lead to smaller planetesimal formation rates but last for longer compared to smaller ℓ (larger planetesimal formation efficiencies). However, smaller ℓ result in general in more planetesimals, see Fig. 2.4. If ℓ is large enough (in the shown study $\ell \gtrsim 50h_g$), i.e. for sufficiently small planetesimal formation efficiencies ε, planetesimal density profiles steeper than the one of initial dust and gas are produced. This might help to explain the difference between the expected profiles of circumstellar accretion disks with r^{-1} and the minimum mass Solar Nebula with $r^{-1.5}$.

The presented pebble flux-regulated planetesimal formation model is quite flexible. Eq. (2.1) should be valid for any process where pebbles are radially transported and form planetesimals over a typical conversion length. In this work, the planetesimal formation efficiency $\varepsilon = 5h_g/\ell$ was kept constant but could, in principle, vary with other disk parameters. E.g., ε can be used to mimic the mass enhancement due to desublimating water vapor in a narrow region just outside the water ice line. Additionally, another condition for planetesimal formation compared to the one used throughout this thesis (Eq. (2.5)) could be used.

What determines the radial planetesimal density slope?

For a radius independent pebble flux, it is possible to predict the slope of the planetesimal density profile, see Eq. (2.37). Another requirement is that the flux of particles is dominated by pebbles, i.e. by particles for which we expect significant particle trapping and planetesimal formation. This depends on aerodynamical coupling to the gas. In this work particles are called "pebbles" if they are in the Stokes number range [0.01,10].

According to the analytical prediction within the planetesimal formation rate model, the planetesimal density profile only depends on the temperature profile. The slope of the planetesimal density profile within this model will always be between the slope of the initial dust profile and the one predicted by Eq. (2.37): $\Sigma_p \propto r^{(q-5)/2}$ with $T \propto r^{-q}$. The slope of initial dust is reproduced for extremely efficient planetesimal formation. In this case dust grows to pebble size and immediately transforms into planetesimals. For sufficiently low planetesimal formation efficiencies, the pebble flux is radius independent due to conservation of mass which then automatically fulfills one of the conditions of the analytical estimate. I have shown that the analytical estimate predicts well the slopes produced in the numerical simulations, see dashed lines in Figs. 2.4 and 2.5.

For an evolving mid-plane temperature, the temperature profile varies over time and so does the profile of produced planetesimals in a given time interval of roughly constant temperature slope. The question remains under which conditions the pebble flux is altered such that it is not constant with respect to r anymore. I.e., what is the critical value for the planetesimal formation efficiency for which planetesimals form from local material only without significant contributions from other regions. Hence, planetesimals are formed faster than pebbles can radially drift and transport mass to other regions. This effect is discussed in Sec. 3.4.1. Setting the timescale of planetesimal formation based on the present pebble mass and the timescale of radial pebble drift equal to each other defines the planetesimal formation efficiency for which locally the highest planetesimal mass can be build (see Eq. (3.42)). Fig. 3.4 shows that this analytical estimate indeed predicts roughly the peak in planetesimal mass as a function of planetesimal formation efficiency. Typical values at which the peak is reached lie between $\varepsilon = 0.1$ and 0.3. For smaller values, a steeper slope according to Eq. (2.37) is expected. For larger values, the planetesimal profiles become closer to the initial dust profile. Generally speaking, for higher ε, more planetesimal mass is produced in the entire disk, whereas smaller values can lead to pebbles drifting through a large zone before forming planetesimals in the inner disk.

Which disk parameters allow the formation of the Solar System?

Chapter 3 presents an extended parameter study of the planetesimal formation rate model shown in Chapter 2. This model is tested with respect to Solar Nebula constraints for initial planetesimals. Using the simulation results on initial planetesimals for different disk parameters allows to constrain different disk parameters for the Solar Nebula. The nine analyzed parameters are the initial disk mass M_{disk}, the disk size r_c, the slope of initial density profile of dust and gas γ, the fragmentation speed v_f, the initial dust-to-gas ratio Z_0, the trap formation time τ_f, the turbulence parameter α_t, the planetesimal formation efficiency ε, and the X-ray luminosity L_X.

Based on literature studies, I suggest mass constraints for initial planetesimals in different disk regions:

- 0.7 – 1 au (Earth/Venus region): $0.1 - 2.77\,M_\oplus$

- 2 – 3 au (asteroid belt): 0.002 – 5 $M_\oplus$
- 4 – 15 au (possible giant forming region): 66 – unknown $M_\oplus$
- 15 – 30 au ("Nice disk"): 10 – unknown $M_\oplus$
- 30 – 50 au (Cold Classical Kuiper belt): 0.008 – 0.1 $M_\oplus$

In the regions inside of 0.7 au and outside of 50 au no initial planetesimals are required. These mass constraints are summarized in Fig. 3.1.

I found that a wide range of parameters allows the formation of the Solar System in terms of the suggested mass constraints. An extremely narrow range for each parameter would have been an indication for parameter fine tuning. However, since a wider range of each disk parameter seems to be possible, the planetesimal formation rate model can be applied within planet formation models that start with dust or pebbles such as population synthesis models (see Völkel et al., 2020).

In order to judge whether a certain parameter range fails to reproduce the Solar System, the suggested mass constraints were transformed into column densities, assuming an expected slope, see Fig. 3.2. The simulation results on initial planetesimals are then compared to both the minimum mass Solar Nebula mass (Figs. 3.7 and 3.8) and the suggested constraints (Figs. 3.9 and 3.10). Two fiducial parameter sets were used from which only one parameter was changed per simulation.

The fragmentation speed and turbulence parameter determine how many particles form that are considered as pebbles. Hence, conclusions on parameters that change the mass budget (e.g. M_disk) depend on these parameters. The fragmentation speed is the more important one of the two since the fragmentation limit depends quadratically on its value. Tab. 3.3 summarizes the possible parameter ranges. In order to meet the suggested constraints on initial planetesimals, the initial disk mass must be $M_\mathrm{disk} \gtrsim 0.1 M_\odot$ for $v_\mathrm{f} \sim 1\,\mathrm{m\,s^{-1}}$ and $M_\mathrm{disk} \gtrsim 0.02 M_\odot$ for $v_\mathrm{f} \gtrsim 10\,\mathrm{m\,s^{-1}}$. The disk was likely smaller than $r_\mathrm{c} \lesssim 50\,\mathrm{au}$ with a power-law index in the inner regions of $\gamma \sim 1$. If the fragmentation speed is too slow, no pebbles are formed and, thus, no planetesimals. This is why I conclude that $v_\mathrm{f} \gtrsim 1\,\mathrm{m\,s^{-1}}$. For the initial dust-to-gas ratio, a wide range seems to be possible, $0.01 \lesssim Z_0 \lesssim 0.03$. For $Z_0 \lesssim 0.003$, simply too little mass ends up in planetesimals. Since no or only little mass outside of 50 au is expected, traps needed at least $300\,t_\mathrm{orb}$ to form or never formed in these outer regions. For the turbulence parameter, a wide range is possible, $\alpha_\mathrm{t} \sim 10^{-5} - 10^{-3}$. However, if $v_\mathrm{f} \sim 1\,\mathrm{m\,s^{-1}}$, the maximum value of α_t should not exceed a few 10^{-4}. By comparing the pebble-to-planetesimal conversion length ℓ to the gas pressure scale height, the constraints are given by $0.002 < h_\mathrm{g}/\ell \lesssim 0.06$. If planetesimal formation is too efficient, too much mass in the outer regions is produced whereas too small efficiencies lead to too few planetesimals in general. The most appealing simulation included accretion heating and the following parameters: $M_\mathrm{disk}/M_\odot = 0.1$, $r_\mathrm{c}/\mathrm{au} = 20$, $\gamma = 1$, $v_\mathrm{f}/\mathrm{cm\,s^{-1}} = 2 \cdot 10^2$, $Z_0 = 0.0134$, $\tau_\mathrm{f}/t_\mathrm{orb} = 1600$, $\alpha_\mathrm{t} = 3 \cdot 10^{-4}$, and $\varepsilon = 0.05$, and $L_\mathrm{X}/\mathrm{erg\,s^{-1}} = 3 \cdot 10^{29}$. The final planetesimal profile of this simulation is shown as dotted line in the top left panel of Fig. 3.10. These parameter constraints will help to choose the initial conditions of future simulations which try to reproduce the Solar System.

Where does planetesimal forming material originate from?

By tracing planetesimal forming material back to their origins, I computed the mass fraction of planetesimals that crossed one or several major ice lines (Chapter 4). The particle tracing used is based on data including radial velocities and size distributions taken from the output of simulations, see Figs. 4.5 and 4.2. The model divides the disk into four different zones based on typical evolutions of planetesimal forming regions, see Fig. 4.1. (1) A region of particle origins from which no particles are reaching the disk radius r_p at which planetesimals are forming at time t. (2) The next region, located further in, contains particles that do reach r_p within the time t but no mass is lost due to planetesimal formation since the critical pebble flux is not reached in that region. (3) The third region is filled with particles that are prone to planetesimal formation. While particles are moving through this zone, mass is lost due to the formation of planetesimals. (4) The innermost region (mostly) describes a zone within which planetesimals are formed and particles fragment. However, it is argued that fragmentation events may only have a minor effect on the mixture of particle origins. With help of these classifications, a differential equation for the survival probability of individual particles is derived (Eq. 4.5) and solved analytically (Appendix C.3).

The regions from which a certain percentage of mass originates from that is contributing to a planetesimal are called "planetesimal formation feeding zones" in this thesis. As already discussed above, large feeding zones allow planetesimal profiles steeper than the original profiles of dust and gas. The analytical model for particle tracing and its analysis in Chapter 4 enable to reveal the underlying physical processes that cause a feeding zone at a certain position in the disk at a given time of disk evolution. These processes are, on the one hand, the changing survival probability of individual particles while pebbles are drifting, controlled by the conversion length of the planetesimal formation model presented in Chapter 2. On the other hand, particle drift reduces the amount of original local mass over time which regulated the mass that can join a drifting pebble swarm, see Figs. 4.3 and 4.6. The relative mass contributions of different regions of origin to a pebble swarm changes due to these reasons while it is drifting (Fig. 4.7).

Assuming fixed locations for the water, CO_2, and CO ice lines following Öberg et al. (2011), relative contributions to planetesimals from different regions divided by these ice lines can be computed as a function of time, see Figs. 4.10 and 4.12. How fast most of the planetesimals are formed depends on whether most of the disk is limited by fragmentation or drift. In the former case average drift is much slower and planetesimal formation lasts longer. The first $\sim 30\%$ of planetesimals formed at $1-2$ au have significant/dominating contributions from particles originating within the water ice line. However, the mass averaged contributions of the final planetesimal populations at the locations of Earth or the asteroid belt have significant contributions from regions outside the water ice line (and/or other major ice lines) if planetesimal formation is not too efficient, see Figs. 4.11 and 4.13. This finding also holds for a scenario where pebbles are accreted onto existing planetary embryos since the composition of pebble swarms determines both the composition of planetesimals forming out of pebble clouds and of pebbles that are attracted by massive objects.

To summarize, radial pebble transport in circumstellar disks plays a crucial role for the composition of planetary building blocks and their distribution in the disk. Pressure bumps in the gas present particle traps, which are favorite regions for planetesimal formation. These particle traps allow forming planetesimals throughout the disk. The efficiency of planetesimal formation can have a huge impact on the mixture of particles forming planetesimals by determining which percentage of particles stems from which location in the disk. Furthermore, due to longer radial transport paths, this results in planetesimal profiles steeper than those of the initial dust and gas distributions, which helps to explain the discrepancy between the minimum mass Solar Nebula and viscous accretion disks.

5.2 Outlook

This section is on potential future projects. The use of a new planetesimal formation rate model, a temperature model that depends on the evolution of particles, and restrictions with respect to computational time and current modeling offers new opportunities or requires new ways to improve the understanding of planet formation.

Connecting two different planetesimal formation rate models

Drążkowska et al. (2016) and Schoonenberg & Ormel (2017) proposed a model where planetesimals are formed whenever the particle-to-gas mass ratio in the mid-plane reaches values above unity. Both models are equivalent to each other and I will hereafter follow the description by Drążkowska et al. (2016). Once their planetesimal formation condition is fulfilled, planetesimals are produced with the rate

$$\dot{\Sigma}_\mathrm{p} = \zeta \frac{\Sigma_\mathrm{d}(\mathrm{St} > 0.01)}{t_\mathrm{orb}}. \tag{5.1}$$

Here, ζ defines the efficiency parameter per orbit with which the mass contained in particles with $\mathrm{St} > 0.01$ is converted to planetesimals. This model does not assume the presence of particle traps. However, the model discussed in Chapter 2 parameterizes features of such traps. I.e., the conversion length ℓ could be a result of traps emerging everywhere in the disk but with a typical mean radial separation. With these traps appearing and disappearing on timescales proportional to the orbit time, pebble traps occur at almost every location in the disk. In this thesis, these features, i.e. the radial separation and lifetimes of traps, were parameterized and did not appear in the gas density. Hence, both models of Lenz et al. (2019) and Drążkowska et al. (2016) can be linked to each other via a structured gas density profile. The turbulence parameter α_t was set to a constant value in both of these papers. A gas profile with Gaussian bumps can be forced by an appropriate structure in $\alpha_\mathrm{t}(r)$, where a dip in $\alpha_\mathrm{t}(r)$ will create a bump in the gas density. The bumps have a lifetime of, e.g., $\tau_\mathrm{l} = 100 t_\mathrm{orb}$ taken at the peak position. After $0.5\tau_\mathrm{l}$ the bump begins to disappear while another bump builds up at a different radius that is not too close to the nearest neighboring bump or the previous location. To avoid constant movement toward or away from the star of all bumps, the disk could be divided into different regions. The centers of these regions are located where initially the ratio of the disk radius to the intended trap distance r/d (e.g. $d = 5h_\mathrm{g}$) are integers. The translation between the planetesimal formation efficiency parameter of Drążkowska et al. (2016) and Lenz et al. (2019) would be given by

$$\frac{\zeta}{t_\mathrm{orb}} \hat{=} \frac{\varepsilon}{\tau_\mathrm{l}}. \tag{5.2}$$

The planetesimal formation condition is taken from Drążkowska et al. (2016), i.e. a critical value for the particle-to-gas ratio in the mid-plane is required. If the traps are sufficiently pronounced and the Stokes numbers of the largest particles are high enough, particle trapping can occur that satisfies the planetesimal formation condition. If the minimum separation of traps is not too large and trap lifetimes are not too long, a smooth planetesimal formation density profile is expected, reproducing the parameterized model discussed in Chapter 2.

Are comets late planetesimals?

Typical diameters of asteroids and comets differ by around one order of magnitude. It is still a mystery why this is the case and also when the first comets have formed. There is evidence that planetesimals are formed via gravoturbulent collapse that is regulated by particle diffusion. Gravitational instability of massive pebble clouds (Johansen et al., 2006; Johansen et al., 2007) seems to be the most promising way to overcome the fragmentation (Blum & Münch, 1993; Blum & Wurm, 2008; Gundlach & Blum, 2014) and drift barrier (Klahr & Bodenheimer, 2006; Birnstiel et al., 2012). The asteroid belt (Bottke Jr et al., 2005a), the Kuiper belt (Fuentes & Holman, 2008; Fraser & Kavelaars, 2008), Jupiter Trojans (Jewitt et al., 2000), and Neptune Trojans (Sheppard & Trujillo, 2010, see Fig. 1.8 for an overview) all share a characteristic size at which a kink feature arises in their size distribution. This characteristic size is around 100 km in diameter which is predicted by diffusion limited gravoturbulent planetesimal formation for typical parameters (Klahr & Schreiber, 2015; Schreiber, 2018). This is inline with Morbidelli et al. (2009) who have shown that asteroids in the main belt were born big (diameter $\gtrsim 80\,\mathrm{km}$). As shown by Blum et al. (2014), comets must have formed via gravitational instability as all alternative formation models would lead to too high tensile strenghts of the surface layers. For the special case of 67P/Churyumov-Gerasimenko, Blum et al. (2017) have shown that this is also true for this object and, on top of this, that it was formed by roughly mm-sized pebbles mixed with microscopic ice particles. However, some people believe that comets are a result of disruptive collisions (e.g. Morbidelli et al., 2015).

Schreiber & Klahr (2018) have shown that particle diffusion becomes weaker with increasing dust-to-gas ratio of the local particle clouds. Photoevaporation reduces the gas densities at late times such that there exists the possibility to form smaller objects formed at times $\gtrsim 10^6\,\mathrm{yr}$. For the collapse, the particle diffusion *on the scales of planetesimal formation* is important. This implies that we need an estimate for mid-plane particle-to-gas ratios at the particle density at which collapse is happening ($f\rho_\mathrm{Hill}$). The dimensionless diffusion coefficient can be described as

$$\delta \approx \delta_{10} \left(\frac{f\rho_\mathrm{Hill}/\rho_\mathrm{g}}{10} \right)^{-p}, \tag{5.3}$$

where $\delta_{10} \approx 1 \cdot 10^{-6} \ldots 2.5 \cdot 10^{-5}$ and $p = 1 \ldots 1.5$ (Schreiber & Klahr, 2018). During the collapse, the particle diffusion parameter goes up and can reach values that are 10 times higher (Schreiber, 2018) which is represented as the upper end of δ_{10}. Hence, the measured diffusion constants are pointing to the right direction but should not be understood as strict values. They might also be linked to the mass efficiency parameter q that arises in the planetesimal size prediction, see Eq. (1.43). Furthermore, δ scales with the particles Stokes number. Unfortunately, the study from Schreiber & Klahr (2018) analyzed only two different Stokes numbers which makes it difficult to identify a scaling law. Once we know more about how the particle diffusion scales with the Stokes number, Eq. (1.43) can be used to predict the evolving size of newborn planetesimals over time.

Evolving gas temperature linked to the size distribution of particles

In Chapter 3 a temperature model based on the size distribution of particles was proposed. This model was not tested in great detail. Hence, it would be of interest to analyze the temperature evolution for the accretion heating model that depends on the size distribution of particles. The size distribution changes the optical depth which has an impact on the gas temperature, see Eq. 3.35. Analyzing this temperature model is a project for itself but it would be of great interest to see how the evolving size distribution changes the temperature in the disk. The results could then be compared to sophisticated models such as the one from Hubeny (1990).

On further evolution of planetesimals

In this work, planetesimals were not interacting with each other or with other material once they have formed. However, once the planetesimal density is high enough, planetesimals collide with each other, replenishing smaller material such as pebbles and dust grains as well as leading to planetesimal growth (e.g. Weidenschilling et al., 1997; Kobayashi et al., 2016). They are also able to accrete pebbles to grow bigger (Ormel & Klahr, 2010). It was found by Visser & Ormel (2016) that pebble accretion onto planetesimals with diameters around 100 km leads to very long growth timescales ($\gtrsim$ a few million years) and only becomes efficient for objects with diameters of a few 100 km or larger. This implies that 100 km planetesimals have to grow via planetesimal-planetesimal collisions before pebble accretion becomes important. The interaction of dust growth to pebbles, dynamic planetesimal formation linked to the pebble flux, and planetesimal-planetesimal collisions was studied in a simple local model by Gerbig et al. (2019). They were not including radial transport, planetesimal growth, or gas evolution. Additionally, they described the system with help of simple differential equations rather than solving more general growth equations. Hence, it would be a valuable project to study the effects of planetesimal-planetesimal interactions and pebble accretion in a simulation that solves for radial transport and particle growth.

The need to improve simple disk evolution models

The long computation times on the order of months of the simulations presented in this thesis make a quick and broader parameter study challenging, especially for the most interesting cases for which the fragmentation speed is on the order of $1\,\mathrm{m\,s^{-1}}$. The implementation of collisions of planetesimals with each other and tracking their growth and dynamical evolution would cause the simulations to run for even longer. Hence, a simple model for the evolution of dust, pebbles, and gas is required. Current simple models such as the two population model (Birnstiel et al., 2012) deviate from codes that solve for particle motion as well as particle growth and fragmentation (e.g. `DustPy`) under certain conditions. Such conditions are, for instance, low $\alpha_\mathrm{t} \lesssim 10^{-4}$ or a structured gas profile with bumps or dips. The two population model struggles under these circumstances to reproduce the results from more sophisticated models that include more physics instead of simplifying some effects (e.g. Birnstiel et al., 2010). Hence, such simple models should be used with caution. When a new effect is implemented into such models, e.g. planetesimal formation, it has to be tested and compared to sophisticated models first, before the results can be fully trusted. Furthermore, simulations in which particles are traced, including their chemical composition and planetesimal formation, are needed to obtain a more comprehensive understanding of planetesimal compositions.

Connecting simulation data to observables

The planetesimal formation model presented in this thesis produces planetesimals almost everywhere in disks. The final mass of the entire planetesimal population can be very close to the initial dust mass. As long as planetesimal-planetesimal collisions do not produce a significant amount of dust, this effect should be observable. Hence, analysis of observables such as the optical depth in the simulations including planetesimal formation would lead to valuable knowledge. This information could be used to answer the question at which time disks become transparent due to too much mass ending up in planetesimals. Once planetesimal-planetesimal collisions are included in those simulations, an effect that replenishes small material, the time evolution of the amount of observable particles that is produced in simulations can be compared to observations (see e.g. Williams et al., 2019).

A Appendix

A Additional information on Chapter 2

A.1 The coagulation approach

The first mathematical expression (in discrete form) for the coagulation process was obtained by von Smoluchowski (1916). It was first written in integral form by Schumann (1940), which is appropriate for a continuous mass spectrum. Consider a dust grain distribution $n_\mathrm{m}(m,r,z)$ as the number of particles per spatial volume and per particle mass interval $[m, m+\mathrm{d}m]$. In protoplanetary disks, n_m is a function of the solid particle mass m *as well as* the distance r and height z (cylindrical coordinates). Since we assume a cylindrically symmetric system, the quantities do not depend on the azimuthal angle φ. Thus, the total dust mass density is

$$\rho_\mathrm{d}(r,z) = \int_0^\infty \mathrm{d}m\; n_\mathrm{m}(m,r,z)\cdot m. \tag{A.4}$$

A further generalized coagulation equation including fragmentation would be (see e. g., Barrow, 1981; Birnstiel et al., 2010)

$$\begin{aligned}\frac{\partial}{\partial t} n_\mathrm{m}(m,t,r,z) = &\int_0^\infty \mathrm{d}m_1 \int_0^\infty \mathrm{d}m_2\; K(m,m_1,m_2,r,z)\\ &\times n_\mathrm{m}(m_1,r,z) n_\mathrm{m}(m_2,r,z),\end{aligned} \tag{A.5a}$$

where the reaction kernel is given by

$$\begin{aligned}K(m,m_1,m_2) := &\frac{1}{2}K(m_1,m_2)\cdot\delta(m_1+m_2-m)\\ &-K(m_1,m_2)\cdot\delta(m_2-m)\\ &+\frac{1}{2}F(m_1,m_2)\cdot\mathcal{D}(m,m_1,m_2)\\ &-F(m_1,m_2)\cdot\delta(m-m_2).\end{aligned} \tag{A.5b}$$

In this expression

$$K(m_1,m_2) := P_\mathrm{c}(m_1,m_2,\Delta v)\cdot\Delta v(m_1,m_2)\cdot\sigma(m_1,m_2)$$

is the coagulation kernel,

$$F(m_1,m_2) := p_\mathrm{f}(m_1,m_2,\Delta v)\cdot\Delta v(m_1,m_2)\cdot\sigma(m_1,m_2)$$

the fragmentation kernel, and

$$\sigma(m_1,m_2) = \pi(a_1+a_2)^2$$

the geometrical cross section , where a_i is the particle radius of the colliding particle with mass m_i. P_c and p_f denote the probability that a collision between two particles of mass m_1 and m_2 with a relative velocity Δv at collision leads to coagulation or fragmentation ($P_\mathrm{c} + p_\mathrm{f} = 1$), respectively. Colliding particles with m_1 and m_2 give a gain term for particles with mass m, determined by the distribution of fragments $\mathcal{D}(m, m_1, m_2)$, where we assume that the distribution is a power-law according to

$$n_\mathrm{m}\,\mathrm{d}m \propto m^{-\xi}\,\mathrm{d}m. \tag{A.6}$$

We follow Brauer et al. (2008a) and use $\xi = 1.83$, but this power-law index may depend on the collision speed (Husmann, 2017, his section 4.2). The Dirac delta-distribution is denoted by $\delta(\cdot)$.

The first term in Eq. (A.5b) corresponds to an increasing number of particles with mass m due to grain growth, i. e., particles with masses m_1 and $m - m_1$ coagulate. The second term represents the loss of particles with mass m (m_1 coagulates with m). The third term stands for the fragmentation due to a collision between particles with mass m_1 and m_2, and includes the fact that subsequently a distribution of some of their mass will occur via fragmentation to smaller sizes. The fourth term describes the fragmentation of particles with mass m_1 and m and thus represents the *loss* of particles with mass m. The factors $1/2$ eliminate double counting of the collisions increasing the number of particles of mass m. We use 27 bins per size decade. The radial grid has 300 points spanning from 0.2 to 800 au. The grid points are logarithmically equally spaced, both in mass and disk radius. In order to optimize computational time, we only numerically consider mass cells up to twice the mass of the current maximum mass in the system at each disk radius, similar to section 2.2 of Lee (2000).

In general, all these quantities can also depend on other material properties such as composition, porosity and charge. To keep it simple we consider just the mass of the colliding particles. As Eq. (A.5a) is proportional to the product of two densities and particle densities become larger toward the mid-plane due to vertical settling, we follow Birnstiel et al. (2010) and approximate the kernels by the mid-plane values. However, the z-dependence is eliminated by vertical integration, assuming a Gaussian z-profile for the particle density. In the code, the *discrete* Smoluchowski equation is solved numerically. See Appendix A of Birnstiel et al. (2010) for details.

A.2 Radial Particle velocities dominated by gas flow

It is worthwhile to estimate the Stokes number below, which the first velocity term in Eq. (2.16) dominates. Therefor we use

$$h_\mathrm{g} \propto r^{(3-q)/2}, \tag{A.7}$$

assuming a falling temperature power-law with exponent q. Further, we assume a gas column density profile following Eq. (2.20) with $\gamma = 1$, $r_\mathrm{c} = 35$ au. This leads to the logarithmic pressure gradient

$$\frac{\partial \ln P}{\partial \ln r} = -\gamma - \frac{3+q}{2} - (2-\gamma)\left(\frac{r}{r_\mathrm{c}}\right)^{2-\gamma} \tag{A.8}$$

which is obtained by using $P = c_\mathrm{s}^2 \rho_\mathrm{g}$ for mid-plane values, see Eq. (2.10). There are regions in the r-St space where the total particle velocity is dominated by the gas velocity, i. e., by the left term in Eq. (2.16). We will now determine the condition on the Stokes number for this term to dominate the radial velocity. In the most cases the dust-to-gas ratio is small on large scales, thus, we assume $\rho_\mathrm{d}/\rho_\mathrm{g} \ll 1$. This way we obtain

$$\frac{3}{\Sigma_\mathrm{g}\sqrt{r}}\left|\frac{\partial}{\partial r}(\Sigma_\mathrm{g} \nu \sqrt{r})\right| \geq \mathrm{St}\frac{h_\mathrm{g}}{r}\left|\frac{\partial \ln P}{\partial \ln r}\right| c_\mathrm{s} \tag{A.9}$$

which can be written in the form

$$\frac{3}{r}\nu\left|\frac{\partial}{\partial \ln r}\ln(\Sigma_\mathrm{g} \nu \sqrt{r})\right| \geq \mathrm{St}\frac{h_\mathrm{g}}{r}\left|\frac{\partial \ln P}{\partial \ln r}\right| c_\mathrm{s} \tag{A.10}$$

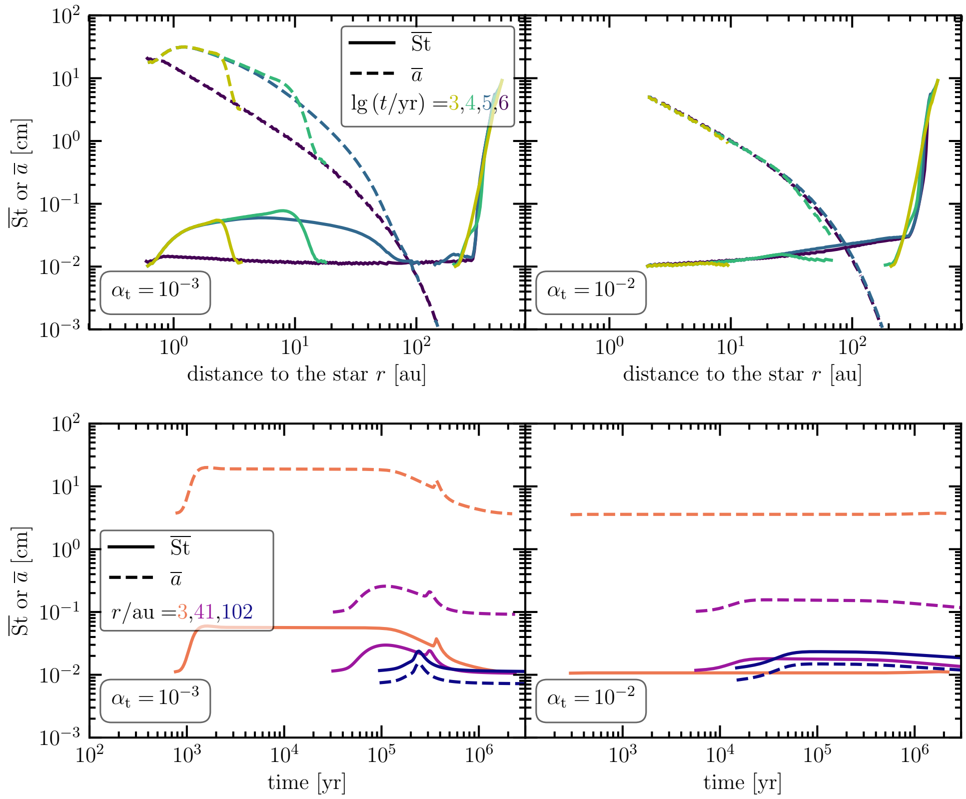

Figure A.1: Evolution of the flux averaged Stokes numbers in the mid-plane (solid) and particle radii (dashed) for a simulation with $\alpha_\mathrm{t} = 10^{-3}$ (left panels) and $\alpha_\mathrm{t} = 10^{-2}$ (right panels). Both are shown as a time series as a function of radius (top panels) and for different radii as a function of time (bottom panels). In all plots the left axis belongs to $\overline{\mathrm{St}}$ and the right one to $\overline{a}$ according to the definition in Eq. (A.14).

By inserting the turbulent viscosity from Eq. (2.7) as well as Eqns. (A.7) and (A.8) we get, for a constant α_t (after rearranging)

$$\begin{aligned} &3\alpha_\mathrm{t}\left|-\gamma-(2-\gamma)\left(\frac{r}{r_\mathrm{c}}\right)^{2-\gamma}+\frac{3-q}{2}-\frac{q}{2}+\frac{1}{2}\right| \\ &\geq \mathrm{St}\left[\gamma+\frac{3+q}{2}+(2-\gamma)\left(\frac{r}{r_\mathrm{c}}\right)^{2-\gamma}\right] \end{aligned} \tag{A.11}$$

which finally yields Eq. (2.23). If $\rho_\mathrm{d}/\rho_\mathrm{g} \ll 1$ is not fulfilled, this value has to be multiplied by $[1+(\rho_\mathrm{d}/\rho_\mathrm{g})^2]$ for mid-plane values. Since Σ_g decreases exponentially for $r/r_\mathrm{c} > 1$, whereas $\nu\sqrt{r}$ increases with r, there exists a radius from which gas is flowing outward. This outflow of gas can drag dust with sufficiently small Stokes numbers along. The transition radius where the gas velocity u_r switches from an inflow ($u_\mathrm{r} < 0$) to an outflow ($u_\mathrm{r} > 0$) can be computed the same way:

$$u_\mathrm{r} \overset{!}{\geq} 0$$

leads with Eq. (2.14) to

$$\frac{\partial}{\partial \ln r} \ln\left(\Sigma_{\mathrm{g}} \alpha_{\mathrm{t}} h_{\mathrm{g}} c_{\mathrm{s}} \sqrt{r}\right)$$
$$= -\gamma - (2-\gamma)\left(\frac{r}{r_{\mathrm{c}}}\right)^{2-\gamma} + 2 - q \leq 0 \tag{A.12}$$

giving

$$r \geq \left(\frac{2-q-\gamma}{2-\gamma}\right)^{1/(2-\gamma)} r_{\mathrm{c}}. \tag{A.13}$$

Since in our simulations the pressure gradient is always negative, drift is also always pointing inward. In this case, the region of outflowing solid matter in the r-St space is given by Eq. (2.23), giving the Stokes number of the velocity sign flip, and Eq. (A.13), giving the disk radius beyond which gas, and thus also these particles, are flowing outward.

A.3 Averaged Size of planetesimal forming material

What is the average size of the material which is building planetesimals? To answer this question we use flux averaging such that

$$\overline{X} := \frac{\sum_{\mathrm{St}_{\min} \leq \mathrm{St} \leq \mathrm{St}_{\max}} X \left|v_{\mathrm{drift}}(r, \mathrm{St})\right| \Sigma_{\mathrm{d}}(r, \mathrm{St})}{\sum_{\mathrm{St}_{\min} \leq \mathrm{St} \leq \mathrm{St}_{\max}} \left|v_{\mathrm{drift}}(r, \mathrm{St})\right| \Sigma_{\mathrm{d}}(r, \mathrm{St})}$$
$$\times \theta(\dot{M}_{\mathrm{peb}} - \dot{M}_{\mathrm{cr}}), \tag{A.14}$$

where X is either Stokes number, St, or particle radius, a, and the sum goes over all particles with Stokes number in the range between $\mathrm{St}_{\min}$ and $\mathrm{St}_{\max}$. The Heaviside function reflects the condition (2.5). We use a flux average, since in our model the contribution to planetesimals scales with it. Fig. A.1 shows that the flux averaged particle size building planetesimals is roughly a constant over time, as long as the dust-to-gas ratio is high enough to keep the drift limit close to the fragmentation barrier. The large peak beyond 300 au stems from the exponential drop in gas density. This yields planetesimals which are built from ~ µm-sized particles. The r-dependence of $\overline{a}$ is mostly determined by the gas column density Σ_{g}, as can be seen from the almost r-independent $\overline{\mathrm{St}}$ values at 10^6 yr, which transforms $\overline{\mathrm{St}}$ via Eq. (2.13) into $\overline{a} \propto \Sigma_{\mathrm{g}}$.

A.4 Necessity of $\mathrm{St}_{\min}$ and $\mathrm{St}_{\max}$

If the flux is not dominated by particles in the range $\mathrm{St}_{\min} \leq \mathrm{St} \leq \mathrm{St}_{\max}$, these parameters become very important. Though, $\mathrm{St}_{\max}$ is only important for the outer disk part where the gas density becomes very low, leading to high Stokes numbers > 1 even for the smallest particles in the simulation (0.1 µm). Fluid dynamical simulations have to show which values of the Stokes number represent the boundaries at which *both* particle trapping and planetesimal formation can occur in a gravo-turbulent scenario. One prerequisite would be the onset of streaming instability which can further regulate planetesimal formation after enough mass has been accumulated. In Fig. 2.1 we plot both the particle flux fulfilling $10^{-2} = \mathrm{St}_{\min} \leq \mathrm{St} \leq \mathrm{St}_{\max} = 10$ and the flux of all particles. In the extreme case where $\mathrm{St}_{\min} = 0$ and $\mathrm{St}_{\max} = \infty$, the difference between the total flux (dashed lines) and the pebble flux shown (solid lines, $\mathrm{St}_{\min} = 10^{-2}$, $\mathrm{St}_{\max} = 10$) would also yield a difference in planetesimals. Since the particles' contribution to planetesimals is weighted by the contribution of their flux to the overall pebble flux, smaller particles also contribute less. Smaller values of $\mathrm{St}_{\min}$, say 10^{-3}, would lead to earlier planetesimal formation, which also persists longer. The edges of the planetesimal zone would also stretch out.

A.5 Total dust and planetesimal mass in the disk

Fig. A.2 shows the integrated mass of planetesimals and smaller particles. Reaching the total solid mass of the MMSN does not necessarily imply that the result is compatible with planetesimal formation in the Solar Nebula. It is more like a necessary condition and, therefore, knowledge about the planetesimal distribution as a function of radius is mandatory. For $\alpha_{\mathrm{t}} = 10^{-2}$ values over the MMSN mass can be reached only for high ε (here 0.8), which is

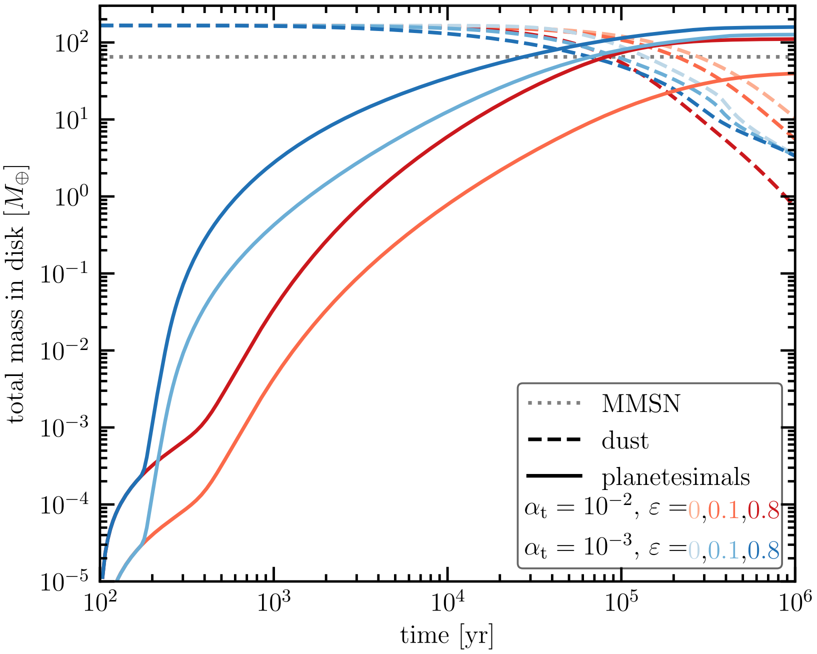

Figure A.2: Total planetesimal mass (solid lines) and total mass of solids not in planetesimals (dashed lines) as a function of time. The gray dotted line shows the total mass in solids of the minimum mass Solar Nebula (MMSN), after Weidenschilling (1977b) and Hayashi (1981). For this plot the same parameters were used as in Fig. 2.4.

unlikely since the efficiency in the planetesimal formation process itself is already lower (Schreiber, 2018, see κ in his Table 7.3).

High α_t leads to wider regions which are fragmentation limited. Hence, more mass is in small, slow drifting particles. The total mass strongly depends on ε. Whereas for mostly drift limited disks, the mass reservoir in the outer disk is transported to the inner part much faster. Over this long distance, particles which were not transformed into planetesimals in the outer part may turn into one in the inner part. This can lead to similar disk masses of the planetesimal population but with a different r-dependent distribution.

A.6 Origin of particles beyond growth barriers

Physical and numerical diffusion mix particles radially, which can lead to particles larger than the growth barriers. They can remain there for a long time if the particle density is low enough to keep collision rates small, see figures A.3 and A.4. Converting particle radius into Stokes number, this effect looks more extreme in the outer disk (figures 2.2 and 2.3) because the gas density decreases with disk radius.

A.7 More detailed derivation of the planetesimal formation condition

In order to be able to form planetesimals, there exists a critical cloud diameter l_corr that has to be reached in order for the cloud to be able to contract while an underlying turbulent particle diffusion is trying to dissolve it (Schreiber, 2018, his section 3.3). This critical length scale can be derived by equating the diffusion and collapse timescale leading to

$$l_\mathrm{corr} = \frac{2}{3}\sqrt{\frac{\delta}{\mathrm{St}}}h_\mathrm{g}. \tag{A.15}$$

Here, δ is the dimensionless diffusion parameter (diffusion constant over $c_\mathrm{s}h_\mathrm{g}$) which acts on the scale of l_corr. Particles have to concentrate and reach Hill density ρ_Hill in a volume l_corr^3. I. e., under self-gravity particles will settle to an effective scale height $\ell_z = l_\mathrm{corr}$ in the z-direction and concentrate azimuthally out of a full $2\pi r$ ring to a length of $\ell_\varphi = l_\mathrm{corr}$. In the radial direction the particles that have been in the trap structure of radial extent d_r will be concentrated

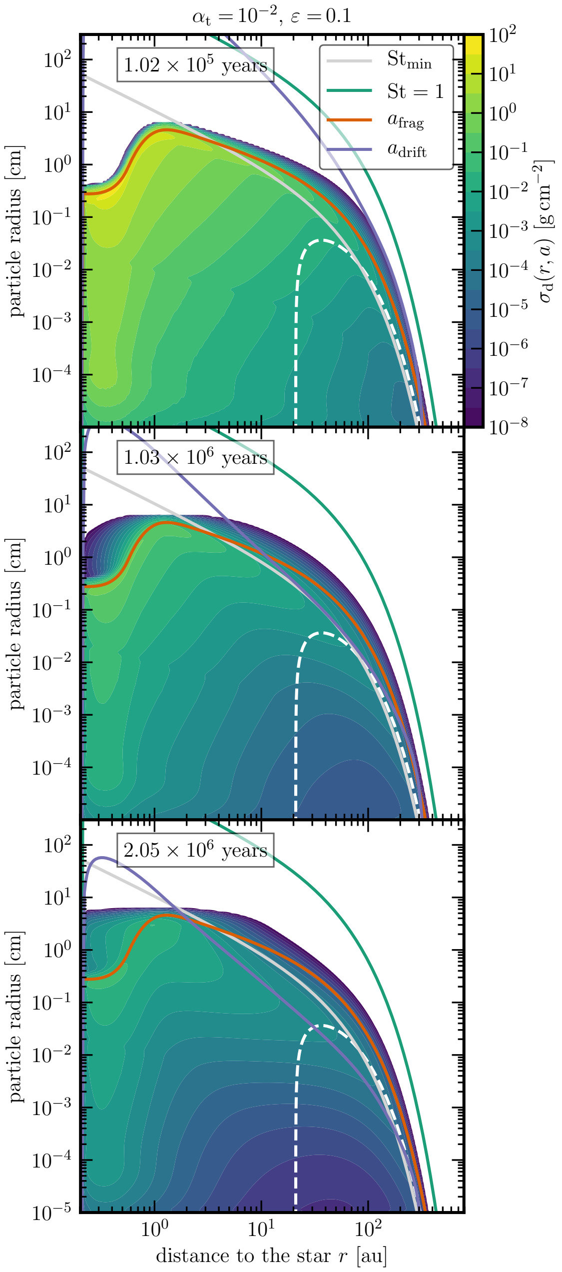

Figure A.3: Same as Fig. 2.2 but showing particle column density per size bin (color) as function of particle radius. Furthermore, instead of the snapshot at 10^4 yr we show $2 \cdot 10^6$ yr. The gray line shows the size above which particles can potentially contribute to planetesimal formation.

within the length $\ell_r = l_{\mathrm{corr}}$, and the particles that would drift the radial distance $\left|v_{\mathrm{drift}}(t_0, \mathrm{St})\right| \tau$ during the time τ are also concentrated within $\ell_r = l_{\mathrm{corr}}$. We add the factor $4\pi/3$ because these particles are more likely to concentrate into

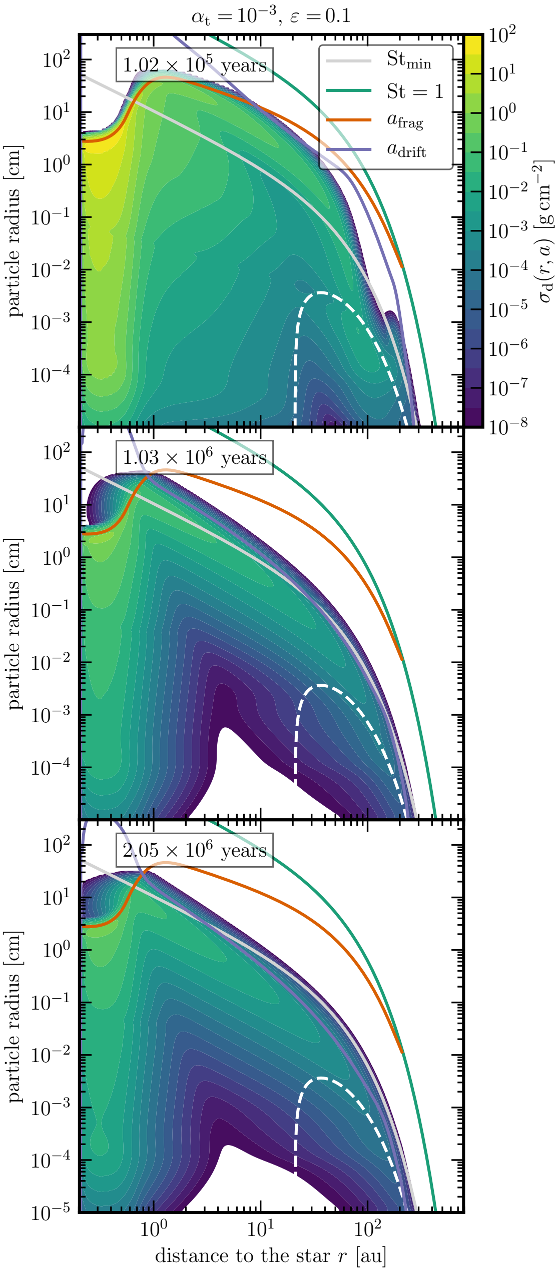

Figure A.4: Same as Fig. 2.3 but showing particle column density per size bin (color) as function of particle radius. Furthermore, instead of the snapshot at 10^4 yr we show $2 \cdot 10^6$ yr. The gray line shows the size above which particles can potentially contribute to planetesimal formation.

a spherical shape than a cubic one. The condition for planetesimal formation then reads

$$\rho_{\mathrm{Hill}} \le \rho_{\mathrm{peb,l_c}} \approx \frac{\varepsilon}{(4\pi/3)\ell_z\ell_r\ell_\varphi/(2\pi r)} \sum_{\mathrm{St_{min}}\le\mathrm{St}\le\mathrm{St_{max}}} \left(\int_{r-d_r/2}^{r+d_r/2} \Sigma_{\mathrm{peb}}(t_1,\mathrm{St})\,\mathrm{d}r + \underbrace{\int_{t_1}^{t} \Sigma_{\mathrm{peb}}(t,\mathrm{St})\left|v_{\mathrm{drift}}(t,\mathrm{St})\right|\mathrm{d}t}_{\approx \Sigma_{\mathrm{peb}}(t_0,\mathrm{St})\left|v_{\mathrm{drift}}(t_0,\mathrm{St})\right|\tau} \right). \tag{A.16}$$

The second term will mostly dominate the first term. The expression

$$\frac{4\pi}{3} l_{\mathrm{corr}}^3 \rho_{\mathrm{Hill}} = m_{\mathrm{p}} \tag{A.17}$$

gives the resulting planetesimal mass (Klahr & Schreiber, 2015; Schreiber, 2018) and, by neglecting the first term, we obtain the same condition as in Eq. (2.5).

The timescale over which the concentration will occur is assumed to be the lifetime of these structures, $\tau = \tau_{\mathrm{l}}$. Since we need a local criterion to make the model work, we have to assume that the particle flux does not change significantly over τ, or if it does, that it will still lead to the same result of either reaching or not reaching Hill density.

B Additional information on Chapter 3

B.1 Photoevaporation

For the gas loss rate due to photoevaporation we follow Picogna et al. (2019) (X-ray and EUV). Note that carbon depletion can have significant effects (Wölfer et al., 2019) which we will not take into account. For the profile provided by Picogna et al. (2019) we used the scaling with star mass from Owen et al. (2012). The equations presented in this section are only for gas, but do not remove particles from the simulation. For the sake of brevity, we define

$$x = 0.7 \frac{r}{\mathrm{au}} \frac{M_\odot}{M_\star}. \tag{B.18}$$

The photoevaporation profile is given by

$$\dot{\Sigma}_{\mathrm{w}} \propto \frac{1}{x^2} \prod_{j=-1}^{5} 10^{c_j \lg(x)^{j+1}} \cdot \sum_{i=0}^{5} (i+1) \cdot c_i \frac{\ln(x)^i}{\ln(10)^i} \tag{B.19}$$

with parameters

$$\begin{aligned} c_{-1} &= -\ \ 2.8562 \\ c_0 &= \ \ \ \ 5.7248 \\ c_1 &= -11.4721 \\ c_2 &= \ \ 16.3587 \\ c_3 &= -12.1214 \\ c_4 &= \ \ \ \ 4.3130 \\ c_5 &= -\ \ 0.5885 \end{aligned} \tag{B.20}$$

The expression is normalized such that the total mass loss rate

$$\dot{M}_{\mathrm{X}} = \int_0^\infty 2\pi r \dot{\Sigma}_{\mathrm{w}} \, \mathrm{d}r \tag{B.21}$$

is given via

$$\begin{aligned} &\lg\left(\frac{\dot{M}_{\mathrm{X}}}{M_\odot/\mathrm{yr}}\right) \\ &= A_{\mathrm{L}} \cdot \exp\left\{\frac{1}{C_{\mathrm{L}}}\left[\ln\left(\lg\left(\frac{L_{\mathrm{X}}}{\mathrm{erg/s}}\right)\right) - B_{\mathrm{L}}\right]^2\right\} + D_{\mathrm{L}}, \end{aligned} \tag{B.22}$$

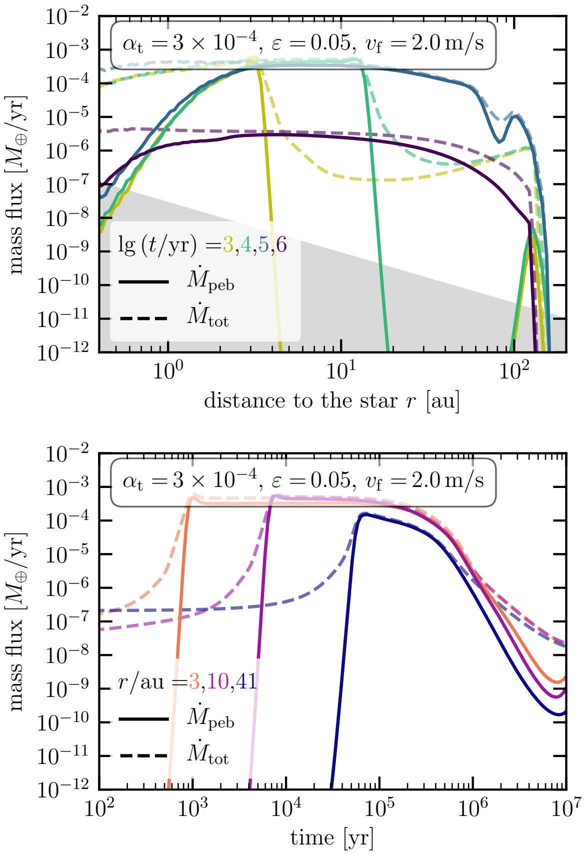

Figure B.5: Pebble flux in units of Earth masses per year for different times as a function of disk radius (upper panel) and as a function of time for different disk locations (lower panel). Here, we show data from the accretion heating simulation (most appealing case, see last row in Tab. 3.1). Solid lines show the pebble flux using the smoothing function Eq.(3.30), dashed lines show the total flux, i.e. taking all solid material into account except planetesimals. For the upper panels, sub-critical fluxes are marked by the gray zone, which are shown in the respective colors in the lower panels.

with parameters

$$\begin{aligned} A_\mathrm{L} &= -2.7326 \\ B_\mathrm{L} &= 3.3307 \\ C_\mathrm{L} &= -2.9868 \cdot 10^{-3} \\ D_\mathrm{L} &= -7.2580. \end{aligned} \tag{B.23}$$

Outside of $120\,\mathrm{au} \cdot M_\star/(0.7 M_\odot)$ we set

$$\dot{\Sigma}_\mathrm{w}\left(r > 120\,\mathrm{au}\frac{M_\star}{0.7 M_\odot}\right) = 3 \cdot 10^{-15}\,\mathrm{g\,cm^{-2}\,s^{-1}} \tag{B.24}$$

due to external FUV radiation.

Also for the case of an inner hole, we follow Picogna et al. (2019). The hole radius r_h is implicitly defined via the radially integrated midplane gas number density

$$\int_0^{r_\mathrm{h}} \frac{\Sigma_\mathrm{g}}{\sqrt{2\pi} h_\mathrm{g} m_\mathrm{g}}\,\mathrm{d}r = 10^{22}\,\mathrm{cm}^{-2}. \tag{B.25}$$

The profile with inner hole becomes

$$\dot{\Sigma}_{\mathrm{w,h}} \propto \frac{a_{\mathrm{h}}}{2\pi r/\mathrm{au}} b_{\mathrm{h}}^{\delta x} \delta x^{c_{\mathrm{h}}-1} \left[\delta x \cdot \ln(b_{\mathrm{h}}) + c_{\mathrm{h}}\right], \tag{B.26}$$

where $\delta x = (r - r_{\mathrm{h}})/\mathrm{au}$ and the parameters are given by

$$\begin{aligned} a_{\mathrm{h}} &= 0.11843, \\ b_{\mathrm{h}} &= 0.99695, \\ c_{\mathrm{h}} &= 0.48835. \end{aligned} \tag{B.27}$$

The gas loss rate is normalized such that

$$1.12\dot{M}_{\mathrm{X}} = \int_0^\infty 2\pi r \dot{\Sigma}_{\mathrm{w,h}} \, \mathrm{d}r. \tag{B.28}$$

B.2 The case of the most appealing simulation including accretion heating

This Appendix concentrates on a special case with accretion heating that is linked to the size distribution of solids. Fig. B.5 shows the pebble flux as a function of disk radius at different snapshots and as a function of time at different disk radii. The interpretation of this Figure is similar to the one given in Lenz et al. (2019). I.e., once the critical flux for planetesimal formation is reached the flux is orders of magnitude larger than the critical value $\dot{M}_{\mathrm{cr}}$ (above the shaded areas in both panels). Photoevaporation (an effect not included in Lenz et al. (2019)) leads to a small increase

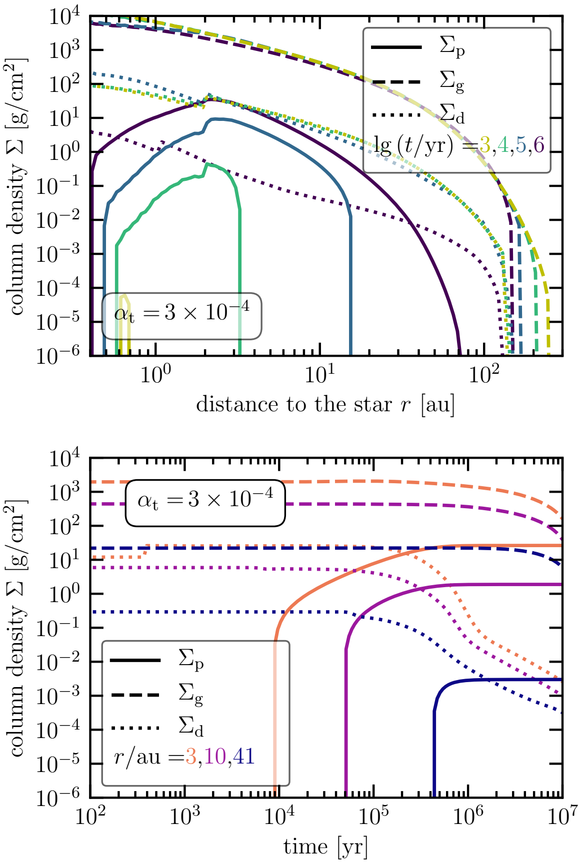

Figure B.6: Same as Fig. 3.5 but for the accretion heating simulation (most appealing case, see last row in Tab. 3.1).

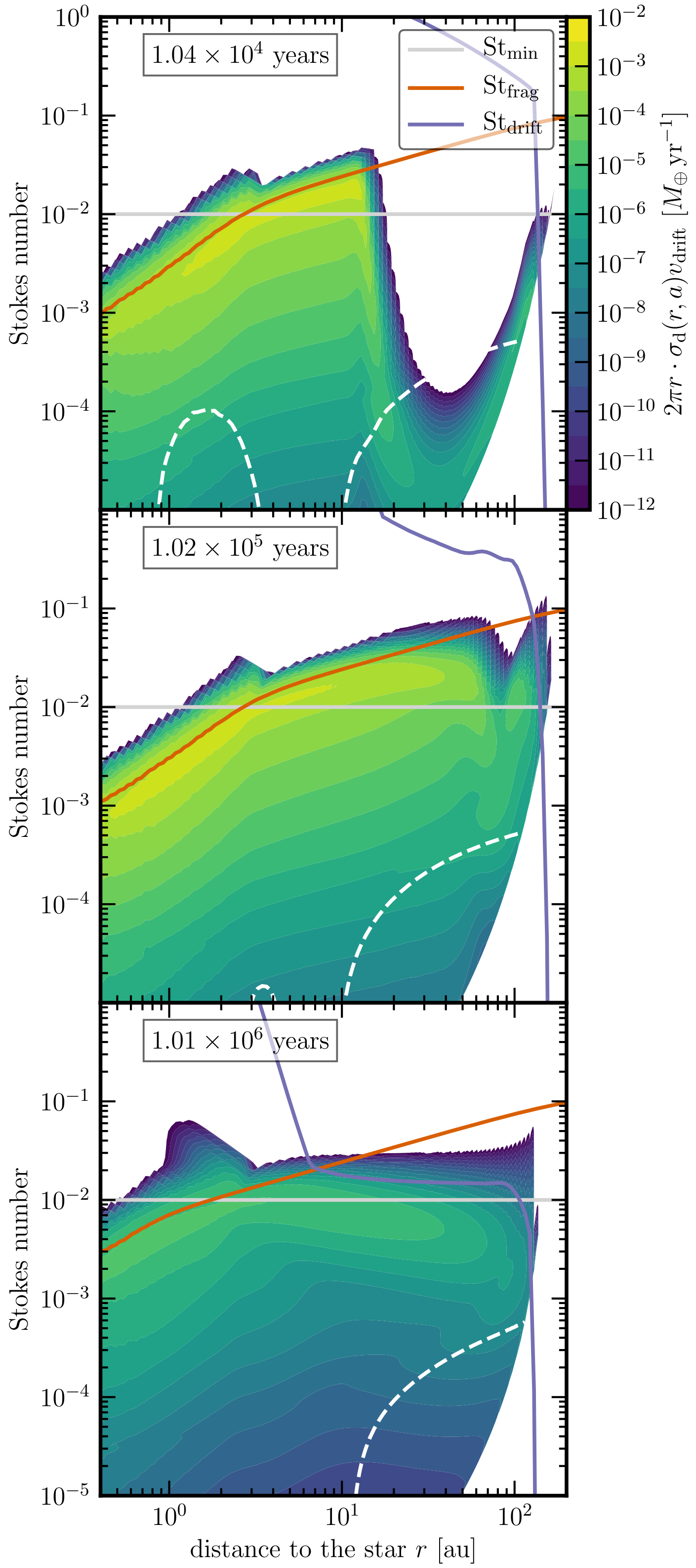

Figure B.7: As Fig. 3.6 but for an example run with accretion heating (most appealing simulation, see last row in Tab. 3.1).

of the pebble flux at late times, see the evolution after $\sim 8 \cdot 10^6$ yr in the lower panel of Fig. B.5. However, this increase has only a negligible effect on the final planetesimal population since the pebble flux has dropped by many orders of magnitude compared to its maximum value.

In Fig. B.6, since in this simulation the gas temperature depends on dust evolution, the ice line radially moves over time. Hence, the kink feature in planetesimals that is clearly visible at early times ($\sim 10^4$ yr) is smeared out at late times ($\sim 10^6$ yr). At all three locations shown in the bottom panel, planetesimal formation is going on for around $\sim 10^6$ yr with significant mass contributions. Note that a higher X-ray luminosity (up to $\sim 10^{30}\,\mathrm{erg\,s^{-1}}$) would not change the results by much as the disk would not vanish before ~ 2 Myr. At this time the planetesimal population has saturated already.

For our most appealing case which includes accretion heating (Fig. B.7), the higher gas midplane temperatures in the inner disk region are leading to smaller maximum Stokes numbers compared to a situation with pure radiation heating. At late times (~ 1 Myr), enough dust was converted into planetesimals causing the opacity to drop and thus gas temperatures are much lower than in the initial phase of disk evolution. As a result, higher Stokes numbers can be reached and significantly more planetesimals are formed within ~ 1 au. This effect is also visible in Figures B.5 and B.6.

C Additional information on Chapter 4

C.1 Sweep-up timescale and minimal feeding zone

Following Birnstiel et al. (2012), the sweep-up timescale of big grains with a number column density N_1 and N_0 of the small grains which are swept up is given by

$$\tau_{\mathrm{sw}} = \frac{N_0}{\dot{N}_1} = \frac{\lambda_{01}}{u_{01}} \frac{N_0}{N_1}, \tag{C.29}$$

where the mean free path of a big particle moving through a swarm of small grains is given by

$$\lambda_{01} = \frac{\sqrt{2\pi} h_{\mathrm{g}}}{N_0 \sigma_{01}} \tag{C.30}$$

with the gas pressure scale height $h_{\mathrm{g}} = c_{\mathrm{s}}/\Omega$ and the cross section ($a_1 \gg a_0$) $\sigma_{01} = \pi a_1^2$. In the fragmentation limited region the relative speed, u_{01}, is given by the absolute value of Eq. (C.47) and the sweep-up timescale reads

$$\tau_{\mathrm{sw,d}} = \frac{8\sqrt{2\pi}}{3 f_{\mathrm{fm}}} \frac{r}{Z c_{\mathrm{s}} \left| \frac{\partial \ln P}{\partial \ln r} \right|}. \tag{C.31}$$

In the case that turbulent relative velocities dominate, the relative velocity in the fragmentation limited region is

$$v_{\mathrm{turb}} = \frac{3}{2} \sqrt{\frac{\alpha_{\mathrm{t}} a_1 \rho_{\mathrm{m}} \pi}{\Sigma_{\mathrm{g}}}} c_{\mathrm{s}} = \sqrt{\frac{3}{2} f_{\mathrm{f}} v_{\mathrm{f}}} \tag{C.32}$$

according to Ormel & Cuzzi (2007) where the Stokes number of the bigger grain is much greater than of the small one. Then the timescale is

$$\tau_{\mathrm{sw,t}} = \frac{16\sqrt{f_{\mathrm{f}} \pi}}{9\sqrt{3} f_{\mathrm{fm}}} \frac{v_{\mathrm{f}}}{\alpha_{\mathrm{t}} Z \Omega c_{\mathrm{s}}}. \tag{C.33}$$

Turbulent velocities dominate whenever

$$\alpha_{\mathrm{t}} > \frac{\sqrt{2 f_{\mathrm{f}}}}{3\sqrt{3}} \frac{v_{\mathrm{f}}}{r\Omega} \left| \frac{\partial \ln P}{\partial \ln r} \right|, \tag{C.34}$$

which is at 1 au roughly equal to $4.13 \cdot 10^{-3}$ for a solar type star, $M_\star = M_\odot$, a temperature power-law index of $q = 0.5$, a gas column density power-law index of $\gamma = 1$, and a fragmentation threshold velocity of $v_{\mathrm{f}} = 10\,\mathrm{m/s}$.

If the condition $\dot{M}_{\mathrm{peb}} \geq m_{\mathrm{p}}/(\varepsilon\tau_{\mathrm{t}})$ is satisfied, the timescale at which new planetesimals are built is given by

$$\tau_{\mathrm{pl}} = \frac{m_{\mathrm{p}}}{\dot{M}_{\mathrm{peb}}}. \tag{C.35}$$

If $\tau_{\mathrm{pl}} \ll \min\{\tau_{\mathrm{sw,d}}, \tau_{\mathrm{sw,t}}\}$, fragments are too slowly swept up by big grains to contribute to the same planetesimal as the swarm to which they belonged to before the fragmentation event. For $\tau_{\mathrm{sw,d}}$, this yields the condition

$$\begin{aligned} \dot{M}_{\mathrm{peb}} \gg\ & 2.204 \cdot 10^{-12}\,\frac{\mathrm{M}_{\oplus}}{\mathrm{yr}} \cdot \frac{f_{\mathrm{fm}}}{0.75}\,\frac{Z}{10^{-2}}\,\frac{\left|\frac{\partial \ln P}{\partial \ln r}\right|}{2.75} \\ & \times \frac{\rho_{\mathrm{m}}}{1.2\,\mathrm{g\,cm^{-3}}} \left(\frac{a_{\mathrm{p}}}{50\,\mathrm{km}}\right)^{3} \left(\frac{T_{10}}{60\,\mathrm{K}}\right)^{1/2} \\ & \times \left(\frac{r}{10\,\mathrm{au}}\right)^{-1-q/2}, \end{aligned} \tag{C.36}$$

which is already well fulfilled by the critical flux of $m_{\mathrm{p}}/(\varepsilon\tau_{\mathrm{t}})$, but usually this critical flux is exceeded by a few orders of magnitude (Lenz et al., 2019). E. g., at 10 au for a trap lifetime of 100 orbits and a trapping efficiency $\varepsilon = 0.1$ this critical flux is of the order of $\sim 10^{-10}\,\mathrm{M}_{\oplus}/\mathrm{yr}$.

With help of the planetesimal formation timescale we can estimate the minimum feeding zone as

$$x_{\min} := -\int_{t_0}^{t_0+\tau_{\mathrm{pl}}} v_{\mathrm{drift}}\,\mathrm{d}t' \approx -\tau_{\mathrm{pl}} v_{\mathrm{drift}}. \tag{C.37}$$

The drift speed in fragmentation limited regions is roughly given by

$$v_{\mathrm{drift}} \approx\ -2.36 \cdot 10^{-4} f_{\mathrm{f}} \frac{10^{-3}}{\alpha_{\mathrm{t}}} \left(\frac{v_{\mathrm{f}}}{10\,\mathrm{m/s}}\right)^{2} \sqrt{\frac{r}{1\,\mathrm{au}}\,\frac{M_{\odot}}{M_{\star}}}\,\frac{\mathrm{au}}{\mathrm{yr}} \tag{C.38}$$

and for drift limited regions it is

$$v_{\mathrm{drift}} \approx\ -6.28 \cdot 10^{-2} f_{\mathrm{d}} \frac{Z}{10^{-2}} \sqrt{\frac{1\,\mathrm{au}}{r}} \sqrt{\frac{M_{\star}}{M_{\odot}}}\,\frac{\mathrm{au}}{\mathrm{yr}}. \tag{C.39}$$

C.2 Trying to model fragmentation effects

In this Appendix we will show some ideas on how one could model particle fragmentation and its effect on the survival probability. The model we present in this Appendix was not used to produce the results shown in this work.

It was shown by Birnstiel et al. (2012) that the evolution of a multi-particle system with a size distribution spreading from micron sized dust to pebble sized objects can be treated as a two-population system with a flux dominant big species and a monomer species. Since the pebble swarm will be dominated by a representative particle size (Birnstiel et al., 2012), fragmentation occurs due to collisions between swarm particles. The fragmentation loss term in the Smoluchowski equation (von Smoluchowski, 1916) gives for a representative size that the number density decreases according to

$$\dot{n} = -p_{\mathrm{f}} \Delta v_{\mathrm{r}} \sigma_{\mathrm{r}} n_{\mathrm{r}} n. \tag{C.40}$$

Here, n is number of monomers per volume in a pebble swarm with origin r_0 at radius r. Since in the most cases the size distributions are top-heavy (e.g. Birnstiel et al., 2011; Birnstiel et al., 2012) and collisions lead to fragmentation for large collision partners, the number density of collision partners n_{r} is the one of representative particle species of the large population. This is just an approximation because small particles that contribute to n do not necessarily lead to a fragmentation event when colliding with the largest particles.

The survival probability can be expressed in terms of the number density as $p(r, r_0) = n(r)/n(r_0)$ which leads to

$$\dot{p}_{\mathrm{f}} = -p_{\mathrm{f}} \Delta v_{\mathrm{r}}(r) \sigma_{\mathrm{r}}(r) n_{\mathrm{r}}(r) p(r, r_0)\,. \tag{C.41}$$

With help of this equation the last term of Eq. (4.5) can be expressed as

$$\frac{\partial p_\mathrm{f}}{\partial r} = \frac{\partial p_\mathrm{f}}{\partial t}\frac{1}{v_\mathrm{drift}} = -p_\mathrm{f}\frac{\Delta v_\mathrm{r}}{v_\mathrm{drift}}\sigma_\mathrm{r} n_\mathrm{r}(r) p(r, r_0)\,. \tag{C.42}$$

The representative size is given by the fragmentation limit (Birnstiel et al., 2012) in the particle radius space

$$a_\mathrm{frag} = f_\mathrm{f}\frac{2}{3\pi}\frac{\Sigma_\mathrm{g}}{\rho_\mathrm{m}\alpha_\mathrm{t}}\left(\frac{v_\mathrm{f}}{c_\mathrm{s}}\right)^2, \tag{C.43a}$$

and expressed as Stokes number

$$\mathrm{St}_\mathrm{frag} = \frac{f_\mathrm{f}}{3\alpha_\mathrm{t}}\left(\frac{v_\mathrm{f}}{c_\mathrm{s}}\right)^2, \tag{C.43b}$$

with $f_\mathrm{f} = 0.37$. The material density is given by ρ_m and the critical relative particle velocity for breakup by v_f. Thus the relative velocity and cross section is

$$\Delta v_\mathrm{r} = c_\mathrm{s}\sqrt{3\alpha_\mathrm{t}\mathrm{St}_\mathrm{frag}} = \sqrt{f_\mathrm{f}}v_\mathrm{f}\,, \tag{C.44}$$

$$\sigma_\mathrm{r}(r) = 4\pi a_\mathrm{frag}^2 = f_\mathrm{f}^2\frac{16}{9\pi}\left(\frac{\Sigma_\mathrm{g}(r)}{\rho_\mathrm{m}\alpha_\mathrm{t}}\right)^2\left(\frac{v_\mathrm{f}}{c_\mathrm{s}(r)}\right)^4, \tag{C.45}$$

and the number density of the representative background at the mid-plane is $n_\mathrm{r} = f_\mathrm{fm}\Sigma_\mathrm{d}/(\sqrt{2\pi}h_\mathrm{d}m_\mathrm{fr})$, with particle scale height h_d (Dubrulle et al., 1995) and the representative mass of particles in the fragmentation limit m_fr, which yields

$$\begin{aligned} n_\mathrm{r}(r) = {} & \frac{81 f_\mathrm{fm}\sqrt{\pi}\rho_\mathrm{m}{}^2\alpha_\mathrm{t}^3}{2^{11/2}f_\mathrm{f}^3}\sqrt{1+\frac{f_\mathrm{f}}{3\alpha_\mathrm{t}^2}\left(\frac{v_\mathrm{f}}{c_\mathrm{s}(r)}\right)^2} \\ & \times\frac{Z(r)\Omega(r)}{\Sigma_\mathrm{g}(r)^2 c_\mathrm{s}(r)}\left(\frac{c_\mathrm{s}(r)}{v_\mathrm{f}}\right)^6 . \end{aligned} \tag{C.46}$$

Here, we introduced the parameter f_fm which is the surface density ratio of the a_frag species to the total density of all species, Σ_d. Values of $f_\mathrm{fm} \approx 0.75$ seem to reproduce results from simulations with hundreds of particle mass bins (Birnstiel et al., 2012). The dust-to-gas ratio is denoted by $Z := \Sigma_\mathrm{d}/\Sigma_\mathrm{g}$. The dominant species in the fragmentation limited region has a drift speed of

$$v_\mathrm{drift} = -\frac{f_\mathrm{f}}{3\alpha_\mathrm{t}}\frac{v_\mathrm{f}^2}{r\Omega}\left|\frac{\partial\ln P}{\partial\ln r}\right|, \tag{C.47}$$

For the sake of brevity we define the *fragmentation coefficient* as

$$\begin{aligned} f_\mathrm{r}(r) &:= -p_\mathrm{f}\frac{\Delta v}{v_\mathrm{drift}}\sigma_\mathrm{r} n_\mathrm{r}(r) \\ &= \frac{27 p_\mathrm{f} f_\mathrm{fm}}{(2f_\mathrm{f})^{3/2}\sqrt{\pi}}\sqrt{1+\frac{f_\mathrm{f}}{3\alpha_\mathrm{t}^2}\left(\frac{v_\mathrm{f}}{c_\mathrm{s}}\right)^2}\frac{\alpha_\mathrm{t}^2}{v_\mathrm{f}^3}\frac{Zc_\mathrm{s}r\Omega^2}{\left|\frac{\partial\ln P}{\partial\ln r}\right|}. \end{aligned} \tag{C.48}$$

In the regions where planetesimal formation is active the Stokes number $\mathrm{St}_\mathrm{frag}$ is of the order of $\sim 10^{-1}$. Typical values of α_t are of the order of $\sim 10^{-3}$ such that $\mathrm{St}_\mathrm{frag}/\alpha_\mathrm{t} \gg 1$ and we can simplify the equation to

$$f_\mathrm{r}(r) \simeq \frac{27 p_\mathrm{f} f_\mathrm{fm}}{2^{3/2} f_\mathrm{f}\sqrt{3\pi}}\frac{\alpha_\mathrm{t}}{v_\mathrm{f}^2}\frac{Zr\Omega^2}{\left|\frac{\partial\ln P}{\partial\ln r}\right|}. \tag{C.49}$$

The resulting linear differential equation (DEQ) is

$$\frac{\partial p}{\partial r} = \left[\frac{\varepsilon}{d(r)} \cdot \theta(r_\mathrm{cr} - r) + f_\mathrm{r}(r) \cdot \theta(r_\mathrm{f} - r)\right] p. \tag{C.50}$$

The general solution is shown in Appendix C.3.

Sweep-up growth can be implicitly included in the model by reducing the fragmentation probability. As a simplification we will use a flux weighted average for St since the flux is the vital quantity in this model. The Stokes number in turn depends on r. In general St is increasing for larger radii and fixed size due to smaller gas densities, leading to less massive particles in the outer parts of the disk, i. e., at larger r_p, for fixed porosity. Accordingly, particles with sizes corresponding to $\mathrm{St}(r_\mathrm{p}) > \mathrm{St}_\mathrm{min}$ have also Stokes numbers larger than St_min for radii $r > r_\mathrm{p}$. For typical disk properties ($\alpha_\mathrm{t} \sim 10^{-4} - 10^{-3}$, $v_\mathrm{f} \sim 1 - 10\,\mathrm{m\,s^{-1}}$) the size barriers keep the particles so small that their Stokes numbers are well below $\mathrm{St}_\mathrm{max} \approx 10$, except at the very outer edge of the disk where the gas density drops steeply. Combining the last two thoughts means that the survival probability p of particles with $\mathrm{St}_\mathrm{min} < \mathrm{St}(r_\mathrm{p}) < \mathrm{St}_\mathrm{max}$ is affected by planetesimal formation within the *entire* planetesimal formation zone extended from r_p to r_cr. But all these aspects depend on disk properties, e. g., the local dust and gas density.

C.3 Survival Probability Solution

The solution to the DEQ (4.5) can be obtained by separation of variables and yields for $r \le r_0$

$$p(r, r_0) = \begin{cases} p(r_\mathrm{f}, r_0) \cdot \exp - \displaystyle\int_r^{\min(r_0, r_\mathrm{f})} \left(\frac{\varepsilon}{d(r')} + f_\mathrm{r}(r')\right) \mathrm{d}r' & , r \le r_\mathrm{f} \\ p(r_0) \cdot \exp - \displaystyle\int_r^{\min(r_0, r_\mathrm{cr})} \frac{\varepsilon}{d(r')} \mathrm{d}r' & , r_\mathrm{f} < r \le r_\mathrm{cr} \\ p(r_0) & , r > r_\mathrm{cr} \end{cases} \tag{C.51a}$$

but note that for positions further in than their origin ($r \le r_0$) *and* within the planetesimal formation zone with fragmentation ($r \le r_\mathrm{f}$) it yields

$$p(r, r_0) = \begin{cases} p(r_0) \cdot \exp - \displaystyle\int_r^{r_0} \left(\frac{\varepsilon}{d(r')} + f_\mathrm{r}(r')\right) \mathrm{d}r' & , r_0 \le r_\mathrm{f} \\ p(r_\mathrm{f}, r_0) \cdot \exp - \displaystyle\int_r^{r_\mathrm{f}} \left(\frac{\varepsilon}{d(r')} + f_\mathrm{r}(r')\right) \mathrm{d}r' & , r_\mathrm{f} < r_0 \le r_\mathrm{cr} \\ p(r_\mathrm{f}, r_0) \cdot \exp - \displaystyle\int_r^{r_\mathrm{f}} \left(\frac{\varepsilon}{d(r')} + f_\mathrm{r}(r')\right) \mathrm{d}r' & , r_0 > r_\mathrm{cr} \end{cases} \tag{C.51b}$$

where

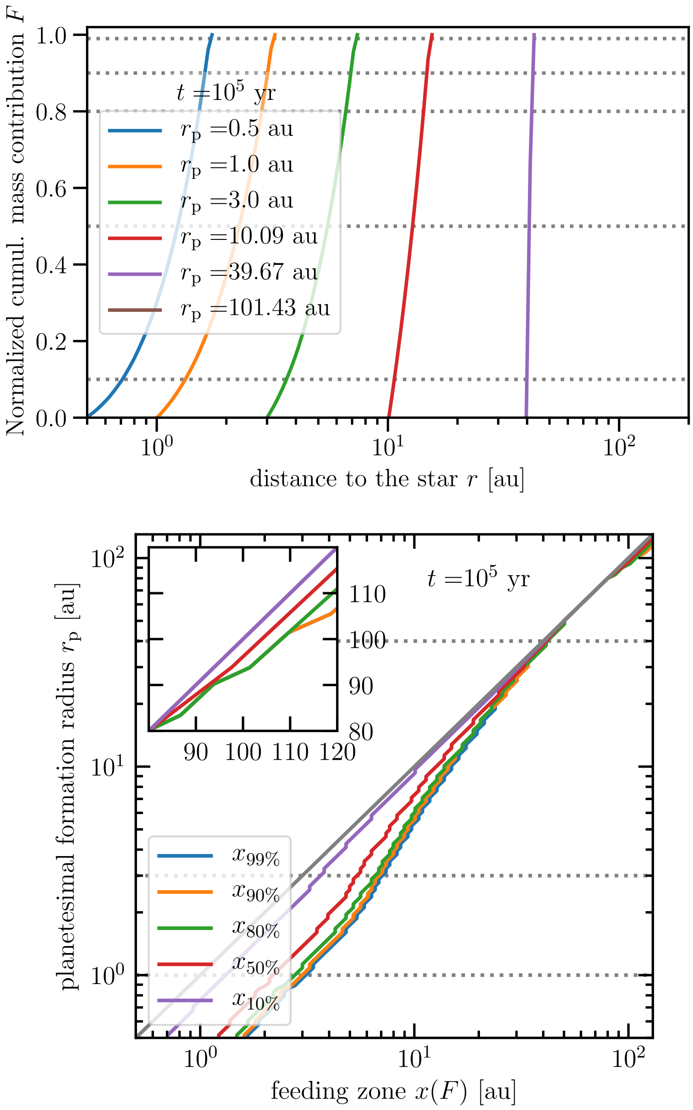

Figure C.8: Same plot as Fig. 4.4 but after 10^5 yr of evolution and for simulation S2.1. For the upper panel, no brown line for $r_p = 100\,$au is shown since no planetesimals are forming at this distance yet.

$$p(r_f, r_0) = \begin{cases} p(r_0) & , r_0 \leq r_f \\ p(r_0) \cdot \exp - \displaystyle\int_{r_f}^{r_0} \frac{\varepsilon}{d(r')} \, \mathrm{d}r' & , r_f < r_0 \leq r_{cr} \\ p(r_0) \cdot \exp - \displaystyle\int_{r_f}^{r_{cr}} \frac{\varepsilon}{d(r')} \, \mathrm{d}r' & , r_0 > r_{cr} \end{cases} \tag{C.51c}$$

is the survival probability at position r_f or, in the case of a particle born within r_f, it is just the initial probability, $p(r_0) := 1$. If we are only interested in the solution within the PFZ without fragmentation, i. e., for $r \leq r_0$ *and* $r_f \leq r < r_{cr}$, the solution is given by

$$p(r,r_0) = \begin{cases} p(r_0)\cdot \exp - \displaystyle\int_r^{r_0} \frac{\varepsilon}{d(r')}\,\mathrm{d}r' & , r_\mathrm{f} < r_0 \le r_\mathrm{cr} \\ \\ p(r_0)\cdot \exp - \displaystyle\int_r^{r_\mathrm{cr}} \frac{\varepsilon}{d(r')}\,\mathrm{d}r' & , r_0 > r_\mathrm{cr} \end{cases} . \tag{C.51d}$$

C.4 The effect of different times and conversion lengths

Feeding zones at different times

Qualitatively, all feeding zones should grow with time but the question is by how much and which effects are responsible for a given feeding zone time evolution.

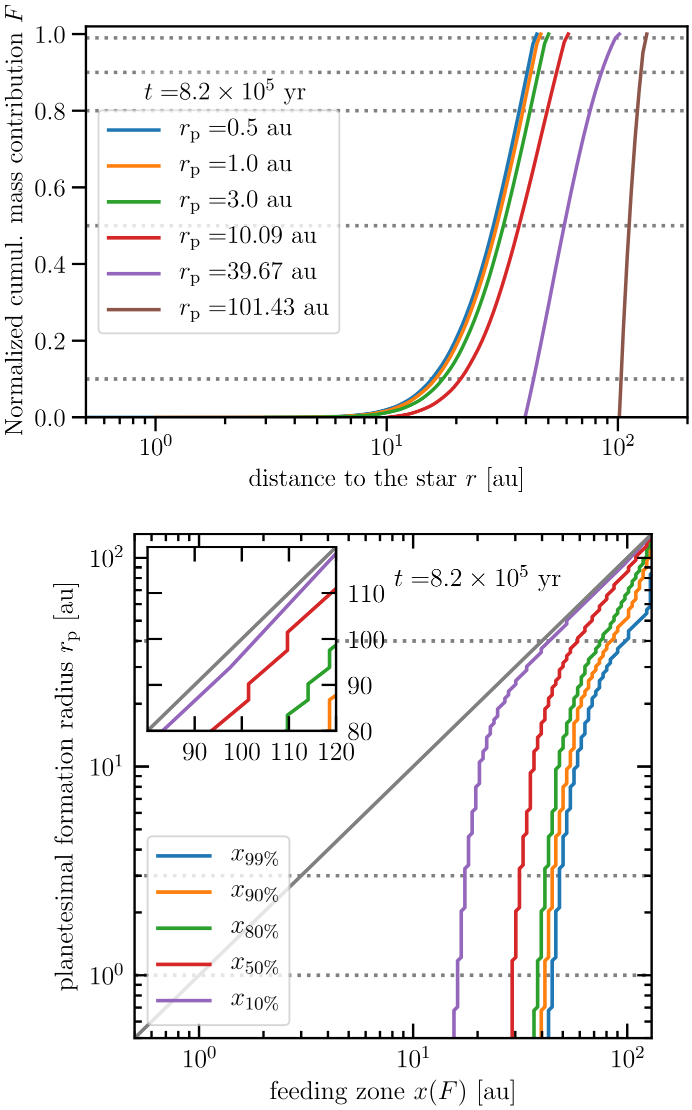

Figure C.9: Same plot as Fig. 4.4 but after $8.2\cdot 10^5$ yr of evolution and for simulation S2.1.

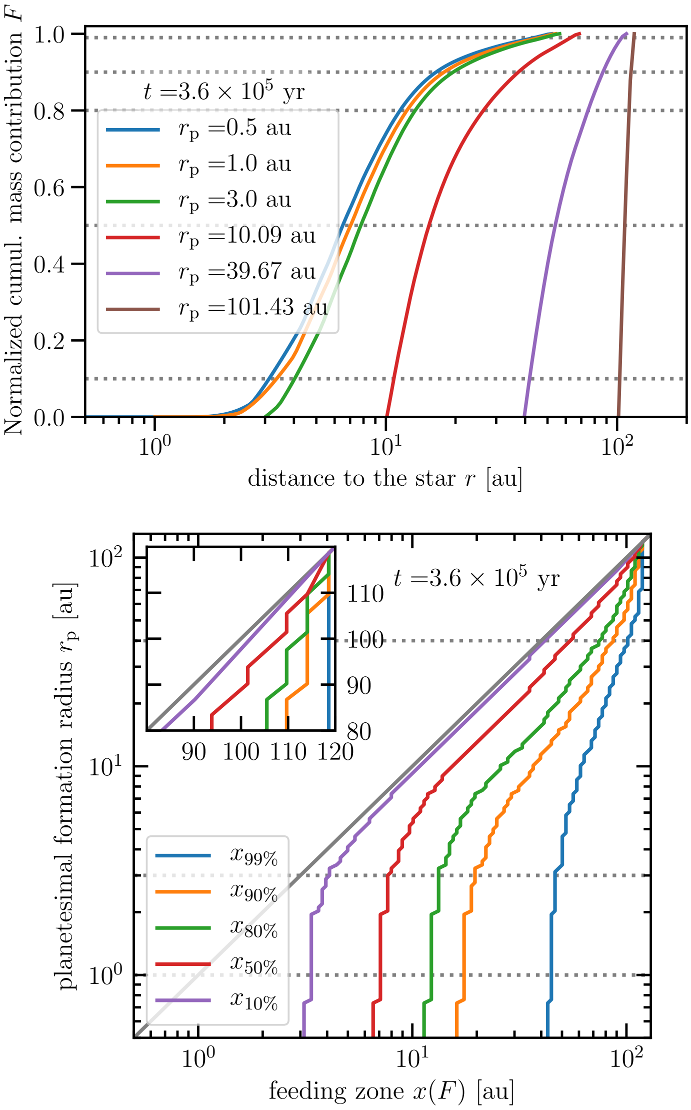

Figure C.10: Same plot as Fig. 4.4 but for simulation S1.2, i.e. a smaller pebble-to-planetesimal conversion length (higher planetesimal formation efficiency).

As an example, we show in Fig. C.8 the planetesimal formation feeding zones for simulation S2.1 (a mostly fragmentation limited disk, see Tab. 4.1) at 10^5 yr. For early times (here 10^5 yr), planetesimal formation is only active in the inner disk ($\lesssim 10$ au) since particle growth is too slow in the outer disk to produce early pebbles. Hence, planetesimal feeding zones are somewhat local in the early phase.

For the same simulation at later times the feeding zones are much wider, see Fig. C.9. If planetesimal formation is not too efficient, at late times (here $\gtrsim 8 \cdot 10^5$ yr) feeding zones can become very large since most of the mass from the inner regions drifted away already and only mass from the outer regions feeds in. However, in the outer disk (here $\gtrsim 40$ au) feeding zones are more local since these regions are much closer to the maximum radius of origin set by the initial conditions. Since the line density in the outer disk is dropping very quickly with disk radius, this effect is also expected for a setup where the initial dust profile is not cut off for Stokes number above a certain value. Within 30 au, the regions of origin of pebbles are almost the same which can be seen by the overlapping curves in the upper panel of Fig. C.9 and by almost vertical lines in the lower panel.

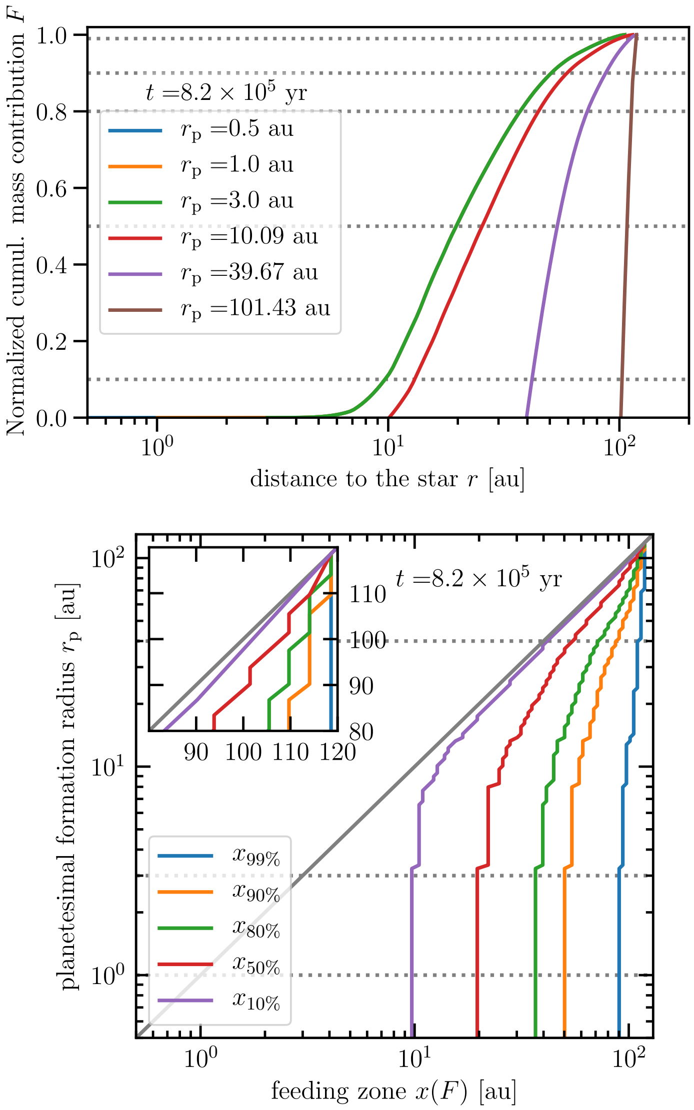

Figure C.11: Same plot as Fig. 4.4 but after $8.2 \cdot 10^5$ yr of evolution and for simulation S1.2.

The case of small conversion lengths

For small conversion lengths ℓ, i.e. large ε, the planetesimal formation feeding zones are expected to shrink since planetesimal formation is removing most of the inward moving mass. Hence, more local material will remain in comparison to planetesimal building blocks with origins at larger distances.

Disk with developing drift limited region

In Fig. C.10 the case of simulation S1.2 at $3.6 \cdot 10^5$ yr is shown. In this simulation the combination of α_t and v_f leads to a mostly drift limited disk. With $\varepsilon = 1$ planetesimal formation is very efficient leading to a particle-to-gas ratio reduction and thus smaller drift limits. As a result only the very inner part of the disk particle growth is limited by fragmentation. The trajectories of pebble swarm fronts are such that these particles spend only a small amount of time inside of ~ 3 au. This leads to the same feeding zone inside this region.

The planetesimal formation feeding zones for the same simulation (S1.2) but at time $8.2 \cdot 10^5$ yr is presented in Fig. C.11. In the top panel, the blue and orange lines overlap with the green one. This is related to those regions within which the feeding zone lines are straight vertical lines in the lower panel caused by pebbles drifting through very fast.

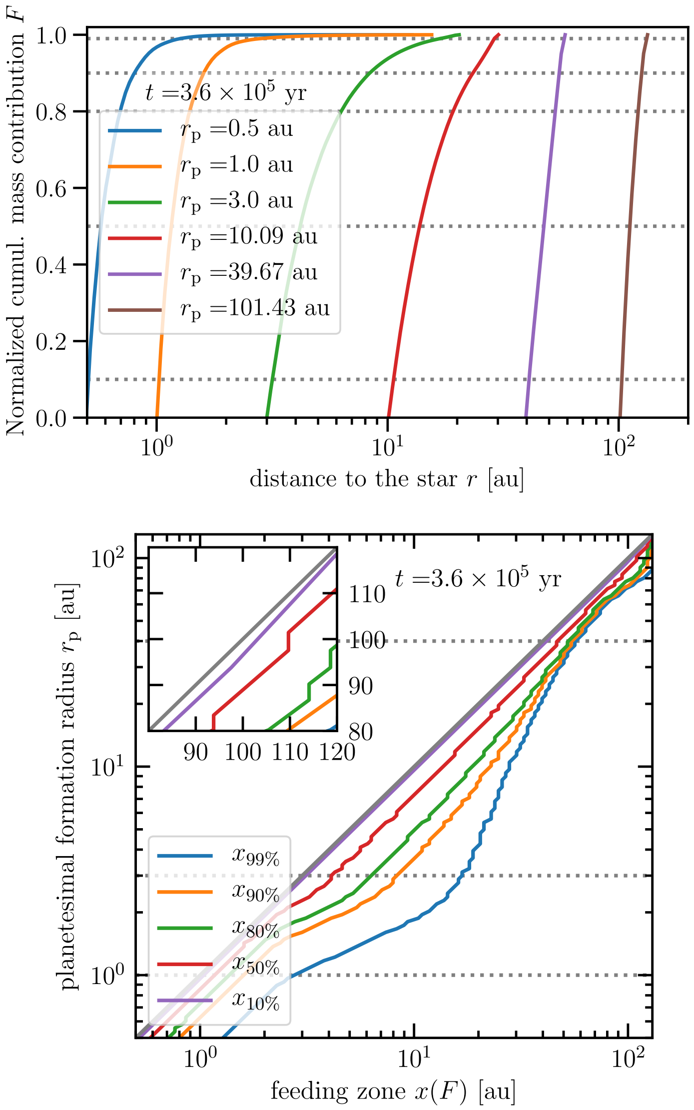

Figure C.12: Same plot as Fig. 4.4 but for simulation S2.2.

Compared to earlier times, see Fig. C.10, the same effects can be identified but the feeding zones are in general larger. This stems from the fact that particles had more time to drift inward which leads to a situation where the local material originates from much further out. This effect is stronger for $r_\mathrm{p} \lesssim 10\,\mathrm{au}$ because particle growth in the disk was not limited by fragmentation over a large amount of time or a large area. However, the high mass loss due to planetesimal formation is able to create somewhat smaller feeding zones relative to the local radial position. I.e., a lot of the inward drifting mass is converted into planetesimals before it can populate the regions further in.

Mostly fragmentation limited disk

The case of a mostly fragmentation limited disk with high planetesimal formation efficiency ($\varepsilon = 1$) is depicted in Fig. C.12. Only a small amount of mass reaches the innermost disk regions (see the blue and orange lines in the top panel) since planetesimal formation is very efficient. E.g., the blue line in the top panel has almost no slope for $r > 1\,\mathrm{au}$ which means that the mass contribution from these regions of origin is negligible. For high planetesimal formation efficiencies, the feeding zones show a situation that is much closer to in situ formation. Since most of the pebble mass is transformed into planetesimals on its way to the inner disk, within a few au planetesimal formation is very local. Around $\sim 10\,\mathrm{au}$ the initial line density of dust provides a lot of mass. This "drags" the feeding zone lines to somewhat larger distances, see lower panel in Fig. C.12.

As shown in Fig. C.13, basically the same features as in Fig. C.12 can be identified but more pronounced since particles had more time to drift inward.

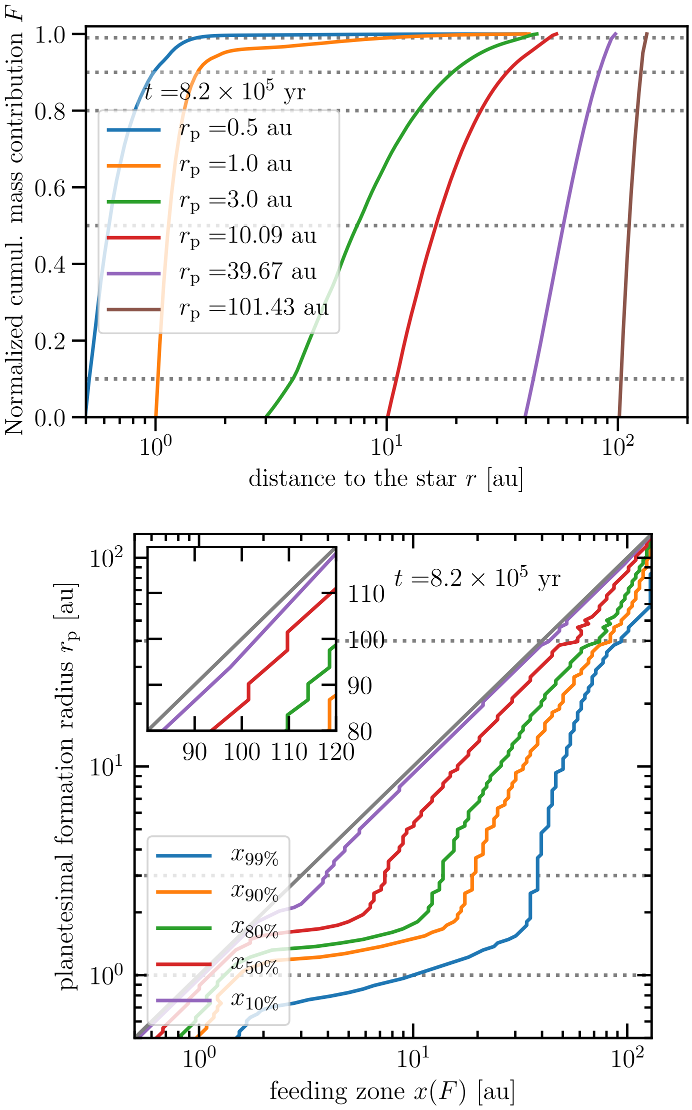

Figure C.13: Same plot as Fig. C.12 but after $8.2 \cdot 10^5$ yr of evolution.

D Mean free path

This Appendix explains how the mean free path of gas can be calculated. The notation used in this Appendix is shown in Tab. D.1. The mean free path is the mean distance molecules or particles travel between two collisions or scattering events. I. e., we define

$$\lambda := \frac{\text{sum of all free paths (per volume)}}{\text{\# of all particles (per volume)}} = \frac{\int \mathrm{d}^3p\, f \int_0^\infty t \|\boldsymbol{u}\|_2\, \mathcal{P}\, \mathrm{d}t}{\int \mathrm{d}^3p\, f}. \tag{D.52}$$

Table D.1: List of symbols and their meaning used in Appendix D.

symbol	meaning
#	number of something
$\delta(\cdot)$	Dirac-delta function
d_{mol}	molecule diameter
f	#particles per unit momentum & spatial volume
$\boldsymbol{F}_{\mathrm{ext}}$	external force vector
$\mathrm{k_B}$	Boltzmann's constant
λ	mean free path
m	mass of molecules
μ	reduced mass
n	#particles per spatial volume
$\dot{n}_{\mathrm{coll}}$	#collisions per unit time & unit volume
Ω_{sa}	solid angle
p_i	momentum of particle i
P	probability that a molecule survives the time t without suffering a collision
$\mathcal{P}\,\mathrm{d}t$	probability that a molecule suffers a collision within $[t, t+\mathrm{d}t]$ after surviving without a collision until t
$\boldsymbol{p}_i$	momentum vector of particle i
$\boldsymbol{p}_{\mathrm{rel}}$	relative momentum between two objects in the center of mass
$\boldsymbol{p}_{\mathrm{tot}}$	total momentum of two objects
σ	cross section
t	time
T	temperature
τ	mean time between collisions
$\boldsymbol{u}$	molecular velocity vector
v_{th}	mean thermal speed for a Maxwell-Boltzmann distribution
$\bar{v}$	mean speed
w	probability per unit time that a molecule suffers a collision
$\boldsymbol{x}$	position vector
$\lVert\cdot\rVert_2$	Euclidean norm

If $\boldsymbol{u}$ changes slowly enough with t, the former can be considered as time independent and one obtains

$$\lambda = \frac{n\bar{v}\tau}{n} = \bar{v}\tau. \tag{D.53}$$

The mean time between collisions is given by

$$\begin{aligned}\tau &= \frac{\text{\# of particles}}{\text{\# of colliding particles per unit time}} \\ &= \frac{1}{\text{probability per } \mathrm{d}t \text{ that a molecule suffers a collision}}.\end{aligned} \tag{D.54}$$

The first equality is proven in section D.4, the second is a simple definition.

The sink and source term for the number of particles in a specific momentum and spatial volume, i. e. f, is given by the collisional integral

$$\left(\frac{\partial f}{\partial t}\right)_{\mathrm{coll}} \mathrm{d}t\,\mathrm{d}^3x\,\mathrm{d}^3p = \left(\left(\frac{\partial f}{\partial t}\right)^{\mathrm{in}}_{\mathrm{coll}} - \left(\frac{\partial f}{\partial t}\right)^{\mathrm{out}}_{\mathrm{coll}}\right) \mathrm{d}t\,\mathrm{d}^3x\,\mathrm{d}^3p\,, \tag{D.55}$$

where $\left(\frac{\partial f}{\partial t}\right)^{\mathrm{out}}_{\mathrm{coll}} \mathrm{d}t\,\mathrm{d}^3x\,\mathrm{d}^3p$ $\left(\left(\frac{\partial f}{\partial t}\right)^{\mathrm{in}}_{\mathrm{coll}} \mathrm{d}t\,\mathrm{d}^3x\,\mathrm{d}^3p\right)$ is the number of collisions during the time between t and $t+\mathrm{d}t$ in which one of the *initial* (*final*) molecules is in $\mathrm{d}^3x\,\mathrm{d}^3p$ about $(\boldsymbol{x},\boldsymbol{p})$. The Boltzmann equation takes the form

$$\frac{\partial f}{\partial t}+\frac{\boldsymbol{p}}{m}\cdot\boldsymbol{\nabla}f+\boldsymbol{F}_{\mathrm{ext}}\cdot\frac{\partial f}{\partial\boldsymbol{p}}=\left(\frac{\partial f}{\partial t}\right)_{\mathrm{coll}}\,. \tag{D.56}$$

The total ($\boldsymbol{p}_{\mathrm{tot}}$) and relative ($\boldsymbol{p}_{\mathrm{rel}}$) momentum are defined as follows

$$\boldsymbol{p}_{\mathrm{tot}}:=\boldsymbol{p}_1+\boldsymbol{p}_2\,,\quad \boldsymbol{p}_{\mathrm{rel}}:=\mu(\boldsymbol{u}_1-\boldsymbol{u}_2)\,, \tag{D.57}$$

where the reduced mass is defined by

$$\mu:=\frac{m_1m_2}{m_1+m_2}\,. \tag{D.58}$$

The inverse transformation is given by

$$\boldsymbol{p}_1=\frac{\mu}{m_2}\boldsymbol{p}_{\mathrm{tot}}+\boldsymbol{p}_{\mathrm{rel}}\,,\quad \boldsymbol{p}_2=\frac{\mu}{m_1}\boldsymbol{p}_{\mathrm{tot}}-\boldsymbol{p}_{\mathrm{rel}}\,. \tag{D.59}$$

Furthermore, we have for the integration variables (Reif, 2009, p. 521)

$$\mathrm{d}^3p_1\,\mathrm{d}^3p_2=\left|\det\frac{\partial(\boldsymbol{p}_1,\boldsymbol{p}_2)}{\partial(\boldsymbol{p}_{\mathrm{tot}},\boldsymbol{p}_{\mathrm{rel}})}\right|\mathrm{d}^3p_{\mathrm{tot}}\,\mathrm{d}^3p_{\mathrm{rel}}=\begin{vmatrix}\frac{m_1}{m_1+m_2} & \frac{m_2}{m_1+m_2}\\ +1 & -1\end{vmatrix}^3\mathrm{d}^3p_{\mathrm{tot}}\,\mathrm{d}^3p_{\mathrm{rel}}=\mathrm{d}^3p_{\mathrm{tot}}\,\mathrm{d}^3p_{\mathrm{rel}}\,. \tag{D.60}$$

The collision integral gives the number of collisions for a particle with momentum $\boldsymbol{p}_1$. The number of collisions per unit time and unit volume is given by (Huang, 1987, p. 93)

$$\dot{n}_{\mathrm{coll}}(\boldsymbol{x}):=\int\mathrm{d}^3p_1\left(\frac{\partial f(\boldsymbol{x},\boldsymbol{p}_1,t)}{\partial t}\right)_{\mathrm{coll}}^{\mathrm{out}}=\int\mathrm{d}^3p_1\int\mathrm{d}^3p_2\int\mathrm{d}\Omega_{\mathrm{sa}}\|\boldsymbol{u}_1-\boldsymbol{u}_2\|_2\,\frac{\mathrm{d}\sigma}{\mathrm{d}\Omega_{\mathrm{sa}}}f_1f_2\,. \tag{D.61}$$

This expression can be interpreted as follows. For each combination of the integration variables $(\boldsymbol{p}_1,\boldsymbol{p}_2)$ the integrand represents the cylinder of interaction of a number of particles with momentum $\boldsymbol{p}_1$ colliding with particles with momentum $\boldsymbol{p}_2$ with base area σ and length $\|\boldsymbol{u}_1-\boldsymbol{u}_2\|_2\,t$ for a small time t. Integrates over all momenta and thus counts the collisions twice over because the collision integral arises as a sink term in the Boltzmann equation of both collision partners!

$$\#\text{colliding particles per unit time}=2\cdot\#\text{collisions per unit time}=2\cdot\frac{1}{2}\dot{n}_{\mathrm{coll}}=\dot{n}_{\mathrm{coll}} \tag{D.62}$$

According to Eq. (D.54) we obtain

$$\tau=\frac{n}{\dot{n}_{\mathrm{coll}}}. \tag{D.63}$$

D.1 Special case: Maxwell-Boltzmann distribution

The Maxwell-Boltzmann distribution is given by (Maxwell, 1860; Boltzmann, 1872)

$$f(\boldsymbol{u})=\frac{n}{(2\pi m\mathrm{k_B}T)^{3/2}}\exp\left(-\frac{m\boldsymbol{u}^2}{2\mathrm{k_B}T}\right) \tag{D.64}$$

leading to a mean thermal speed of

$$v_{\mathrm{th}}=\bar{v}:=\frac{\int\mathrm{d}^3p\,f\|\boldsymbol{u}\|_2}{\int\mathrm{d}^3p\,f}=\sqrt{\frac{8\mathrm{k_B}T}{\pi m}}. \tag{D.65}$$

If we assume that the total cross section of molecular collisions σ is insensitive to the energy of the collision, e. g. a purely geometrical of $\sigma=\pi d_{\mathrm{mol}}^2$, where d_{mol} is the molecular diameter, and we have thermal equilibrium, we can estimate $\dot{n}_{\mathrm{coll}}$. Transforming to the variables total ($\boldsymbol{p}_{\mathrm{tot}}$) and relative ($\boldsymbol{p}_{\mathrm{rel}}$) momentum — see Eq. (D.57) for the definitions, Eq. (D.59) for the inverse transformation, Eq. (D.60) for the transformation of the differentials — we find (Huang, 1987, p. 94)

$$\dot{n}_{\text{coll}} = \frac{n^2}{m(2\pi m k_B T)^3} \int d^3 p_{\text{tot}} \exp\left(-\frac{\boldsymbol{p}_{\text{tot}}^2}{4 m k_B T}\right) \tag{D.66}$$

$$\times \int d^3 p_{\text{rel}} \frac{\|\boldsymbol{p}_{\text{rel}}\|_2}{\mu} \exp\left(-\frac{\boldsymbol{p}_{\text{rel}}^2}{2\mu k_B T}\right) \underbrace{\int d\Omega_{\text{sa}} \frac{d\sigma}{d\Omega_{\text{sa}}}}_{=\sigma} . \tag{D.67}$$

The $\boldsymbol{p}_{\text{tot}}$-integral can be directly evaluated and gives $(4\pi m k_B T)^{3/2}$. The $\boldsymbol{p}_{\text{rel}}$-integral can be calculated in spherical coordinates with subsequent and reads $4\pi\mu(2k_B T)^2/2$. As for $m_1 = m_2 = m$ the reduced mass becomes $\mu = m/2$, we obtain

$$\dot{n}_{\text{coll}} = \sqrt{2}\sigma n^2 v_{\text{th}} . \tag{D.68}$$

Hence, the mean free path reads

$$\lambda = \tau \bar{v} = \frac{n}{\dot{n}_{\text{coll}}} \bar{v} = \frac{1}{\sqrt{2}} \frac{1}{n\sigma} . \tag{D.69}$$

D.2 Special case: all collision partners at rest

Let's now consider the case where we throw a ball into a forest — many times. Doing this so many times that we reach statistical significance, we can then calculate the mean of all free paths. In the following we choose the geometrical case and the x-direction for the direction of the particle moving with $\bar{v}$. Particle 1 (the "ball") has the specific velocity $\bar{v}$ in x-direction

$$f_1 = \delta(m u_x - m\bar{v}) \left[\prod_{i=2}^{3} \delta(m u_i) \right] n \tag{D.70}$$

and all collision partners are at rest (the "forest")

$$f_2 = \left[\prod_{i=1}^{3} \delta(m u_i) \right] n . \tag{D.71}$$

Via Eq. (D.61) the collision time becomes

$$\tau = \frac{n}{\dot{n}_{\text{coll}}} = \frac{1}{\bar{v}} \frac{1}{n\sigma} \tag{D.72}$$

giving the mean free path which was already derived by Clausius (1859, his Eq. (6))

$$\lambda = \tau \bar{v} = \frac{n}{\dot{n}_{\text{coll}}} \bar{v} = \frac{1}{n\sigma} . \tag{D.73}$$

D.3 Special case: always direct collisions

This scenario gives the minimum mean free path for a geometrical cross section. We can always choose the coordinate system such that the collision occurs along the x-axis. Assuming that all molecules move with speed $\bar{v}$, we get

$$f_1 f_2 = n^2 \delta\left(p_{1,x} - \bar{v}\right) \delta\left(p_{1,y}\right) \delta\left(p_{1,z}\right) \cdot \delta\left(p_{2,x} + \bar{v}\right) \delta\left(p_{2,y}\right) \delta\left(p_{2,z}\right) . \tag{D.74}$$

The sign flip in the Dirac-delta functions in the x-direction assures that the particles are colliding. This situation directly leads to

$$\dot{n}_{\text{coll}} = 2\bar{v}\sigma n^2 , \tag{D.75}$$

giving a mean free path of

$$\lambda = \frac{n}{\dot{n}_{\mathrm{coll}}}\bar{v} = \frac{1}{2}\frac{1}{n\sigma}. \tag{D.76}$$

D.4 τ equals the inverse of the probability that a molecule suffers a collision per unit time

This section follows Reif (2009, pp. 463). To describe collisions, we first define

$$P(t) = \text{probability that a molecule survives the time } t \text{ without suffering a collision} \tag{D.77}$$

and

$$w\,\mathrm{d}t = \text{probability that a molecule suffers a collision within } [t, t+\mathrm{d}t]. \tag{D.78}$$

One can derive a differential equation which can be solved for a given w. Therefore, the probability that a molecule survives the time $t+\mathrm{d}t$ without suffering a collision is given by the same probability for the time t times the probability to survive $\mathrm{d}t$ without a collision:

$$P(t+\mathrm{d}t) = P(t)\cdot(1-w\,\mathrm{d}t)$$

which can be written in the form

$$P(t) + \frac{\mathrm{d}P}{\mathrm{d}t}\mathrm{d}t = P(t) - P(t)w\,\mathrm{d}t.$$

This leads to the simple differential equation

$$\frac{1}{P}\frac{\mathrm{d}P}{\mathrm{d}t} = -w. \tag{D.79}$$

The DEQ is solved by

$$P(t) = \exp\left(-\int_0^t w(t')\,\mathrm{d}t'\right). \tag{D.80}$$

We further define

$$\begin{aligned}\mathcal{P}\,\mathrm{d}t &= \text{probability that a molecule suffers a collision within } [t, t+\mathrm{d}t] \text{ after surviving without a collision until } t && \text{(D.81)}\\ &= P(t) - P(t+\mathrm{d}t) = -\frac{\mathrm{d}P}{\mathrm{d}t}\mathrm{d}t && \text{(D.82)}\end{aligned}$$

which gives

$$\mathcal{P}(t) = \exp\left(-\int_0^t w(t')\,\mathrm{d}t'\right)w(t). \tag{D.83}$$

The mean time between collisions is defined as

$$\tau = \bar{t} := \int_0^\infty \mathcal{P}(t)t\,\mathrm{d}t. \tag{D.84}$$

If the speed of the molecules changes slowly enough (slower than $\sim w^{-1}$) one can consider w to be constant which allows to solve the integral giving

$$\begin{aligned}\tau &= \int\limits_0^\infty \exp(-wt) wt \, \mathrm{d}t \overset{\alpha := wt}{=} \frac{1}{w} \int\limits_0^\infty \exp(-\alpha)\alpha \, \mathrm{d}\alpha \\ &= \frac{1}{w} \left\{ \left[-\exp(-\alpha)\alpha \right]_0^\infty - \int\limits_0^\infty (-1) \exp(-\alpha) \right\} = \frac{1}{w} \left[-(\alpha+1) \exp(-\alpha) \right]_0^\infty \\ &= \frac{1}{w}.\end{aligned} \tag{D.85}$$

E Growth timescale and drift limit

In this section I first present the default method of deriving the growth timescale. In the second section I will show another approach which differs by a factor of 2 in the result of τ_{growth}.

E.1 The classical path of deriving τ_{growth}

We can define a growth timescale by assuming perfect sticking upon collisions,

$$\tau_{\text{growth}} := \frac{a}{\dot{a}}. \tag{E.86}$$

This timescale describes the typical time during which the size is doubled. I will now show the approach presented by Stepinski & Valageas (1997) and Kornet et al. (2001) to calculate the growth rate $\dot{a}$. Particles prefer collisions with the largest and heaviest particles as the mass gain from the collision rate is the greatest for these kind of collisions. Hence, monodisperse growth mirrors the behavior of the dominant particle species in a colloidal system very well if fragmentation plays only a minor role. For *monodisperse* coagulation, i. e. all particles have the same size, which is a good approximation for the growth of particles dominating the total mass at a specific radius in the disk, the mass growth can be expressed as

$$\dot{m} \simeq \frac{m}{\tau} = \rho_{\mathrm{d}} \sigma \Delta v, \tag{E.87}$$

with the geometrical cross section $\sigma = 4\pi a^2$ and assuming the collision timscale to be $\tau = n\sigma\Delta v$. Note that this way we obtain the same result as Eq. (E.96) apart from a factor of $1/2$. Assuming constant porosity (ρ_{m} constant) we have $\mathrm{d}m/\mathrm{d}a = 4\pi\rho_{\mathrm{m}}a^2$ which gives through the chain rule $\dot{m} = 4\pi\rho_{\mathrm{m}}a^2\dot{a} = \sigma\rho_{\mathrm{m}}\dot{a}$. Using Eq. (E.87), this gives the growth rate

$$\dot{a} = \Delta v \frac{\rho_{\mathrm{d}}}{\rho_{\mathrm{m}}} \tag{E.88}$$

and the growth timescale becomes

$$\tau_{\text{growth}} = \frac{a\rho_{\mathrm{m}}}{\rho_{\mathrm{d}}\Delta v}. \tag{E.89}$$

We further assume, for simplicity, that we have a relative velocity given by turbulent motion of equal sized particles for $\mathrm{St} \ll 1$, i. e. $\Delta v \simeq c_{\mathrm{s}} \sqrt{3\alpha_{\mathrm{t}}\mathrm{St}}$ (Ormel & Cuzzi, 2007). Assuming the Epstein regime we have a Stokes number of

$$\mathrm{St}_{\mathrm{Ep}} = \frac{\rho_{\mathrm{m}}}{\rho_{\mathrm{g}}} \frac{a}{v_{\mathrm{th}}} \Omega. \tag{E.90}$$

Evaluating this for *mid-plane* values $\rho_{\mathrm{g},0}(r) = \Sigma_{\mathrm{g}}(r)/(h_{\mathrm{g}}\sqrt{2\pi})$ (g $\leftrightarrow$ d for the dust) reads

$$\mathrm{St}_{\mathrm{Ep},0} = \frac{\pi}{2} \frac{a\rho_{\mathrm{m}}}{\Sigma_{\mathrm{g}}}. \tag{E.91a}$$

The same way we obtain for the Stokes regime at the mid-plane

$$\mathrm{St}_{\mathrm{St},0} = \frac{\sqrt{8\pi}}{9}\frac{a^2\rho_{\mathrm{m}}c_{\mathrm{s}}}{\Sigma_{\mathrm{g}}\nu_{\mathrm{mol}}} = \frac{2\pi}{9}\frac{a^2\rho_{\mathrm{m}}}{\Sigma_{\mathrm{g}}\lambda_{\mathrm{g}}}. \tag{E.91b}$$

Inserting $\Delta v \simeq c_{\mathrm{s}}\sqrt{3\alpha_{\mathrm{t}}\mathrm{St}}$ and (E.91a) or (E.91b) (mid-plane values) into (E.89) gives for $\mathrm{St} \gg \alpha_{\mathrm{t}}$

$$\tau_{\mathrm{growth}} \simeq \frac{\sqrt{2\pi}}{\sqrt{3}\Omega\Sigma_{\mathrm{d}}}\frac{a\rho_{\mathrm{m}}}{\sqrt{\cancel{\alpha_{\mathrm{t}}\mathrm{St}}+\mathrm{St}^2}} = \begin{cases} \sqrt{\frac{8}{3\pi}}\frac{1}{Z\Omega} & \text{Epstein drag} \\ 3\sqrt{\frac{3}{2\pi}}\frac{\lambda_{\mathrm{g}}}{aZ\Omega} & \text{Stokes drag} \end{cases} \approx \begin{cases} \frac{1}{Z\Omega} & \text{Epstein drag} \\ \frac{2\lambda_{\mathrm{g}}}{aZ\Omega} & \text{Stokes drag} \end{cases}. \tag{E.92}$$

E.2 The “new” method

By considering only coagulation, i. e., setting the fragmentation kernel in Eq. A.5b to $F(m', m'') \equiv 0$, a tremendous simplification of the Smoluchowski equation is possible. Following Brauer (2008), we are assuming a mass distribution with only one mass $m_0(t)$ with constant mass density ρ:

$$n_{\mathrm{m}}(m,t) = \frac{\rho}{m_0(t)}\delta(m - m_0(t)) \; . \tag{E.93}$$

Inserting this into Eq. (A.5a) and integrating over all masses m, using the number density

$$n = \int_0^\infty n_{\mathrm{m}}(m,t)\,\mathrm{d}m \overset{(\mathrm{E.93})}{=} \frac{\rho}{m_0(t)}, \tag{E.94}$$

we get

$$\dot{n} = -\frac{1}{2}K(m_0, m_0)n(m_0)^2. \tag{E.95}$$

This leads via Eq. (E.94) to

$$\dot{m}_0(t) = \frac{1}{2}\rho K(m_0, m_0) = \frac{1}{2}\rho\sigma\Delta v \tag{E.96}$$

which gives

$$\dot{a} = \frac{1}{2}\cdot\Delta v\frac{\rho_{\mathrm{d}}}{\rho_{\mathrm{m}}} \overset{z=0}{=} \frac{1}{2}\cdot\Delta v\frac{\Sigma_{\mathrm{d}}}{\sqrt{2\pi}h_{\mathrm{d}}\rho_{\mathrm{m}}}. \tag{E.97}$$

Since we assume perfect sticking, the kernel is given by $K(m_0, m_0) = \Delta v(m_0, m_0)\cdot\sigma(m_0, m_0)$. Due to the fact that particles always double their mass in collisions, the number density is decreasing whereby the mass of individual particles is increasing while the system evolves. Note that compared to canonical derivations (Stepinski & Valageas, 1997; Kornet et al., 2001) there is a factor of $1/2$ different in Eq. (E.96). The only difference in comparison to the former Section is Eq. (E.96) compared to Eq. (E.87). In the canonical approach, a collision time $\tau = \lambda/\Delta v$ is used where the mean free path is $\lambda = 1/(n\sigma\Delta v)$. Here, the factor of $1/2$ is naturally included in the Smoluchowski equation and thus also shows up in the result for the mass growth rate and in the growth timescale as a factor of 2. The approach presented in this Section is based on the Smoluchowski equation which is also used in the simulations presented in this thesis. The canonical approach of the previous Section depends on the definition of the collision time and the mean free path as well as the connection between the mean and relative particle speed.

With the growth rate presented in this Section, the growth timescale becomes

$$\tau_{\mathrm{growth}} \simeq \frac{\sqrt{2\pi}}{\sqrt{3}\Omega\Sigma_{\mathrm{d}}} \frac{a\rho_{\mathrm{m}}}{\mathrm{St}} = \begin{cases} 4\sqrt{\dfrac{2}{3\pi}} \dfrac{1}{Z\Omega} & \text{Epstein drag} \\ \\ 3\sqrt{\dfrac{6}{\pi}} \dfrac{\lambda_{\mathrm{g}}}{aZ\Omega} & \text{Stokes drag} \end{cases} . \tag{E.98}$$

With help of Eq. E.98 the drift limited can be derived. For particles with $\mathrm{St} \ll 1$, the drift velocity is given by

$$v_{\mathrm{drift}} = \mathrm{St}\frac{h_{\mathrm{g}}}{r}\frac{\partial \ln P}{\partial \ln r} c_{\mathrm{s}}. \tag{E.99}$$

The drift timescale is defined as

$$\tau_{\mathrm{drift}} = \frac{r}{|v_{\mathrm{drift}}|}. \tag{E.100}$$

Setting the growth timescale, Eq. (E.98), and the drift timescale equal to each other yields the drift limit (Klahr & Bodenheimer, 2006; Birnstiel et al., 2012)

$$a_{\mathrm{drift}} = \underbrace{\frac{\sqrt{3}}{2\sqrt{2\pi}}}_{\approx 0.543\cdot 2/\pi} \left(\frac{v_{\mathrm{K}}}{c_{\mathrm{s}}}\right)^2 \frac{\Sigma_{\mathrm{d}}}{\rho_{\mathrm{m}}} \left|\frac{\partial \ln P}{\partial \ln r}\right|^{-1} . \tag{E.101}$$

This is exactly the drift limit derived by Birnstiel et al. (2012) *including* their fudge factor of $f_{\mathrm{d}} = 0.55$ (see their Eq. (18) and their Tab. 1). But they did not take the factor of $1/2$ from Eq. (E.96) into account and, additionally, the factor $\sqrt{3\pi/8}$ was set to unity. Here, their fitting factor is "naturally" incorporated in the drift limit. This is, on first sight, remarkable since in the work of Birnstiel et al. (2012) the fudge factor $f_{\mathrm{d}} = 0.55$ was found by experimenting with different values and comparing the results of the simple two population model with simulation results produced with the methods presented in Birnstiel et al. (2010). As mentioned above, monodisperse growth — which was used to derive the drift limit — describes the growth of the representative species. Since the fitting factor of Birnstiel et al. (2012) was used in order to fit this species, it is not surprising that this factor is already in the equations. Additionally, the code of Birnstiel et al. (2010) is based on the Smoluchowski equation. Hence, deriving the growth timescale based on that equation should lead to estimates close to the results of these numerical simulations.

Bibliography

Abod, C. P., Simon, J. B., Li, R., et al. 2018, arXiv preprint arXiv:1810.10018 40, 41

Adachi, I., Hayashi, C., & Nakazawa, K. 1976, Progress of Theoretical Physics, 56, 1756 10, 28, 69

Anderson, D. E., Bergin, E. A., Blake, G. A., et al. 2017, ApJ, 845, 13 70

Andrews, S. M., Wilner, D., Hughes, A., Qi, C., & Dullemond, C. 2010, ApJ, 723, 1241 19, 28, 56

Andrews, S. M., Huang, J., Pérez, L. M., et al. 2018, ApJL, 869, L41 5, 9, 25

Arlt, R., & Urpin, V. 2004, A&A, 426, 755 24

Armitage, P. J. 2010, Astrophysics of planet formation (Cambridge University Press) 8, 55, 56

Asplund, M., Grevesse, N., Sauval, A. J., & Scott, P. 2009, Annual Review of Astronomy and Astrophysics, 47, 481 56

Auffinger, J., & Laibe, G. 2017, MNRAS, 473, 796 41

Baehr, H., Klahr, H., & Kratter, K. M. 2017, ApJ, 848, 40 56

Bai, X.-N., & Stone, J. M. 2010, ApJ, 722, 1437 41

—. 2014, ApJ, 796, 31 24, 56

Balbus, S. A., & Hawley, J. F. 1991, ApJ, 376, 214 24

Barge, P., & Sommeria, J. 1995, A&A, 295, L1 45

Barker, A. J., & Latter, H. N. 2015, Mon. Not. R. Astron. Soc., 450, 21 24

Barrow, J. D. 1981, Journal of physics A: Mathematical and General, 14, 729 99

Batygin, K., & Brown, M. E. 2010, ApJ, 716, 1323 49

—. 2016, The Astronomical Journal, 151, 22 49

Batygin, K., & Laughlin, G. 2015, Proceedings of the National Academy of Sciences, 112, 4214 46

Beitz, E., Güttler, C., Blum, J., et al. 2011, ApJ, 736, 34 29

Bergin, E. A. 2009, arXiv preprint arXiv:0908.3708 72

Béthune, W., Lesur, G., & Ferreira, J. 2016, A&A, 589, A87 24, 25, 56

Béthune, W., Lesur, G., & Ferreira, J. 2017, A&A, 600, A75 38

Birnstiel, T., Andrews, S. M., & Ercolano, B. 2012, A&A, 544, A79 110

Birnstiel, T., Dullemond, C. P., & Brauer, F. 2010, A&A, 513, A79 19, 24, 27, 28, 29, 32, 38, 49, 50, 51, 70, 91, 96, 99, 100, 126

Birnstiel, T., Fang, M., & Johansen, A. 2016, Space Science Reviews, 205, 41 13, 30

Birnstiel, T., Klahr, H., & Ercolano, B. 2012, A&A, 539, A148 14, 23, 24, 27, 32, 45, 58, 60, 66, 69, 73, 76, 88, 95, 96, 111, 112, 126

Birnstiel, T., Ormel, C., & Dullemond, C. 2011, A&A, 525, A11 73, 88, 111

Birnstiel, T., Dullemond, C. P., Zhu, Z., et al. 2018, ApJL, 869, L45 55

Blum, J., Gundlach, B., Mühle, S., & Trigo-Rodriguez, J. M. 2014, Icarus, 235, 156 95

Blum, J., & Münch, M. 1993, Icarus, 106, 151 12, 24, 25, 29, 45, 69, 95

Blum, J., & Wurm, G. 2008, Annu. Rev. Astron. Astrophys., 46, 21 24, 25, 29, 45, 69, 95

Blum, J., Gundlach, B., Krause, M., et al. 2017, MNRAS, 469, S755 24, 95

Boltzmann, L. 1872, Wiener Berichte, 66, 275 10, 121

Bond, J. C., O'Brien, D. P., & Lauretta, D. S. 2010, ApJ, 715, 1050 69

Booth, R. A., & Ilee, J. D. 2019, MNRAS, 487, 3998 72, 87, 88

Bordukat, S. 2019, Bachelor's thesis, Ruperto-Carola University Heidelberg 48

Bosman, A. D., Tielens, A. G., & van Dishoeck, E. F. 2018a, A&A, 611, A80 87

Bosman, A. D., Walsh, C., & van Dishoeck, E. F. 2018b, A&A, 618, A182 87

Bottke Jr, W. F., Durda, D. D., Nesvornỳ, D., et al. 2005a, Icarus, 175, 111 16, 17, 39, 95

—. 2005b, Icarus, 175, 111 47

—. 2005c, Icarus, 179, 63 47

Bottke Jr, W. F., Nolan, M. C., Greenberg, R., & Kolvoord, R. A. 1994, Icarus, 107, 255 47

Brasser, R., Duncan, M., & Levison, H. 2006, Icarus, 184, 59 49

—. 2007, Icarus, 191, 413 49

Brasser, R., Duncan, M., Levison, H., Schwamb, M., & Brown, M. 2012, Icarus, 217, 1 49

Brauer, F. 2008, PhD thesis, Ruperto-Carola University of Heidelberg 125

Brauer, F., Dullemond, C. P., & Henning, T. 2008a, A&A, 480, 859 24, 38, 100

Brauer, F., Henning, T., & Dullemond, C. P. 2008b, A&A, 487, L1 25

Brown, M. E., Trujillo, C., & Rabinowitz, D. 2004, ApJ, 617, 645 49

Campins, H., Davis, D., Weidenschilling, S., et al. 1996, ASP Conf. Ser. Vol. 107, Completing the Inventory of the Solar system 46

Carrera, D., Gorti, U., Johansen, A., & Davies, M. B. 2017, ApJ, 839, 16 40

Carrera, D., Johansen, A., & Davies, M. B. 2015, A&A, 579, A43 30, 40

Carry, B. 2012, Planetary and Space Science, 73, 98 26

Chapman, S. 1916, Philosophical Transactions of the Royal Society of London. Series A, Containing Papers of a Mathematical or Physical Character, 216, 279 10, 50

Chatterjee, S., & Tan, J. C. 2013, ApJ, 780, 53 46

Cheng, N.-S. 2009, Powder Technology, 189, 395 9, 50

Chiang, E., & Goldreich, P. 1997, ApJ, 490, 368 30, 55

Chiang, E., & Laughlin, G. 2013, MNRAS, 431, 3444 46

Clausius, R. 1859, Philosophical Magazine and Journal of Science, 17, 81 122

Cuzzi, J. N., Dobrovolskis, A. R., & Champney, J. M. 1993, Icarus, 106, 102 54

Cuzzi, J. N., Hogan, R. C., Paque, J. M., & Dobrovolskis, A. R. 2001, ApJ, 546, 496 8, 27, 54

Cuzzi, J. N., Hogan, R. C., & Shariff, K. 2008, ApJ, 687, 1432 24

Cuzzi, J. N., & Zahnle, K. J. 2004, ApJ, 614, 490 15, 70, 79, 87

D. N. C. Lin, J. P. 1980, Mon. Not. R. astr. Soc., 191 8

D'Alessio, P., Cantö, J., Calvet, N., & Lizano, S. 1998, ApJ, 500, 411 6

Davis, D. R., & Ryan, E. V. 1990, Icarus, 83, 156 12

Delbo, M., Walsh, K., Bolin, B., Avdellidou, C., & Morbidelli, A. 2017, Science, 357, 1026 18, 26, 91

Desch, S. J., Estrada, P. R., Kalyaan, A., & Cuzzi, J. N. 2017, ApJ, 840, 86 54

Desch, S. J., Kalyaan, A., & Alexander, C. M. 2018, The Astrophysical Journal Supplement Series, 238, 11 87

Dittrich, K., Klahr, H., & Johansen, A. 2013, ApJ, 763, 117 24, 25, 30, 31, 71

Dohnanyi, J. 1969, Journal of Geophysical Research, 74, 2531 12

Dones, L., Weissman, P. R., Levison, H. F., & Duncan, M. J. 2004, in Astronomical Society of the Pacific Conference Series, Vol. 323, Star Formation in the Interstellar Medium: In Honor of David Hollenbach, ed. D. Johnstone, F. C. Adams, D. N. C. Lin, D. A. Neufeeld, & E. C. Ostriker, 371 49

Drążkowska, J., & Alibert, Y. 2017, A&A, 608, A92 16, 19, 25, 40, 48, 79, 87

Drążkowska, J., Alibert, Y., & Moore, B. 2016, A&A, 594, A105 25, 39, 40, 41, 53, 91, 94, 95

Drążkowska, J., & Dullemond, C. P. 2018, A&A, 614, A62 38

Drążkowska, J., Windmark, F., & Dullemond, C. 2013, A&A, 556, A37 25

Drążkowska, J., Windmark, F., & Dullemond, C. P. 2014a, A&A, 567, A38 39

Drążkowska, J., Windmark, F., & Okuzumi, S. 2014b, Proceedings of the International Astronomical Union, 9, 208 25, 39

Dubrulle, B., Morfill, G., & Sterzik, M. 1995, Icarus, 114, 237 11, 27, 41, 54, 112

Dullemond, C., & Dominik, C. 2005, A&A, 434, 971 24

Dullemond, C. P., Birnstiel, T., Huang, J., et al. 2018, ApJL, 869, L46 5, 15, 25

Ehrenfreund, P., Charnley, S., & Wooden, D. 2004, Comets II, 115 69

Epstein, P. S. 1924, Physical Review, 23, 710 9, 27, 50

Eriksson, L. E., Johansen, A., & Liu, B. 2020, arXiv preprint arXiv:2001.11042 53

Estrada, P. R., Cuzzi, J. N., & Morgan, D. A. 2016, ApJ, 818, 200 25, 39

Facchini, S., Birnstiel, T., Bruderer, S., & van Dishoeck, E. F. 2017, A&A, 605, A16 72

Fernandez, J., & Ip, W.-H. 1984, Icarus, 58, 109 48

Fick, A. 1855, Annalen der Physik, 170, 59 54

Flaherty, K. M., Hughes, A. M., Rose, S. C., et al. 2017, ApJ, 843, 150 8

Fraser, W. C., & Kavelaars, J. 2008, The Astronomical Journal, 137, 72 16, 17, 39, 95

Fu, W., Li, H., Lubow, S., Li, S., & Liang, E. 2014, ApJL, 795, L39 30

Fuentes, C. I., & Holman, M. J. 2008, The Astronomical Journal, 136, 83 16, 17, 39, 49, 95

Gail, H.-P., & Trieloff, M. 2017, A&A, 606, A16 69

Gerbig, K., Lenz, C. T., & Klahr, H. 2019, A&A, 629, A116 66, 73, 87, 96

Gerbig, K., Murray-Clay, R. A., Klahr, H., & Baehr, H. 2020, arXiv preprint arXiv:2001.10552 18, 53, 71

Goldreich, P., & Lynden-Bell, D. 1965, MNRAS, 130, 97 56

Goldreich, P., & Ward, W. R. 1973, ApJ, 183, 1051 23, 24, 40, 41

Gomes, R., Levison, H. F., Tsiganis, K., & Morbidelli, A. 2005, Nature, 435, 466 48

Gough, D. 1981, in Physics of Solar Variations (Springer), 21–34 55

Gradie, J. C., Chapman, C. R., & Tedesco, E. F. 1989, in Asteroids II, ed. R. P. Binzel, T. Gehrels, & M. S. Matthews, 316–335 47

Güdel, M., Guinan, E. F., & Skinner, S. L. 1997, ApJ, 483, 947 57

Gundlach, B., & Blum, J. 2014, ApJ, 798, 34 24, 29, 45, 69, 95

Güttler, C., Blum, J., Zsom, A., Ormel, C. W., & Dullemond, C. P. 2010, A&A, 513, A56 23

Haisch, K. E. J., Lada, E. A., & Lada, C. J. 2001, ApJLetters, 553, L153 9

Hansen, B. M. 2009, ApJ, 703, 1131 46

Hansen, B. M., & Murray, N. 2012, ApJ, 751, 158 46

Hartmann, L., Calvet, N., Gullbring, E., & D'Alessio, P. 1998, ApJ, 495, 385 8

Hayashi, C. 1981, Progress of Theoretical Physics Supplement, 70 19, 30, 39, 46, 48, 60, 61, 65, 103

Helled, R., & Schubert, G. 2008, Icarus, 198, 156 47

Hill, G. W. 1878, American journal of Mathematics, 1, 5 17

Huang, J., Andrews, S. M., Dullemond, C. P., et al. 2018, ApJL, 869, L42 25

Huang, K. 1987, Statistical Mechanics, 2nd edn. (John Wiley & Sons) 121, 122

Hubeny, I. 1990, ApJ, 351, 632 66, 95

Husmann, T. 2017, PhD thesis, University of Duisburg-Essen 100

Ida, S., & Lin, D. 2008, ApJ, 673, 487 46

Jeans, J. H. 1902, Philosophical Transactions of the Royal Society of London. Series A, Containing Papers of a Mathematical or Physical Character, 199, 1 5, 17

Jewitt, D., Luu, J., & Trujillo, C. 1998, The Astronomical Journal, 115, 2125 49

Jewitt, D. C., Trujillo, C. A., & Luu, J. X. 2000, The Astronomical Journal, 120, 1140 17, 39, 95

Johansen, A., Henning, T., & Klahr, H. 2006, ApJ, 643, 1219 23

Johansen, A., Klahr, H., & Henning, T. 2006, ApJ, 636, 1121 19, 24, 40, 41, 45, 91, 95

—. 2011, A&A, 529, A62 41

Johansen, A., Mac Low, M.-M., Lacerda, P., & Bizzarro, M. 2015, Science Advances, 1, e1500109 37, 47

Johansen, A., Oishi, J. S., Mac Low, M.-M., et al. 2007, Nature, 448, 1022 24, 40, 41, 45, 95

Johansen, A., Youdin, A., & Klahr, H. 2009a, ApJ, 697, 1269 24

Johansen, A., Youdin, A., & Mac Low, M.-M. 2009b, ApJL, 704, L75 23, 24, 40

Johansen, A., & Youdin, A. N. 2007, ApJ, 662, 627 24

Johansen, A., Youdin, A. N., & Lithwick, Y. 2012, A&A, 537, A125 24

Kaib, N. A., & Quinn, T. 2008, Icarus, 197, 221 49

Kant, I. 1755, Trans. by Ian Johnston. Arlington, VA: Richer Resources 5

Kataoka, A., Tanaka, H., Okuzumi, S., & Wada, K. 2013, A&A, 557, L4 13, 18, 24, 39

Klahr, H., & Bodenheimer, P. 2006, ApJ, 639, 432 14, 23, 45, 69, 95, 126

Klahr, H., & Hubbard, A. 2014, ApJ, 788, 21 24

Klahr, H., Pfeil, T., & Schreiber, A. 2018, Handbook of Exoplanets, 2251 24, 25

Klahr, H., & Schreiber, A. 2015, Proceedings of the International Astronomical Union, 10, 1 18, 19, 25, 26, 39, 45, 53, 71, 91, 95, 106

Klahr, H. H., & Bodenheimer, P. 2003, ApJ, 582, 869 24

Klarmann, L., Ormel, C., & Dominik, C. 2018, A&A, 618, L1 70

Klessen, R. S., Spaans, M., & Jappsen, A.-K. 2005, Proceedings of the International Astronomical Union, 1, 337 5, 40

Kobayashi, H., Tanaka, H., & Okuzumi, S. 2016, ApJ, 817, 105 19, 39, 87, 96

Kokubo, E., & Ida, S. 1996, Icarus, 123, 180 87

Kokubo, E., Kominami, J., & Ida, S. 2006, ApJ, 642, 1131 46

Kolmogorov, A. N. 1991, Proceedings of the Royal Society of London. Series A: Mathematical and Physical Sciences, 434, 15 8

Kornet, K., Stepinski, T. F., & Rózyczka, M. 2001, A&A, 378, 180 124, 125

Kothe, S., Güttler, C., & Blum, J. 2010, ApJ, 725, 1242 13

Kresak, L. 1977, Bulletin of the Astronomical Institutes of Czechoslovakia, 28, 65 47

Krijt, S., Ciesla, F. J., & Bergin, E. A. 2016a, ApJ, 833, 285 24

Krijt, S., Ormel, C. W., Dominik, C., & Tielens, A. G. 2015, A&A, 574, A83 39

—. 2016b, A&A, 586, A20 24, 74

Krijt, S., Schwarz, K. R., Bergin, E. A., & Ciesla, F. J. 2018, ApJ, 864, 78 87

Lambrechts, M., & Johansen, A. 2012, A&A, 544, A32 16, 49

Laplace, P. S., & Young, T. 1821, Elementary illustrations of the Celestial mechanics of Laplace (J. Murray) 5

Larson, R. B. 2003, Reports on Progress in Physics, 66, 1651 5

Latter, H. N., & Papaloizou, J. 2017, MNRAS, 474, 3110 24

Lee, J.-E., Bergin, E. A., & Nomura, H. 2010, The Astrophysical Journal Letters, 710, L21 70

Lee, M. H. 2000, Icarus, 143, 74 100

Leinhardt, Z. M., & Stewart, S. T. 2009, Icarus, 199, 542 29

Lenz, C. T. 2016, Master thesis, Goethe University, Frankfurt am Main 6, 7, 15, 20

Lenz, C. T., Klahr, H., & Birnstiel, T. 2019, ApJ, 874, 36 23, 45, 46, 48, 52, 53, 54, 62, 66, 67, 70, 74, 88, 94, 95, 108, 111

Lesur, G., & Papaloizou, J. C. 2010, A&A, 513, A60 24

Levison, H. F., Duncan, M. J., & Thommes, E. 2012, The Astronomical Journal, 144, 119 87

Levison, H. F., Kretke, K. A., Walsh, K. J., & Bottke, W. F. 2015, Proceedings of the National Academy of Sciences, 112, 14180 46

Levison, H. F., Morbidelli, A., Tsiganis, K., Nesvornỳ, D., & Gomes, R. 2011, The Astronomical Journal, 142, 152 48

Levison, H. F., Thommes, E., & Duncan, M. J. 2010, The Astronomical Journal, 139, 1297 49

Lissauer, J. J. 1993, Annual review of astronomy and astrophysics, 31, 129 16

Lodders, K. 2003, ApJ, 591, 1220 30

Lüst, R. 1952, Zeitschrift Naturforschung Teil A, 7, 87 5, 38

Lynden-Bell, D., & Pringle, J. 1974, MNRAS, 168, 603 5, 8, 19, 28, 29, 52

Lyra, W. 2014, ApJ, 789, 77 24

Lyra, W., & Klahr, H. 2011, A&A, 527, A138 24

Lyra, W., & Umurhan, O. 2018, arXiv preprint arXiv:1808.08681 24

Malhotra, R. 1995, AJ, 110, 420 48

Mamajek, E. E. 2009in , American Institute of Physics, 3–10 9

Manger, N., & Klahr, H. 2018, MNRAS, 480, 2125 24, 31, 71

Massey, H., & Mohr, C. 1933, Proceedings of the Royal Society of London. Series A, Containing Papers of a Mathematical and Physical Character, 141, 434 50

Mathis, J. S., Rumpl, W., & Nordsieck, K. H. 1977, ApJ, 217, 425 30

Maxwell, J. C. 1860, Philosophical Magazine and Journal of Science, 19, 19 10, 121

Min, M., Dullemond, C., Kama, M., & Dominik, C. 2011, Icarus, 212, 416 30

Minton, D. A., & Malhotra, R. 2010, Icarus, 207, 744 47

Misener, W., Krijt, S., & Ciesla, F. J. 2019, ApJ, 885, 118 73

Morbidelli, A., Bottke, W. F., Nesvornỳ, D., & Levison, H. F. 2009, Icarus, 204, 558 17, 26, 39, 47, 91, 95

Morbidelli, A., Crida, A., Masset, F., & Nelson, R. P. 2008, A&A, 478, 929 49

Morbidelli, A., Levison, H. F., Tsiganis, K., & Gomes, R. 2005, Nature, 435, 462 48

Morbidelli, A., Tsiganis, K., Crida, A., Levison, H. F., & Gomes, R. 2007, The Astronomical Journal, 134, 1790 48

Morbidelli, A., Walsh, K. J., O'Brien, D. P., Minton, D. A., & Bottke, W. F. 2015, arXiv preprint arXiv:1501.06204 47, 95

Morbidelli, A., Bitsch, B., Crida, A., et al. 2016, Icarus, 267, 368 46

Morfill, G., & Völk, H. 1984, ApJ, 287, 371 54

Musiolik, G., Teiser, J., Jankowski, T., & Wurm, G. 2016, ApJ, 818, 16 12

Musiolik, G., & Wurm, G. 2019, ApJ, 873, 58 45, 56

Nakagawa, Y., Sekiya, M., & Hayashi, C. 1986, Icarus, 67, 375 10, 28, 39, 52, 69

Nakamoto, T., & Nakagawa, Y. 1994, ApJ, 421, 640 55, 66

Nelson, R. P., Gressel, O., & Umurhan, O. M. 2013, MNRAS, 435, 2610 24

Nesvornỳ, D., & Morbidelli, A. 2012, The Astronomical Journal, 144, 117 49

Nesvornỳ, D., & Vokrouhlickỳ, D. 2016, ApJ, 825, 94 49

Nesvornỳ, D., Vokrouhlickỳ, D., Bottke, W. F., Noll, K., & Levison, H. F. 2011, The Astronomical Journal, 141, 159 49

Nesvornỳ, D., Vokrouhlickỳ, D., & Morbidelli, A. 2013, ApJ, 768, 45 48

Newton, I. 1729, The mathematical principles of natural philosophy. By Sir Isaac Newton. Translated into English by Andrew Motte. To which are added, The laws of the moon's motion, according to gravity. By John Machin Astron. Prof. Gresh. and Secr. R. Soc. In two volumes (Benjamin Motte, at the Middle-Temple-Gate, in Fleetstreet) 50

Öberg, K. I., Murray-Clay, R., & Bergin, E. A. 2011, ApJL, 743, L16 15, 81, 94

O'Brien, D. P., & Greenberg, R. 2005, Icarus, 178, 179 47

Okuzumi, S. 2009, ApJ, 698, 1122 24

Okuzumi, S., Tanaka, H., Kobayashi, H., & Wada, K. 2012, ApJ, 752, 106 13, 18, 24, 39

Ormel, C., & Cuzzi, J. 2007, A&A, 466, 413 11, 14, 28, 54, 110, 124

Ormel, C., & Klahr, H. 2010, A&A, 520, A43 19, 23, 38, 45, 69, 96

Ormel, C., Paszun, D., Dominik, C., & Tielens, A. 2009, A&A, 502, 845 12

Ormel, C. W. 2017, in Formation, Evolution, and Dynamics of Young Solar Systems (Springer), 197–228 45, 69

Ostriker, J. P. 1963, ApJ, 138, 281 55

Owen, J. E., Clarke, C. J., & Ercolano, B. 2012, MNRAS, 422, 1880 38, 106

Pan, M., & Sari, R. 2005, Icarus, 173, 342 49

Papaloizou, J., & Lin, D. 1995, ARA&A, 33, 505 38

Petersen, M. R., Julien, K., & Stewart, G. R. 2007a, ApJ, 658, 1236 24

Petersen, M. R., Stewart, G. R., & Julien, K. 2007b, ApJ, 658, 1252 24

Pfalzner, S., Steinhausen, M., & Menten, K. 2014, The Astrophysical Journal Letters, 793, L34 9

Pfeil, T., & Klahr, H. 2019, ApJ, 871, 150 6, 25, 55, 56, 65

Picogna, G., Ercolano, B., Owen, J. E., & Weber, M. L. 2019, MNRAS 55, 106, 107

Pinilla, P., Birnstiel, T., Ricci, L., et al. 2012, A&A, 538, A114 15, 63, 87

Pohl, A. 2018, PhD thesis, Ruperto-Carola University Heidelberg 6

Pollack, J. B., Hubickyj, O., Bodenheimer, P., et al. 1996, Icarus, 124, 62 20

Pontoppidan, K. M., Salyk, C., Bergin, E. A., et al. 2014, in Protostars and Planets VI, ed. H. Beuther, R. S. Klessen, C. P. Dullemond, & T. Henning, 363 69

Pringle, J. E. 1981, ARA&A, 19, 137 8, 27, 30, 38, 55

Raettig, N., Klahr, H., & Lyra, W. 2015, ApJ, 804, 35 24, 30

Raettig, N., Lyra, W., & Klahr, H. 2013, ApJ, 765, 115 24

Rafikov, R. R. 2003, The Astronomical Journal, 125, 942 87

Rayleigh, L. 1892, The London, Edinburgh, and Dublin philosophical magazine and journal of science, 34, 59 50

Raymond, S. N., & Izidoro, A. 2017, Science advances, 3, e1701138 48

Reeks, M. 1983, Journal of Aerosol Science, 14, 729 54

Reif, F. 2009, Fundamentals of Statistical and Thermal Physics (Waveland Press) 121, 123

Safronov, V. S. 1969, Evoliutsiia Doplanetnogo Oblaka. (English transl.: Evolution of the protoplanetary cloud and formation of Earth and the planets, NASA Tech. Transl. F-677, Jerusalem: Israel Sci. Transl. 1972) 5, 10, 16, 23, 24, 27, 28, 40

Saumon, D., & Guillot, T. 2004, ApJ, 609, 1170 47

Savage, B. D., & Jenkins, E. B. 1972, ApJ, 172, 491 29

Schoonenberg, D., & Ormel, C. W. 2017, A&A, 602, A21 91, 94

Schoonenberg, D., Ormel, C. W., & Krijt, S. 2018, A&A, 620, A134 16, 19, 48, 53, 79, 87

Schreiber, A. 2018, PhD thesis, Ruperto-Carola University Heidelberg 18, 19, 25, 26, 30, 39, 40, 41, 45, 53, 71, 91, 95, 103, 106

Schreiber, A., & Klahr, H. 2018, ApJ, 861, 47 41, 95

Schumann, T. 1940, Quarterly Journal of the Royal Meteorological Society, 66, 195 99

Sekiya, M. 1998, Icarus, 133, 298 23

Semenov, D., & Wiebe, D. 2011, The Astrophysical Journal Supplement Series, 196, 25 72

Semenov, D., Hersant, F., Wakelam, V., et al. 2010, A&A, 522, A42 72

Shakura, N. I., & Sunyaev, R. A. 1973, A&A, 24, 337 5, 8, 9, 27, 55

Sheppard, S. S., & Trujillo, C. A. 2010, ApJL, 723, L233 17, 39, 95

Simon, J. B., Armitage, P. J., Li, R., & Youdin, A. N. 2016, ApJ, 822, 55 25, 40

Singer, K. N., McKinnon, W. B., Gladman, B., et al. 2019, Science, 363, 955 49

Squire, J., & Hopkins, P. F. 2018a, MNRAS, 477, 5011 23

—. 2018b, ApJL, 856, L15 23

Stammler, S., & Birnstiel, T. in prep. 49

Stammler, S. M., Birnstiel, T., Panić, O., Dullemond, C. P., & Dominik, C. 2017, A&A, 600, A140 16, 24, 87

Stammler, S. M., DraÌ§żkowska, J., Birnstiel, T., et al. 2019, The Astrophysical Journal Letters, 884, L5 5, 15, 53

Steffl, A., Cunningham, N., Shinn, A., Durda, D., & Stern, S. 2013, Icarus, 223, 48 46

Steinpilz, T., Joeris, K., Jungmann, F., et al. 2019, Nature Physics, 1 14, 45

Stepinski, T. F., & Valageas, P. 1997, A&A, 319, 1007 124, 125

Stokes, G. G. 1851, On the effect of the internal friction of fluids on the motion of pendulums, Vol. 9 (Pitt Press Cambridge) 10, 28, 51

Stoll, M. H., & Kley, W. 2014, A&A, 572, A77 24

—. 2016, A&A, 594, A57 24

Takeuchi, T., & Lin, D. 2002, ApJ, 581, 1344 29

Tanaka, H., Himeno, Y., & Ida, S. 2005, ApJ, 625, 414 10, 39

Tanaka, H., Inaba, S., & Nakazawa, K. 1996, Icarus, 123, 450 12

Teague, R., Guilloteau, S., Semenov, D., et al. 2016, A&A, 592, A49 8

Teiser, J., & Wurm, G. 2009, MNRAS, 393, 1584 13

Thommes, E. W., & Duncan, M. J. 2006, The accretion of giant-planet cores, ed. H. Klahr & W. Brandner, 129 48

Thommes, E. W., Duncan, M. J., & Levison, H. F. 1999, Nature, 402, 635 48

Toomre, A. 1964, ApJ, 139, 1217 56

Trujillo, C. A., & Brown, M. E. 2001, The Astrophysical Journal Letters, 554, L95 49

Tsiganis, K., Gomes, R., Morbidelli, A., & Levison, H. 2005, Nature, 435, 459 48

Turner, N. J., Fromang, S., Gammie, C., et al. 2014, Protostars and Planets VI, 411 8

Tyrrell, H. J. V. 1964, Journal of Chemical Education, 41, 397 54

Urpin, V., & Brandenburg, A. 1998, MNRAS, 294, 399 24

Vagnozzi, S. 2019, Atoms, 7, 41 56

Vidotto, A. A., Gregory, S. G., Jardine, M., et al. 2014, MNRAS, 441, 2361 57

Visser, R. G., & Ormel, C. W. 2016, A&A, 586, A66 19, 87, 96

Volk, K., & Gladman, B. 2015, The Astrophysical Journal Letters, 806, L26 46

Völkel, O., Klahr, H., Mordasini, C., Emsenhuber, A., & Lenz, C. 2020, arXiv preprint arXiv:2004.03492 70, 93

von Smoluchowski, M. 1916, Z. Phys., 17, 557 14, 28, 50, 91, 99, 111

Wada, K., Tanaka, H., Suyama, T., Kimura, H., & Yamamoto, T. 2009, ApJ, 702, 1490 29

Wahl, S. M., Hubbard, W. B., Militzer, B., et al. 2017, Geophysical Research Letters, 44, 4649 47, 48

Walsh, K. J., Morbidelli, A., Raymond, S. N., O'Brien, D. P., & Mandell, A. M. 2011, Nature, 475, 206 46, 47

Weidenschilling, S., Spaute, D., Davis, D., Marzari, F., & Ohtsuki, K. 1997, Icarus, 128, 429 96

Weidenschilling, S. J. 1977a, MNRAS, 180, 57 10, 28, 51, 52, 69

—. 1977b, Astrophysics and Space Science, 51, 153 13, 19, 39, 46, 48, 60, 61, 64, 103

—. 1980, Icarus, 44, 172 24

—. 1995, Icarus, 116, 433 23, 40

Weizsäcker, C. F. 1948, Zeitschrift für Naturforschung A, 3, 524 5, 27

Weizsäcker, C. F. V. 1943, Zeitschrift für Astrophysik, 22, 319 5

Wetherill, G., & Stewart, G. 1993, Icarus, 106, 190 87

Whipple, F. L. 1972, in From plasma to planet, 211 10, 15, 25, 45, 51, 69

Williams, J. P., Cieza, L., Hales, A., et al. 2019, The Astrophysical Journal Letters, 875, L9 96

Windmark, F., Birnstiel, T., Güttler, C., et al. 2012a, A&A, 540, A73 13

Windmark, F., Birnstiel, T., Ormel, C. W., & Dullemond, C. P. 2012b, A&A, 544, L16 18, 24, 25, 39, 55

Wölfer, L., Picogna, G., Ercolano, B., & van Dishoeck, E. F. 2019, MNRAS, 490, 5596 106

Wooden, D. 2008, Space Science Reviews, 138, 75 69

Wooden, D. H. 2000, Earth, Moon, and Planets, 89, 247 69

Yang, C. C., Johansen, A., & Carrera, D. 2017, A&A, 606, A80 30, 40, 53

Yang, C.-C., Mac Low, M.-M., & Johansen, A. 2018, ApJ, 868, 27 37

Youdin, A. N., & Goodman, J. 2005, ApJ, 620, 459 19, 23, 40, 45

Youdin, A. N., & Lithwick, Y. 2007, Icarus, 192, 588 29, 53

Youdin, A. N., & Shu, F. H. 2002, ApJ, 580, 494 24, 40

Zhang, K., Bergin, E. A., Schwarz, K., Krijt, S., & Ciesla, F. 2019, ApJ, 883, 98 87

Zhang, K., Bosman, A. D., & Bergin, E. A. 2020, The Astrophysical Journal Letters, 891, L16 87

Zsom, A., Ormel, C., Güttler, C., Blum, J., & Dullemond, C. 2010, A&A, 513, A57 14, 23, 45

Zvyagina, E., Pechernikova, G., & Safronov, V. 1974, Soviet Astronomy, 17, 793 24

Publications

The following papers published or submitted have been part of this thesis:

- **Lenz, C. T.**, Klahr, H., & Birnstiel, T. 2019
  Planetesimal Population Synthesis: Pebble Flux-regulated Planetesimal Formation
  ApJ, 874, 36
- **Lenz, C. T.**, Klahr, H., Birnstiel, T., Kretke, K. & Stammler, S. 2020
  Toward Constraining the Parameter Space for the Solar Nebula. The Influence of Disk Properties on Planetesimal Formation
  A&A, accepted
- **Lenz, C. T.**, Krijt, S., Klahr, H., Pinilla, P., & Birnstiel, T. 2020
  On Planetesimal Formation Feeding Zones and Tracing Their Material
  submitted

Other (upcoming) publications including contributions from me that are not part of this thesis:

- Gerbig, K., **Lenz, C. T.**, & Klahr, H. 2019
  Linking planetesimal and dust content in protoplanetary disks via a local toy model
  A&A, 629, A116
- Völkel, O., Klahr, H., Mordasini, C., & **Lenz, C. T.** 2020
  The impact of pebble flux-regulated planetesimal formation on giant planet formation
  submitted, arXiv:2004.03492
- Latka, R., Krijt, S., Pascucci, I., Klahr, H., Birnstiel, T., & **Lenz, C. T.** 2020
  Stellar-mass dependent disk evolution: explaining disk masses and sizes
  in prep.

Acknowledgments

> *“We are like dwarfs on the shoulders of giants, so that we can see more than they, and things at a greater distance, not by virtue of any sharpness of sight on our part, or any physical distinction, but because we are carried high and raised up by their giant size.”*
>
> – Bernard de Chartres

I have big gratitude for my advisor Hubert Klahr, who discussed scientific topics with me for four years. I will always remember your way of explaining complex processes by simple estimates and comparisons.

I am very thankful for many scientific discussions with the following people: Joanna Drążkowska, for many discussions about planetesimals formation models, a problem we both worked on. Til Birnstiel, who explained details of his code to me and discussed the underlying assumptions. Sebastiaan Krijt and Paola Pinilla, who both were able to spark off a fire that awakened my interest in science when I was not able to do so. Thank you for very enthusiastic discussions. I would like to thank Chris Ormel, Alessandro Morbidelli, Kees Dullemond, Matias Garate, Vince Carpenter, Grigorii Smirnov-Pinchukov, Sierk van Terwisga, Lucia Klarmann, and Sebastian Marino for many fruitful discussions and their interest in my work. Special thanks for science discussions and beyond go to: Andreas Schreiber, Oliver Völkel, Irina Smirnova-Pinchukova, and Grigorii Smirnov-Pinchukov. Also, thank you, Andreas, for the awesome LaTeX template! I am very grateful to the proofreaders: Stefan Strohauer, Oliver Völkel, Kristin Raykova, Andreas Schreiber, and my father. Your suggestions helped to improve this thesis and make it easier to read. I am also thankful to Stefan Strohauer and Kristin Raykova for great support over several years.

I would like to thank my office mates for helping each other, for example with little tricks to matplotlib, or for discussing new ideas. These are Adriana Pohl, Andreas Schreiber, Paul Molliere, Christoph Engler, Hector Hiss, Hans Baehr, Sven Buder, Natascha Manger, Arianna Musso-Barcucci, Josha van Houdt, and Johanna Coronado.

Another special thanks goes to the bachelor students who I have supervised with pleasure: Konstantin Gerbig and Marie Steinmeyer. The discussions we had helped to improve my teaching skills and it was a great pleasure to me, to see your ever growing interest on astrophysics and the development how you tackle scientific questions.

My family and friends always supported me, especially over the last two intensive months. Thank you for keeping me on track! I will never forget your unconditional support during the time I worked on this thesis.

I also want to thank Mario Trieloff, who kindly agreed to referee this work.

Declaration of Originality

Declaration of Originality

I hereby declare that this thesis is my own work and
that I have used no other than the stated sources and aids.

Declaration

Ich versichere, dass ich diese Arbeit selbstständig verfasst habe und
keine anderen als die angegebenen Quellen und Hilfsmittel benutzt habe.

Heidelberg, June 5, 2020

(Christian T. Lenz)